



Universidad de Valladolid



PROGRAMA DE DOCTORADO EN QUÍMICA

TESIS DOCTORAL:

**Interstellar Dust Analogues: Structure,
Survivability and Physical Processes**

Presentada por Germán Molpeceres de Diego para
optar al grado de
Doctor por la Universidad de Valladolid

Dirigida por:
Belén Maté Naya

UNIVERSITY OF VALLADOLID

Abstract

Faculty Name

Departamento de Física Molecular IEM-CSIC

Doctor in Chemistry

Interstellar Dust Analogues: Structure, Survivability and Physical Processes

by Germán MOLPECERES

Astronomical surveys require of laboratory and theoretical data for its interpretation. Cosmic dust structure is heavily linked with its observed physico chemical properties. In this thesis we have employed dust analogues, either generated in the laboratory or computationally, to study a series of processes with relevance in the physics and chemistry of the interstellar medium.

Acknowledgements

Me gustaría recalcar que agradecer a todas las personas que en mayor o menor medida han hecho posible cristalizar esta tesis es imposible, y por lo tanto quiero pedir disculpas a todas aquellas personas que no figuren en estos párrafos.

Sin mas dilación, me gustaría dedicar el agradecimiento mas cálido a los principales artífices de que esto haya sido posible, empezando por mis padres y siguiendo por mi supervisora, la Dra Belén Maté. Inmediatamente después la lista continua con los demás miembros del grupo: el Prof. Rafael Escribano, el Prof. Víctor Herrero, la Dra Isabel Tanarro y el Dr. Vicente Timón. Creo firmememnte que la sinergia existente entre la espectroscopía, la física de plasmas y el modelado teórico presente en el grupo suma (y mucho) a la calidad de la investigación llevada a cabo en el departamento de Física Molecular. Asimismo, creo que nunca podré llegar a estar lo suficientemente agradecido a mi directora de tesis por la libertad a la hora de abordar los diferentes temas que hemos afrontado en estos cuatro años.

Querría agradecer también a cada uno de mis supervisores individuales durante las estancias de investigación, a saber: Dr. Albert Rimola de la Universidad Autónoma de Barcelona, Prof. Naoki Watanabe del Instituto de Ciencia de Baja Temperatura, Universidad de Hokkaido y el Prof. Johannes Kästner del instituto de Química Teórica de la Universidad de Stuttgart. De todos y cada uno de ellos he adquirido competencias y habilidades para los difíciles años que están por llegar. A los colaboradores Alcoyanos por sus medidas de densidad hielos también les estoy agradecido, destacando a M.A Satorre, de la UPV.

Probablemente sea posible tener mas suerte de la que he tenido yo para encontrar excelentes compañeros y amigos en las estancias, pero creo que es francamente difícil. En cada uno de los sitios que he visitado he hecho buenos amigos. Joan, Sergi, Egil y Sonia en Barcelona, así como a todo el grupo GETAB de la UAB. En Japón Tetsuya, Yasuhiro, Yukiko, Tomaru, Ayane y Tomoya y demás miembros del equipo de los Watanabe-sensei y Kouchi-sensei (especial mención merece Taniguchi-san). Finalmente, en Stuttgart todo el grupo del prof Kästner merece un agradecimiento sincero, por hacer de mi estancia un placer. Sin embargo, Sonia (en este caso de Vigo, que fallos tenemos todos) debe tener un hueco especial, pues ha asumido el rol de post doc de apoyo durante la escritura de la tesis a las mil maravillas. Unas palabras especiales también para Joel, mi gran colega del CSIC.

Quiero agradecer profundamente a mis dos grupos de amigos, tanto de la universidad como del colegio su compañía estos años, así como a Antía por el apoyo durante gran parte de la tesis. Sería demasiado largo nombraros a todos ahora y cada uno sabe la magnitud de su contribución. De mi etapa mas reciente no quiero dejar pasar la oportunidad de agradecer a Ali su apoyo incondicional.

Para terminar, en ronda miscelánea, quiero agradecer la financiación por medio de las ayudas para la formación de doctores. A la Universidad de Valladolid y en especial al grupo de química teórica de allí, por mostrarme la belleza del modelado computacional (gracias Carmen y Antonio).

Mis más sinceros agradecimientos a los miembros del tribunal, los doctores Guillermo Muñoz Caro, Stephanie Cazaux, Alberto Lesarri, Pedro Gómez y Elena Jiménez.

En Madrid, a 14 de Enero de 2019

Germán Molpeceres

Contents

Abstract	iii
Acknowledgements	v
Contents	vii
List of Abbreviations	xi
List of Figures	xiii
List of Tables	xvii
1 Astrochemistry: From Molecules to Condensed Systems	1
1.1 Introduction	1
1.2 Solid State Materials in Astrochemistry	4
1.2.1 Ices	4
1.2.2 Dust	6
Carbonaceous Materials in the ISM	8
Siliceous Materials in the ISM	9
Chemical Analogues	11
1.3 Objectives of the Thesis	11
References	12
2 Methodology	19
2.1 Vibrational Spectroscopy of Solids	19
2.1.1 Differences Between Gas and Solid Phase Spectra	19
2.1.2 Harmonic Description of the Vibrations	21
2.2 Theoretical Background	23
2.2.1 Kohn-Sham Formalism	24
2.2.2 Density Functional Theory in Extended Systems	26
2.2.3 Evaluation of Vibrational Frequencies and Infrared Intensities	30
2.2.4 Transition State Theory	32
2.3 Experimental Techniques	34
2.3.1 Experimental Setup for IR Spectroscopy and Electronic Processing	35
2.3.2 Experimental Setup for Carbonaceous Sample Growth: PECVD	38
2.3.3 Experimental Quantification of Total Infrared Intensities and Absorption Cross Sections	40
References	42
3 Structure and Spectral Features of Hydrogenated Amorphous Carbon	45

3.1	Introduction	45
3.2	Methods	51
3.2.1	Theoretical approach: Generation of carbonaceous HAC packed chemical analogues and IR spectra calculation.	52
3.2.2	Experimental Setup: HAC Generation and IR Spectroscopy	53
3.2.3	Theoretical approach: determination of the UV-Vis spectrum of HAC analogues	54
3.2.4	Theoretical Approach: determination of IR emission of isolated domains in HAC analogues	55
3.3	Results: IR Absorption spectra of HAC analogues	57
3.3.1	Structural Models	57
3.3.2	Description of the Infrared Absorption Spectra	59
3.3.3	Density Variations	61
3.3.4	Evaluation of the Composition of the HAC analogues from the Spectra	62
3.4	Results: UV absorption and Infrared emission of HAC analogues	67
3.4.1	UV absorption: UV bump	69
3.4.2	IR emission	72
3.5	Conclusion: Astrophysical implications	76
	References	79
4	Survivability of Carbonaceous Dust Chemical Analogues	87
4.1	Introduction	87
4.1.1	Dense vs Diffuse Molecular Clouds: The case of the 3.4 μm band	88
4.1.2	Cosmic Rays Interaction with Carbonaceous Grains: Previous Works	90
4.2	Experiment and Model	92
4.2.1	Experimental setup	92
4.2.2	Calibration of the Electron Gun	94
4.2.3	Kinetic Model	95
4.3	Results	98
4.3.1	Montecarlo Simulations	98
4.3.2	HAC analogues processing	100
4.3.3	Kinetic Study	103
4.4	Astrophysical Implications	108
	References	109
5	Surface Reactions on Dust Grains: Water formation over Forsterite	115
5.1	Introduction	116
5.2	Theoretical Methods	119
5.2.1	Surface Model	120
5.2.2	Computational Methods	121
5.3	Results	125
5.3.1	Oxygen Adsorption	125
5.3.2	Hydrogen Diffusion: Products Formation	128
	OH formation	128
	H ₂ O formation	131
	Desorption of the products	132

5.3.3	Rate Constant Calculation	134
5.4	Conclusion and Astrophysical Implications	137
	References	138
6	Conclusions	143
A	Producción Científica	147
B	Curriculum Vitae	153
C	Resumen de la Tesis	157

List of Abbreviations

a:C	Amorphous Carbon (Material Science Notation)
a:C-H	Hydrogenated Amorphous Carbon (Material Science Notation)
AC	Atomic Charge
B3LYP	Becke 3-parameter Lee Yang Park Exchange-Correlation Functional
BSSE	Basis Set Superposition Error
COM	Complex Organic Molecules
CR	Cosmic Rays
DFT	Density Functional Theory
DFPT	Density Functional Perturbation Theory
DIB	Diffuse Interstellar Bands
DRC	Distinguished Reaction Coordinate
ERE	Extended Red Emission
FTIR	Fourier Transform InfraRed
Fo	Forsterite
HAC	Hydrogenated Amorphous Carbon (Astrophysical Notation)
HV	High Vacuum
IR	InfraRed
ISM	InterStellar Medium
LH	Langmuir Hinshelwood adsorption mechanism
LET	Linear Energy Transfer
PAH	Polycyclic Aromatic Hydrocarbons
PBC	Periodic Boundary Conditions
PBE	Perdew Burke Ernzerhof Exchange-Correlation Functional
PECVD	Plasma Enhanced Chemical Vapour Deposition
PES	Potential Energy Surface
QMMM	Quantum Mechanics Molecular Mechanics
QMS	Quadrupole Mass Specrometer
RC	Rings and Chains HAC paradigm
RF	Radio Frequency
SCF	Self Consistent Field
SD	Spin Density
SG	Substitued Graphite HAC paradigm
TST	Transition State Theory
UIE	Unidentified Infrared Emission
UV	UltraViolet
ZPE	Zero Point Energy

List of Figures

1.1	Astronomers Periodic Table. The size of the elements indicate the abundance.	2
1.2	Summarized view of the cosmic matter cycle	3
1.3	Phase diagram of Solid Water.	5
1.4	Infrared spectra showing some of the most relevant ice features.	6
1.5	Barnard68 Dark Cloud	7
1.6	Diamond unit cell and Buckminster Fullerene C_{60} , two crystalline carbonaceous materials found in the ISM	8
1.7	Amorphous packings of hydrogenated amorphous carbon analogues showing diversity in their C/H ratio and structure.	9
1.8	Different Olivine Structures as a function of its Iron content	10
2.1	Diagram showing different vibrational normal modes	20
2.2	Schematic representation of the PES of a system during a chemical reaction	33
2.3	Transversal cross section of the vacuum chamber in the optic plane	36
2.4	Lateral View of our High Vacuum Chamber.	37
2.5	Physical Processes in Plasma Polymerization	38
2.6	General chemical fragmentations and recombinations in a plasma polymerization.	39
2.7	Experimental scheme for our carbonaceous, plasma grown polymers	40
3.1	Different evolutionary stages of a dust grain particle as a function of the distance to the formation region.	46
3.2	Averaged UV Bump together with individual features observed toward different sources	48
3.3	Unidentified Infrared Emission features of a Planetary Nebula (NGC 7027), of a Photodissociation Region (Orion Bar) and the nuclear region of an HII galaxy (NGC4536)	49
3.4	3.4 and 5-8 μm absorption profiles with its associated gaussian decomposition of the main molecular modes corresponding to IRAS 08572+3915 (upper panel) and laboratory generated HAC samples (lower panel)	50
3.5	$sp^3/sp^2/H$ Ternary diagram of amorphous carbon materials.	51
3.6	Theoretical Model Validation on Solid Phenantrene	53
3.7	Molecular models considered in the evaluation of the properties of chemical HAC analogues.	58
3.8	Packed HAC archetypes at different densities.	58
3.9	Experimental and Theoretical Spectra of HAC samples.	60
3.10	IR Spectra of HAC analogues as a function of the density	62

3.11	Gaussian Decomposition of the laboratory analogues for our HAC archetypes	63
3.12	Ternary Diagram position of theoretical and Experimental HAC models.	66
3.13	HAC photgraphitic islands bonded to polymeric material as proposed by Duley et al	68
3.14	UV absorption of different 1.25 gcm^{-3} analogues normalized with respect the SG analogue	70
3.15	Normalized UV absorption of different HAC archetypes as a function of the density.	71
3.16	Emission curves obtained for the two different HAC archetypes at 1.25 gcm^{-3} .	74
3.17	Emission curves obtained for the two different HAC archetypes as a function of the density.	75
3.18	Emission curve of an arophatic analogue.	76
3.19	Infrared absorption comparison of our analogues with information from IRAS 08572+3915	77
4.1	$3.4 \mu\text{m}$ absorption band towards diffuse clouds	88
4.2	Cosmic Ray Energy Distribution from Atmospheric Air Showers	91
4.3	HAC samples grown in our laboratory	93
4.4	Scheme of the electron gun used in our experiments	94
4.5	Calibration of the Electron Gun.	95
4.6	Classical Electron Trajectories in Different HAC Materials	100
4.7	Infrared Spectra of our deposited HAC analogues between $3300\text{-}1100 \text{ cm}^{-1}$. Sample thickness of 500 nm .	101
4.8	$3.4 \mu\text{m}$ band decrease upon processing and Gaussian deconvolution analysis such band	102
4.9	Asymmetric stretches $3.4 \mu\text{m}$ band decay of the HAC materials	103
4.10	Total decay of the $3.4 \mu\text{m}$ band of the HAC materials	104
4.11	Normalized decay curves for the destruction of the total $3.4 \mu\text{m}$ band with high energy ions (Godard et al, 2011) and electrons (our results)	106
5.1	General scheme for the reaction network leading to the formation of interstellar H_2O .	117
5.2	Dust and Ice IR spectra of MYSO AFGL 7009S	118
5.3	General Langmuir-Hinshelwood Mechanism Scheme with only H diffusion	119
5.4	Lateral and Top view of the model forsterite surface.	120
5.5	Zoom of the sites with different adsorption capabilities considered in this job.	120
5.6	Cluster employed in the benchmark study (this image correspond to the singlet state)	121
5.7	Triplet and Singlet adsorbed oxygen on the Forsterite surface.	126
5.8	Mg1-O_{ads} coordinate energy scan in the Forsterite-O singlet and triplet adduct.	127
5.9	DFT Optimized Structures Found During H Diffusion Yielding Forsterite-OH	128
5.10	ZPE corrected reaction path profile for the formation of Forsterite-OH	130

5.11 DFT Optimized Structures Found During H Diffusion Yielding Forsterite- H ₂ O	131
5.12 ZPE corrected reaction path profile for the formation of Forsterite-H ₂ O .	133
5.13 Calculated desorption curves of the OH and H ₂ O from the Fo-OH and Fo-H ₂ O adducts. Desorption energies include ZPE corrections.	134
5.14 Arrhenius Plots Between 450 and 50 K Representing Rate Constants with and without Tunneling Corrections (Eckart & Fermann-Auerbach)	136

List of Tables

3.1	Relative energies of the RC and SG HAC analogues as a function of the density	59
3.2	Assignments of main vibrations of HAC analogues spectra.	61
3.3	Gaussian Decomposition Parameters employed in our HAC experimental IR spectra fit.	64
3.4	Optimized area of individual gaussian components in the 3.4 μm band feature in the experimental HAC analogues	65
3.5	Atomic composition ratio from profile decomposition and from models in HAC chemical analogues.	65
4.1	Different Molecular Clouds and classification attending to their physical parameters	89
4.2	LETs of the HAC materials (530 nm, C/H=1) as a function of the density using 10000 trajectories	100
4.3	Band decomposition of unprocessed HAC Deposits (all in cm^{-1})	102
4.4	Parameters for the different kinetic models employed in the fit of the e^- processing of HAC	105
4.5	Extrapolated e^- - Cosmic rays destruction rates in diffuse clouds under the monoenergetic proton approximation for our HAC samples	107
4.6	Literature Comparison of Cosmic Rays C-H destruction Rates	107
4.7	Characteristic times for C-H bond destruction by cosmic rays and UV photons in dense and diffuse clouds	108
5.1	Exchange-correlation functional calibration study on gas phase clusters	122
5.2	Spin Densities and Atomic Charges of the atoms involved in the Forsterite-Oxygen adsorption in the Singlet and Triplet State (in atomic units)	126
5.3	Atomic Charges and Spin Densities of the hydrogen atom for the different adsorbates in the $\text{O}+\text{H} \rightarrow \text{OH}$ reaction (in atomic units)	129
5.4	Atomic Charges and Spin Densities of the diffusing hydrogen atom for the different adsorbates in the $\text{OH}+\text{H} \rightarrow \text{H}_2\text{O}$ reaction (in atomic units)	132
5.5	Energies and ZPE corrected energies for the thermodynamic adsorption and desorptions studied in this work	135
5.6	DFT Calculated ZPE Barrier Heights, Module of the Imaginary Transition Frequencies and Tunneling Crossover Temperatures	135

Dedicado a mis padres

Chapter 1

Astrochemistry: From Molecules to Condensed Systems

1.1 Introduction

When writing a thesis introduction it is always difficult to choose the initial words. Which is the optimal starting point? Is Big Bang a good choice for natural sciences dissertations? And Socrates for philosophy? Luckily for the sake of this document, in our case we can make a safe bet starting between $\sim 4 \cdot 10^5 - 1 \cdot 10^9$ years after the Big Bang, when the heaviest element considered in this thesis, silicon, was ejected from supernova explosions and mass-loss processes in late type stars. (Yamamoto, 2017).

The standard cosmological model states that baryonic matter, that is protons, electrons, neutrons, atoms and so on, only account for five percent of the total universe mass (Lazarides, 1999). The rest of the mass is thought to be distributed between ~ 25 % percent of Cold Dark Matter and ~ 70 % of Dark Energy. Such a low percentage of baryonic mass, however, is employed in processes such as nucleosynthesis, planet formation, galaxy dynamics and, of course, chemistry.

Hydrogen is the most dominant element in the universe and in our Solar System, with helium and carbon following next, having a mean abundance several orders of magnitude lower (two and three respectively) than Hydrogen (Asplund et al., 2009). For other atoms the gap in abundances gets progressively lower (see, for instance the so called "Astronomers Periodic Table", fig 1.1). The H/X ratio is maintained more or less constant in several universe regions and, even at so low abundances, a set of nearly 180 molecules and molecular ions has been positively detected in the gas phase (Müller, Stutzki, and Schlemmer, 2009). More molecules are in the pipeline for detection, and whole sets of chemical families (Polycyclic Aromatic Hydrocarbons, as an example) are also subject of intense exploration (Léger et al., 1989), pointing to an enormous diversity when it comes to potential chemical and physico-chemical processes happening in space. An up to date inventory of molecules detected in space is carried out by the Physikalisches Institut of the Köln University <https://www.astro.uni-koeln.de/cdms/molecules>

Chemical processes in astrochemistry span a great variety of thermal (from 4 to 2000 K) (Decin et al., 2010), and photophysical (Öberg, 2016) conditions. Matter in space

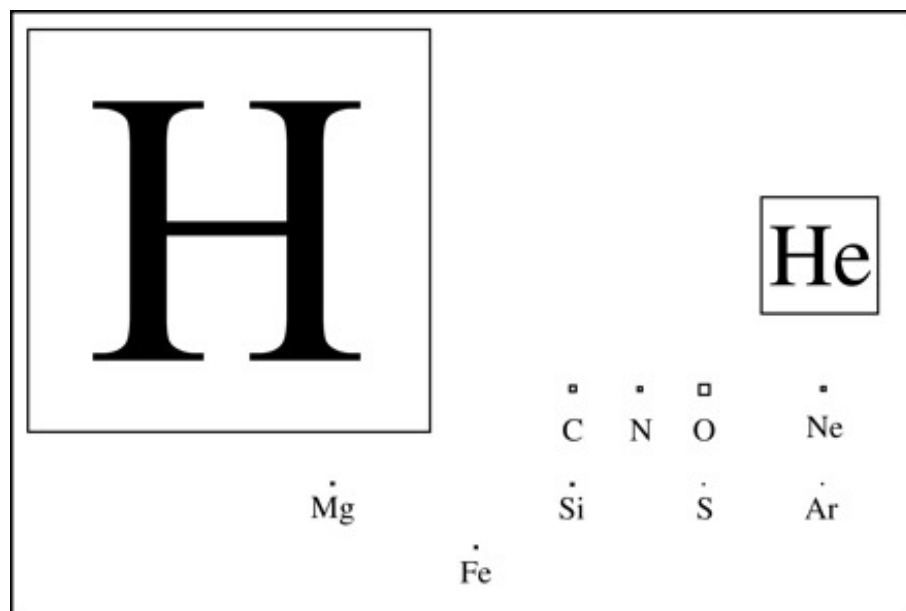


FIGURE 1.1: Astronomers Periodic Table. The size of the elements indicate the abundance.

Adapted from (McCall, 2006)

can be found not only in several chemical forms, but also in several physical phases. In cold regions, solid material and gas phase molecules co-exist forming increasingly more complex astronomical objects. It is because of this that astrochemistry is a key discipline when unraveling important astronomical problems such as how the nano-sized solid particles aggregate to form planets, how complex molecules are formed and inoculated in our own solar system, or what is the chemical evolution of the universe. The ambitious scope of the discipline has led in recent years to the foundation of Astrobiology, a discipline with a deep interest in how prebiotic molecules and more complex structures may have evolved in astronomical objects (e.g. meteorites, asteroids, or comets) and could have been delivered to our solar system.

Molecular abundances are likely the most important figure when trying to simulate chemistry under astrophysical conditions, since they give insight on the chemical evolution and actual composition of an astronomical object. Gas phase models are often not enough for accounting for the observational abundance. In that regard physical processes involving a third, generally solid, body are required. However this is a topic that will be further covered in next sections. For the time being a brief description of the astronomical regions with relevance to the studies of this thesis will be presented.

Cosmic material is not homogeneously distributed. Different regions with different physicochemical properties have different molecular abundances. In the end, the chemical composition of an interstellar region is driven by the evolutionary state of the star or stars around the molecular and atomic material. Astronomers nowadays state that stars are formed within dense clouds, initiating the **cosmic cycle of matter**, (See fig 1.2). Dense clouds are regions of the space in which the baryonic fraction of the total mass is concentrated. They are cold objects (~ 15 K), shielded from UV radiation, whose

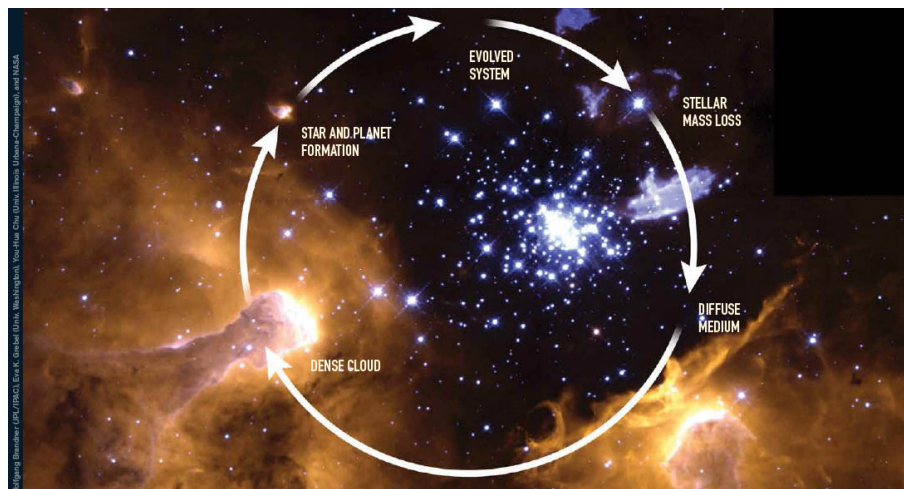


FIGURE 1.2: Summarized view of the cosmic matter cycle
 Extracted from <http://astrobiowalk.gsfc.nasa.gov/2.html>

chemistry is mainly driven by barrierless reactions, and cosmic ray induced chemistry. They are called "dense" because they contain much of the chemical material present in the interstellar medium, with particle densities of nearly 10^4 particles cm^{-3} (Snow and McCall, 2006). These clouds present an optically thick regime where photons are absorbed by dust particles in the edges of the object. The increasing density in denser regions of the cloud eventually leads to gravitational collapse and to the formation of **protostars**. At the early stages of this collapse, the energy is mainly gravitational and the growth increase is slow but steady. When the density is large enough, hydrogen will start to fuse into helium, an intrinsic characteristic of a main sequence star (i.e the sun). A main sequence star will continue burning hydrogen in its core until it is exhausted, at which time hydrogen starts burning at its surface. Helium burning in the core eventually leads to nucleosynthesis of more complex nuclei such as carbon, oxygen, magnesium, depending on the type of star. The evolution of a main sequence star yields different stellar objects, depending on their stellar mass (Asymptotic Giant Branch, Supergiant, Supernova etc), but eventually they collapse into white dwarfs, neutron stars or black holes in the case of the supernovas. It is important to remark that the material surrounding a young star could orbit around it, forming protoplanetary disks, the seed for planets and planetoids. In any case, for our purpose here, heavy elements (at least with respect to helium) are expelled to the interstellar medium during the stellar life cycle.

Molecular material ejected to circumstellar environments eventually reaches the interstellar medium. The amount of material that is expelled depends greatly on the evolutionary stage of the parent star. In the case of an Asymptotic Giant Branch star, carbon, oxygen and silicon are ejected at very high temperatures. Eventually cooling leads to nucleation of refractory material as dust and the formation of simple molecules (CO or H_2O) (Decin et al., 2010).

In the ISM the stellar material is inoculated in what we call diffuse clouds. They are regions that are intermediate in its physicochemical properties between hot and energetic stellar and circumstellar regions, and the cold environments found in dense clouds.

They are also intermediate in their photophysical behavior, with UV photons density not as high as in stellar regions but not as low as in dense clouds. Their optical extinction coefficients A_v are below 1 and the particle density is of the order of hundreds of particles cm^{-3} (Snow and McCall, 2006). Chemistry in the inside of these clouds is essentially driven by atom addition and ion-molecule reactions (Yamamoto, 2017), mainly of hydrogen. The temperature is very low, of about 30 - 40 K, but somewhat higher than in dense molecular clouds, due to the radiative heat coming (mainly) from hydrogen dissociation. There are other regions, called translucent clouds (Jannuzi et al., 1988), in which we can see an intermediate behavior between dense and diffuse clouds.

Diffuse clouds can eventually collapse by gravitational instability or clouds coalescence (Yamamoto, 2017), acquiring enough density to be shielded from the UV interstellar field by dust grains (Draine, 2003b; Draine, 2003a), starting the cycle again. Dense cloud, gravitational collapse, material ejection from stars. This, in a very brief way, constitutes the so called cosmic cycle of matter. Some of the matter can be incorporated to small size objects of hundreds or thousands of kilometers (asteroids or comets in our Solar System) that can be traced and sampled, providing us key information about the composition and chemical evolution of our stellar surrounding. See for example the recent Rosetta mission or the Murchinson meteorite (Martins et al., 2008; Goesmann et al., 2015).

1.2 Solid State Materials in Astrochemistry

Solid state materials are of crucial importance in the cosmochemical picture and cycle, since they fulfill a series of roles that we will describe in further detail in the next section. Two main families of compounds are categorized as solids in the ISM.

If we speak of weakly bounded molecular crystals, solids that are gas, liquid or mixtures of them at room temperature, we are referring to ices, that will have an important role during our discussions later. However, if we speak about refractory material (minerals, amorphous covalent solids, etc), we are referring to dust, the main concern of this thesis.

1.2.1 Ices

Ices in an astrochemical context usually differ substantially from their traditional frozen water meaning. In fact, what in the common everyday language we call ice is only one particular phase of the very diverse solid water diagram (See Fig 1.3).

Following that phase diagram, what we understand for ice is only the I_h phase (Hexagonal ice) of water. In the astrochemical community, however, the word ice refers to a wide range of solid materials that condense at the typical temperature and pressure conditions of a given astronomical region. Very broadly, they correspond to the so called "van der Waals solids".

The formation of ices in the ISM is strongly dependent on the chemical composition on the region and its defining characteristics T , H/H_2 ratio, photophysical conditions, etc. In regions with a high amount of atomic hydrogen, ices are dominated by H_2O , CH_4 , or NH_3 , and other hydrogen saturated molecules (D'Hendecourt, Allamandola, and

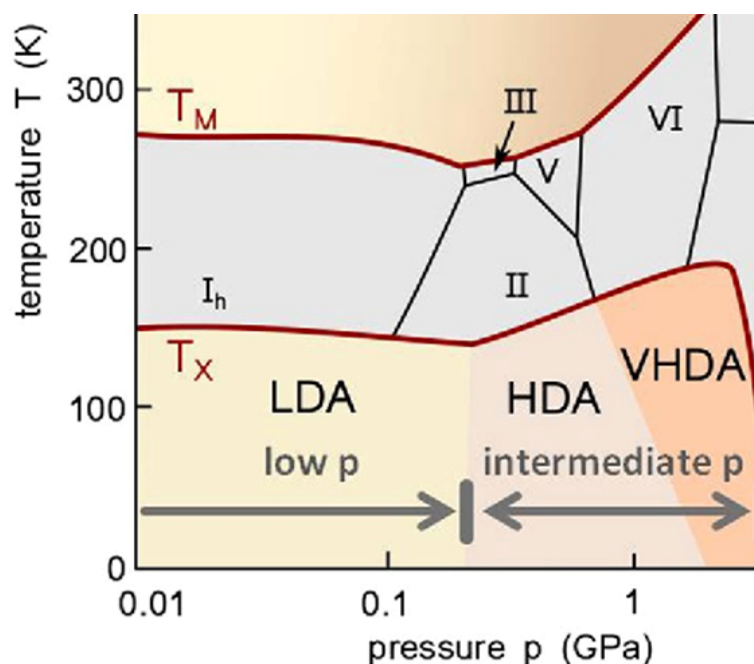


FIGURE 1.3: Phase diagram of Solid Water.
 Extracted and adapted from Stern and Loerting, 2017

Greenberg, 1985). In regions with a small H/H_2 ratio, typically denser regions, different ices are formed, with CO being the main constituent. (D'Hendecourt, Allamandola, and Greenberg, 1985). In these regions, at much lower temperatures, complex ices are usually formed (Hollenbach et al., 2009; Öberg et al., 2011; Boogert, Gerakines, and Whittet, 2015). Observations of the icy features in different sources are presented in Fig 1.4.

Chemistry in the gas phase takes place via barrierless reactions (Herbst and Dishoeck, 2009; Balucani, Ceccarelli, and Taquet, 2015; Redondo, Barrientos, and Largo, 2017) or by quantum tunneling (Hasegawa and Herbst, 1993; Meisner and Kästner, 2016; Álvarez-Barcia et al., 2016) and in the condensed phase via gas-grain reactions (Hasegawa and Herbst, 1993; Herbst and Dishoeck, 2009; Öberg et al., 2011; Cernicharo et al., 2012; Reboussin et al., 2013). In any case richer, molecular chemistry is allowed as a consequence of the abrupt decay of the UV field. The exact structure of icy grains is a complex subject of debate. The extreme low temperatures within a dense cloud ensure that all the molecules in the gas phase sooner or later will stick to grains (Willacy and Millar, 1998). The complex chemistry of ice mantles in dense clouds opens other possible paths for reactivity including cosmic rays (CR) driven chemistry, secondary UV driven chemistry, etc (Schutte, 2002; Modica and Palumbo, 2010; Dawes et al., 2007; Muñoz Caro et al., 2014). Formation of radicals, diffusion, recombination are typical processes leading to more complex molecular compositions (Öberg, Bottinelli, and Van Dishoeck, 2009). Until now we have only spoken about ices and conditions relative to the ISM, but cometary and planetary ices also enrich the chemical diversity of our universe. We are not going to enter in further detail about these topics, but we would like to emphasize the importance of the spectroscopic, laboratory based descriptions of interstellar ices,

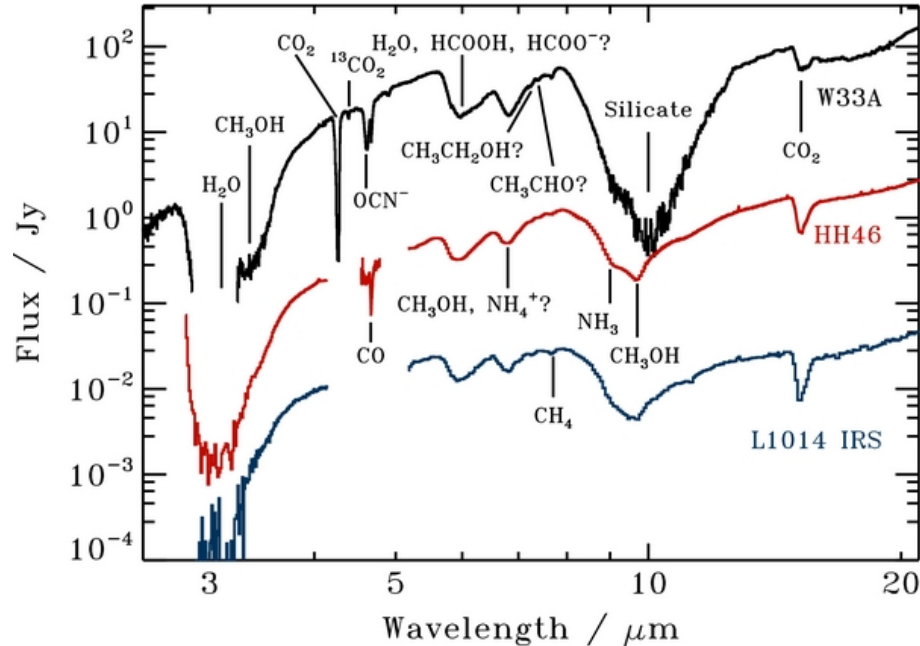


FIGURE 1.4: Infrared spectra showing some of the most relevant ice features.

Extracted and adapted from Öberg et al., 2011

their reactivity and the interaction with energetic radiation.

1.2.2 Dust

The importance of interstellar cosmic dust to the physical properties of an astronomical region is out of any possible doubt. The role of different components of interstellar dust permeates almost every possible sub-field, including chemistry, spectroscopy, modeling, theoretical calculations, etc (Whittet, 2003). The study of cosmic dust involves merging knowledge of several disciplines across different fields of natural sciences. A combination of solid state physics, astrophysics, surface chemistry, and inorganic chemistry would be a good descriptor of the different fields the study of cosmic dust involves. Incidentally the chemical and spectroscopic properties of analogues of cosmic dust are the central topic of this thesis.

Dust grains presence in the ISM can be detected in two main ways. The first one requires a radiation source (a star) to characterize their spectroscopic and diffractometric behavior: UV-Vis extinction (Stecher and Donn, 1965), IR absorption (Dartois et al., 2007) and reflection and polarization of light in aligned dust grains (Davis and Greenstein, 1951). Depending on the dust concentration, they can effectively absorb all the starlight background radiation, leading to notorious photographs as the one shown in Fig 1.5. The second way to detect dust is due to its emission capabilities both as thermal continuum emission (Sellgren, 1984; Witt, Schild, and Kraiman, 1984; Sellgren et al., 1985) in the mid and far IR and as discrete bands (Draine and Anderson, 1985; Desert, Boulanger, and

Shore, 1986; Scott, Duley, and Jahani, 1997) in the mid IR. We will address the spectral features of carbonaceous particles in Chapter 3.



FIGURE 1.5: Barnard68 Dark Cloud

The role of microscopic dust particles is essential for a wide range of physical processes spanning the ISM, for example:

- Dust grains act as "templates" (sometimes referred as catalysts) for the formation of chemical species in the ISM, the reaction to form molecular hydrogen being paradigmatic (Cazaux et al., 2005).
- They are radiation filters, absorbing high energy photons (UV and X-Ray) and to some extent cosmic rays (Draine, 2003b; Draine, 2003a).
- They play a role in stellar evolution, acting as coolants (McNally, 1973).
- Interstellar dust grains are the building block of planetesimals, when microscopic scale grains coagulate to very small (cm) particles (Goldreich and Ward, 1973).

In general, cosmic dust can be categorized as refractory material belonging to two big subfamilies: carbonaceous and siliceous material (Tielens and Allamandola, 1987; Whittet, 2003). For an extra degree of complexity, the structure in which dust grains are found is also relevant for their properties, varying between amorphous and crystalline, with

a general tendency to be found as amorphous materials. On top of that, photophysical processes can alter different regions of the same grain leading to heterogeneous compositions of the same parent material (Jones et al., 2013).

Carbonaceous Materials in the ISM

First of all, let us begin with the exotic crystalline phases of carbon found in the ISM (Fig 1.6). Already in the 90's the idea of nanodiamonds in the space was considered and condensed in the celebrated conference paper of fancy name "Methanol in the Sky with Diamonds" (Allamandola et al., 1991) and gathered in a 1993 paper (Allamandola et al., 1993). This idea was supported by the observation in absorption of a band at 6.8 μm . Recent investigations in this field have incorporated this initial hypothesis, nowadays commonly accepted (Goto et al., 2009). With respect to fullerenes, the literature is abundant, especially debating their possible pathway of formation (Micelotta et al., 2012). The unequivocal identification though, came from the positive identification of two bands in diffuse media at 963.27 and 957.75 nm (Campbell et al., 2015).

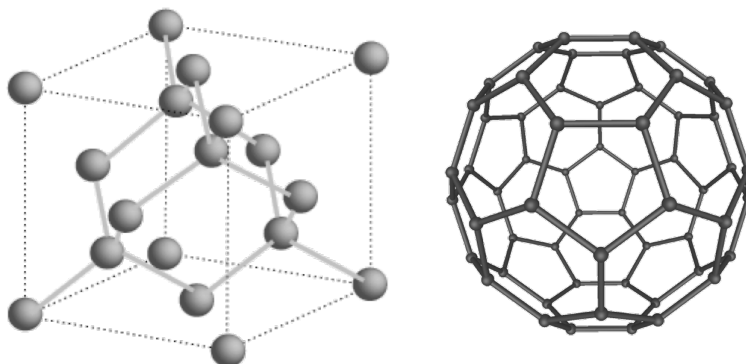


FIGURE 1.6: Diamond unit cell and Buckminster Fullerene C_{60} , two crystalline carbonaceous materials found in the ISM

Even though these crystalline phases have been identified, most of the solid phase carbon in the ISM must be locked in some kind of hydrogenated amorphous carbon (a:C-H in materials science literature and HAC within the astrophysics community). (Dartois et al., 2007; Chiar et al., 2013; Jones et al., 2013; Jones et al., 2014). The amorphous nature of these materials is what makes very difficult to constrict the carbon budget locked up in interstellar dust, with estimates ranging from 5% to 30% (Sandford et al., 1991; Snow and Witt, 1995; Furton, Laiho, and Witt, 1999). Some representations of possible packings of hydrogenated amorphous carbon are presented in fig 1.7.

The variability in the mean structures for these materials is accompanied by variability also in the chemical analogues employed for their study. In laboratory experiments several methods have been proposed to generate this kind of materials, ranging from laser ablation of carbon precursors (Mennella et al., 1999; Jäger et al., 2008; Gadallah, Mutschke, and Jäger, 2013), pyrolysis of precursors (Scott and Duley, 1996; Gadallah, Mutschke, and Jäger, 2013), plasma deposition (Kovačević et al., 2005; Maté et al., 2014;

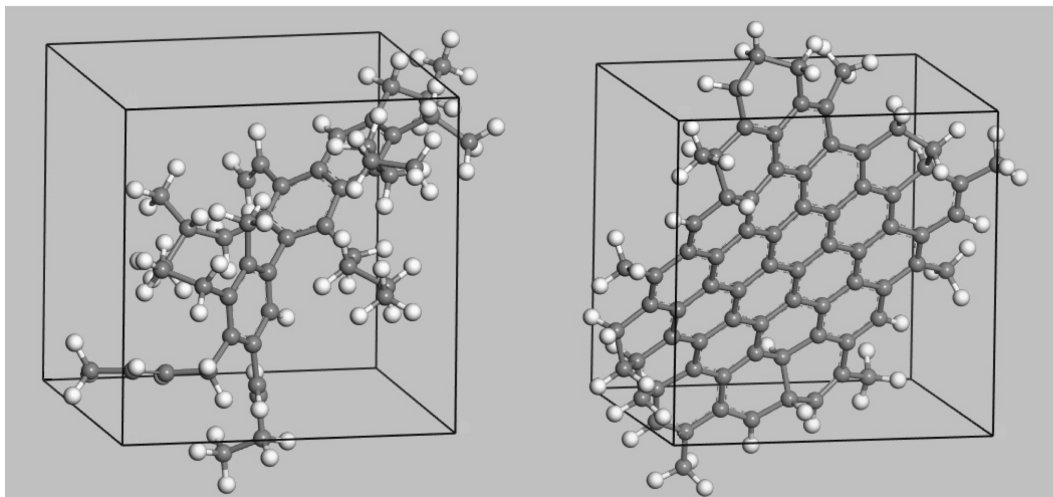


FIGURE 1.7: Amorphous packings of hydrogenated amorphous carbon analogues showing diversity in their C/H ratio and structure.

Maté et al., 2016), combustion of hydrocarbons (Pino et al., 2008), or photolysis of hydrocarbons (Dartois et al., 2004; Dartois et al., 2005). This diversity is also translated to computational models employing molecular analogues (Jeloaica and Sidis, 1999; Steglich et al., 2013) or solid state models (Timón et al., 2015; Molpeceres et al., 2017). An extremal structure is the amorphous or barely hydrogenated carbon (a:C or AC) (Kouchi, 2014). In amorphous carbon, there is a great concentration of dangling bonds (superficial, valence unbalanced chemical active sites in a surface), that influence the chemistry in contrast with the saturated HAC materials in which adsorption is driven by dispersion forces leading to physisorption (Wakelam et al., 2017). A subject of present debate is the amount of aromatic condensed rings (if any) that are present with respect to aliphatic branches, and the incorporation of heteroatoms into the equation as well (Dartois et al., 2007; Kwok and Zhang, 2011; Steglich et al., 2013; Kwok and Zhang, 2013). The variety of processes, structures and spectral properties makes understanding the physicochemical properties of carbonaceous dust a challenging and rewarding task when combining tools and methods of different branches of physics and chemistry.

The spectral features of HAC grains are generally observed in absorption, tracing their characteristic aliphatic C-H absorption band (Chapters 3 & 4), but they can also be detected in continuum and discrete emission depending on the particular size of the grain (Chapter 3). The interaction with energetic particles lead to changes in the structure altering the spectroscopic features of the analogues and thus increasing the complexity around the subject.

Siliceous Materials in the ISM

Siliceous material is the second big family when it comes to the general chemical classification of interstellar dust. The identification of siliceous dust has been determined by the unequivocal assignments of O-Si stretches and O-Si-O bends (Jaeger et al., 1998)

of silicates, the main siliceous bearing type of material, at around $10 \mu\text{m}$ and $20 \mu\text{m}$ respectively. Moreover, SiC clusters have been also identified (Frenklach, Carmer, and Feigelson, 1989; Anders et al., 1989). Silicates are also found both in crystalline and in amorphous phases in space, with an estimated prevalence of 95% amorphous ones to a 5% of crystalline material (Jaeger et al., 1998) in the ISM. For the crystalline ones, olivines (Fig 1.1) with general formula $\text{Fe}_{1-x}\text{Mg}_x\text{SiO}_4$, and pyroxenes $\text{Fe}_{1-x}\text{Mg}_x\text{SiO}_3$, are the most abundant.

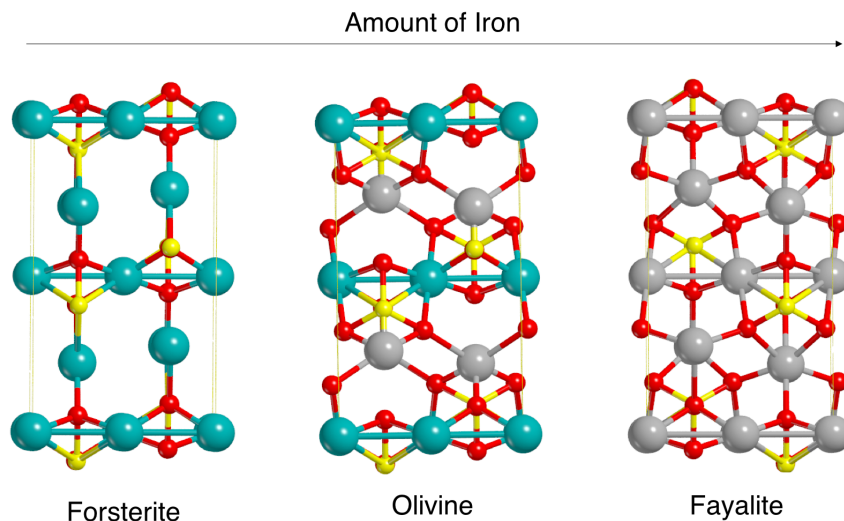


FIGURE 1.8: Different Olivine Structures as a function of its Iron content

There is a degree of interconversion between amorphous and crystalline silicates, from the former to the latter via thermal annealing (Ábrahám et al., 2009) and from crystalline to amorphous via energetic processing (Bajt et al., 2005; Bringa et al., 2007). These processes can happen in different regions, from the formation regions in oxygen rich giant stars, ejecting SiO to the interstellar media to cometary nuclei. Depending on the physicochemical conditions in the region the proportion of amorphous to crystalline may vary as a consequence of higher temperatures (circumstellar disks) or higher proportion of cosmic rays (diffuse and dense media).

Some advantages of siliceous over carbonaceous dust from a chemical analogue study perspective are that:

1. The chemical composition of amorphous silicates is more easily traceable with respect to the enormous degree of deviation of structures from HAC.
2. The forces involving gas-grain interactions are more easily described in silicate grains, with the formation of long lasting covalently bonded adsorbates between molecules and active sites in the surface (Chapter 5) (Navarro-Ruiz et al., 2015).
3. The structure of crystalline materials is adequate as a semiquantitative approximation to the properties of amorphous materials, at least for chemical processes studies (Martínez-González, Navarro-Ruiz, and Rimola, 2018).

This reduced structural complexity allows us to estimate the reactivity over these dust surfaces, in order to study chemical processes occurring in the surface of dust grains, as will be dealt with in Chapter 5.

Chemical Analogues

To generate a realistic dust particle we would require a refractory material with mixed carbonaceous and siliceous domains with different phases within it. From the experimental (and theoretical) point of view this is an unbearable task but even if possible such particle only would be a good approximate representation of a particle in a concrete region at a given grain size (Jones et al., 2013). For the study of the dust properties, different structural models are employed. Some studies are done in crystalline phases of silicates or carbonaceous matter. Some others revolve about laboratory generation of amorphous analogues, formed in very diverse ways from parent crystalline phases or directly depositing amorphous materials. In computational simulations, crystalline and amorphous phases can also be employed. Some of these models, commonly referred by us as **chemical analogues** are going to be used along this thesis to evaluate spectral capabilities, resilience in astrophysical environments, and chemical reactions on top of them.

Chemical analogues have been used to extract spectroscopic and diffractometric data and to positively identify crystalline phases in our Solar System (planetary, interplanetary or cometary material) and in the ISM. For example basalt, calcite, montmorillonite (Muñoz et al., 2012), graphite, olivine, forsterite (Contini, 1996; Poteet et al., 2011) or buckminster fullerene C_{60} (Campbell et al., 2015). The detection of spectroscopic features and diffractometric patterns associated with amorphous materials has been also extensively validated (Chiar et al., 2000; Muñoz Caro et al., 2006; Dartois et al., 2007; Vries and Costantini, 2009; Fritz et al., 2011; Muñoz et al., 2012; Steglich et al., 2013) using structural models constructed either in the laboratory or computationally.

1.3 Objectives of the Thesis

The structure of the thesis is designed as follows.

The second chapter is devoted to the description of the tools that we are going to employ in the different chapters, providing a theoretical basis for the experimental and theoretical simulations carried out during these years. Techniques that are specific or constitute a minor part of a chapter are described in the method section of that chapter.

In the third chapter we will describe the relationship between structure and spectral properties of a series of HAC analogues, studying their IR absorption, UV absorption and IR emission. Our intention with this theoretical work is to shed some light to the debate on the aliphatic to aromatic ratio in interstellar amorphous carbonaceous materials and how this ratio affects their spectroscopic features. We have employed DFT calculations to simulate these features.

The fourth chapter goes a step forward in the complexity of the simulated processes employing concepts derived in chapter 3 to obtain information regarding the prevalence of carbonaceous material in different astrophysical environments. This chapter presents the results of laboratory simulations of destruction of HAC when processed with high energy particles such as electrons, also guided by literature results using other cosmic ray analogues. These results are related with the radiation and energetic shielding attributed to dust particles.

The fifth and last chapter of results changes the structural complexity of carbonaceous amorphous materials to surfaces of crystalline silicates for studying their role as templates for reactions. For that, we will rely on the relative chemical simplicity of these materials to calculate the thermodynamic and kinetic properties of a possible reaction route to form water in the ISM.

As can be seen, our general purpose is to develop strategies for the study of the different processes in which dust play a major role, tackling its different competences within the big astrochemical picture.

References

- Ábrahám, P., A. Juhász, C. P. Dullemond, Á Kóspál, R. Van Boekel, J. Bouwman, Th Henning, A. Moór, L. Mosoni, A. Sicilia-Aguilar, and N. Sipos (2009). "Episodic formation of cometary material in the outburst of a young Sun-like star". In: *Nature* 459.7244, pp. 224–226. arXiv: [0906.3161](#).
- Allamandola, L. J., S. A. Sandford, A. G. G. M. Tielens, and T. Herbst (1991). "Methanol in the sky with diamonds". In: *54th Annual Meeting of the Meteoritical Society*. Vol. 766. LPI Contributions.
- Allamandola, LJ, SA Sandford, AG Tielens, and TM Herbst (1993). "Diamonds in dense molecular clouds: a challenge to the standard interstellar medium paradigm". In: *Science* 260.5104, pp. 64–66.
- Álvarez-Barcia, Sonia, Marie Sophie Russ, Jan Meisner, and Johannes Kästner (2016). "Atom tunnelling in the reaction $\text{NH}_3^{++} + \text{H}_2 \rightarrow \text{NH}_4^{++} + \text{H}$ and its astrochemical relevance". In: *Faraday Discussions* 195.0, pp. 69–80.
- Anders, Edward, Roy S. Lewis, Tang Ming, and Ernst Zinner (1989). "Interstellar Grains in Meteorites: Diamond and Silicon Carbide". In: *Interstellar Dust*. Ed. by L. J. Allamandola and A. G. G. M. Tielens. Dordrecht: Springer Netherlands, pp. 389–402. ISBN: 978-94-009-2462-8.
- Asplund, M., N. Grevesse, A. J. Sauval, and P. Scott (Sept. 2009). "The Chemical Composition of the Sun". In: 47, pp. 481–522. arXiv: [0909.0948](#) [[astro-ph.SR](#)].
- Bajt, S., R. A. Baragiola, E. M. Bringa, J. P. Bradley, Z. R. Dai, C. A. Dukes, T. Felter, G. A. Graham, S. O. Kucheyev, M. J. Loeffler, M. C. Martin, A. Tielens, D. Torres, and W. van Breugel (Mar. 2005). "Amorphization of Forsterite Grains Due to High Energy Heavy Ion Irradiation – Implications for Grain Processing in ISM". In: *36th Annual Lunar and Planetary Science Conference*. Ed. by S. Mackwell and E. Stansbery. Vol. 36. Lunar and Planetary Inst. Technical Report.

- Balucani, Nadia, Cecilia Ceccarelli, and Vianney Taquet (2015). "Formation of complex organic molecules in cold objects: the role of gas phase reactions". In: *Monthly Notices of the Royal Astronomical Society Letters* 5.January, pp. 1–5. arXiv: [1501.03668](#).
- Boogert, Adwin, Perry Gerakines, and Douglas Whittet (2015). "Observations of the Icy Universe". In: arXiv: [1501.05317](#).
- Bringa, E. M., S. O. Kucheyev, M. J. Loeffler, R. A. Baragiola, A. G. G. M. Tielens, Z. R. Dai, G. Graham, S. Bajt, J. P. Bradley, C. A. Dukes, T. E. Felter, D. F. Torres, and W. van Breugel (2007). "Energetic Processing of Interstellar Silicate Grains by Cosmic Rays". In: *The Astrophysical Journal* 662.1, pp. 372–378.
- Campbell, E. K., M. Holz, D. Gerlich, and J. P. Maier (2015). "Laboratory confirmation of C60+ as the carrier of two diffuse interstellar bands". In: *Nature* 523.7560, pp. 322–323.
- Cazaux, S, P Caselli, A G G M Tielens, J LeBourlot, and M Walmsley (2005). "Molecular Hydrogen formation on grain surfaces". In: *Journal of Physics: Conference Series* 6.1, p. 155. arXiv: [0502291](#) [[arXiv:astro-ph](#)].
- Cernicharo, J., N. Marcelino, E. Roueff, M. Gerin, A. Jiménez-Escobar, and G. M. Muñoz Caro (2012). "Discovery of the methoxy radical, CH₃O, toward B1: Dust grain and gas-phase chemistry in cold dark clouds". In: *Astrophysical Journal Letters* 759.2, p. L43.
- Chiar, J. E., A. G. G. M. Tielens, D. C. B. Whittet, W. A. Schutte, A. C. A. Boogert, D. Lutz, E. F. van Dishoeck, and M. P. Bernstein (2000). "The Composition and Distribution of Dust along the Line of Sight toward the Galactic Center". In: *The Astrophysical Journal* 537.2, pp. 749–762. arXiv: [0002421](#) [[astro-ph](#)].
- Chiar, J. E., A. G. G. M. Tielens, A. J. Adamson, and A. Ricca (2013). "The structure, origin, and evolution of interstellar hydrocarbon grains". In: *Astrophysical Journal* 770.1, p. 78.
- Contini, Marcella (1996). "X-ray rings by grain diffraction". In: *Astrophysics and Space Science* 238.2, pp. 217–222.
- Dartois, E., G M Muñoz Caro, D. Deboffle, and L D'Hendecourt (2004). "Diffuse interstellar medium organic polymers". In: *Astronomy and Astrophysics* 423.3, pp. L33–L36.
- Dartois, E., G. M. Muñoz Caro, D. Deboffle, G. Montagnac, and L. D'Hendecourt (2005). "Ultraviolet photoproduction of ISM dust". In: *Astronomy and Astrophysics* 432, pp. 895–908.
- Dartois, E., T. R. Geballe, T. Pino, A.-T. Cao, A. Jones, D. Deboffle, V. Guerrini, Ph. Bréchignac, and L. D'Hendecourt (2007). "IRAS 08572+3915: constraining the aromatic versus aliphatic content of interstellar HACs". In: *Astronomy and Astrophysics* 463.2, pp. 635–640.
- Davis Jr., L. and J. L. Greenstein (Sept. 1951). "The Polarization of Starlight by Aligned Dust Grains." In: *The Astrophysical Journal* 114, p. 206.
- Dawes, Anita, Adam Hunniford, Philip D. Holtom, Robin J. Mukerji, Robert W. McCullough, and Nigel J. Mason (2007). "Low energy 13C+ and 13C2+ ion irradiation of water ice". In: *Physical Chemistry Chemical Physics* 9.22, pp. 2886–2893.
- Decin, L. et al. (2010). "Warm water vapour in the sooty outflow from a luminous carbon star." In: *Nature* 467.7311, pp. 64–7. arXiv: [arXiv:1104.2316v1](#).
- Desert, F. X., F. Boulanger, and S. N. Shore (May 1986). "Grain temperature fluctuations - A key to infrared spectra". In: 160, pp. 295–300.
- D'Hendecourt, L.B., L.J. Allamandola, and J.M. Greenberg (Nov. 1985). "Time dependent chemistry in dense molecular clouds. I - Grain surface reactions, gas/grain interactions and infrared spectroscopy". In: *Astronomy & Astrophysics* 152, pp. 130–150.

- Draine, B. T. (2003a). "Scattering by Interstellar Dust Grains. II. X-Rays". In: *The Astrophysical Journal* 598.2, pp. 1026–1037. arXiv: [0308251 \[astro-ph\]](#).
- (2003b). "Scattering by Interstellar Dust Grains: Optical and Ultraviolet". In: *The Astrophysical Journal* 598.2, pp. 1017–1025. arXiv: [0304060 \[astro-ph\]](#).
- Draine, B. T. and N. Anderson (May 1985). "Temperature fluctuations and infrared emission from interstellar grains". In: 292, pp. 494–499.
- Frenklach, M., C. S. Carmer, and E. D. Feigelson (1989). "Silicon carbide and the origin of interstellar carbon grains". In: *Nature* 339.6221, pp. 196–198. arXiv: [nature.vol.342.30nov1989](#).
- Fritz, T. K., S. Gillessen, K. Dodds-Eden, D. Lutz, R. Genzel, W. Raab, T. Ott, O. Pfuhl, F. Eisenhauer, and F. Yusef-Zadeh (2011). "Line derived infrared extinction toward the galactic center". In: *Astrophysical Journal* 737.2. arXiv: [1105.2822](#).
- Furton, Douglas G., John W. Laiho, and Adolf N. Witt (1999). "The Amount of Interstellar Carbon Locked in Solid Hydrogenated Amorphous Carbon". In: *The Astrophysical Journal* 526.2, pp. 752–763. arXiv: [9908035v1 \[arXiv:astro-ph\]](#).
- Gadallah, K. A. K., H. Mutschke, and C. Jäger (2013). "Analogues of solid nanoparticles as precursors of aromatic hydrocarbons". In: *Astronomy & Astrophysics* 554, A12.
- Goesmann, Fred et al. (2015). "Organic compounds on comet 67P/Churyumov-Gerasimenko revealed by COSAC mass spectrometry". In: *Science* 349.6247.
- Goldreich, P. and W. R. Ward (Aug. 1973). "The Formation of Planetesimals". In: *The Astrophysical Journal* 183, pp. 1051–1062.
- Goto, M., Th. Henning, A. Kouchi, H. Takami, Y. Hayano, T. Usuda, N. Takato, H. Terada, S. Oya, C. Jäger, and A. C. Andersen (2009). "Spatially resolved 3 μm spectroscopy of elias 1: Origin of diamonds in protoplanetary disks". In: *Astrophysical Journal* 693.1, pp. 610–616. arXiv: [0811.2220](#).
- Hasegawa, Tatsuhiko I. and Eric Herbst (1993). "New gas-grain chemical models of quiescent dense interstellar clouds - The effects of H₂ tunnelling reactions and cosmic ray induced desorption". In: *Monthly Notices of the Royal Astronomical Society* 261.1, pp. 83–102.
- Herbst, Eric and Ewine F. van Dishoeck (2009). "Complex Organic Interstellar Molecules". In: *Annual Review of Astronomy and Astrophysics* 47.1, pp. 427–480.
- Hollenbach, David, Michael J. Kaufman, Edwin A. Bergin, and Gary J. Melnick (2009). "Water, O₂, and ice in molecular clouds". In: *Astrophysical Journal* 690.2, pp. 1497–1521. arXiv: [0809.1642](#).
- Jaeger, C., F. J. Molster, J. Dorschner, T. Henning, H. Mutschke, and L. B. F. M. Waters (Nov. 1998). "Steps toward interstellar silicate mineralogy. IV. The crystalline revolution". In: 339, pp. 904–916.
- Jäger, C., H. Mutschke, Th. Henning, and F. Huisken (2008). "Spectral Properties of Gas-phase Condensed Fullerene-like Carbon Nanoparticles from Far-ultraviolet to Infrared Wavelengths". In: *The Astrophysical Journal* 689.1, pp. 249–259. arXiv: [0903.0759](#).
- Jannuzi, Buell, John Black, Charles Lada, and Ewine. F van Dishoeck (Oct. 1988). "The small molecular cloud toward HD 169454". In: *The Astrophysical Journal* 332.
- Jeloaica, L. and V. Sidis (1999). "DFT investigation of the adsorption of atomic hydrogen on a cluster-model graphite surface". In: *Chemical Physics Letters* 300.1, pp. 157–162.

- Jones, A. P., L. Fanciullo, M. Köhler, L. Verstraete, V. Guillet, M. Bocchio, and N. Ysard (2013). "The evolution of amorphous hydrocarbons in the ISM: dust modelling from a new vantage point". In: *Astronomy & Astrophysics* 558, A62. arXiv: [1411.6293](#).
- Jones, Anthony P., Nathalie Ysard, Melanie Köhler, Lapo Fanciullo, Marco Bocchio, Elisabetta Micelotta, Laurent Verstraete, and Vincent Guillet (2014). "The cycling of carbon into and out of dust". In: *Faraday Discussions* 168.0, pp. 313–326. arXiv: [1411.5877](#).
- Kouchi, Akira (2014). "Amorphous Carbon". In: *Encyclopedia of Astrobiology*. Ed. by Ricardo Amils, Muriel Gargaud, José Cernicharo Quintanilla, Henderson James Cleaves, William M. Irvine, Daniele Pinti, and Michel Viso. Berlin, Heidelberg: Springer Berlin Heidelberg, pp. 1–2.
- Kovačević, E., I. Stefanović, J. Berndt, Y. J. Pendleton, and J. Winter (2005). "A Candidate Analog for Carbonaceous Interstellar Dust: Formation by Reactive Plasma Polymerization". In: *The Astrophysical Journal* 623.1, pp. 242–251.
- Kwok, Sun and Yong Zhang (2011). "Mixed aromatic-aliphatic organic nanoparticles as carriers of unidentified infrared emission features". In: *Nature* 479.7371, pp. 80–83.
- (2013). "Unidentified infrared emission bands: Paks or maons?" In: *The Astrophysical Journal* 771.1, pp. 5–9. arXiv: [1304.7629](#).
- Lazarides, G. (1999). "Introduction to Cosmology". In: arXiv: [9904502 \[hep-ph\]](#).
- Léger, A, L Verstraete, L D'Hendecourt, D Défourneau, O Dutuit, W Schmidt, and J Lauer (1989). "The PAH Hypothesis and the Extinction Curve". In: *Interstellar Dust* 135, p. 173.
- Martínez-González, José, Javier Navarro-Ruiz, and Albert Rimola (2018). "Multiscale Computational Simulation of Amorphous Silicates' Structural, Dielectric, and Vibrational Spectroscopic Properties". In: *Minerals* 8.8, p. 353.
- Martins, Zita, Oliver Botta, Marilyn L. Fogel, Mark A. Sephton, Daniel P. Glavin, Jonathan S. Watson, Jason P. Dworkin, Alan W. Schwartz, and Pascale Ehrenfreund (2008). "Extraterrestrial nucleobases in the Murchison meteorite". In: *Earth and Planetary Science Letters* 270.1-2, pp. 130–136. arXiv: [0806.2286](#).
- Maté, Belén, Isabel Tanarro, Miguel A. Moreno, Miguel Jiménez-Redondo, Rafael Escribano, and Víctor J. Herrero (2014). "Stability of carbonaceous dust analogues and glycine under UV irradiation and electron bombardment". In: *Faraday Discuss.* 168.0, pp. 267–285.
- Maté, Belén, Germán Molpeceres, Miguel Jiménez-Redondo, Isabel Tanarro, and Víctor J. Herrero (2016). "High-Energy Electron Irradiation of Interstellar Carbonaceous Dust Analogs: Cosmic-Ray Effects on the 3.4 μ m absorption band". In: *The Astrophysical Journal* 831.1, p. 51.
- McCall, Benjamin J. (2006). "Dissociative recombination of cold H₃⁺ and its interstellar implications". In: *Philosophical Transactions of the Royal Society A: Mathematical, Physical and Engineering Sciences* 364.1848, pp. 2953–2963.
- McNally, D. (1973). "Dust and Star Formation". In: *Interstellar Dust and Related Topics*. Vol. 52. Dordrecht: Springer Netherlands, p. 549.
- Meisner, Jan and Johannes Kästner (2016). "Reaction rates and kinetic isotope effects of H₂⁺ + OH → H₂O + H". In: *Journal of Chemical Physics* 144.17, p. 174303. arXiv: [1605.08776](#).
- Mennella, V., J. R. Brucato, L. Colangeli, and P. Palumbo (1999). "Activation of the 3.4 Micron Band in Carbon Grains by Exposure to Atomic Hydrogen". In: *The Astrophysical Journal Letters* 524.1, p. L71.

- Micelotta, Elisabetta R., Anthony P. Jones, Jan Cami, Els Peeters, Jeronimo Bernard-Salas, and Giovanni Fanchini (2012). "The Formation of Cosmic Fullerenes from Aromatic Clusters". In: *The Astrophysical Journal* 761.1, p. 35.
- Modica, P. and M. E. Palumbo (2010). "Formation of methyl formate after cosmic ion irradiation of icy grain mantles". In: *Astronomy and Astrophysics* 519, A22.
- Molpeceres, Germán, Vicente Timón, Miguel Jiménez-Redondo, Rafael Escribano, Belén Maté, Isabel Tanarro, and Víctor J Herrero (2017). "Structure and infrared spectra of hydrocarbon interstellar dust analogs". In: *Physical Chemistry Chemical Physics* 19.2, pp. 1352–1360.
- Muñoz Caro, G. M., G. Matrajt, E. Dartois, M. Nuevo, L. D'Hendecourt, D. Deboffle, G. Montagnac, N. Chauvin, C. Boukari, and D. Le Du (2006). "Nature and evolution of the dominant carbonaceous matter in interplanetary dust particles: effects of irradiation and identification with a type of amorphous carbon". In: *Astronomy & Astrophysics* 459.1, pp. 147–159.
- Muñoz Caro, G. M., E. Dartois, P. Boduch, H. Rothard, A. Domaracka, and A. Jiménez-Escobar (2014). "Comparison of UV and high-energy ion irradiation of methanol ammonia ice". In: *Astronomy & Astrophysics* 566, A93. arXiv: [1405.5332](#).
- Müller, H. S. P., J. Stutzki, and S. Schlemmer (June 2009). "The Cologne Database for Molecular Spectroscopy, Cdms, in Times of Herschel, SOFIA, and Alma". In: *64th International Symposium On Molecular Spectroscopy*, WH07.
- Muñoz, O, F Moreno, D Guirado, D D Dabrowska, H Volten, and J W Hovenier (2012). "The Amsterdam–Granada Light Scattering Database". In: *Journal of Quantitative Spectroscopy and Radiative Transfer* 113.7, pp. 565–574.
- Navarro-Ruiz, Javier, José Ángel Martínez-González, Mariona Sodupe, Piero Ugliengo, and Albert Rimola (2015). "Relevance of silicate surface morphology in interstellar H₂ formation. Insights from quantum chemical calculations". In: *Monthly Notices of the Royal Astronomical Society* 453.1, pp. 914–924.
- Öberg, Karin I. (2016). "Photochemistry and Astrochemistry: Photochemical Pathways to Interstellar Complex Organic Molecules". In: *Chemical Reviews* 116.17, pp. 9631–9663. arXiv: [1609.03112](#).
- Oberg, Karin I, Sandrine Bottinelli, and Ewine F Van Dishoeck (2009). *Cold gas as an ice diagnostic toward low mass protostars*. arXiv: [0901.1019](#).
- Öberg, Karin I., A. C. Adwin Boogert, Klaus M. Pontoppidan, Saskia Van Den Broek, Ewine F. Van Dishoeck, Sandrine Bottinelli, Geoffrey A. Blake, and Neal J. Evans (2011). "The Spitzer ice legacy: Ice evolution from cores to protostars". In: *Astrophysical Journal* 740.2, p. 109. arXiv: [1107.5825](#).
- Pino, Thomas, Emmanuel Dartois, A.-T Cao, Yvain Carpentier, Thierry Chamaillé, R Vasquez, Anthony Jones, Louis Dhendecourt, and Philippe Brechignac (Nov. 2008). "The 6.2 m band position in laboratory and astrophysical spectra: A tracer of the aliphatic to aromatic evolution of interstellar carbonaceous dust". In: *Astronomy and Astrophysics* 490, pp. 665–672.
- Poteet, C. A., S. T. Megeath, D. M. Watson, N. Calvet, I. S. Remming, M. K. McClure, B. A. Sargent, W. J. Fischer, E. Furlan, L. E. Allen, J. E. Bjorkman, L. Hartmann, J. Muzerolle, J. J. Tobin, and B. Ali (June 2011). "A Spitzer Infrared Spectrograph Detection of Crystalline Silicates in a Protostellar Envelope". In: *The Astrophysical Journal Letters* 733, L32, p. L32. arXiv: [1104.4498](#).

- Reboussin, L., V. Wakelam, S. Guilloteau, and F. Hersant (2013). "Grain-surface reactions in molecular clouds: The effect of cosmic rays and quantum tunnelling". In: *Monthly Notices of the Royal Astronomical Society* 440.4, pp. 3557–3567. arXiv: 1403.5189.
- Redondo, Pilar, Carmen Barrientos, and Antonio Largo (2017). "Complex Organic Molecules Formation in Space Through Gas Phase Reactions: A Theoretical Approach". In: *The Astrophysical Journal* 836.2, p. 240.
- Sandford, S. A., L. J. Allamandola, A. G. G. M. Tielens, K. Sellgren, M. Tapia, and Y. Pendleton (Apr. 1991). "The Interstellar C-H Stretching Band near 3.4 Microns: Constraints on the Composition of Organic Material in the Diffuse Interstellar Medium". In: *The Astrophysical Journal* 371, p. 607.
- Schutte, W A (2002). "Production of Organic Molecules Ices in Interstellar". In: *Science* 30.6, pp. 1409–1417.
- Scott, A. and W. W. Duley (1996). "The Decomposition of Hydrogenated Amorphous Carbon: A Connection with Polycyclic Aromatic Hydrocarbon Molecules". In: *The Astrophysical Journal* 472.2, pp. L123–L125.
- Scott, A. D., W. W. Duley, and H. R. Jahani (1997). "Infrared Emission Spectra from Hydrogenated Amorphous Carbon". In: *The Astrophysical Journal* 490.2, pp. L175–L177.
- Sellgren, K. (Feb. 1984). "The near-infrared continuum emission of visual reflection nebulae". In: *The Astrophysical Journal* 277, pp. 623–633.
- Sellgren, K., L. J. Allamandola, J. D. Bregman, M. W. Werner, and D. H. Wooden (Dec. 1985). "Emission features in the 4-13 micron spectra of the reflection nebulae NGC 7023 and NGC 2023". In: *The Astrophysical Journal* 299, pp. 416–423.
- Snow, Theodore P. and Benjamin J. McCall (2006). "Diffuse Atomic and Molecular Clouds". In: *Annual Review of Astronomy and Astrophysics* 44.1, pp. 367–414.
- Snow, Theodore P. and Adolf N. Witt (1995). "The Interstellar Carbon Budget and the Role of Carbon in Dust and Large Molecules". In: *Science* 270.5241, pp. 1455–1460.
- Stecher, T. P. and B. Donn (Nov. 1965). "On Graphite and Interstellar Extinction". In: *The Astrophysical Journal* 142, p. 1681.
- Steglich, M, C Jäger, F Huisken, M Friedrich, W Plass, H.-J. Räder, K Müllen, and Th. Henning (2013). "the Abundances of Hydrocarbon Functional Groups in the Interstellar Medium Inferred From Laboratory Spectra of Hydrogenated and Methylated Polycyclic Aromatic Hydrocarbons". In: *The Astrophysical Journal Supplement Series* 208.2, p. 26. arXiv: 1308.4080.
- Stern, J and T Loerting (2017). "Crystallisation of the amorphous ices in the intermediate pressure regime". In: *Scientific Reports* 7.1, p. 3995.
- Tielens, A. G. G. M. and L. J. Allamandola (1987). "Composition, structure, and chemistry of interstellar dust". In: *Interstellar Processes*. Vol. 134. Springer, Dordrecht, pp. 397–469.
- Timón, Vicente, Óscar Gálvez, Belén Maté, Isabel Tanarro, Víctor J. Herrero, and Rafael Escribano (2015). "Theoretical model of the interaction of glycine with hydrogenated amorphous carbon (HAC)". In: *Physical Chemistry Chemical Physics* 17.43, pp. 28966–28976.
- Vries, C. P. de and E. Costantini (2009). "Physical properties of amorphous solid interstellar material from X-ray absorption spectroscopy of Scorpius X-1". In: *Astronomy and Astrophysics* 497.2, pp. 393–398.

- Wakelam, Valentine, Emeric Bron, Stephanie Cazaux, Francois Dulieu, Cécile Gry, Pierre Guillard, Emilie Habart, Liv Hornekær, Sabine Morisset, Gunnar Nyman, Valerio Pirronello, Stephen D. Price, Valeska Valdivia, Gianfranco Vidali, and Naoki Watanabe (2017). *H₂ formation on interstellar dust grains: The viewpoints of theory, experiments, models and observations*. arXiv: [1711.10568](https://arxiv.org/abs/1711.10568).
- Whittet, D.C.B. (2003). *Dust in the galactic environment*. Vol. 1. Institute of Physics Pub, p. 405. ISBN: 0750306246.
- Willacy, K. and T. J. Millar (1998). "Desorption processes and the deuterium fractionation in molecular clouds". In: *Monthly Notices of the Royal Astronomical Society* 298.2, pp. 562–568.
- Witt, A. N., R. E. Schild, and J. B. Kraiman (June 1984). "Photometric study of NGC 2023 in the 3500 Å to 10000 Å region - Confirmation of a near-IR emission process in reflection nebulae". In: *The Astrophysical Journal* 281, pp. 708–718.
- Yamamoto, Satoshi (2017). *Introduction to Astrochemistry*. ISBN: 978-4-431-54170-7.

Chapter 2

Methodology

This chapter is devoted to the description of the different tools used during the research carried out in this thesis. This work combines theoretical calculations with experimental measurements for determining different properties and processes occurring in carbonaceous and siliceous dust chemical analogues.

In that regard, the link between the calculations and the experiments from a methodological point of view is the determination of the infrared spectra of laboratory or in silico chemical analogues. Following this link, the section is mainly devoted to the formal description of the vibrations in a solid, with emphasis in the molecular like vibrations in the mid IR. For doing so, steps to the construction of the so called "Dynamical Matrix", which contains the information of the normal modes of the solid, are going to be enumerated.

Secondly, we will dedicate some effort to the description of the theoretical methods used in our calculation of the electronic energies and forces, required for the computation of the IR spectra. Density Functional Theory (DFT) and how this theory is applied to periodic systems with many electrons will be the goal of the section.

Once the essential basis for the calculation of the IR spectrum of solids is established, we will move forward to the description of our laboratory. We will here describe our experimental set up, both for IR spectroscopy and for plasma growth of chemical analogues. A brief mention on the quantification of IR intensities is going to be done at the end of the chapter.

2.1 Vibrational Spectroscopy of Solids

2.1.1 Differences Between Gas and Solid Phase Spectra

Infrared (IR) spectroscopy is concerned with the excitation of the vibrational degrees of freedom, periodic motions of the nuclear positions of a molecule. For an individual transition to be allowed, the dipole moment of the molecule should change during the absorption. Complex vibrational motions are decomposed as the sum of normal modes, vibrational features identified by their characteristic frequency. Different normal modes involve stretchings and bendings of the interatomic bonds within a molecule. Fig 2.1 represents some of these periodic motions.

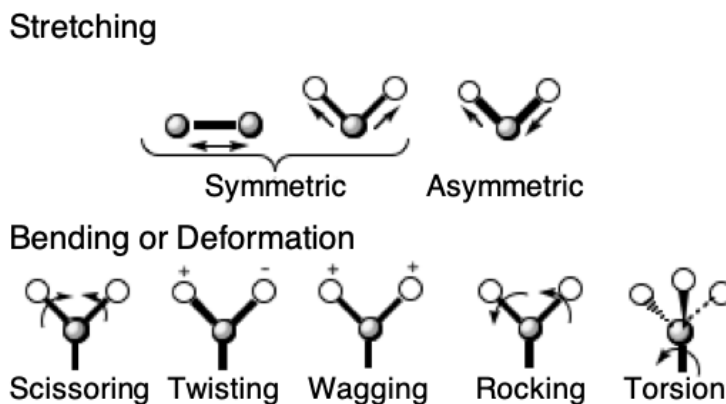


FIGURE 2.1: Diagram showing different vibrational normal modes
Adapted from <https://chemistry.stackexchange.com>

Infrared spectra in the solid phase holds the same basic principle that in the gas phase, but some important particularities arise from the condensed nature of the sample. In general, these differences come from the intermolecular interactions that govern the solid phase, and can be enumerated as in Sherwood, 1972:

- Fine structure of the bands, as a consequence of excitation of rotational levels, is not observed. The molecules in the crystal are fixed and thus rotation is not allowed.
- The interaction of one molecule with the surrounding atoms in the lattice has an influence in the IR spectra in the form of **splittings** and **frequency shiftings**. This effect is also observed because of the interaction between vibrational modes in the lattice. The collection of these two factors is sometimes named *Factor Group Splitting*.
- In crystalline solids, a whole new type of vibrations appears, observed in the far IR region ($< 500 \text{ cm}^{-1}$). These features account for the collective motion of all the atoms in the cell, as opposed to the localized nature of the vibration in a molecule.
- Combination of the internal vibrations with this collective features found in the far IR also can cause **splits** and shifts of fundamentals, depending on the symmetry of the resulting combination band.

More effects can be observed in the spectra that are not a direct consequence of the interaction of the atoms and vibrations within the lattice. They include macroscopic size effects (scattering) or interaction of a photon with the crystal field (LO-TO splitting). Furthermore, the application of external forces (high pressures) or perturbations (inclusion of defects) can lead to additional splittings/shiftings.

A large part of the experiments and computer simulations presented in this work are carried out in amorphous solids in the mid IR so we would like to add some remarks regarding the main differences between the spectroscopy of amorphous and ordered materials:

- Band shapes and widths usually differ, as a result of the disordered environment that molecules appreciate when no symmetry is present.
- Appearance of forbidden bands a result of such loss of symmetry (Escribano et al., 2014; Hudson, Gerakines, and Loeffler, 2015).
- Mode Mixing: The amount of vibrational states in an spectral region makes difficult to define clearly separated normal modes.

2.1.2 Harmonic Description of the Vibrations

In general, in the mid IR region, we tend to think in **harmonic** frequencies to interpret our observations. In the harmonic approximation we consider the trajectories that the atoms describe when they vibrate with small amplitude along a certain coordinate from their equilibrium positions. From a fundamental point of view, such description implies the acceptance of the Born-Oppenheimer approximation. Therefore, we consider small classical displacements of the nuclei around their equilibrium positions, in a potential created by the electrons of the system, moving at much higher velocity.

In a Newtonian formulation, the equation describing the classical motion from the equilibrium position is:

$$m_n \ddot{r}_{n,i} = - \frac{\partial V}{\partial r_{n,i}}, \quad (2.1)$$

where m_n denotes the nucleus mass, $r_{n,i}$ represents the cartesian displacements (i) of the nucleus (n) from its equilibrium position R_n and V represents the potential energy of the system. In the harmonic approximation the term $\partial V / \partial r_{n,i}$ can be substituted for a Taylor's series of up to the quadratic terms:

$$V \approx V_0 + \sum_{n,i} \left(\frac{\partial V}{\partial r_{n,i}} \right) r_{n,i} + \frac{1}{2} \sum_{n,m,i,j} \left(\frac{\partial^2 V}{\partial r_{n,i} \partial r_{m,j}} \right) r_{n,i} r_{m,j}. \quad (2.2)$$

In eq 2.2 V_0 is zero as in equilibrium it represents the origin of energies. $\sum_{n,i} (\partial V / \partial r_{n,i}) r_{n,i}$ is also zero as it represents the forces, that are null at the equilibrium position (that is the reason behind the statement "Vibrational frequencies are only meaningful in relaxed structures"). As a consequence of this, we can approximate V as:

$$V \approx \frac{1}{2} \sum_{n,m,i,j} \left(\frac{\partial^2 V}{\partial r_{n,i} \partial r_{m,j}} \right) r_{n,i} r_{m,j}. \quad (2.3)$$

Inserting this term in eq 2.1 we obtain:

$$m_n \ddot{r}_{n,i} = - \sum_{m,j} \left(\frac{\partial^2 V}{\partial r_{n,i} \partial r_{m,j}} \right) r_{m,j}. \quad (2.4)$$

The position vector for a vibration can be approximately treated as a plane wave of frequency ω :

$$r_{n,i} = \frac{u_{n,i}}{\sqrt{m_n}} e^{i(\vec{q}\vec{R}_n + \omega t)}, \quad (2.5)$$

where $u_{n,i}$ is an unitary vector and the product $\vec{q}\vec{R}_n$ represents the product of the vibration propagation vector and the position vector of an atom respectively. The concept of wave vector, useful to understand \vec{q} will be treated later, but qualitatively it can be seen as an arbitrary vector in the momentum space of the unit cell lattice once Periodic Boundary Conditions (PBC) are imposed. The product represents the phase change between two analogous vibrations separated by a unit cell.

Plugging eq 2.5 in eq 2.4 and solving the differential equation gives an eigenvalue equation of $3N \times 3N$ dimension of the type:

$$\omega^2 \vec{u} = D(\vec{q}) \vec{u}. \quad (2.6)$$

$D(\vec{k})$ is a central object in solid vibrational spectroscopy, and is called **Dynamical Matrix**. It contains all the information of the system vibrations in the harmonic approximation. The Dynamical matrix is also the Fourier Transform of the **force constant matrix (matrix of the energy second derivatives)**:

$$D_{n,m,i,j}(\vec{q}) = \frac{1}{\sqrt{m_i m_j}} \sum_{\vec{R}_i - \vec{R}_j} \left(\frac{\partial^2 V}{\partial r_{n,i} \partial r_{m,j}} \right) e^{-i\vec{q}(\vec{R}_i - \vec{R}_j)}. \quad (2.7)$$

The elements of this matrix can be determined theoretically once the second derivatives of the energy are obtained. Diagonalizing this matrix yields the vibrational eigenmodes and eigenvalues of the vibrations, which are the displacement vectors of the motion and the vibrational frequencies respectively. The concept of group vibrations, widely employed in experiments, in which similar atoms appear at similar frequencies becomes natural at the light of this, since it is expected that terms in the Dynamical matrix between atoms with similar mass and type of binding should yield similar eigenvalues.

Dynamical matrix eigenvectors are chosen to be orthonormal. The trajectories in the above mentioned formalism are treated as a superposition of plane waves of frequency ω_α and amplitude $A = u_{n,\alpha,i} / \sqrt{m_n}$, with α being an index mapping the $3N$ plane waves. Mass reduced normal modes coordinates (Q_α) can thus be derived as $\vec{r} = \sum_\alpha Q_\alpha \vec{u}_\alpha$.

Up to now, we have derived the dynamics of the atoms regardless of the excitation mechanism. However, in IR spectroscopy, we deal with the interaction of an infrared photon with a vibrational mode known as **phonon**. In solids, photons can only interact with phonons with $\vec{q} = 0$ because momentum of infrared photons is much lower than the dimensions of the momentum space's lattice (also known as First Brillouin zone, see section 1.2.2) and no excitation mechanism is viable for phonons of $\vec{q} \neq 0$ that need higher momentum particles such as neutrons.

We say that a vibration is *active* if a photon of the same frequency than a vibrational mode is absorbed upon interaction with the sample. In IR spectroscopy, active vibrations appear when a net change in the dipole moment (or in packed structures, polarizability) is obtained when absorbing a photon. The intensity of the absorption of α index can be determined as:

$$I_{IR}^{\alpha} = \frac{\rho\pi}{3c} \left| \frac{\partial \vec{\mu}}{\partial Q_{\alpha}} \right|^2, \quad (2.8)$$

where ρ is the molecular density, c is the speed of light and $\vec{\mu}$ is the dipole moment, in this case of an isolated molecule. This expression has a lengthy derivation starting from the radiation balance equation. We refer the reader to chapter 7 of Wilson, Decius, and Cross, 1980. It is important to remark though that such an expression is made assuming a linear response between the dipole moment and the normal mode elongation.

The associated solid state magnitude to the molecular dipole moment is the vectorial sum of the individual dipoles per unit cell volume (Ω), also known as electric polarizability (\vec{P}). Inserting this definition in eq 2.8 we obtain:

$$I_{IR}^{\alpha} = \frac{\rho\pi}{3c} \Omega \left| \frac{\partial \vec{P}}{\partial Q_{\alpha}} \right|^2, \quad (2.9)$$

where the polarizability is a tensorial magnitude and it is common to express the infrared intensities with respect the components of the diagonalized polarizability tensor.

$$I_{IR}^{\alpha} \propto \sum_{i=1}^3 \left(\frac{\partial P_i}{\partial Q_{\alpha}} \right)^2. \quad (2.10)$$

In section 2.2 we will explain how to obtain these normal modes and infrared intensities in a quantitative way using first principles. After that, we will present the fundamentals of the experimental techniques most frequently employed in this work.

2.2 Theoretical Background

Until now we have developed the general framework for infrared spectroscopy. Now we are going to present a brief introduction on how to determine electronic energies and related properties, in order to predict the infrared spectra employed to compare with experimental observations in this work. Under the Born-Oppenheimer approximation the potential experimented by the nuclei, required to compute the vibrational spectra, is defined as the electronic energy of the system.

2.2.1 Kohn-Sham Formalism

Solving the vibrational problem theoretically is equivalent to solve the electronic structure problem of a collection of particles around their equilibrium position. Born Oppenheimer factorization of the total wave function of a quantum mechanical system states that the wave function can be expressed as the product of the electronic (much faster motion) and the nuclear part (immobile with respect of the electrons) of it ($\Psi_{tot} = \Psi_{elec} \Psi_{nuc}$). The wave function, a central object in the description of a quantum system is the mathematical description of a particular quantum state. In order to obtain the values of the electronic energy, the famous Schrödinger equation must be solved. This equation, once applied the Born-Oppenheimer approximation can be written as:

$$\hat{H}_R^{el}(r_i) \Psi_R^{el}(r_i) = E^{el}(R) \Psi_R^{el}(r_i). \quad (2.11)$$

In this equation, $\Psi_R^{el}(r_i)$ denotes the electronic wavefunction, $E^{el}(R)$ the electronic energy and $\hat{H}_R^{el}(r_i)$ the molecular hamiltonian, that takes the form:

$$\hat{H}_R^{el}(r_i) = -\sum_i \frac{1}{2} \nabla_i^2 + \sum_{i,j \neq i} \frac{1}{|r_i - r_j|} - \sum_{i,n} \frac{Z_n}{|r_i - R_n|} + \sum_{n,m \neq n} \frac{Z_n Z_m}{|R_n - R_m|}, \quad (2.12)$$

where the first term represents the kinetic energy operator, the second one the electron-electron interaction (i, j indexes), the third one the nucleus-electron interaction (n, i indexes respectively) and the fourth, the nucleus-nucleus interaction (n,m indexes). Let us group the third and fourth term under the *external potential* term.

$$V_{r_i}^{ext} = -\sum_{i,n} \frac{Z_n}{|r_i - R_n|} + \sum_{n,m \neq n} \frac{Z_n Z_m}{|R_n - R_m|}. \quad (2.13)$$

Solving the electronic Schrödinger equation for a collection of particles is a many body problem involving 3N degrees of freedom, and thus the wavefunction is 3N dependent. Hohenberg and Kohn reformulated the electronic problem in their celebrated (and Nobel prize deserving) 1964 paper (Hohenberg and Kohn, 1964) demonstrating that the external potential, and hence the total energy is a functional of the electron density $\rho(r)$, effectively reducing the dimensionality of the problem to three degrees of freedom (for the homogeneous electron gas model at least) founding the basis of modern **Density Functional Theory**.

The energy of a system in its functional form is therefore:

$$E[\rho(r)] = \int V_r^{ext} \rho(r) d^3r + F[\rho(r)]. \quad (2.14)$$

In this expression, $F[\rho(r)]$ is named the *Universal Functional*, a somewhat fancy name for a still unresolved molecular physics problem, the determination of the mathematical form of it. Given the lack of applicability of eq 2.14, some years later, Kohn and Sham (Kohn and Sham, 1965) reformulated the problem again, separating the $F[\rho(r)]$ term

representing the density of a collection of N electrons interacting among themselves into two terms $T[\rho]$ and $E_{xc}[\rho]$ representing the energy of N non-interacting electrons and the collection of all the interaction energies, namely the electronic exchange and correlation. The functional form of the energy in the Kohn-Sham formalism is:

$$E[\rho(r)] = T_0[\rho(r)] + \int d^3r [\rho(r)] \left(V^{ext}(r) + \frac{1}{2} \int dr' \frac{\rho(r')}{|r-r'|} \right) + E_{xc}[\rho(r)], \quad (2.15)$$

where T_0 is the kinetic energy of the collection of non interacting electrons and E_{xc} is the exchange correlation energy. The term $\int dr' \frac{\rho(r')}{|r-r'|}$ is commonly abbreviated V_h (Hartree Potential). All the terms are solvable with the exception of E_{xc} . For the other ones, exact solution comes from the second big approximation of the Kohn-Sham method. This approximation involves the treatment of the total electronic density as the sum of monoelectronic (non-interacting) wave functions $\psi(r)$; $\rho(r) = \sum_b [\psi_b(r)]^2$. The term E_{xc} however is unknown in this formalism.

The different ways on how to compute the exchange-correlation energy, that accounts for approximately a 10% of the total energy, constitute a very active research field in theoretical chemistry. Computational accuracy increases from the so called Local Density Approximation (LDA) functionals with a sole dependence on the electronic density at a point, the Generalized Gradient Approximation (GGA) functionals that include a dependance on the gradient of the electron density at that point, and other schemes including the laplacian of the electron density (meta GGA) or combination with other electronic structure methods (hybrid methods, double hybrids etc). In the series of works presented in this thesis, PBE (Perdew et al., 1996), a GGA functional, has been employed in the study of spectroscopic properties of carbonaceous materials, and B3LYP (Becke, 1993), a hybrid method, better for the evaluation of kinetic barriers (Andersson and Grüning, 2004) has been employed for the study of the reactivity on siliceous interstellar dust analogues.

Applying the variational method to eq 2.15, we arrive to a Schrödinger-like eigenvalue equation:

$$H^{KS}\Psi_i(r_i) = \epsilon_i\Psi_i(r_i), \quad (2.16)$$

with a Kohn-Sham Hamiltonian:

$$H^{KS} = -\frac{\hbar^2}{2m}\nabla^2 + V_H(r) + V^{ext}(r) + \frac{\delta E_{xc}}{\delta\rho}. \quad (2.17)$$

$\Psi_i(r_i)$ represent monoelectronic wavefunctions that, in real applications are expanded in a linear combination of basis functions $\Psi_i = \sum_\mu c_{i\mu}\phi_\mu$. The secular equation for the Kohn-Sham method after applying the variational principle is therefore:

$$\sum_{\mu} \left(h_{v\mu}^{KS} + \epsilon S_{v\mu} \right) c_{\mu i} = 0, \quad (2.18)$$

with $h_{v\mu}^{KS} = \langle \phi_v | H^{KS} | \phi_{\mu} \rangle$, $S_{v\mu} = \langle \phi_v | \phi_{\mu} \rangle$ and $c_{\mu i}$ the matrix of coefficients of the linear expansion. The method of solving eq 2.18 is guessing a set of coefficients for the basis functions, normally matching atomic densities and obtaining $S_{v\mu}$. After that, a new set of basis coefficients is calculated using the newly obtained $S_{v\mu}$. This process is repeated until self consistency is achieved when a converged set of eigenvalues (Energies) and eigenvectors (Monoelectronic crystalline, molecular etc, wave functions) is obtained.

Until now a summary of how to calculate electronic energies has been presented considering a general linear combination of orbitals disregarding the periodicity of the problem. In the next paragraphs the mathematical form of the differently employed basis functions and the application of periodicity will be presented.

2.2.2 Density Functional Theory in Extended Systems

The most common way to evaluate the Kohn-Sham equations is to expand the single-particle eigenstates into a set of basis functions. Doing this, numerical methods can be used for solving the Schrödinger like equation. Different codes are available to solve these equations and to obtain energy related properties. Among several differences for the codes used in this thesis, the most important one is the type of basis functions employed. For the spectroscopic studies in condensed phase, plane waves basis functions have been used whereas in reactivity studies on top of surfaces gaussian basis sets have been the method of choice. Traditionally in solid state physics, the description of the evaluation of the energy has been done in a plane wave formalism including pseudopotentials (use of a function for the simulation of the core electrons) and that is the formalism that will be explained here. In the last part of the section and in its correspondent chapter, the employment of gaussian basis set as implemented in the CRYSTAL code, will be briefly discussed.

Disregarding if we are treating with extended amorphous materials, infinite crystalline bulks, surfaces or defective structures, obtaining the energies, wave functions and related properties of systems beyond the nano scale is prohibitely expensive from a computational point of view. The solution of this problem was given by Felix Bloch, and surprisingly enough no Nobel prize was awarded to him for it. Happily enough, he did receive it in 1952 for his contributions to the development of the nuclear magnetic resonance technique, but that is a completely different story out of the scope of our present topic.

Bloch theorem, in its original formulation is:

$$\psi(r + T) = e^{i\vec{k}T} \psi(r), \quad (2.19)$$

where T holds for the multiples of a lattice ($T = N_1 a_1 + N_2 a_2 + N_3 a_3$), where a_i represent the lattice vectors of a 3D solid) vector and k is a wave vector that can be associated

with each wave function. k values are usually restricted to be within one unit cell in the momentum space of a lattice. By convention, this unit cell is generally considered only in the so called First Brillouin Zone which is the irreducible momentum space representation. The most important consequence of Bloch's theorem is that no explicit information on the position of all atoms in the system is needed to extract information from its wave function, whereas information on the unit cell and propagation into certain directions (\vec{k}) is the only requirement. Another possible interpretation involves considering that the monoelectronic eigenfunctions of the Kohn-Sham equations can be written as a modulated periodic function $u_j(r)$:

$$\psi_{k,j}(r) = e^{i\vec{k}r} u_j(r), \quad (2.20)$$

with eq 2.20, $u_j(r)$ can be expanded in a **set of plane waves** of the form:

$$u_j(r) = \sum_G c_{j,G} e^{iGr}. \quad (2.21)$$

G is the momentum space counterpart of the lattice vectors, and fulfills the condition $G = 2\pi/T$. The term $c_{j,G}$ refers to the coefficients of the linear expansion of plane waves. Momentum space (or reciprocal) lattice vectors are labelled using b_i by convention ($G = N_1 b_1 + N_2 b_2 + N_3 b_3$). Combining eq 2.20 and eq 2.21 we can expand our eigenfunctions as:

$$\psi_{k,j}(r) = \sum_G c_{j,k+G} e^{i(k+G)r}. \quad (2.22)$$

This periodicity condition also holds for an effective potential experimented by the electrons in the cell. (V_{eff}) expanded in a Fourier Series:

$$V_{eff}(G) = \frac{1}{\Omega} \int V_{eff}(r) e^{-iGr} d^3r, \quad (2.23)$$

with Ω being the cell volume. Kohn-Sham equations in the notation of Bloch states:

$$\left(\frac{\hbar^2}{2m} \nabla + V_{eff}(r) \right) \psi_{k,j}(r) = \epsilon_{k,j} \psi_{k,i}(r). \quad (2.24)$$

In theory, we are now considering the problem of a finite number of electrons in infinite possible values of (\vec{k}). However, electronic wave functions vary smoothly between neighboring k points. Because of this it is safe to consider only a discrete distribution of points wherein the energy should vary enough. Mathematically, this corresponds from the transition of an integral to a weighted sum of the following type, with weights $w_i \leq 1$:

$$const \int F_k dk = \sum_i w_i F(k_i). \quad (2.25)$$

Different schemes of k-points sampling have been developed being equispaciated grids the most used ones (Monkhorst and Pack, 1976). In our work with amorphous materials, large lattice, no-symmetry insulators are simulated and thus only one point (named Γ) is needed. In the work with siliceous surfaces, however, a small sampling (enough for insulators) has been used and will be discussed in that chapter.

The use of fast Fourier Transform techniques allows us to represent real space concepts such as the electron density in a very efficient way in the momentum space. Kohn-Sham equations can be expressed in a Fourier representation whose deduction will not be given here:

$$\sum_G \left(\frac{\hbar^2}{2m} \|k + G\|^2 \delta_{GG'} + V_{eff}(G' - G) \right) c_G^{k_j} = \epsilon_{k_j} c_G^{k_{ij}}. \quad (2.26)$$

In principle, an infinite number of plane waves can be used in the Fourier expansion. In reality, the number of plane waves is cut off to a certain kinetic energy with the following condition.

$$E_{pw} \geq \frac{\hbar^2}{2m} \|k + G\|^2. \quad (2.27)$$

We have presented here the essential points to understand how to calculate energies in periodic systems using plane wave basis sets. Now, some notes on Gaussian basis sets in extended systems and pseudopotentials will be given.

Plane wave basis sets are essentially delocalized and will be used when presenting the results obtained in the study of the spectroscopic features of carbonaceous dust chemical analogues with CASTEP (Clark et al., 2005). However, in the study of reactivity we have employed atom centered localized basis sets, as implemented in the CRYSTAL code (Dovesi et al., 2014).

Gaussian Basis Sets

Gaussian Basis Sets are localized, normally on an atom. We can recall the general eigenfunction expansion:

$$\Psi_{r,k} = \sum_{\mu} c_{\mu,i}(k) \phi_{\mu}(r, k), \quad (2.28)$$

with $\phi_{\mu}(r, k) = \sum_G \varphi(r - A_{\mu} - G) e^{ikG}$. μ corresponds to the index of the atom on which the basis function is centered, A_{μ} are the coordinates of the localized atom, and φ are known as atomic orbitals. φ can take several mathematical forms, but in our reactivity applications Gaussian functions of fixed coefficients d_i , and exponents α_i , have been employed:

$$\varphi(r - A_{\mu} - G) = \sum_i^{Num.Gauss} d_i e^{\alpha_i (r - A_{\mu} - G)^2}. \quad (2.29)$$

The derivation of the eigenvalue Kohn-Sham equations is essentially the same, but some terms involving more-than-one center integrals are easier to solve with gaussian type orbitals whereas the kinetic energy term becomes more expensive. Each combination of different employed gaussians can be grouped into shells, containing the information of the atomic orbitals with the same quantum numbers n and l . Additionally non conventional shells of higher l quantum number (polarization functions) and n quantum number (diffuse functions) can be used to increase angular and radial flexibility of atomic orbitals, giving a better description of the chemical bonding.

The use of a gaussian basis set in this context is justified by the relative cheap cost of the evaluation of the exact exchange term that allows us to access to hybrid functionals, better suited for kinetic studies. This will be reviewed in Chapter 5. Using gaussian basis sets has other disadvantages such as the basis set superposition error that arise from the unrealistic combination of orbitals in regions where no real interaction is taking place. The selection not only of the type of the basis set but also the size is an important task that should be done taking into account the purpose of the calculation.

Pseudopotentials

Core electrons (electrons that do not belong to the valence shell of an atom) generally do not participate in a chemical bond, so they are usually not important when accounting for things like reactivity or vibrational properties. Core electrons are usually very much attracted by the nucleus and little to no overlapping can be found between their monoelectronic wave functions. This is the same as to say that core electrons are essentially invariant with respect to the chemical environment, and they can remain "frozen" (giving rise to the non very creative... "Frozen Core Approximation"). Application of a pseudopotential usually is done substituting the whole Coulomb potential for a newly generated pseudopotential, instead of adding a term to the classical nucleus Coulomb potential, for efficiency purposes:

$$\left(\frac{1}{2} \nabla^2 + V^{ps}(r) + V^H(r) + V^{xc}(r) \right) \psi(r) = \epsilon \psi(r). \quad (2.30)$$

The more frozen electrons, the less Kohn-Sham equations should be calculated explicitly. Pseudopotentials in the literature can come in several "flavors" depending on their mathematical structure and properties of it. In our works we have employed either "Norm conserving pseudopotentials" or no pseudopotentials at all.

The original mathematical form of norm conserving pseudopotentials, given by Hamann et al (Hamann, Schlüter, and Chiang, 1979) is:

$$V_{ps}(r) = \sum_l \sum_m |Y_{l,m}\rangle V_{lm}(r) \langle Y_{l,m}|, \quad (2.31)$$

where $|Y_{l,m}\rangle$ is referred to one particle wavefunctions of angular momentum l and angular momentum projection m . The way to obtain a pseudopotential is to fit expression 2.31 or analogous ones using data from all electron simulations on the atomic species, for each angular momentum channel.

Norm conserving pseudopotentials are fitted to fulfill two required conditions.

1. The norm of the pseudowavefunction for the core electrons (sum of the diagonal elements of the operator) should be equal between pseudo wave function and exact wavefunction. This is, the number of electrons should be formally identical in the effective potential and the pseudopotential
2. The all-electron and pseudo wave function should yield the same behaviour for the valence electrons.

2.2.3 Evaluation of Vibrational Frequencies and Infrared Intensities

The previous section dealt with the calculation of the energy and wave functions of packed systems. From this pair of quantities, all information of the system, after mathematical manipulation, can be extracted. We are interested in how to construct the dynamical matrix in eq 2.7 and what are the first principles ways to solve eq 2.10.

For the calculation of the dynamical matrix in extended systems we must compute each element of the matrix numerically. Atomic forces should be minimized in order to obtain reliable force constants since, as has been shown in the first section, harmonic approximation is only meaningful when the structure is relaxed. Geometry optimization to minimize these atomic forces is performed and implemented in a variety of codes, and for the structures considered here, the limited memory version of the famous BFGS algorithm has been employed (Liu and Nocedal, 1989). Once forces have been computed, force constants and therefore the dynamical matrix can be evaluated using finite-displacements of the atoms in each cartesian vector direction, using the finite differences technique. Considering a general system with N atoms the minimum number of energy evaluations in order to obtain the force constant matrix is 3N (6N if we consider positive and negative cartesian displacements) calculations with no symmetry constraints. With the force constant matrix calculated, obtaining eigenvectors and eigenvalues is a matter of diagonalizing it.

This method has the advantage of being system independent and general, but has some problems associated with it. Recalling the equation for the dynamical matrix, for a given nuclear potential, V:

$$D_{n,m,i,j}(\vec{q}) = \frac{1}{\sqrt{m_i m_j}} \sum_{\vec{R}_i - \vec{R}_j} \left(\frac{\partial^2 V}{\partial r_{n,i} \partial r_{m,j}} \right) e^{-i\vec{q}(\vec{R}_i - \vec{R}_j)}. \quad (2.32)$$

We can infer that in the same way that for the evaluation of the energy, the vector \vec{q} should be mapped in order to obtain all the cell **phonons**, and usually big simulation cells (usually called supercells) should be employed in order to avoid interaction between units cells in the phonon displacement (incommensurate vibrations). For the calculation of incommensurate points, Density Functional Perturbation Theory (DFPT) (Refson, Tulip, and Clark, 2006) is used. DFPT translates the problem of obtaining the unperturbed eigenvectors (monoelectronic wavefunctions) of a displaced (perturbed) system to obtaining the perturbed eigenvectors of the initial system. Because of this, the

solutions fulfill Bloch Theorem and are not incommensurate anymore since they hold they periodicity of the cell.

With respect to the infrared intensities, let us recall that they are proportional to the change in the polarizability (the total dipole moment of the cell per unit volume) with respect to the coordinate of the vibration displacement. Taylor expansion of the dipole moment with respect to a small displacement (truncated to the linear term) gives:

$$\mu_i = \mu_{0,i} + \sum_{i,\alpha} \left(\frac{\partial \mu_i}{\partial Q_\alpha} \right) Q_\alpha, \quad (2.33)$$

where Q_α is the normal coordinate associated with the α mode and i maps the cartesian components. The normal mode coordinates are related with the atomic displacements via the eigenvectors of the vibration U_α for an atom n , by the relation:

$$X_{i,n}^\alpha = Q_\alpha U_\alpha(i, n). \quad (2.34)$$

The derivatives of μ in this basis are:

$$\frac{d\mu_i}{dQ_\alpha} = \sum_{n,i} \frac{\partial \mu_i}{\partial \tau_{i,n}} U_\alpha(i, n), \quad (2.35)$$

where $\tau_{i,n}$ represents a small displacement of atom n in direction i . Recalling eq 2.8:

$$I_{IR}^m \propto \sum_{i=1}^3 \left(\frac{\partial \mu_i}{\partial Q_\alpha} \right)^2 = \sum_i \left| \sum_j \sum_n \frac{\partial \mu_i}{\partial \tau_{j,n}} U_\alpha(j, n) \right|^2 \quad (2.36)$$

with j being other cartesian atomic displacement. It has been mentioned that in solids, polarizability is the quantity to use. The change in macroscopic polarizability as a consequence of an atomic displacement is determined by the so called Born effective charge tensor:

$$Z_{n,j,i}^* = \Omega \frac{\partial P_{mac,j}}{\partial \tau_{n,i}}, \quad (2.37)$$

defined as a 3x3 matrix for each atom in the cell, representing the change in the total polarization (vectorial sum of dipole moments) as a consequence of atomic displacements. In order to maintain electro neutrality the sum of all elements of the tensor should be zero. As in the case of frequencies, the polarization derivatives are obtained numerically. We can then rewrite the equation for the infrared intensity:

$$I_{IR}^\alpha \propto \sum_i \left| \sum_j \sum_n Z_{n,j,i}^* U_\alpha(j, n) \right|^2. \quad (2.38)$$

We therefore have summarized here how to obtain infrared intensities and frequencies in extended systems. All the simulation packages employed in this work allow the calculation of such quantities with a high numerical precision under the presented approximations, making use of efficient algorithms. When the spectrum is calculated, artificial Gaussian or Lorentzian broadening schemes are employed to simulate the transmission infrared spectra (schemes for reflection are also available). The work flow to compute an infrared spectrum then is:

1. Generate an initial guess for a geometric structure.
2. Compute eigenvalues and eigenvectors of the Kohn-Sham equations for the guess.
3. Relax the forces of the guess until convergence and a stationary point is found.
4. Perturb the system with small displacements of cartesian coordinates to compute the dynamical matrix and the Born Charges tensor.
5. Compute the spectra and provide widths to the bands.

2.2.4 Transition State Theory

For a general reaction:



we can define a macroscopic rate of reaction of the type:

$$\frac{dA}{dt} = -\frac{dB}{dt} = k_{A \rightarrow B} A^n \quad (2.40)$$

where $k_{A \rightarrow B}$ is named *rate constant of reaction*, and is a central object in chemical kinetics. Calculation of $k_{A \rightarrow B}$ is often a crucial task in the description of chemical reactivity from first principles and several theoretical schemes have been developed. Among them, Transition State Theory (TST) (Eyring, 1935) is the most employed one, due to its conceptual simplicity and easy implementation.

The general idea behind transition state theory is that chemical reactions can be described at the microscopic level as the inter conversion between two molecular structures that are connected by a path defined by an internal coordinate, also known as reaction coordinate. This coordinate represents a molecular vibration whose force constant is negative, yielding and imaginary eigenvalue. The rest of the force constants for the system are positive. Therefore, all the internal coordinates are energetic minima with the exception of the reaction coordinate, being maximum. Fig 2.2 represent the cut of the potential energy surface (PES) for this particular coordinate.

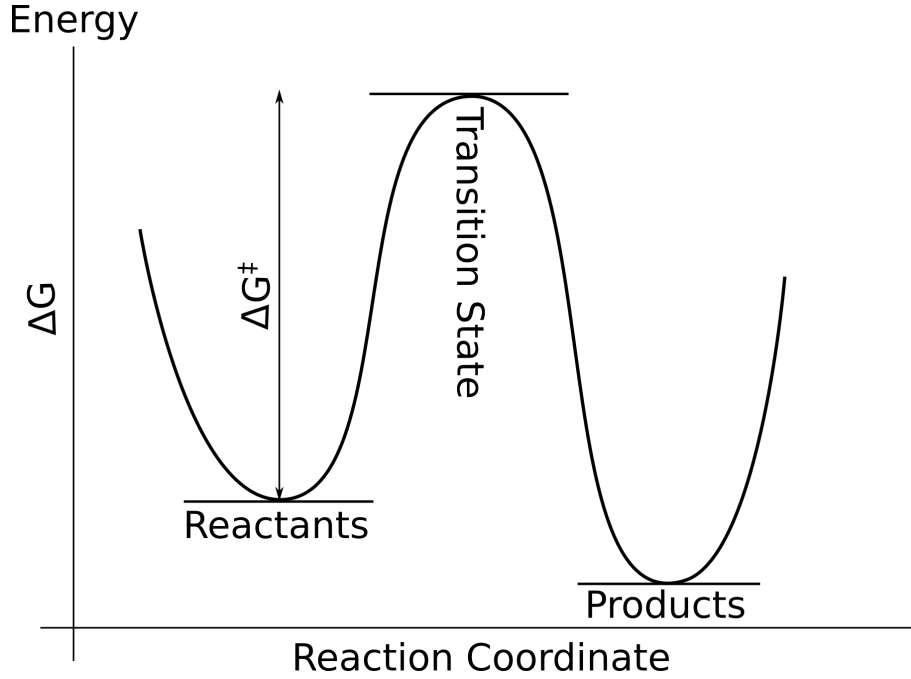


FIGURE 2.2: Schematic representation of the PES of a system during a chemical reaction

Note that the energy axis in Fig 2.2 represents Gibbs' free energy instead of electronic energy given the finite temperature nature of the rate constant. ΔG^\ddagger is the so called activation energy, the energy required to overcome the barrier. The relationship between the rate constant and the free energy of activation is summarized in the Eyring equation:

$$k^{TST} = \frac{k_b T}{h} e^{-\frac{\Delta G^\ddagger}{RT}}, \quad (2.41)$$

with k_b being the Boltzmann Constant, T the system Temperature, h the Planck Constant, ΔG^\ddagger the Gibbs' energy activation barrier and R the ideal gas constant. Note that $\Delta G = \Delta H + \Delta S$. In its statistical thermodynamics formulation:

$$G = E_{elec} + PV + E_{ZPE} + TS, \quad (2.42)$$

where E_{ZPE} is the zero point energy of the system. The calculation of the system entropy, S , is carried out in the harmonic approximation as:

$$S = k_b T \left(\frac{\partial \ln Q}{\partial T} \right) + k_b \ln Q, \quad (2.43)$$

with Q being the partition function of the system. Factorization of the total partition function is as follows:

$$Q = q_{trans} q_{rot} q_{vib} q_{elec}, \quad (2.44)$$

and thus entropy:

$$S = S_{trans} + S_{rot} + S_{vib} + S_{elec}. \quad (2.45)$$

The translation partition functions, q_{trans} does not change between reactants and transition states for unimolecular processes, as the ones considered in this thesis. Since we are interested in entropy differences, $\Delta S_{trans} = 0$. We are working in condensed systems so the rotational degrees of freedom are inhibited and $q_{rot} = 1$. The electronic partition function q_{elec} is also 1 because we are working in the ground state. For our purposes, therefore only q_{vib} is meaningful and can be calculated as:

$$q_{vib} = \int \frac{h\nu}{e^{\frac{h\nu}{k_b T}} - 1} F(\nu) d\nu, \quad (2.46)$$

with ν being the vibrational eigenvalues and $F(\nu)$ the phonon density of states. When calculating the vibrational eigenvalues only at $\vec{q} = 0$, this integral can be represented as the discrete product of modes, in analogy with its molecular counterpart (McQuarrie, 2000).

$$q_{vib} = \prod_{i=1}^{3N-6(7)} \frac{e^{-\frac{h\nu_i}{2k_b T}}}{1 - e^{-\frac{h\nu_i}{k_b T}}}. \quad (2.47)$$

The different upper limits represent respectively the productory for the reactants (3N-6) or for the transition state (3N-7) due to the inclusion or the lack of inclusion of the imaginary transition eigenvalue.

We are now in position to determine ΔG^\ddagger with the calculation of the vibrational entropy. The calculation of the rate constant in the Polanyi-Wigner equation (Eq 2.41) is straightforward. This equation can be improved including quantum tunneling effects by means of a multiplicative correction factor κ . Different schemes for the calculation of κ will be considered in chapter 5.

Transition state theory has been improved over the course of the years with the inclusion of variational schemes to account for recrossing. This is, crossing the energetic barrier in both directions of the reaction coordinate instead of considering only the univocal reactions to products direction.

2.3 Experimental Techniques

The first part of this chapter will be dedicated to explaining the inner workings of our basic spectroscopic experiment, to measure the infrared spectra of samples at interstellar like conditions. A brief description of every component of our experimental setup will be given. The basic concepts of our carbonaceous samples preparation technique, with a quick glance to our plasma reaction chamber, will be presented later.

2.3.1 Experimental Setup for IR Spectroscopy and Electronic Processing

The spectroscopy and irradiation experiments are carried out in a high vacuum setup. It consists on a stainless steel cylindrical chamber with different ports at different levels. Residual pressure in the chamber is maintained at 5×10^{-8} mbar using a turbopump (Pfeifer HiPace 300) with a nominal pumping speed of 260 l/s for N₂ assisted by a rotary oil pump (Pfeifer DUO20 20 m³/h). The pressure in the chamber is measured using a Penning gauge (Carrasco et al., 2002). In the chamber either a closed-cycle helium cryostat (Advanced Research Systems), or a cylindrical stainless-steel liquid nitrogen Dewar container could be installed. At the cold end of both cryogenic systems a sample holder is placed in close thermal contact. The sample holder for infrared transmission experiments has a 10 mm diameter open window. When using the closed-cycle helium cryostat the temperature of the sample can be controlled between 14 K and 300 K (with 0.5 K accuracy) using silicon diode detectors and a Lakeshore 325 temperature controller. In the experiments performed with the liquid nitrogen cryostat, the temperature is measured with Pt-100 sensors and can be controlled between 85 K and 300 K by means of a home-made temperature controller (an upgraded version of that described in Carrasco et al., 2002). The selection of either the closed-cycle-helium or the liquid-nitrogen cryostat is made depending on the experiment we want to perform, determined by the influence of the temperature in each particular sample.

The cylindrical vacuum chamber has several openings provided with high vacuum flanges (CF35 and CF100). The cryostat is situated in the larger top CF 100 flange together with a vacuum rotary platform. This allows us to face the sample alternatively to different ports within the irradiation plane. The CF35 flanges in the optic plane are employed for the electron gun, or the UV lamp, and for KBr IR transparent windows (see Fig 2.3). The quadrupole mass spectrometer is located in a lower plane, together with electrical feedthroughs, a pressure gauge and gas inlets. Figure 2.4 shows a schematic lateral view of our chamber with the liquid nitrogen cryostat.

We have three independent gas inlet lines, two of them provided with Alicat mass flow controllers, to introduce the gases in the chamber. For the introduction of room temperature liquids, we have a thermalized line to regulate the input pressure of the desired sample. This line is equipped with a needle valve to control the input flow. We back-fill the chamber with an homogeneous pressure when working with these lines. This allow us to grow ice layers with homogeneous thickness (Molpeceres et al., 2016). Alternatively, for deposition of low sublimation-point solids a homemade oven that works under vacuum was employed. See for example our works with glycine (Maté et al., 2011; Maté et al., 2014).

The two analytical techniques most used in our experiments are mass spectrometry and, of course, infrared spectroscopy. When it is necessary to monitor the thickness of an ice layer that is been grow, laser interferometry is also available (Molpeceres et al., 2016). To induce chemical or structural changes in our samples we could irradiate them with different sources, either electron gun or a UV lamp.

With the scheme of the chamber explained, what remains is a description of the analytic techniques used in our experiments:

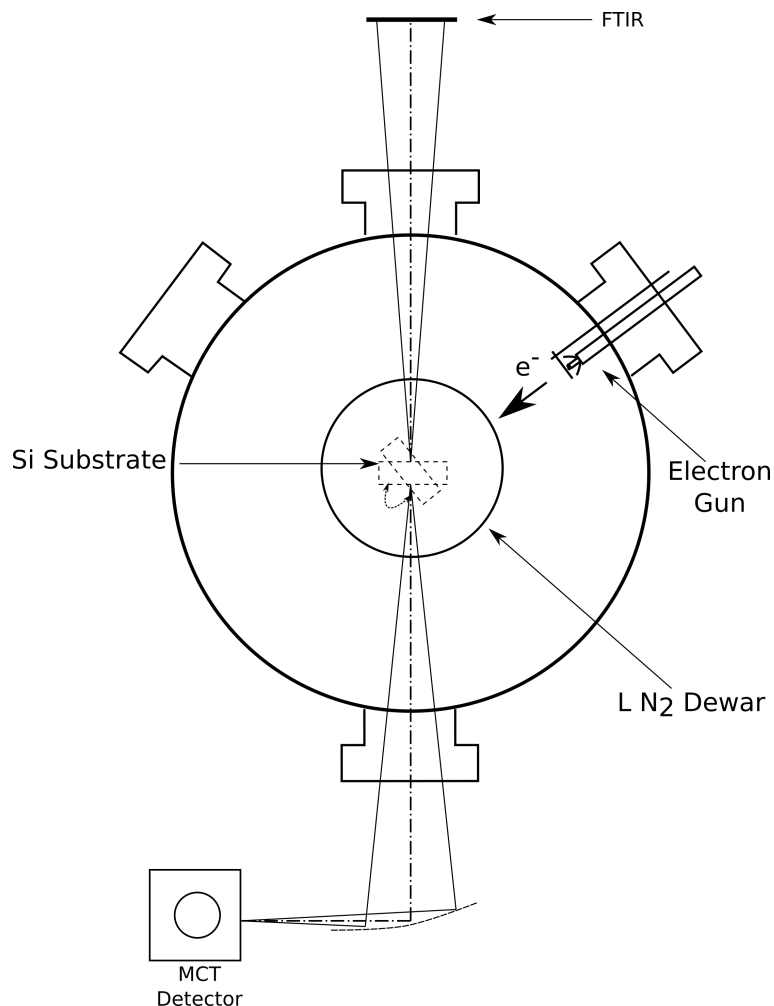


FIGURE 2.3: Transversal cross section of the vacuum chamber in the optic plane

- **QMS** : A quadrupole mass spectrometer (QMS) Inficon Transpector 2 is available for monitoring the gas phase. The mass analyzer is differentially pumped from the main chamber with a small turbopump. The use of the mass analyzer is dual. First, when depositing gases, it monitors the purity and stability of the incoming gas and for mixtures it allows to measure composition ratios. Second, it monitors the gases that arise during thermal program desorption or processing experiments.
- **Fourier Transform Infrared Spectrometer (FTIR)** : The spectroscopic analysis is done using a Bruker Vertex 70 infrared spectrometer provided with an external liquid nitrogen refrigerated Hg-Cd-Te detector. Two different IR lamps and beam splitters are available to cover the 500 -16000 cm^{-1} spectral range. The spectrometer and external optical path is purged with dry air. The spectrometer allows to work with a maximum resolution of 0.5 cm^{-1} , but for the experiments performed in this thesis we have used resolutions that varied between 1-8 cm^{-1} , depending on the nature of the studied species. Between 100 and 400 scans were accumulated and equally weighted.

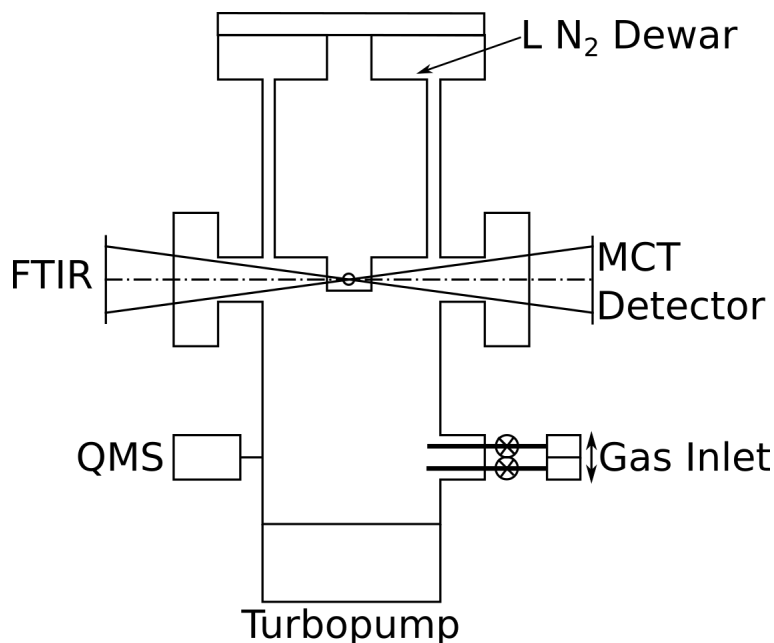


FIGURE 2.4: Lateral View of our High Vacuum Chamber.

- Electron Gun** : We have a homemade high energy electron gun, that provides electrons with energies between 1 and 5 keV. The emission element is made of a 130 mm diameter tungsten wire that is bended forming a spiral of ~ 10 mm long. A grounded aluminum grid with 20 mm diameter circular shape is situated at 10 mm from the filament. Such grid is made of a very fine a mesh. The electrons are attracted to it and acquire a given energy that is function of the applied potential in the filament, -5 kV in our experiments (Maté et al., 2014). A power source stabilize the emission and guarantee the reproducibility of the experiments. The important magnitude for our experiments is the electron flux that reach the sample. We have calibrated the electron gun placing a conducting material in the sample holder, in the same position of the sample and measuring the electron current that it is received. The distance between the electron gun grid and the sample is 30 mm. Details on the calibration and the irradiation experiments will be given in chapter 4.

The setup employed in our experiments is very flexible and allows us to obtain infrared spectra of a wide variety of samples, and perform extensive irradiation experiments. As for the measurements with refractory materials, they should be introduced in the chamber *a priori*. The HAC samples are grown in a different setup, a plasma reactor that will be described below. The next section will be dedicated to explain the chemical mechanism of formation of the HAC analogues, that is called Plasma Enhanced Chemical Vapor Deposition, and a general scheme of the reactor we use to grow them.

2.3.2 Experimental Setup for Carbonaceous Sample Growth: PECVD

The generation of an amorphous carbonaceous sample can be essentially understood as an anisotropic growth of an organic polymer inside a plasma reaction chamber as stated in Grill, 1994. Polymers obtained from this technique are highly branched and cross linked.

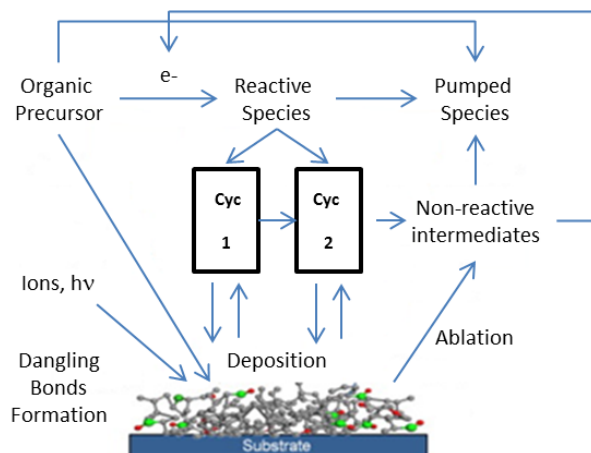


FIGURE 2.5: Physical Processes in Plasma Polymerization
Extracted from (Thiry et al., 2016)

Plasma grown polymers have several characteristics:

- No repeating unit can be extracted from a group of monomers like in conventional polymers.
- Even though the monomer plays an important role, more crucial are the plasma parameters. There is not a product that univocally can be identified as the plasma polymer of a monomer (Methane, Acetylene, Ethylene...). Different materials can be produced from different plasma parameters.
- There is no need for a chemical functional group for the formation of the polymer in plasma polymerization.

Plasma polymerization can be summarized in Fig 2.5. Four elementary chemical processes could be pointed as the main ones in the polymerization processes: Initiation, Propagation, Termination and Reinitiation.

In the first step, radicals and atoms are produced upon molecule-electron and molecule-ion collision. Molecules that undergo energetic collisions and generated free radicals adsorb on top of the substrate surface, in our case an infrared silicon plate, placed inside the reactor. The propagation step concerns the to the interaction of free radicals in the gas phase or between radicals and the adsorbed seed. Gas phase oligomers can subsequently accrete on top of the surface of the absorbed polymer. The termination step is similar to the propagation one, but ending with a closed polymer chain. The last step, the reinitiation is optional and happens when chain fragments can be reconverted into radicals, starting the process again.

This chaotic mechanism allows obtaining amorphous materials with different properties than their crystalline counterparts, and a wide range of materials can be obtained varying the plasma parameters. In addition to that, the position in which the substrate is located is also an important factor that defines in which magnitude the different processes will happen.

A summary of the chemical species involved in the plasma polymerization can be found in Fig 2.6.

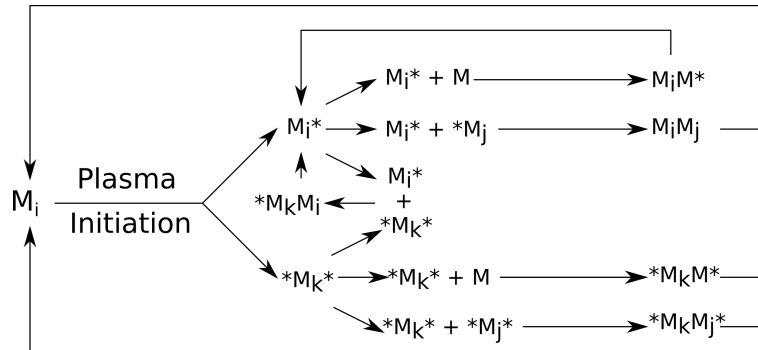


FIGURE 2.6: General chemical fragmentations and recombinations in a plasma polymerization.

Adapted from Grill, 1994

In the previous scheme it is presented the different breakings for a species M_i and some possible combinations leading to new species M_i that are subsequently destroyed again to re-initiate the cycle. The termination steps are also present, and the possibilities of radicals formation increase with the number of species that are generated from the first precursor. The polymerization continues until the plasma is turned off and no new species are generated or until all the formation radical steps are inhibited.

For the creation of such polymers (hydrogenated amorphous carbon) we have employed a experimental set up of which the general scheme is presented in Fig 2.7. The scheme shows an inductively coupled RF discharge reactor. Background pressure in the chamber before plasma generation is on the order of 3×10^{-3} mbar (Maté et al., 2014). A gas precursor (CH_4) diluted in a gas carrier (He) is introduced in the reaction chamber with a pressure of 0.2 mbar in flow using two mass flow Alicat controllers. The setup is evacuated using a turbopump and monitored using two different pressure gauges (Capacitive and Piranni-Penning). The reaction chamber consists in Pyrex glass tube of 30 cm length and 4 cm of diameter on top of which a Cu coil (8 cm) is curled around the central part of the reactor. The plasma is initiated by feeding the coil with a 13.56 MHz via a RF generator. The plasma has a maintained 40 W power during the deposition time. An IR transparent silicon disc of 25 mm of diameter and 1 mm of thickness is introduced in the reactor on top of a rectangular glass tray (to avoid deposition on both sides of the plate). The position of the substrate along the reactor axis is relevant for the growth of the polymer. Substrates placed within the coil experience more energetic conditions than the ones placed downstream (after the coil). The gas phase is monitored using a quadrupole mass spectrometer situated after a $50 \mu\text{m}$ diaphragm and deferentially pumped by another turbopump system.

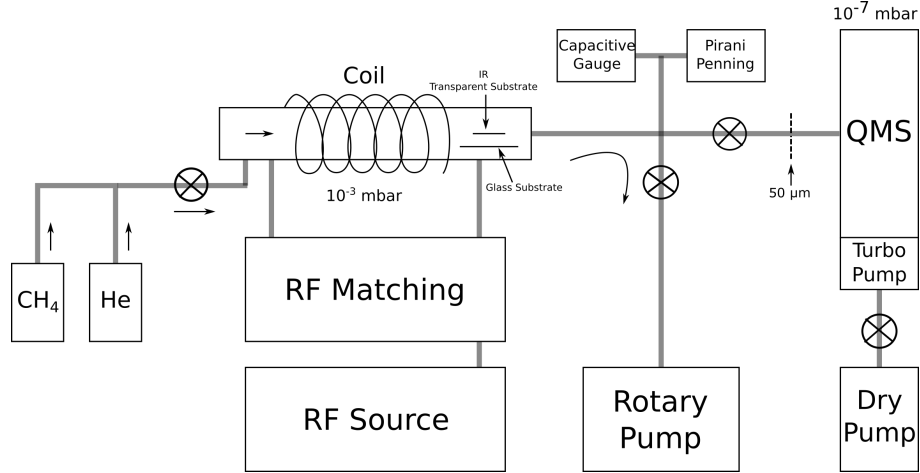


FIGURE 2.7: Experimental scheme for our carbonaceous, plasma grown polymers

2.3.3 Experimental Quantification of Total Infrared Intensities and Absorption Cross Sections

In experimental absorption spectroscopy the intensity of a transition is directly related with the amount of absorbers and the geometry of the of the experimental setup. Knowing the intensity of the incoming radiation, $I_0(\nu)$, it is possible to determine the intensity of the beam passing through a media employing the well known Lambert-Beer law:

$$\frac{I(\nu)}{I_0(\nu)} = e^{-\alpha(\nu)\rho x}, \quad (2.48)$$

with $\alpha(\nu)$ being the absorption coefficient of the sample, ρ the macroscopic density of absorbers in the sample, and x the optical path length. The spectroscopic derivation of the absorption coefficient leads to:

$$\int \alpha(\nu) d\nu = \sum_i (N_i - N_f) \left(\frac{h B_{fi} \nu_{fi}}{c} \right), \quad (2.49)$$

where N_i and N_f represent respectively the populations of the initial and final vibrational level, c is the speed of light and B_{fi} is Einstein's stimulated absorption coefficient for that particular transition. The experimental quantity obtained in experimental absorption spectroscopy is the so called Absorbance (*Abs*), that in terms of the Lambert-Beer law is given by:

$$Abs(\nu) = \log_{10} \frac{I(\nu)}{I_0(\nu)} \quad (2.50)$$

combining eq 2.49 and eq 2.50:

$$Abs(\nu) = 0.434\alpha(\nu)\rho x. \quad (2.51)$$

The integrated absorption cross section (in $\text{cm}\cdot\text{molecule}^{-1}$), also defined as line strength, A , of a transition is an intrinsic magnitude of the transition between ν_1 and ν_2 :

$$A = \int_{\nu_1}^{\nu_2} \alpha(\nu) d\nu. \quad (2.52)$$

Band strengths are of tantamount importance when quantifying the number of absorbers in a sample. Determining band strengths for different samples is an active field of research with many applications for the interpretation of the infrared data obtained from astrophysical missions.

For the derivation of absorption cross sections and band strengths we employ the imaginary part of the complex index of refraction (k). The relation between the absorption coefficient and the imaginary component is obtained from Lambert's law and is represented as:

$$\alpha = \frac{4\pi k}{\nu\rho}. \quad (2.53)$$

The integrated band strengths allow for the quantification of species using IR spectroscopy. Band strengths can be easily calculated from the IR absorption spectra of samples with known density and layer thickness. Employing the relationships between absorbance and absorption coefficient, or the relation between the imaginary component of the refractive index and the absorption coefficient, we arrive to the two possible expressions for the determination of the band strengths:

$$A' = 2.303 \frac{1}{\rho x} \int_{\nu_1}^{\nu_2} Abs(\nu) d\nu, \quad (2.54)$$

or:

$$A = \frac{4\pi}{\rho} \int_{\nu_1}^{\nu_2} k(\nu)\nu d\nu. \quad (2.55)$$

These integrals run over the whole profile of a band. In the case of blended absorptions, such as the ones we are going to encounter during this thesis, several approximations have been done, such as comparing the band strengths of gas phase isolated molecules with the ones present and blended in a solid (Dartois et al., 2007; Chiar et al., 2013). Even though this scheme could yield good results, we must remember that band strengths are magnitudes of a particular species in particular physical conditions. Obtaining such magnitudes in different environments and phases is of mandatory importance for the astrochemical community. (Molpeceres et al., 2016; Molpeceres et al., 2017b; Molpeceres et al., 2017a).

The integrated absorption coefficients A , are the magnitudes obtained from our computational simulations and are directly comparable with our experimental results via a conversion factor.

References

- Andersson, Stefan and Myrta Grüning (2004). "Performance of density functional for calculating barrier heights of chemical reactions relevant to astrophysics". In: *Journal of Physical Chemistry A* 108.37, pp. 7621–7636.
- Becke, Axel D (1993). "Density-functional thermochemistry. III. The role of exact exchange". In: *The Journal of Chemical Physics* 98.7.
- Carrasco, E., J. M. Castillo, R. Escribano, V. J. Herrero, M. A. Moreno, and J. Rodríguez (2002). "A cryostat for low-temperature spectroscopy of condensable species". In: *Review of Scientific Instruments* 73.10, p. 3469.
- Chiar, J. E., A. G.G.M. Tielens, A. J. Adamson, and A. Ricca (2013). "The structure, origin, and evolution of interstellar hydrocarbon grains". In: *Astrophysical Journal* 770.1, p. 78.
- Clark, S. J., M. D. Segall, C. J. Pickard, P. J. Hasnip, M. I. J. Probert, K. Refson, and M. C. Payne (2005). "First principles methods using CASTEP". In: *Z. Kristallogr.* 220, pp. 567–570.
- Dartois, E., T. R. Geballe, T. Pino, A.-T. Cao, A. Jones, D. Deboffle, V. Guerrini, Ph. Bréchnignac, and L. D'Hendecourt (2007). "IRAS 08572+3915: constraining the aromatic versus aliphatic content of interstellar HACs". In: *Astronomy and Astrophysics* 463.2, pp. 635–640.
- Dovesi, Roberto, Roberto Orlando, Alessandro Erba, Claudio M. Zicovich-Wilson, Bartolomeo Civalleri, Silvia Casassa, Lorenzo Maschio, Matteo Ferrabone, Marco De La Pierre, Philippe D'Arco, Yves Noël, Mauro Causà, Michel Rérat, and Bernard Kirtman (2014). "CRYSTAL14: A program for the ab initio investigation of crystalline solids". In: *International Journal of Quantum Chemistry* 114.19, pp. 1287–1317.
- Escribano, Rafael, Vicente Timon, Óscar Gálvez, Belén Maté, Miguel a Moreno, and Victor J. Herrero (2014). "On the Infrared Activation of the Breathing Mode of Methane in Ice". In: *Physical Chemistry Chemical Physics*, pp. 16694–16700.
- Eyring, Henry (1935). "The Activated Complex in Chemical Reactions". In: *The Journal of Chemical Physics* 3.2, pp. 107–115.
- Grill, A. (1994). *Cold Plasma Materials Fabrication: From Fundamentals to Applications*. Wiley. ISBN: 9780780347144.
- Hamann, D. R., M. Schlüter, and C. Chiang (1979). "Norm-Conserving Pseudopotentials". In: *Phys. Rev. Lett.* 43 (20), pp. 1494–1497.
- Hohenberg, P. and W. Kohn (1964). "Inhomogeneous Electron Gas". In: *Phys. Rev.* 136 (3B), B864–B871.
- Hudson, R. L., P. A. Gerakines, and M. J. Loeffler (2015). "Activation of weak IR fundamentals of two species of astrochemical interest in the Td point group – the importance of amorphous ices". In: *Phys. Chem. Chem. Phys.* 17 (19), pp. 12545–12552.
- Kohn, W. and L. J. Sham (1965). "Self-Consistent Equations Including Exchange and Correlation Effects". In: *Phys. Rev.* 140 (4A), A1133–A1138.

- Liu, Dong C. and Jorge Nocedal (1989). "On the limited memory BFGS method for large scale optimization". In: *Mathematical Programming* 45.1-3, pp. 503–528. arXiv: [arXiv: 1011.1669v3](https://arxiv.org/abs/1011.1669v3).
- Maté, Belén, Yamilet Rodriguez-Lazcano, Oscar Gálvez, Isabel Tanarro, and Rafael Escribano (2011). "An infrared study of solid glycine in environments of astrophysical relevance." In: *Physical Chemistry Chemical Physics* 13.26, pp. 12268–12276.
- Maté, Belén, Isabel Tanarro, Miguel A. Moreno, Miguel Jiménez-Redondo, Rafael Escribano, and Víctor J. Herrero (2014). "Stability of carbonaceous dust analogues and glycine under UV irradiation and electron bombardment". In: *Faraday Discuss.* 168.0, pp. 267–285.
- McQuarrie, D.A. (2000). *Statistical Mechanics*. University Science Books.
- Molpeceres, Germán, Miguel Angel Satorre, Juan Ortigoso, Carlos Millán, Rafael Escribano, and Belén Maté (2016). "Optical Constants and Band Strengths of CH₄:C₂H₆ Ices in the Near- and Mid- Infrared". In: *The Astrophysical Journal* 825.2, p. 156.
- Molpeceres, Germán, Miguel Angel Satorre, Juan Ortigoso, Alexandre Zanchet, Ramón Luna, Carlos Millán, Rafael Escribano, Isabel Tanarro, Víctor J. Herrero, and Belén Maté (2017a). "Physical and spectroscopic properties of pure C₂H₄ and C₂H₄:CH₄ ices". In: *Monthly Notices of the Royal Astronomical Society* 466.2, pp. 1894–1902.
- Molpeceres, Germán, Vicente Timón, Miguel Jiménez-Redondo, Rafael Escribano, Belén Maté, Isabel Tanarro, and Víctor J Herrero (2017b). "Structure and infrared spectra of hydrocarbon interstellar dust analogs". In: *Physical Chemistry Chemical Physics* 19.2, pp. 1352–1360.
- Monkhorst, H and J Pack (1976). "Special points for Brillouin zone integrations". In: *Physical Review B* 13.12, pp. 5188–5192. arXiv: [arXiv:1011.1669v3](https://arxiv.org/abs/1011.1669v3).
- Perdew, John P., Kieron Burke, Matthias Ernzerhof, Department of Physics, and New Orleans Louisiana 70118 John Quantum Theory Group Tulane University (1996). "Generalized Gradient Approximation Made Simple". In: *Physical Review Letters* 77.18, pp. 3865–3868.
- Refson, K, P R Tulip, and S J Clark (2006). "Variational density-functional perturbation theory for dielectrics and lattice dynamics". In: *Phys. Rev B* 73, p. 155114.
- Sherwood, P.M.A. (1972). *Vibrational Spectroscopy of Solids*. Cambridge monographs in physical chemistry. Cambridge University Press. ISBN: 9780521084826.
- Thiry, Damien, Stephanos Konstantinidis, Jérôme Cornil, and Rony Snyders (2016). "Plasma diagnostics for the low-pressure plasma polymerization process: A critical review". In: *Thin Solid Films* 606, pp. 19–44.
- Wilson, E.B., J.C. Decius, and P.C. Cross (1980). *Molecular Vibrations: The Theory of Infrared and Raman Vibrational Spectra*. Dover Books on Chemistry Series. Dover Publications. ISBN: 9780486639413.

Chapter 3

Structure and Spectral Features of Hydrogenated Amorphous Carbon

The results section of the thesis starts with this chapter, devoted to the study of the structural and spectroscopic properties of chemical analogues of carbonaceous dust. These structural properties will be studied mainly from the theoretical point of view, and will be compared also with the experimental results obtained in our group, bridging the gap between calculations and experiments. The quantum chemical calculations presented will address two different archetypes associated with hydrogenated amorphous carbon (HAC). Infrared absorption and emission curves of these interstellar carbonaceous dust chemical analogues will be determined indicating always the limit of applicability of the model applied.

The results of this chapter contains information published in three articles: "Structure and infrared spectra of hydrocarbon interstellar dust analogs" (Molpeceres et al., 2017), "Plasma generation and processing of interstellar carbonaceous dust analogs" (Peláez et al., 2018) and the final one, "UV-heating and IR-photocooling of interstellar dust packed chemical analogues", (to be submitted to the *Astronomy & Astrophysics* journal).

3.1 Introduction

The structure of interstellar dust grains is not homogeneous for its whole. The chemical structure of the grains greatly depends on the formation processes, its age, or the energetic processing mechanism happening on each particular astronomical region. Our efforts to understand cosmic dust are focused on unravel the internal chemical structure and composition of the different regions of the grain.

For carbonaceous (and siliceous) dust, an excellent study of the properties of dust particles of different sizes in different astronomical regions has been published by Jones (Jones et al., 2013). In this article, they determine the spectroscopic behavior of different dust analogues using optical data. One of the key points that arise from their study, and in fact from many other previous studies, is that in carbonaceous dust, one key quantity is the aromatic to aliphatic carbon ratio, or better said the $C(sp^2)/C(sp^3)$ ratio. Fig 3.1 shows the different stages of a dust grain particle. (Adapted from Jones et al., 2013).

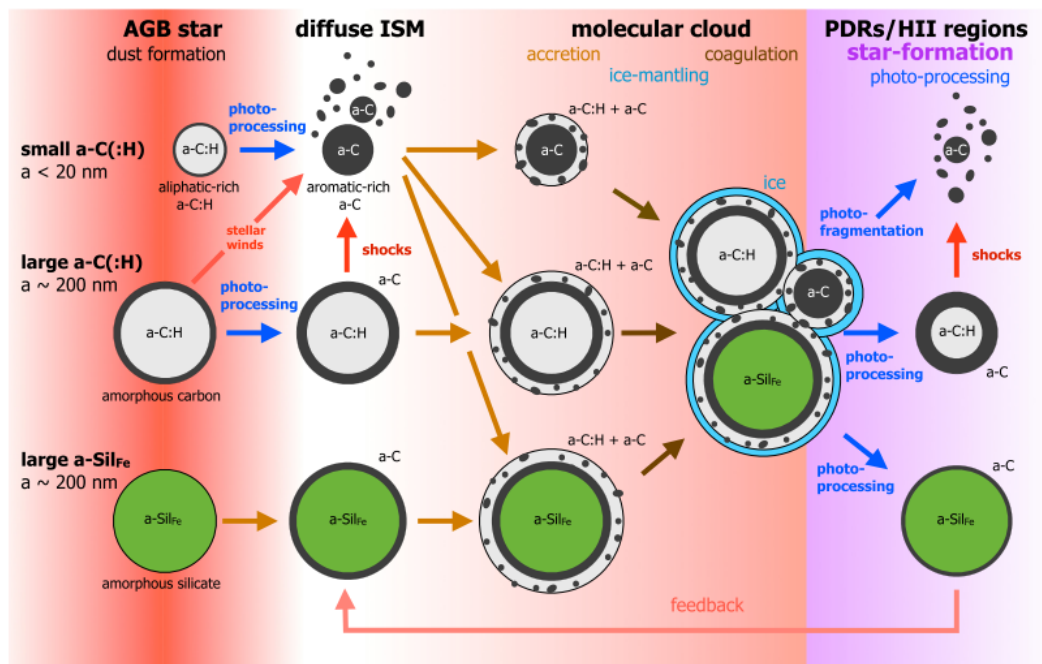


FIGURE 3.1: Different evolutionary stages of a dust grain particle as a function of the distance to the formation region.

Extracted from Jones et al., 2013

As can be seen, at early stages of formation, amorphous carbonaceous particles are mainly aliphatic with thin mantles of aromatic rich amorphous or barely hydrogenated amorphous carbon. Different processing mechanisms, such as processing with UV photons, induce dehydrogenation and aromatization (such processes will be studied in Chapter 4). In a molecular cloud, in which temperatures are extremely low, accretion of volatile compounds can happen on top of the dust grain, effectively shielding it from further processing. The study of accretion and chemical processes on top of siliceous material will be considered in Chapter 5. As a result of this, processing and formation of ice mantles imply that carbonaceous dust grains spectral features are non homogeneous across lines of sight. (Bartlett and Duley, 1996; Jager, Mutschke, and Henning, 1998; Pino et al., 2008; Kwok and Zhang, 2011; Hammonds et al., 2015)

Several astronomical spectral features can be attributed to carbonaceous matter in solid or gas phases, in the form of different size dust grains or big gas phase polycyclic aromatic hydrocarbons (PAH). The recognizable, carbonaceous associated features can be summarized as the diffuse interstellar bands (DIB), the extended red emission (ERE), the **220 nm UV bump**, the **IR emission bands**, also known as unidentified IR emission (UIE) and the **mid-IR absorption bands**. The bold text indicates the features that will be studied during this chapter.

Diffuse Interstellar Bands, DIBs, are one of the oldest known interstellar features and a prodigious discovery at the time they were detected (Heger, 1922). The history of such discovery is out of the scope of the present work, but McCall and Griffin, 2013 presents an excellent review, including digitalization and comparison of the original 1919 spectrum with modern spectra. Concerning the nature of the bands, they are ubiquitously

found in absorption and they have a rich profile that change slightly from source to source. More than 500 different bands have been found in the visible range between $\sim 470 - 662$ nm. They are nowadays generally attributed to free flying carbon bearing molecules, such PAHs and linear carbon clusters (Kroto and Jura, 1992; Snow, 1997; Krełowski, 2002), even though only two lines remain assigned (two C_{60}^+ lines Campbell et al., 2015). The arguments in favor of a molecular origin of these bands can be found in Geballe, 2016, including the presence of fine structure components and lack of excess polarization for the absorptions, indicating rotational structure and the lack of magnetically aligned dust grains, respectively.

The extended red emission (ERE) first discovery was not as old as the that of DIBs. It was first observed more than 35 years ago (Schmidt, Cohen, and Margon, 1980) in reflection nebulae and in other astronomical regions since then (Gordon, Witt, and Friedmann, 1998; Lai, Witt, and Crawford, 2017). This feature is usually found in environments like planetary nebulae and in the diffuse interstellar medium. It is commonly attributed to photoluminescence from a semiconductor in the visible range. Along with carbonaceous materials (Duley, Seahra, and Williams, 1997; Berné et al., 2008), silicon nanoparticles are also considered a viable candidate (Witt and Vijh, 2003).

As has been previously said, the simulation of the two aforementioned features is not explicitly treated in our chemical analogues and only this mention is going to be held. However, the other three spectroscopic signatures of carbonaceous material have been determined for different analogues and are going to be presented. Discussion on UV-Bump, Infrared Absorption (especially for the $3.4 \mu m$ band) and comments on potential infrared emission of packed carbonaceous materials are the main topics of the chapter.

Starting from the most energetic feature, the so called **UV bump** in the ultraviolet (UV) extinction curve, detected in 1965 for the first time (Stecher and Donn, 1965), is commonly associated to carbonaceous grains of some sort with a small degree of hydrogenation. Candidates include graphite, amorphous carbon or HAC. Small, planar PAH molecules have also been considered, leading to discussion in the literature (Kwok and Zhang, 2011; Kwok and Zhang, 2013). The UV bump is a spectral feature found at a more less constant 217.5 nm position but with variations in the width between 30 and 80 nm. Fig 3.2 shows this feature toward several sources.

The UV bump arises from electronic band transitions and is generally attributed to the aromatic sub units within the grain. Following the scheme of Fig 3.1, this feature will be more intense in photo-processed materials (Mennella et al., 1998; Duley and Seahra, 1999). It has been discussed in the literature than HAC materials can be the carriers of this electronic absorptions (Gadallah, Mutschke, and Jäger, 2011; Mennella et al., 1998; Duley and Hu, 2012). Photon and ion irradiation of highly aliphatic materials have been proven to raise the magnitude of the UV bump (Mennella et al., 1996; Gadallah, Mutschke, and Jäger, 2011), supporting the experimental evidence towards the aromatic nature of the carriers of this band.

The so called **Unidentified Infrared Emission** (UIE, sometimes called UIR) is a well known feature appearing between $3-20 \mu m$, the region of molecular vibrations and functional group modes. The spectral complexity of the feature is specially rich in the $5-8.9 \mu m$ region. In this zone, the vibrations of carbon-carbon or carbon-hydrogen nature are essentially aliphatic and aromatic bendings, and aromatic or olefinic stretchings.

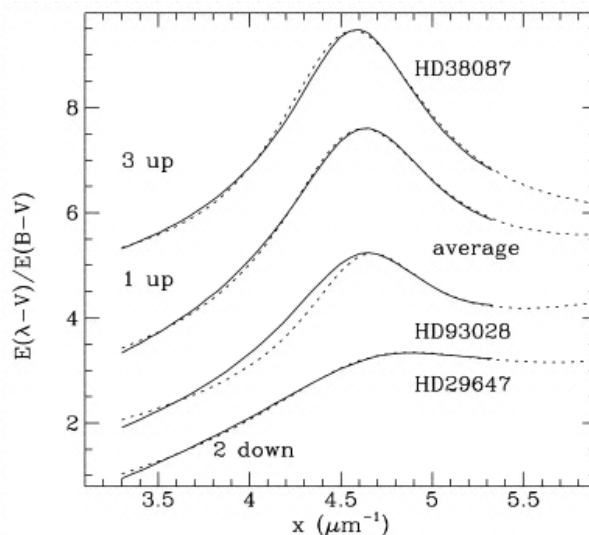


FIGURE 3.2: Averaged UV Bump together with individual features observed toward different sources
 Extracted from Mennella et al., 1998

The debate about the identity of the molecular carriers of these vibrations generally discards solid particles in favor of free flying polycyclic aromatic hydrocarbons (PAH) (Allamandola, Tielens, and Barker, 1985; Salama and Allamandola, 1995; Tielens, 2008; Peeters, 2011). The most important reason for such assumption is that these features can be found in cold environments. PAHs can undergo a temperature spike up to a color temperature of 1000 K upon absorption of a **single photon** before photorelaxation, a temperature too high for heating micron size grains. Small species, holding limited heat capacity, are then required (Sellgren, 1984). In fact PAHs fulfill these requirements (Leger and Puget, 1984; Allamandola, Tielens, and Barker, 1985; Puget and Leger, 1989). Among the achievements of this theory, we have that it shows good fits of some astronomical sources (reflection nebulae) and also that their associated bands have been so extensively studied that nowadays they can be employed as a tracer for star formation rates (Calzetti, 2011). Another great advantage of the PAH hypothesis is that is flexible enough to accommodate different features by employing PAH derivatives such as hydrogenated PAHs, PAH with aliphatic substituents, clusters of PAH etc (Peeters, 2011).

However, the PAH hypothesis requires a mixture of different PAHs of very different nature to reproduce the observed emission, and at this date, not a single PAH molecule has been positively identified in the ISM (Thaddeus, 2006). This is the reason behind the suggestion of small mixed aliphatic/aromatic nanoparticles (Peeters, 2011; Kwok and Zhang, 2011), in the boundary between solid and the molecular scale, as possible carriers (Duley and Williams, 2011; Kwok and Zhang, 2011; Duley and Hu, 2012; Kwok and Zhang, 2013). This hypothesis includes therefore an explanation for the aliphatic components. Fig 3.3 shows the general shape of UIE profile with narrow vibrational mode emissions and broad emission plateaus, generally attributed to superposition of different bending modes with aliphatic ones (Kwok, 2016).

The last spectroscopic feature of carbonaceous materials considered in this introduction

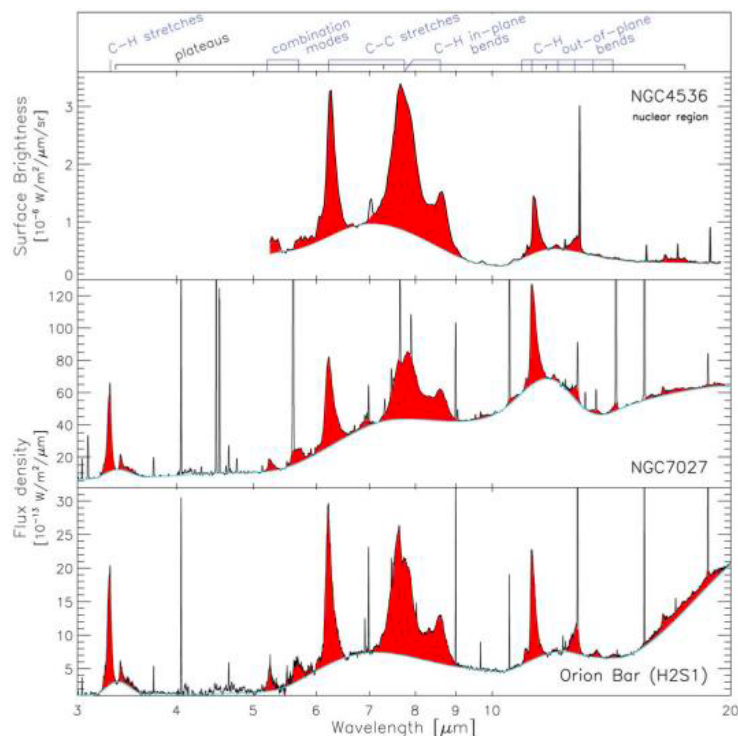


FIGURE 3.3: Unidentified Infrared Emission features of a Planetary Nebula (NGC 7027), of a Photodissociation Region (Orion Bar) and the nuclear region of an HII galaxy (NGC4536)

Extracted from Peeters, 2011

is the mid IR absorption bands. The absorption bands are ubiquitously observed in diffuse media and appear in a fairly clean spectral region. Bands are attributed without hesitation to CH aliphatic stretching vibrations in the $3.4 \mu\text{m}$ range and to aliphatic bendings in the $6.8 \mu\text{m}$ range, with some components of aromatic and even olefinic stretchings (Dartois et al., 2007) in solid dust grains. The profile of the bands admits a decomposition and a discussion on the basis of symmetric and antisymmetric $-\text{CH}_3$ and $-\text{CH}_2$ vibrations with an small shoulder around $3.3 \mu\text{m}$ associated with aromatic stretchings (Dartois et al., 2007; Chiar et al., 2013). The correlation between the $3.4 \mu\text{m}$ band with other observed absorption features is good when comparing with aliphatic bending modes at 6.85 and $7.27 \mu\text{m}$. Correlations with olefinic or ring aromatic absorptions is not so straightforward since these components are usually hard to find in observations. Fig 3.4 shows an example of observed mid IR absorption bands compared with the IR spectra of a laboratory analogue.

From the plethora of possible solid analogues spanning these absorptions, HAC materials are among the best in terms of agreement with observations. As has been mentioned, the classifications and rationalizations concerning HAC structures are not straightforward, given the amorphous nature of the samples. Especially important is the sp^3/sp^2 ratio that indirectly links the amount of condensed rings and aliphatic branches, presently a matter of hot debate (Dartois et al., 2007; Godard and Dartois, 2010; Chiar et al., 2013; Gadallah, Mutschke, and Jäger, 2013; Peláez et al., 2018). Because it helps to classify

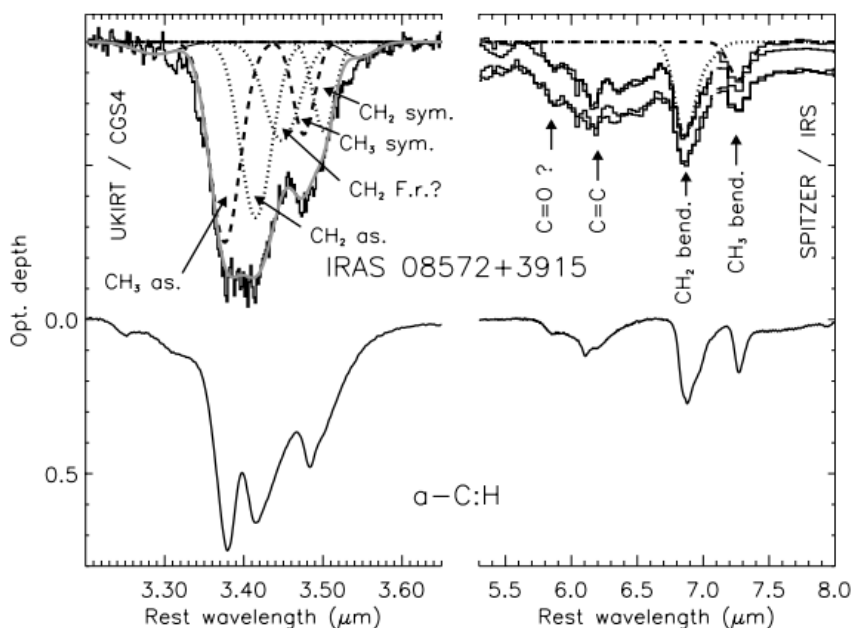


FIGURE 3.4: 3.4 and 5-8 μm absorption profiles with its associated gaussian decomposition of the main molecular modes corresponding to IRAS 08572+3915 (upper panel) and laboratory generated HAC samples (lower panel)

Extracted from (Dartois et al., 2007)

carbonaceous materials in relation to its sp^3/sp^2 ratio, we would like to introduce here the application of **ternary diagrams** to this problem. The ternary diagram consists on a triangle (see Fig 3.5) where the vertices represent, respectively graphite (sp^3), diamond or graphene (sp^2) and hydrogen (H_2). The sp^3 , sp^2 or H fractions determine the position of the carbonaceous materials in the diagram. HAC (or a:C-H in the materials science literature) lies in the lower center part of the triangle, is generally considered a semiconductor material with a band-gap in the region of the above described UV Bump.

The different chemical analogues employed for HAC particles in the literature fluctuate between aromatic islands linked by aliphatic chains or condensed aromatic structures with aliphatic edges (Dartois et al., 2005; Steglich et al., 2013). In order to interpret astronomical data, usually Gaussian deconvolution of the total band is performed (see Fig 3.4), giving an estimation of the HAC chemical composition. This procedure should be taken with care given the high degree of overlapping and mode mixing present in the $3.4\mu\text{m}$ band in amorphous materials (Jacob et al., 1993). Even solid state NMR, being a better choice than IR spectroscopy for some applications, is not a selective enough tool for differentiating between these materials (Jacob et al., 1993).

As mentioned in the first paragraph of this chapter our purpose here is to test the different spectroscopic features of selected HAC archetypes and compare them with observations and experiments. Density functional theory (DFT) calculations are employed in our own constructed structural models for calculating UV and IR absorption spectra

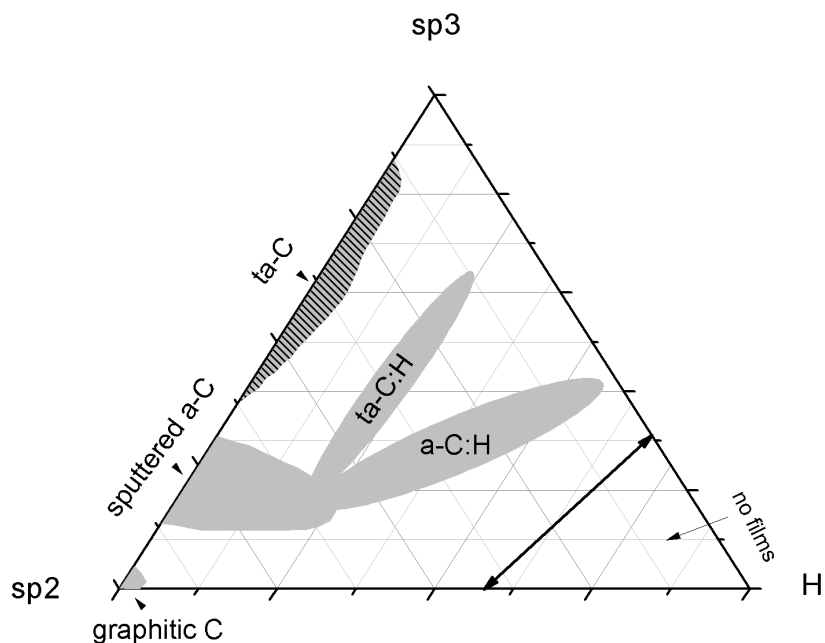


FIGURE 3.5: $sp^3/sp^2/H$ Ternary diagram of amorphous carbon materials.

and simulated IR emission curves. These curves will make use of the infrared absorption coefficients and mode positions as input. The comparison with astronomical observations is made using spectra from the literature whereas the experimental analogues for comparison have been grown in our group.

3.2 Methods

The chapter drifts between experiments and theory and their inter relationships, and we have wanted to reproduce this diversity in the order presented in this section

1. In section 3.2.1 we develop the method we have employed to generate amorphous carbonaceous packed materials. This makes use of the theoretical tools presented in Chapter 2. We will explain here the procedures followed for the relaxation of our structures and for the calculation of the infrared spectra after relaxation. A simple model employing phenantrene is also presented as a test of the quality of our approximations.
2. Description of the experimental conditions for the growth of the HAC chemical analogues and for the acquisition of the infrared spectra of the generated samples. This section makes use of the experimental techniques presented in Chapter 2.
3. Description of the computational tools required for the calculation of the UV-Vis absorption spectrum of the relaxed structures.

4. Derivation of the equation used for the calculation of the IR emission spectra of the optimized structures.

3.2.1 Theoretical approach: Generation of carbonaceous HAC packed chemical analogues and IR spectra calculation.

The theoretical models employed for the optimization of structures and calculation of the mid infrared and UV-Vis (in the 200-400 nm) spectra make use of the methods from Density Functional Theory (DFT) codes. However, before obtaining a proper structure for minimization and properties calculations, a computationally cheap pre-screening of structures is needed in order to discard very unfavorable geometries and configurations. Such a screening is performed using a Monte Carlo algorithm as implemented in the Amorphous cell code (Akkermans, Spenley, and Robertson, 2013). This code places the molecular geometry of a species within a unit cell (cubic in all our cases) with a certain lattice constant to match a cell density (ρ). A user defined number of configurations are tested and inter- and intramolecular close contacts are minimized at that density. This pre-screening minimization is realized using the universal force field (Rappé et al., 1992), a force field routinely used in this kind of cheap calculations. The number of configurations employed vary between $10^2 - 10^3$.

Following energetic criteria from the force field pre optimization we select one structure to perform an ulterior DFT optimization. The electronic and geometric optimization is performed in a plane wave pseudopotential formalism using the CASTEP code (Clark et al., 2005). For the evaluation of the exchange-correlation term we have employed the generalized gradient approximation in its Perdew–Burke–Ernzerhof (PBE) (Perdew et al., 1996) formulation. The plane wave expansion of the total electronic wave function employs a kinetic energy cutoff of 680.0 eV along with norm conserving pseudopotentials with a k-point integration of the Γ point, because in amorphous samples without symmetry, reciprocal space points should be degenerated. We have also employed the ad-hoc Grimme-D2 dispersion correction (Grimme, 2006) a r^6 atom pair wise dispersion correction for the energies and interatomic forces. For the geometry optimizations we have used the following convergence criteria: 1×10^{-5} eV per atom for the energy, 0.03 eV/Å⁻¹ for the forces between atoms and 0.001 Å for the interatomic displacements.

Once the structure is converged we can calculate different properties such as the vibrational spectra, thermodynamic properties, optical constants (needed for the UV absorption spectra), etc. For the vibrational spectra, DFPT as explained in the previous chapter, has been employed.

This methodology gives us information about the band positions and intensities but is not able to provide any information on band widths and band profiles. In all of our calculations we have employed an empirical broadening using Gaussian functions of 40 cm⁻¹ FWHM. A fairly large value, to account for the amorphous nature of the sample. In order to test the goodness of our approach we have compared the results of our model with the NIST spectra for crystalline phenantrene (NIST, 1980), Fig 3.7). This image shows in four panels (from top to bottom) respectively: (a) the spectra of crystalline phenantrene extracted from the database, (b) the calculated spectra of crystalline phenantrene broadened with 8 cm⁻¹ with crystalline structure in its P2₁ symmetry space

group; c) amorphous phenantrene using our method (8 cm^{-1} , three packed molecules, 1 gcm^{-3}), and d) amorphous phenanthrene (40 cm^{-1} , three packed molecules, 1 gcm^{-3}).

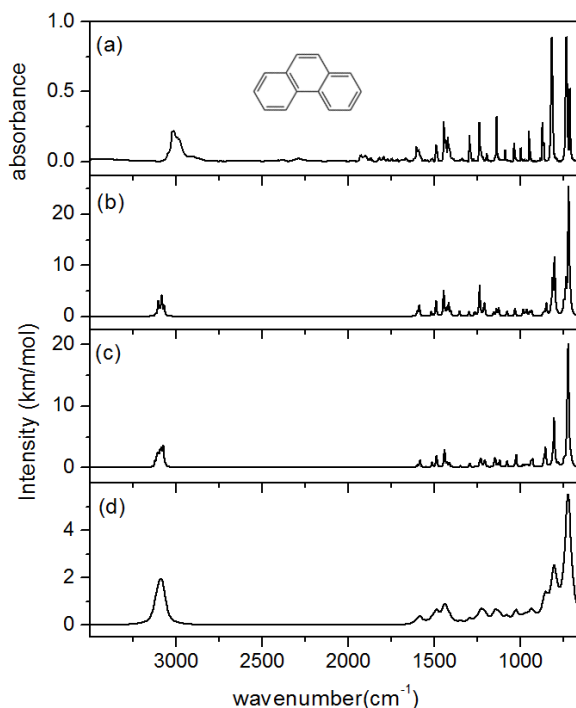


FIGURE 3.6: Theoretical Model Validation on Solid Phenantrene

To the best of our knowledge no spectrum of amorphous phenantrene has been published in the literature. Experimental and theoretical spectra in crystalline samples have a good degree of agreement. The calculations are able to simulate the main absorptions, with slight differences in the bending mode region. Such differences could arise either from a slight error in the position of the hydrogens from the X-RAY structure or from the lack of a homogeneous broadening scheme across the spectra, a problem that could also be found in our HAC calculations. Comparison between the calculated amorphous sample and the crystalline one confirms the expected outcome, the splitting and merging of different vibrations due to the break of the symmetry. This validation was performed in order to determine the viability of DFT to calculate the spectra of carbonaceous materials generated by randomly packing molecular analogues

3.2.2 Experimental Setup: HAC Generation and IR Spectroscopy

PECVD has been the method employed to grow the samples used for comparison with our calculations. The details for plasma polymerization techniques have been explained in section 2.3.2, so here we will only focus on the specific experimental conditions. We have introduced mixtures of CH_4 and He inside our plasma reactor, in a proportion of 1:2 (5 sccm : 10 sccm) to reach a total pressure of 0.3 mbar in flow. Deposits are grown on top of IR transparent silicon plates of 2.5 cm of diameter. Typical residence times for the gases in the chamber are on the order or a few seconds, ~ 3 seconds. As it

will mentioned later, we have created two main types of materials. The first one (E1), highly aliphatic, was grown placing the silicon substrate slightly outside the coil (5 cm downstream from the flow direction). In this position we try to mimick "soft" formation conditions, with the deposited radicals not suffering reprocessing for a total deposition time of 8 min. The second set of samples (E2) were obtained placing the substrate within the coil, seeking to resemble "harsh" conditions with deposition times of ~ 30 min. A last step, energetic processing with a H_2 plasma for 10 min, has been added to these last samples in order to create more graphitic structures.

Once the samples are grown, they are kept in vacuum conditions until they are place into the high vacuum chamber described in section 2.3.1. Infrared spectra of the samples have been taken at normal incidence in transmission with a resolution of 4 cm^{-1} in the range between $4500 - 500 \text{ cm}^{-1}$.

3.2.3 Theoretical approach: determination of the UV-Vis spectrum of HAC analogues

The evaluation of the absorption curves is performed once the monoelectronic wave functions are known, that were calculated using CASTEP as explained above. The basis of the method is to evaluate the sum shown in 3.1, for a given direction of the position operator, at a value of the polarization of the incident electric field, which is the same as to determine the inter band transition moment integral corrected by a volumetric factor (Palik, 1998). The evaluation of the imaginary part of the dielectric constant can be done in terms of the position operator as:

$$\epsilon_2(\omega) = \frac{2e^2\pi}{\Omega\epsilon_0} \sum_{k,i,j} |\langle \psi_k^i | u.r | \psi_k^j \rangle|^2, \quad (3.1)$$

with Ω being the volume of the cell, r is the position operator, u the polarization vector of the incident electric field, ϵ_0 is the permittivity of the vacuum.

The dielectric constant is a sum of the real and imaginary part $\epsilon = \epsilon_1 + i\epsilon_2$, both of them connected via the Kramers-Kronig relations, the mathematical operations relating response functions. The refractive index is expressed as:

$$N = n + ik, \quad (3.2)$$

where n and k are related with the real and imaginary part of the dielectric constant as:

$$n^2 = \frac{1}{2} \left([\epsilon_1^2 + \epsilon_2^2]^{1/2} + \epsilon_1 \right), \quad (3.3)$$

$$k^2 = \frac{1}{2} \left([\epsilon_1^2 + \epsilon_2^2]^{1/2} - \epsilon_1 \right). \quad (3.4)$$

On the other hand the absorption coefficient, given in units of m^{-1} is linked with the imaginary part of the refractive index via this expression:

$$\alpha(\omega) = \frac{2k\omega}{c}. \quad (3.5)$$

The scattering contribution to the extinction curve depends on the macroscopic geometry of the sample and it has not been simulated. Therefore, only the absorption contribution to the UV bump, that is observed in astrophysical media in extinction, can be simulated. In this chapter we will present the most relevant and better characterized spectral region corresponding to band transitions in the UV-Vis. We are going to use normalized data for our results because of our above mentioned incapacity of simulating the scattering. This technique can also be applied to the study of core-level spectroscopies (Morris et al., 2014). The above mentioned operations have been integrated at the Γ point using OPTADOS (Morris et al., 2014) with a fixed gaussian broadening of the spectral features of 0.5 eV.

3.2.4 Theoretical Approach: determination of IR emission of isolated domains in HAC analogues

As it has been mentioned above there exists a long lasting debate about the carriers of the UIE features. The IR spectrum of amorphous packed molecules is essentially the calculation of the molecular spectrum in a force field generated by the periodic boundary conditions (PBC) of the system. That is not possible in crystalline solids because of the lattice modes. We use this property in our advantage assuming that the simulated HAC particles are **small enough** to experience **transient heating**, meaning they can be excited to high temperatures upon absorption of a single UV photon. For comparison with the data available in the literature, we have implemented a slightly modified version of a canonical photocoooling model in order to account for the modified magnitudes in packed molecules. The differences include, a set of modes and absorption coefficients that depend on the intermolecular interactions in the packing, and the calculation of the specific heat from those packed structures.

The algorithm has been implemented in several previous works (Cook and Saykally, 1998; Pech, Joblin, and Boissel, 2002a; Álvaro Galué and Díaz Leines, 2017). The radiative emission rate of the k^{th} mode is given by:

$$\phi_{k,v}(U) = A_{k,v-1} \frac{n(U - v h \nu_k)}{n(U)}, \quad (3.6)$$

where $A_{k,v-1}$ represents Einstein's spontaneous emission coefficient for the vibration in the v -th vibrational level and $n(U)$ or $(n(U - v h \nu_k))$ represent the density of vibrational states at a given thermal energy U including all the vibrational states or excluding the v -th one, respectively. The main point of the model is that, considering that the thermal energy greatly exceeds the energy of an individual mode $U \gg v h \nu_k$ (as in the events of absorption of a high energy photon inducing transient heating, release of chemical energy etc), the different vibrational modes can be populated according to a Boltzmann

distribution for each mode, being these population numbers a function of the effective temperature for the particle.

$$\phi_{k,\nu} = \phi_k(T) = A_{k,0\leftarrow 1} \left(e^{\frac{-h\nu_k}{kT}} - 1 \right)^{-1}. \quad (3.7)$$

The emission rate over all modes is given by:

$$\phi(T) = \sum_i A_{k,0\leftarrow 1} \left(e^{\frac{-h\nu_i}{kT}} - 1 \right)^{-1}. \quad (3.8)$$

Moreover, the Einstein coefficients for emission can be determined using:

$$A_k = \frac{8\pi}{N_{AC}} * \nu_k^2 * \alpha(\nu_k) = 1.2512 \cdot 10^{-7} * \nu_k^2 * \alpha(\nu_k), \quad (3.9)$$

with ν_k being the mode wavenumber in cm^{-1} and $\alpha(\nu_k)$ the absorption cross section (in km/mol), both obtained from our CASTEP calculations. Each emission component is broadened using a Lorentzian shape curve:

$$g_k(\nu) = \frac{1}{\pi} \frac{\Gamma_k(T)}{(\nu - \nu_k(T))^2 + \Gamma_k(T)^2}, \quad (3.10)$$

with $\Gamma_k(T)$ being the band width, extracted from the literature ($10cm^{-1}$) as a common ground value for accounting for inhomogeneous broadening under a confinement scenario (Álvaro Galué and Díaz Leines, 2017). Anharmonic effects in the vibrations are considered to be temperature dependent and are introduced *ad-hoc* using available experimental values from Pech, Joblin, and Boissel, 2002a for coronene, the most archetypical π domain:

$$\nu_k(T) = \nu_i(0) + \Delta + \chi T; \Delta = 13.5cm^{-1}; \chi = -0.0352K^{-1}. \quad (3.11)$$

The spectroscopic emission rate is therefore $\sum_k g_k(\nu) \phi_k(T) / \phi(T)$. Now, the only thing we need for our model is to thermalize our system with the environment, considering an effective temperature T_i (typically 1000 K in isolated PAH (Léger et al., 1989), lower in packed molecules) and a final temperature T_f . We have chosen an astrophysical relevant temperature as T_f , 50K. The excursion from T_i to T_f is governed by the material heat capacity $C_v(T)$, also obtained by CASTEP in its Γ point sampling approximation.

Therefore, the radiative cooling flux (S) is described by:

$$S(\nu, T) \simeq \int_{T_i}^{T_f} \sum_k \frac{g_k(\nu) \phi_k(T)}{\phi(T)} C_v(T) dT. \quad (3.12)$$

Equation 3.12 is integrated numerically with a resolution of $1cm^{-1}$ to obtain the corresponding emission curves.

3.3 Results: IR Absorption spectra of HAC analogues

3.3.1 Structural Models

The structure of the bearers of the $3.4 \mu\text{m}$ band, widely observed in diffuse clouds, has been hypothesized to be a mixture of carbonaceous solids with different amount of sp^2 , sp^3 , and H . These three dimensional structures have a combination of aromatic islands with aliphatic chains of different length. One of the two extremal paradigms for such structures that has been considered in this work contains small aromatic islands (one or two condensed rings) linked by aliphatic (and eventually olefinic) chains. We will call this paradigm: *Rings and Chains* (RC) (Pendleton and Allamandola, 2002; Dartois et al., 2005; Kwok and Zhang, 2013; Molpeceres et al., 2017). The other model under investigation, closer to the typical PAH structure, assumes a quasiplanar graphite structure with aliphatic functional groups at the edges (Chiar et al., 2013; Steglich et al., 2013; Molpeceres et al., 2017). This paradigm is named in this thesis as *Substitued Graphite* (SG). The deviation from pure PAHs structures is key and a highly interesting topic nowadays. It is argued whether PAHs and HAC can coexist independently, or represent two different stages of one single carbonaceous material (Jones et al., 2013; Chiar et al., 2013).

In our simulations of topologies of HAC analogues, we have randomly packed and screened configurations of a single molecular unit of medium size (50-100 atoms) at densities between 0.7 and 3 g cm^{-3} (0.7, 1.0, 1.5, 2.0, 3.0) using a Montecarlo procedure. Basic units for the RC and SG models have been taken from two works, the first one from Dartois et al., 2005 and the second from Steglich et al., 2013, (see Fig 3.7). In the first work, the molecular model was obtained using a neural network model in which structures were fed into a machine learning algorithm in order to match the features observed in the interstellar medium. The molecular model of Steglich, on the other hand, is obtained combining the data of tens of PAHs with the ultimate goal of producing a molecular unit accounting for both the UV Bump and the IR features.

The packed structures were optimized using CASTEP, until a global minimum on the potential energy surface (PES) of the system was obtained. All the convergence criteria were fulfilled in all cases. Fig 3.8 represents optimized packed RC and SG structures at the considered densities in this work applying PBC. The different images are shifted along the crystallographic axes for visualization purposes.

Table 3.1 shows the electronic energies as a function of the density. Several conclusions can be extracted as a result of this. As can be seen in Fig 3.8, the magnitude of the steric interactions dominates at high densities, especially in the case of the RC analogue. Even though the structure of each individual molecule is not greatly altered, these steric interactions present a great hindrance in the total structure, leading to very high energies, and likely to endothermic formation pathways. Furthermore, our results concerning the influence of the density and should be taken as a comparative measure between extremal values. The optimized densities of these pack analogues have a qualitative nature. We are not in a position to discuss the kinetic arguments behind the formation mechanism of these materials, neither from our calculations nor from the experiments. The plasma polymerization formation process is energetic enough to surpass individual

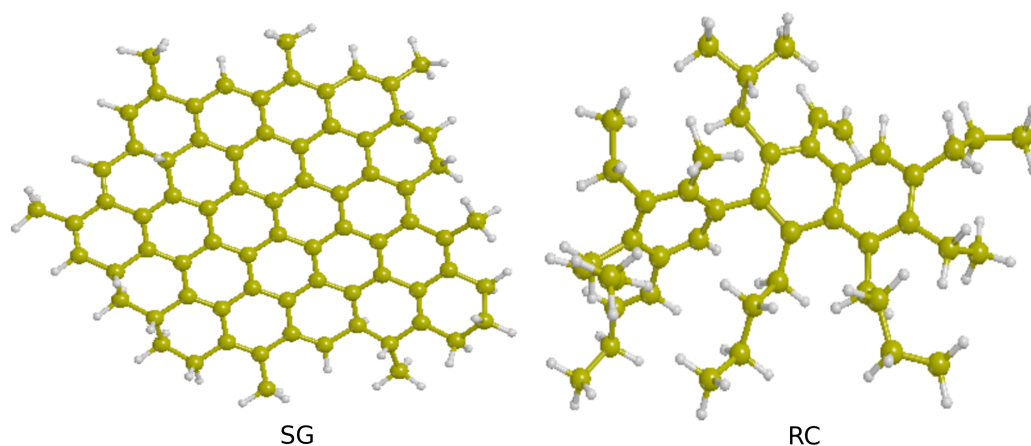


FIGURE 3.7: Molecular models considered in the evaluation of the properties of chemical HAC analogues.

barriers that eventually lead to fluctuations in the density of the material, meaning that the most stable density is difficult to estimate.

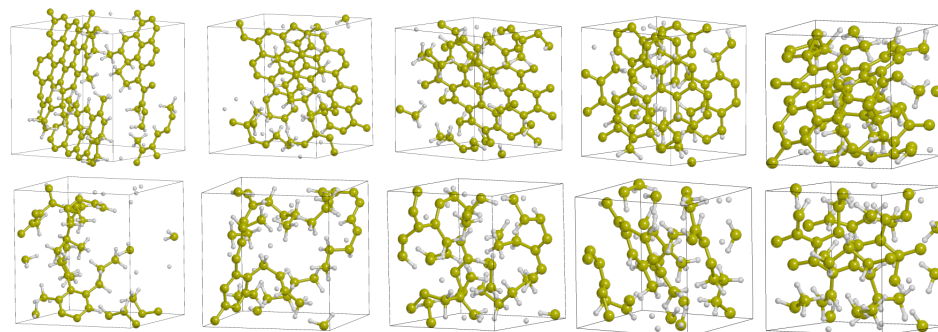


FIGURE 3.8: Packed HAC archetypes at different densities. From left to right (0.7, 1.0, 1.5, 2.0, 3.0 gcm^{-3}). Top - SG. Bottom - RC.

The electronic energy of the optimized analogues is highly dependent on the density. Steric interactions within the unit cell usually overcome the stabilization from the very weak interaction between molecules in neighboring cells. These interactions could be classified as dispersion interactions, but we are not able to discriminate other possible side interactions, as π stacking (Tran et al., 2004) favoring higher densities in SG analogues.

The precise density of experimentally grown HACs is not known and could vary between 1-2 gcm^{-3} as a function of the hydrogen content (Robertson, 2002), in contrast with the densities of amorphous carbon (2-2.3 gcm^{-3}) (Iwaki, 2002). Two conclusions can be extracted; the amount of hydrogen bearing functional groups ($-CH_3$, $-CH_2-$)

TABLE 3.1: Relative energies of the RC and SG HAC analogues as a function of the density

$\rho(gcm^{-3})$	RC Model	SG Model
	$\Delta E(eV)$	$\Delta E(eV)$
0.7	0.00	0.48
1.0	0.60	0.00
1.5	5.76	1.04
2.0	29.06	13.37
3.0	27.73	80.86

implies termination of the carbon skeleton. This produces a functional group that contributes negatively to stabilization, by steric interactions, which favors lower densities. Secondly, it is important to remark (again) that the concept of density is misleading. In laboratory generated samples we can find domains of different density as evinced in microscopic studies of HAC samples (Iarlori, Galli, and Martini, 1994; Golubok et al., 2000; Peláez et al., 2018). Therefore, extracting quantitative conclusions on the density attending to theoretical measurements is tricky. Our calculations suggest a density between 0.7 and 1.5 gcm^{-3} for our analogues, the lower values being more likely, specially in the case of the RC analogue. What we can definitely conclude is that high density packings lead to structures with enough steric hindrance to be discarded using mainly energetic criteria. Such conclusion will be further confirmed at the light of the absorption infrared spectra, shown in the next section.

3.3.2 Description of the Infrared Absorption Spectra

In the first place we show the infrared spectra of the most stable theoretical analogues per archetype and the experimental spectra recorded in our lab for comparison with the models, attending to the "soft" (E1) and "harsh" (E2) generation procedure. For the theoretical analogues, RC and SG, we have selected the most stable structures, following the energetic criteria presented in the previous section.

The spectra for both experimental and theoretical analogues are characterized by two main features, as can be seen in Figure 3.9. An absorption maximum is found in the CH stretching region (3000-2900 cm^{-1}) attributed to $-CH_3$, $-CH_2$ and $-CH$ functional groups, with small contribution of the aromatic $-CH$ stretching modes. The second visible features are the absorptions in the bending region, comprised between 1700-700 cm^{-1} , mainly accounting for CC and C=C stretching groups and different bending modes. As will be shown later, reducing the discussion on vibrations to isolated functional groups is not completely correct in these amorphous materials, showing a big degree of mode mixing. The agreement between the experimental and theoretical spectra is reasonable in absolute wavenumber and intensities. What is more appealing though is the excellent agreement between intensity ratio of the CH stretching and bending modes. This intensity ratio, is of great help to extract conclusions regarding the structure of the experimental analogues. Energetic processing of laboratory HAC materials show a graphitisation, becoming more similar to the SG analogue (Godard et al., 2011; Gadallah, Mutschke, and Jäger, 2011; Alata et al., 2014). The different calculated

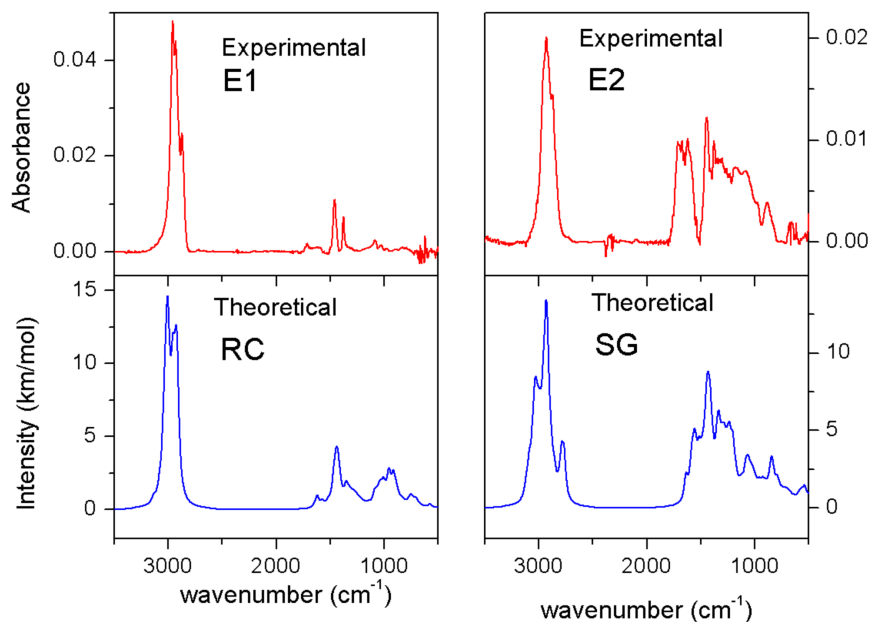


FIGURE 3.9: Experimental and Theoretical Spectra of HAC samples.

archetypes could be examples of different evolutionary stages of the same seeds (Jones et al., 2013). Regardless of whether the two structures are related, we should note that there also exists certain discrepancy between the experimental and calculated spectra when looking at the CH stretchings around 3000 cm^{-1} . As a possible explanation of this mismatch we propose a critical dependence of this band on the exact amount of CH_2 and CH_3 groups (Molpeceres et al., 2017). Also, the SG analogue includes a component at lower wave numbers $\sim 2700\text{ cm}^{-1}$, as a result of the inclusion of a (CH) tertiary carbon, accounting for observed features in astrophysical environments (Allamandola et al., 1992).

From the analysis of the calculated normal mode eigenvectors for each vibration, we can assign the spectra. It is worth noting though that given the amorphous nature of the sample a significant degree of *mode mixing* is expected. This is, modes involving a blend of several atoms or atomic groups for the same vibrations, and in some cases different vibrational modes at the same frequency. This expected behavior is observed in our calculations, and therefore our assignment should be done on the basis of main vibrations instead of pure vibrations. We name main vibrations to those with the longest atomic displacement or elongation, producing a higher net local dipole moment. These assignments are collected in Table 3.2.

Our assignments are less obvious when treating vibrations below 1500 cm^{-1} , and the analysis of the eigenvectors is specially useful in this case. For RC samples, this is specially true, because it gives us an insight in the $1150\text{-}790\text{ cm}^{-1}$ region, a very noisy region in the spectra of experimental samples.

TABLE 3.2: Assignments of **main** vibrations of HAC analogues spectra.

SG		RC	
Position cm^{-1}	Assignment ^{1,2}	Position cm^{-1}	Assignment
3140-3080	CH; ar-str	3130-3040	CH,CH ₂ ; ar-str, ol-str
3080-2980	CH ₃ ,CH ₂ ,CH; a-str, a-str, ar-str	3040-2970	CH ₃ ,CH ₂ ; a-str,a-str
2980-2830	CH ₂ ,CH ₃ ; s-str, s-str	2970-2940	CH ₂ ,CH ₂ ; s-str, a-str
2830-2700	CH; ter-str	2940-2830	CH ₃ ,CH ₂ ; s-str, s-str
1690-1520	CC, CC; str, ar-str	1650	CC; ol-str
1520-1370	CH ₃ , CH ₂ ,CH; a-bn, bn ³ , bn	1590-1500	CC; ar-str
1370-1300	CH ₃ ; s-bn	1500-1380	CH ₃ , CH ₂ ; a-bn, s-bn
1300-1150	CH ₂ ,CH,CH; bn, ar-bn, ter-bn	1380-1290	CH ₃ ; s-bn
1150-950	CH, CH, CH ₂ ; ip-ar-bn, ter-bn, bn	1290-1150	CH ₂ ; bn
950-750	CH, CH ₃ ; oop-ar-bn, bn	1150-980	CH ₃ ,CH ₂ ,CH; bn, bn, bn
		980-790	CH, CH ₃ ; oop-ar-bn, bn

1. str stretching, bn bending
2. a-, s-, ar-, ol-, oop-, ip-, ter- note antisymmetric, symmetric, aromatic, olefinic, out of plane, in-plane and tertiary modes, respectively.
3. Not labeled vibrations do not show a marked normal mode decomposition

3.3.3 Density Variations

Once described the nature of the vibrational modes, the influence of the density in them has been studied. In Fig 3.10 we present the calculated spectra of the RC and SG analogues at densities between 0.7 and 2.0 gcm^{-3} . We have discarded the study of the 3.0 gcm^{-3} based in bibliographic and energetic arguments, but also in spectroscopic ones because of the lack of sense in the obtained spectra, including very hindered vibrations.

At low densities we do not observe a huge change of the spectrum with density (upper panels in Fig 3.10), favoring our previous statements based on energetic criteria. Recalling those remarks here, we suggest that a total density guess from first principles is risky and only an interval can be provided, pointing also that in a real particle several domains with different densities may be found. For the upper extremal value of the density (2 gcm^{-3} , lower panels in Fig 3.10), the intensity ratio between the 3300-2800 cm^{-1} and the 1700-800 cm^{-1} regions does not resemble any of the spectra we have seen of laboratory generated HAC materials or of carbonaceous ISM features. For example, the dominating peak below 2700 cm^{-1} in the SG material, is clearly anomalous and an inspection of the eigenmode reveals a long elongation displacement of a hydrogen atom towards the electron density of a π C=C bond of a twisted olefinic near lying group. This H-C=C interaction resembles some other typical non covalent interactions that usually are accompanied by broad bandwidths, as in the case of hydrogen bonds. In the case of the RC analogue, the C-H stretchings show a marked hypsochromic shift, a consequence of stronger force constants derived from shorter elongation without a side interaction, as in the π C=C example. This is another factor in favor of discarding high density samples. What remains for discussion is the spectra of an intermediate

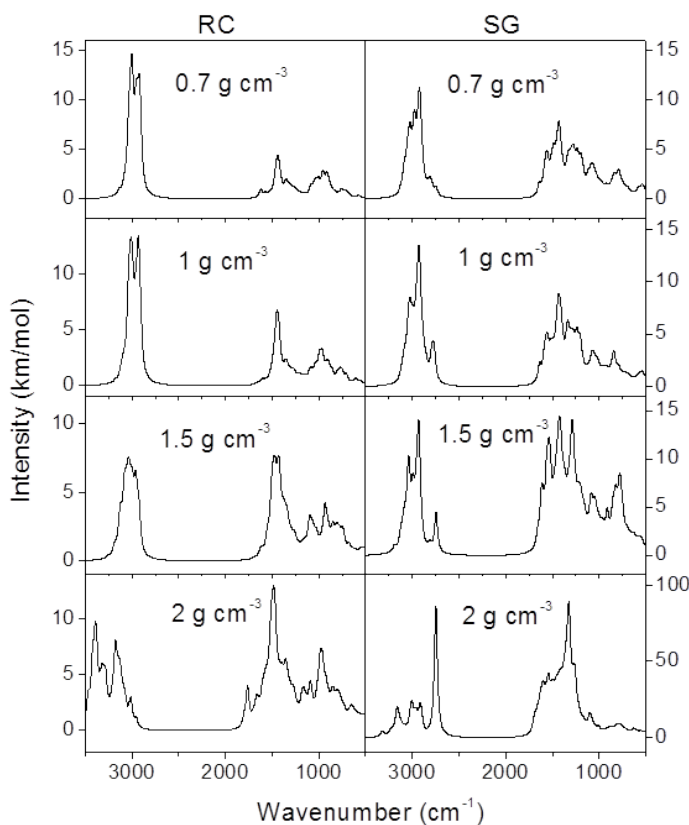


FIGURE 3.10: IR Spectra of HAC analogues as a function of the density

density value (1.5 g cm^{-3}). Here we can observe a well defined structure of the bands, but the intensity ratio between the $3300\text{--}2800 \text{ cm}^{-1}$ and the $1700\text{--}800 \text{ cm}^{-1}$ regions is not in accordance with observations. Moreover, as shown before, the energetic criteria is not favorable at this density. This allow us to confirm the conclusions obtained with energetic criteria.

3.3.4 Evaluation of the Composition of the HAC analogues from the Spectra

The evaluation of the composition of our experimental HAC analogues, E1 and E2, can be estimated from the IR spectra of the samples.

As early as the beginning of the 90's, Jacob and Möller (Jacob et al., 1993), published a review in experimental techniques for evaluation of the fraction of $\text{C } sp^3$, $\text{C } sp^3$ and H in thin layers of hydrogenated amorphous carbon. In such review, IR spectroscopy usually loses when comparing with more specific techniques such as Nuclear Magnetic Resonance (solid NMR) or Electric Energy Loss Spectroscopy (EELS). The reason for that is that the information extracted from IR spectra relies in the decomposition of the components of the strong $3.4 \mu\text{m}$ absorption band in terms of symmetric and antisymmetric $-\text{CH}_3$, $-\text{CH}_2$ and $-\text{CH}$ vibrations. Usually the information regarding the $\text{C}=\text{C}$ stretching bands in the 1600 cm^{-1} range is excluded, due to the weakness of these absorptions

in the IR. However, IR spectra constitute the only univocal experimental technique for comparing the spectrum with observational data coming from infrared telescopes.

In this work we have analyzed the $3.4 \mu\text{m}$ band of our experimental spectra employing the decomposition scheme proposed in Chiar et al., 2013, not considering a Fermi resonance component proposed in Dartois et al., 2007. Fig 3.11 shows the decomposition of the relevant absorption features into gaussian bands. Gaussians to fit CO stretching have been employed for both materials but no quantification of this band has been done. In the E1 sample, the profile between $1800\text{-}1550 \text{ cm}^{-1}$ has been multiplied by a factor of 10, for better visualization with respect to the values of the E2 sample. The parameters of the Gaussians used in the decomposition along with integrated band strengths extracted from Chiar et al., 2013 are given in Table 3.3. The band positions and widths of their spectra have been adapted to a sufficiently good fit for our samples.

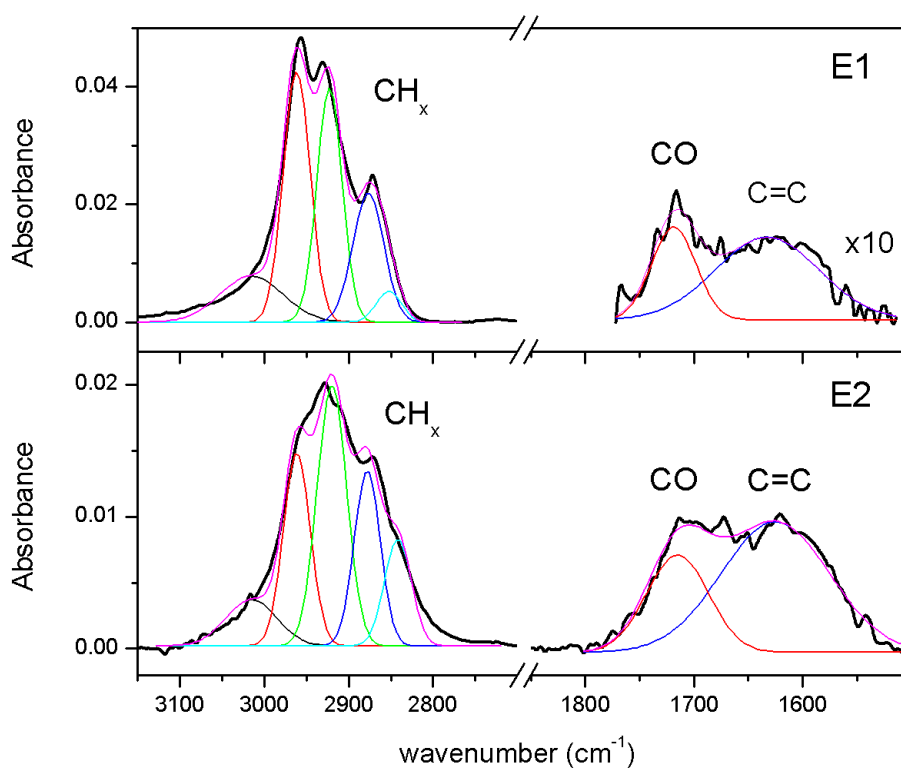


FIGURE 3.11: Gaussian Decomposition of the laboratory analogues for our HAC archetypes

In laboratory grown HAC materials it is critical to avoid exposure to residual environmental water or CO_2 since these molecules often affect the growth of the material, with defects that are not very numerous in the total amount but are easily noticeable by IR spectroscopy. The presence of a $\text{C}=\text{O}$ bond, with a relatively enormous, spectral band strength, makes this vibration appear in the spectrum even at very low concentration levels. This contamination may be unavoidable, depending on the growth conditions (Kovačević et al., 2005) without a proper and difficult precondition of the gaseous sample. In the case of the E2 sample, the "aging" process from the H_2 plasma induces a larger contamination than in the case of the E1 sample. Noticing that, and since the $\text{C}=\text{C}$ stretching band only involves carbon atom displacements, it is a safe assumption

TABLE 3.3: Gaussian Decomposition Parameters employed in our HAC experimental IR spectra fit.

Mode	Peak (cm^{-1})	FWHM (cm^{-1})	Band strenght (A_i) ¹ (cm^{-1}) $\times 10^{18}$
E1 (RC Analogue)			
CH stretch arom	3015	88	2.58
CH ₃ a-stretch ²	2961	37	24.3
CH ₂ a-stretch	2922	35	15.2
CH ₃ s-stretch	2876	43	23.7
CH ₂ s-stretch	2852	35	14.8
C=C stretch	1632	113	0.275
E2 (SG Analogue)			
CH stretch arom	3015	70	2.58
CH ₃ a-stretch	2961	38	24.3
CH ₂ a-stretch	2919	41	15.2
CH ₃ s-stretch	2878	43	23.7
CH ₂ s-stretch	2842	35	14.8
C=C stretch	1625	100	0.275

1. Band strenghts per functional group, in the case of the C=C bond atomic C band strenghts have been employed
2. a-, s- represent antisymmetric and symmetric components, respectively

to say that the E2 sample has a larger content of carbon, and therefore a higher C/H ratio. We can estimate the Csp^3 , Csp^2 & H content from the fit using the output individual areas from the constrained optimization. The obtained areas per component and analogue are shown in Table 3.4.

Again, the quantitative results obtained from the fits provide a value an order of magnitude higher in the E2 sample than in the E1 for the CC band. The other areas are usually higher in the E1 analogue, as a consequence of its large amount of hydrogen, required for the formation of the functional groups enveloped beneath the total $3.4 \mu m$ absorption band. The derivation of the Csp^3 , Csp^2 & H content relations from band decomposition relies in the solution of the balance presented in the next system of equations.

$$\begin{cases} C(sp^3) = \sum_{i=1}^4 n_{i,sp^3} A_{i,sp^3} I_{i,sp^3} \\ C(sp^2) = \sum_{i=1}^2 n_{i,sp^2} A_{i,sp^2} I_{i,sp^2} \\ H = \sum_{i=1}^5 n_{i,H} A_{i,H} I_{i,H} \\ C(sp^3) + C(sp^2) + H = 1 \end{cases}$$

In this set of equations, $n_{i,type}$ represents the number of atoms of a kind per i -th vibrational mode (1 for all carbon vibration in the $3.4 \mu m$, 2 in the C=C band and variable in the case of H), $A_{i,type}$ is the integrated band strength per i th vibrational mode and $I_{i,type}$ is the output area of the fit, again per vibrational mode.

At this point we can compare the composition of our experimental HAC analogues, obtained from the just described gaussian fit, with the composition of calculated models

TABLE 3.4: Optimized area of individual gaussian components in the 3.4 μm band feature in the experimental HAC analogues

Mode	Sample	I_i (cm^{-1})
CH stretch arom	E1	0.74
	E2	0.26
CH ₃ a-stretch ¹	E1	1.70
	E2	0.59
CH ₂ a-stretch	E1	1.50
	E2	0.87
CH ₃ s-stretch	E1	1.02
	E2	0.51
CH ₂ s-stretch	E1	0.20
	E2	0.32
C=C stretch	E1	0.14
	E2	1.24

1. a-, s- represent antisymmetric and symmetric components, respectively

of HAC. In the case of the theoretical structures, obtaining the hybridization information and atomic composition is made simply by counting atoms in the model structures. Table 3.5 shows the atomic composition ratio obtained for the four HAC analogues investigated, two experimental and two theoretical. With the data in this table we have represented in Fig 3.12 the HAC materials in a ternary diagram.

TABLE 3.5: Atomic composition ratio from profile decomposition and from models in HAC chemical analogues.

	E1 profile		E2 Profile	
	decomposition	RC model	Decomposition	SG model
Csp^3	0.12	0.23	0.02	0.17
Csp^2	0.36	0.20	0.92	0.43
H	0.52	0.57	0.06	0.40

We can conclude that a fairly good degree of agreement has been found between the infrared spectra of our samples and the computationally calculated infrared spectra (see Fig 3.9). The similarity in the IR spectra allows us to consider that the average proportion of functional groups must be equivalent. However, Fig 3.12 show some relevant disagreements. The reasons for such discrepancy are scattered along the different discussions held in the chapter, so we gather them here.

1. We have observed in this kind of amorphous materials that we have a substantial amount of **mode mixing**. As a consequence of this, the decomposition of a profile in isolated vibrational modes has an intrinsic error associated in which a component is under or over estimated according to the real nature of the vibrations in that particular range
2. The selection of the decomposition scheme is not univocal, and different gaussian fittings can lead to similar reproduction of the global band profile. This factor

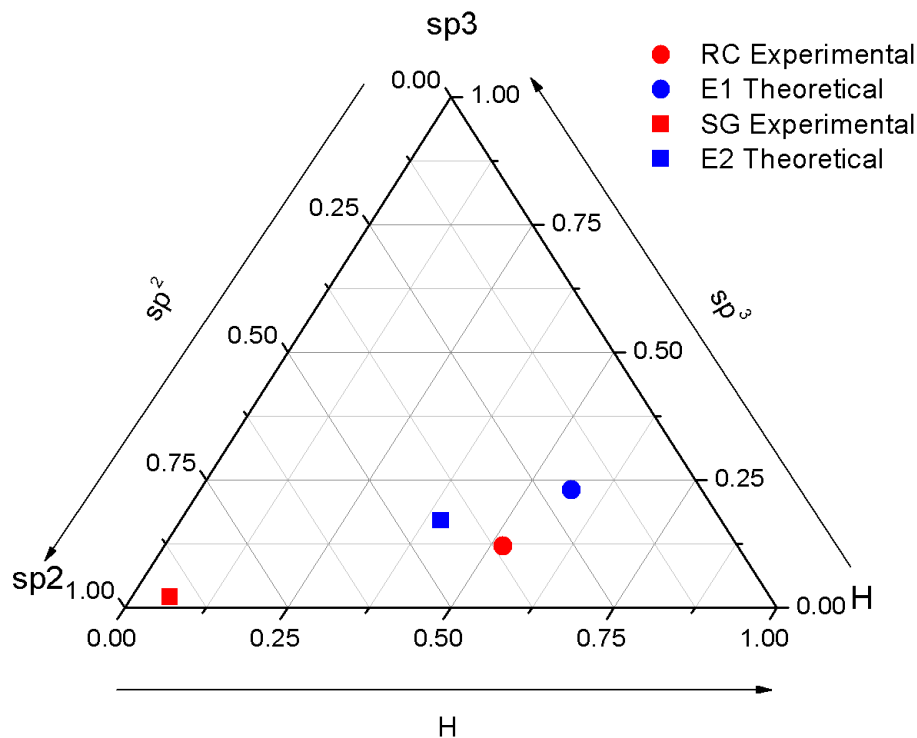


FIGURE 3.12: Ternary Diagram position of theoretical and Experimental HAC models.

also introduces small numerical errors in the system of equations. The presence of contaminants on top of it, can also distort the band decomposition scheme.

- Absorption strengths in the form of individual band strengths are not univocal either, and are not easily obtained neither from first principles nor from experiments. Usually, calibrations are made using a molecular standard (Dartois et al., 2007) with some *ad hoc* corrections for taking the surroundings into account (Chiar et al., 2013).
- The correct estimation of sp^2 carbon depends on the evaluation (with all the above mentioned limitations) of the area of individual Gaussians of weak features, with band strengths one order of magnitude (3015 cm^{-1} feature) or two orders of magnitude (1625 cm^{-1}) lower than those of the aliphatic components (see Table 3.3).

All the above mentioned factors contribute in a bigger or smaller extent, but we believe the composition discrepancy observed between the aromatic archetypes is mainly due to the last factor. In aromatic abundant materials, we propose that the gaussian decomposition scheme is generally not suitable for the evaluation of the graphitic content and leads to a strong overestimation of the material aromatic component. In the RC/E1 archetype this is minimized though, because the relative amount of sp^2 carbon in the structure is lower.

The general conclusion of our work here is that it is possible to reproduce the IR features of amorphous materials from first principles. We have employed our models to rationalize the behavior of our own experimentally grown materials, including spectral

assignment, effect of the density and problems behind the sole relying on IR data to unveil the structure.

3.4 Results: UV absorption and Infrared emission of HAC analogues

Until now we have dealt with particles of arbitrary size, with an easy counterpart from experimental results. In absorption spectroscopy, the larger the number of absorbents in a given region, the more intense the absorption feature. However, in emission spectroscopy, this is not necessarily the case.

The reason behind it is the nature of the radiative emission phenomena. A general scheme for an arbitrary chemical species A is shown here:



where ν_1 and ν_2 represent the frequency of the incident and escaping electromagnetic radiation, respectively, with $\nu_1 > \nu_2$. In equation 3.13 we consider incident electromagnetic radiation as the excitation mechanism, but several mechanisms can induce emission at different wavelengths, such as electric fields or thermal excitations from exothermic reactions (Popovic, 1982; Duley and Williams, 2011). Equation 3.13 shows a simplified version of the emission mechanism, in which in a quantum mechanical picture two or more processes must happen. In the first place, an unspecified mechanism will promote the system to an excited state with a determined lifetime. Afterwards relaxation can take place in many ways, being one of them visible fluorescence or phosphorescence (depending on the spin multiplicities of the excited states). Once in the electronic ground state, the system evolves to the vibrational ground state (assuming 0 K). With much longer radiation times (10^{-1} vs 10^{-9} s) we call this last process either vibrational relaxation or photocooling (Lin, 1976; Álvaro Galué and Díaz Leines, 2017). It has been accepted for a long time that this photocooling process is the mechanism operating behind the appearance of the UIE bands, regardless of the carrier (Purcell, 1976; Allamandola, Tielens, and Barker, 1985; Duley, 1988; Duley and Williams, 1988). These mid IR emission features appear in the range between 6-11 μm on the top of infrared plateaus, and are undoubtedly attributed to aromatic C-H and C-C vibrations. They span in a wide variety of shapes, strongly dependent on the line of sight (Sellgren, 2001; Vega et al., 2010; Shannon et al., 2018).

One of the most widely used procedures for explaining the appearance of these bands is to employ infrared data of mixtures of polycyclic aromatic hydrocarbons (PAH) to fit the astronomical spectra. The PAH hypothesis has obtained astounding successes along the years, with good degree of accordance in the fits of the UIE features (Allamandola, Tielens, and Barker, 1985; Puget and Leger, 1989; Pech, Joblin, and Boissel, 2002b; Li, 2007), the perfect fulfillment of the above mentioned excitation-relaxation mechanism in laboratory experiments (Shan, Suto, and Lee, 1992; Sandford, Bernstein, and Materese, 2013; Marciniak et al., 2015), and chemical mechanisms able to account for their formation in

circumstellar and interstellar environments (Jones et al., 2011; Kislov, Sadovnikov, and Mebel, 2013; Seok, Hirashita, and Asano, 2014).

The PAH model has been improved over the course of the years to increase its range of applicability: chemical modifications of PAH, different oxidation states, arbitrarily blended mixtures of PAH, defective structures etc. The main problem associated with the mixture of gas phase species is that no single PAH molecule has been detected in astronomical objects (Thaddeus, 2006; Kwok and Zhang, 2013). On top of that, UIE bands have been detected in regions where the energetic processing leads to efficient destruction of labile PAHs (Micelotta, Jones, and Tielens, 2009a; Micelotta, Jones, and Tielens, 2009b; Tappe, Rho, and Reach, 2006).

These and other factors have led to alternative modifications of the PAH hypothesis, criticizing mainly the artificial composition of the spectra as the mixture of an arbitrary number of PAHs and PAHs derivatives, and the free flying regime in which these molecules are thought to be. The possibility of composing a fitted spectra with several mixtures of PAH with conveniently prepared broadenings associated with exotic oxidation states (Zhang and Kwok, 2015), and the necessity to include aliphatic chains (Kwok, Volk, and Bernath, 2001) to explain the broad plateaus, have been also criticised.

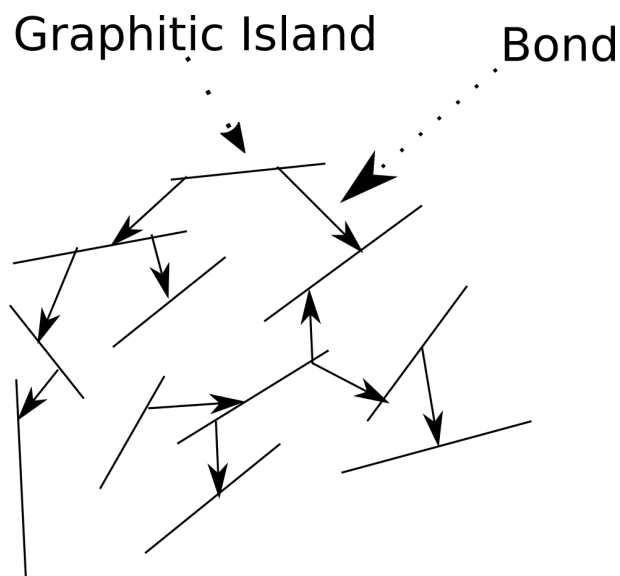


FIGURE 3.13: HAC photgraphitic islands bonded to polymeric material as proposed by Duley et al
Adapted from Duley and Williams, 1988

As early as 1988, Duley proposed that HAC particles could in fact emit in the IR (Duley, 1988; Duley and Williams, 1988) what lead him to decompose the internal structure of a small HAC particle in several subcomponents: 1. amorphous diamond like structures 2. amorphous graphite like structures 3. amorphous polymers 4. void components, see Fig 3.13 for illustration. Studies of amorphous carbon (AC) particles date also from those years (Tielens and Allamandola, 1987; Robertson and O'Reilly, 1987), with more recent structural works based in Raman spectroscopy (Ferrari and Robertson, 2000). Kwok and coworkers have pointed to mixed aromatic/aliphatic particles as the carriers of

UIE (Kwok and Zhang, 2011; Kwok and Zhang, 2013). Recent evolutionary models of the C cycle in the ISM (Jones et al., 2013; Chiar et al., 2013; Jones et al., 2014) consider that there should exist a relationship between the carriers of the predominantly aliphatic IR absorption bands and the aromatic IR emission features. Energetic processing, as the one shown in the previous section with H₂ or UV photons (Dartois et al., 2007; Gadallah, Mutschke, and Jäger, 2013; Molpeceres et al., 2017) lead to aromatization of the structure and subsequently to the potential appearance of UIE features. Mechanical sputtering of hydrocarbon fragments can also lead to PAH like molecules or very small grains able to emit without an efficient alternative cooling side mechanism (Dominik, Jones, and Tielens, 1995; Krasnokutski et al., 2017).

Our intention in this section is to probe the IR emission capabilities of the analogues presented in the past section, exploring first their UV photoexcitation as a function of the packing scheme and the chemical nature. The molecular structural models employed in this section are the same from which we obtained the infrared absorption spectra in the previous section.

3.4.1 UV absorption: UV bump

Duley and Hu, 2012 have grown in the laboratory small hydrogenated amorphous carbon of sp^2/sp^3 ratio of ~ 0.4 , intermediate between our SG and RC paradigms, showing both UV absorption and IR vibration features that could be responsible of the UIE bands. It is known that photoexcitation could lead to transient heating in small aromatic islands with a small number of condensed aromatic rings (Duley and Williams, 1988; Duley and Seahra, 1999; Jones et al., 2013), although other mechanisms could be more efficient, specially the energy released from the formation of H₂ (Duley and Williams, 2011). Even if we assume that alternative mechanisms to photoexcitation may also contribute, we are going to study the former because it is the more common excitation mechanism in the gas phase and should provide a lower bound for other side mechanisms in condensed phase.

Our goal is to theoretically determine the magnitude of the UV bump feature in our archetypes, that show a radically different degree of ring condensation. The UV bump, as explained in the introduction, is a feature that is attributed to aromatic electronic transitions, specially to the $\pi - \pi^*$ band transitions. Its association with carbonaceous material of some type has been thoroughly validated (Dartois et al., 2005; Jones et al., 2013; Gavilan et al., 2017).

In this work, we have employed the same molecular models that were used to simulate the IR absorption spectra, but restricting the densities under consideration to 1-1.5 gcm^{-3} . In particular, we have tested models of three different densities (1, 1.25, 1.5 gcm^{-3}) of the RC and SG analogues. We may note that a quasiplanar derivative of circumcoronene C₅₄H₁₈ has also been studied, but this structure will not be considered in this thesis in detail. Its presence is required to explain the appearance of some bands and only a brief mention of it will be given. The electronic bands of our analogues have been calculated, and the absorption coefficients for each overlap of the electronic eigenstates at the Γ point of the first Brillouin zone have been evaluated employing eq 3.1. Before presenting the absorption curves we would like to remark some structural

considerations regarding the different packings. Whereas for the absorption infrared spectra structural planarity only modulates the band positions and intensities, in the case of the $\pi - \pi^*$ transitions, planar structures are known to be favorable in order to fulfill symmetry criteria. SG analogues conserve a quasiplanar structure around the π system in its optimized structure, improving overlap between different eigenstates in the eq 3.1 $\langle \psi_k^i | u.r | \psi_k^j \rangle$ equation term. This quasiplanar structure is not found in the RC analogue. The mean distance between layers of the quasiplanar structure has been measured to be in the order of 3-4 Å, indicating that individual sub units in a packing are relatively separated and weakly bounded via dispersion forces as shown in Fig 3.8. Figure 3.14 shows the normalized (to the most intense feature) UV absorption curve of the 1.25 gcm^{-3} SG and RC analogues.

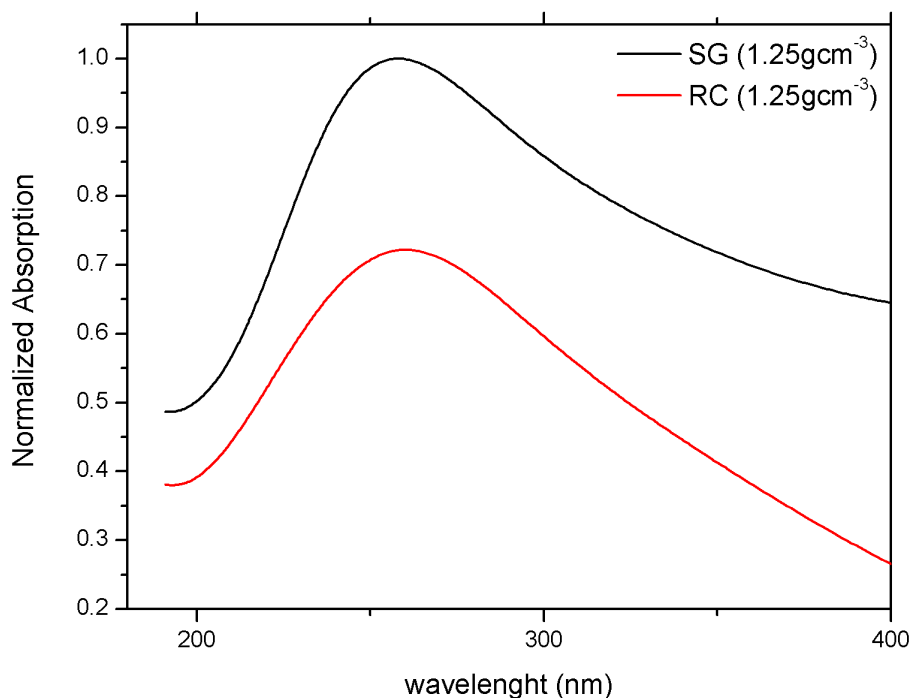


FIGURE 3.14: UV absorption of different 1.25 gcm^{-3} analogues normalized with respect the SG analogue

In absolute terms the RC analogue only accounts for 0.6 or 0.7 of the total absorption efficiency of the SG one. The SG analogue, with a higher amount of condensed rings, show a much higher absorption as expected from the visual inspection of the structure. Nevertheless, at this density the RC analogue does show absorption. In amorphous solids, the position of the absorption features is more or less constant (Mennella et al., 1996; Gadallah, Mutschke, and Jäger, 2011) as observed in our calculations. Our models reproduce fairly well the shape and position of the UV bump. The maximum around 250-260 nm is, however, shifted with respect to the typical 220 nm position. The explanation behind this discrepancy is methodological and attributed to the limitations of the method, due to three main factors out of the reach of our present computational capabilities. These reasons are:

1. The eigenstates derived from the Kohn-Sham equations are not formally the same

eigenstates of the Schrödinger ones. The former are built as the orbitals that reconstruct the electronic density and the latter are the true eigenfunctions of the hamiltonian operator (Godby, 1992). This discrepancy can induce a shift in the gap between electronic states, represented in our absorption curve. A very interesting article dealing with this problem from a molecular point of view can be found in Van Meer, Gritsenko, and Baerends, 2014.

2. Employment of GGA functionals (non local in nature) and introduction of pseudopotentials also induce a small shift in frequencies. This factor can be understood as an intrinsic limitation of our method of calculation, and could be minimized with the employment of hybrid functionals, currently non affordable in our context.
3. The structural models on average could not be the exact carriers of the band, summing also the extinction contribution from macroscopic grains

We have also studied the influence of the density in the absorption efficiency. This dependence is shown in Fig 3.15 normalized with respect to the most intense feature of each archetype.

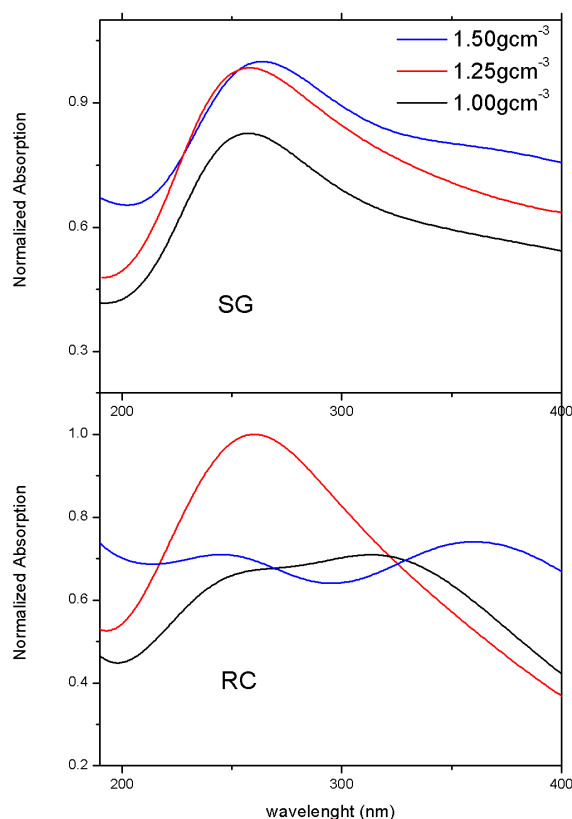


FIGURE 3.15: Normalized UV absorption of different HAC archetypes as a function of the density.

In general, intermediate densities provide the higher absorption efficiency. However, many factors are in play here. In the SG archetype the shape is more or less the same with a modulation of the intensities. The absorption efficiency is 20% lower in the 1

gcm^{-3} than the other two. However, the variation could be attributed to many factors as we have mentioned, so it is risky to venture other conclusion than the fact that we can observe a $\pi - \pi^*$ transition. In the case of the RC analogue the situation is much more interesting, because an erratic behavior is found. We have tested the optical activity of other pre screened packed molecules finding similar results. We would like to point out that the normalized intensities can be misleading. The absolute absorption efficiency of the RC analogue is on average 50-60% lower than the one in the SG analogue. Describing what we have observed in the RC analogue we can see that in the extremal values of 1.0 and 1.5 gcm^{-3} a flat behavior is observed. Nevertheless, this is the expected behavior, since the low amount of condensed rings of the RC archetype (see Fig 3.7) should not yield an effective excitation in clear opposition with the SG archetype.

Recalling the UV absorption & IR emission correlation presented in Duley and Hu, 2012 it is expected that the SG isolated domains should undergo a thermal spike to finally lead to the population of the electronic ground state vibrational levels that eventually lead to the UIE bands. We can not confirm that the RC analogue can experience such excitation, given the marked dependency on the local density of the domain (island in the Robertson and O'Reilly, 1987; Duley, 1988 terminology). In any case, we are going to estimate the appearance of the IR emission of the RC analogues in order to supply more information regarding the viability of the appearance of these physical processes in them. The magnitude of the total thermal spike in these particles is approximated in Duley and Williams, 1988, by:

$$\Delta T = \frac{hv}{(3N - 6)k}. \quad (3.14)$$

For photons in the range of 8-10 eV, in clusters with five to eight rings, the authors claim a temperature increase of between 1000-1500 K. This estimation should be taken with care and depends on a wide variety of factors not included in the above equation. The number of side groups and the packing density, among others, are factors expected to be relevant. As a compromise we have employed a somewhat low value of the temperature spike induced by UV photons, in order to provide at least a lower bound for the emission efficiency. The compromise value chosen to be used as input in the next section is 750 K, in accordance with the values provided by (Scott, Duley, and Jahani, 1997).

3.4.2 IR emission

We have employed the photoemission model defined in the methods section to calculate the infrared emission curves of our analogues. The novel aspect proposed with our calculations is the modulation of the emission bands as a function of the density. In traditional astronomical spectra fits with PAH vibrational information it is common to use an arbitrary weighted number of molecular species to obtain a good agreement. This reliance on molecular data disregarding the effect of intermolecular interactions gives rise to solutions founded on very complex chemical arguments. Here, we work under the assumption that the matrix in which the aromatic islands is embedded could provide a meaningful modulation mechanism for the vibrational modes. We propose, as an

approximation, that molecules combining aliphatic and aromatic domains reproduce this embedding. This modulation mechanism reduce the chemical complexity associated when employing a big number of PAH molecules. We are not in a position to completely discard the role of free-flying PAH molecules in the interpretation of astronomical data. However, as explained in Zhang and Kwok, 2015, there are arguments to doubt of a full explanation of UIE on the basis of only free-flying molecules. Other authors, (Álvaro Galué and Díaz Leines, 2017) have very recently incorporated arguments of PAH embedding on implicit disordered matrices, but we have not been able to find a model that includes this embedding in an explicit way when calculating vibrations from first principles, as we intend to do here with packed HAC molecular analogues.

The problem with packed small particles is the possibility of relaxation side mechanisms through lattice modes (Lin, 1976). From our calculations we have noticed than in amorphous materials we do not observe these modes, and the low frequency modes are more correctly associated with torsions and hindered rotations, in clear analogy with a molecular picture.

It is important to remark that the main limitation of our model is the presence of aliphatic contributions to the spectra. In the classical PAH hypothesis and in the MAON alternative (Kwok and Zhang, 2011) they are broad components responsible for the spectral plateau on top of which aromatic absorptions appear (Kwok, Volk, and Bernath, 2001). As has been said, first principle calculation of the band width is not possible with our methodology. Empirical broadening of the aliphatic modes is also problematic with no clear information to guide us. The solution we have adopted was to identify the eigenmodes highly associated with aliphatic features, between 1420 and 1470 cm^{-1} (it is important to remember mode mixing effects), and to reduce their width to 2 cm^{-1} instead of the 10 cm^{-1} employed in the rest of the spectra. In this way we minimize the artificial intensity increase in aromatic features as a consequence of band overlapping, but we lose the possibility to simulate the broad plateau associated with the UIE.

Fig 3.16 represents the emission curves of both the SG and RC analogues at 1.25 gcm^{-3} . For computational saving reasons we have populated the vibrational modes corresponding to the interval between 700 - 2000 cm^{-1} , considering the modes below that frequency saturated at the spike temperature (750 K) and the modes above (2900 - 3000 cm^{-1}) to be too energetic to effectively affect the populations of the bending modes.

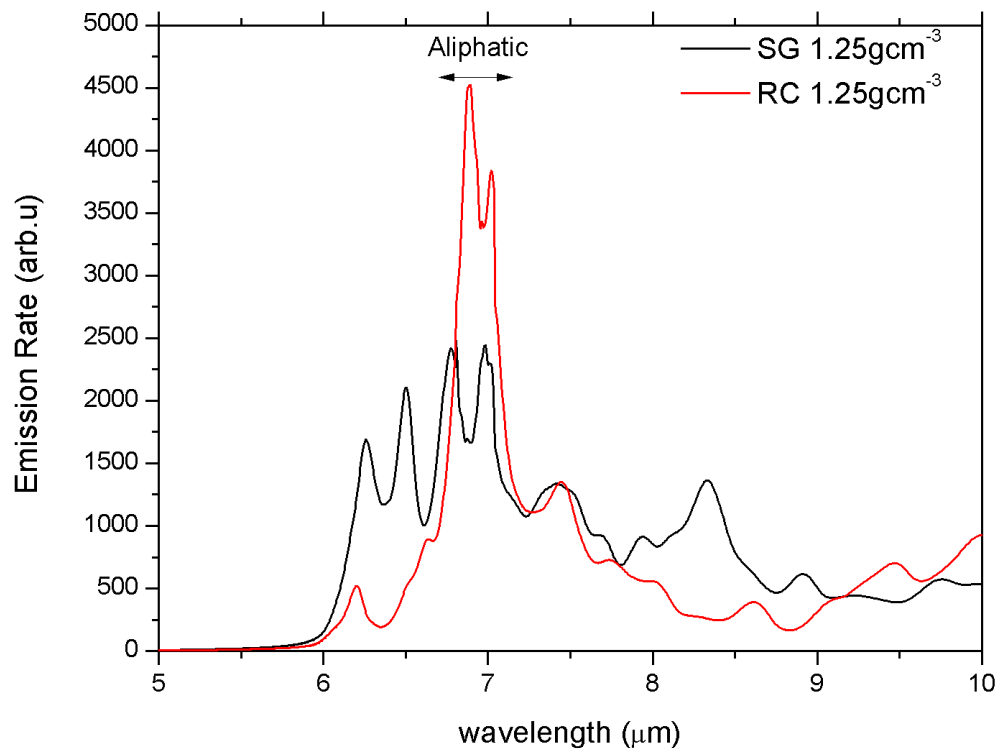


FIGURE 3.16: Emission curves obtained for the two different HAC archetypes at 1.25gcm^{-3} .

From this figure we can infer that in the case of the RC analogue, the aliphatic component is highly dominant with a residual contribution from the small aromatic sub units. In the case of the SG analogue, the aromatic vibrational modes are populated, along with the aliphatic ones, giving a rich spectra that is able to reproduce astronomical observations at $6.2\ \mu\text{m}$, the $7.4\text{-}7.6\ \mu\text{m}$ multiplet or the $8.4\ \mu\text{m}$, near the $8.6\ \mu\text{m}$ feature.

Again we have probed the effect of the density in our analogues in their infrared emission spectra. It is shown in Fig 3.17:

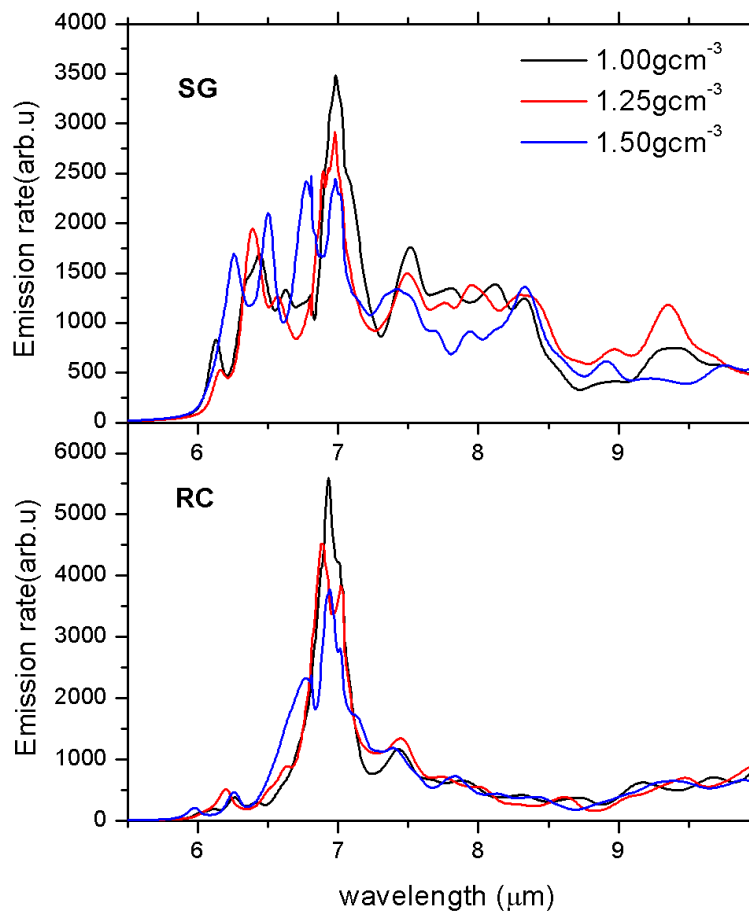


FIGURE 3.17: Emission curves obtained for the two different HAC archetypes as a function of the density.

In the first place, we can see that the RC analogue does not exhibit the expected behavior of an emitting particle. Given our proportion of aliphatic to aromatic groups we can not distinguish in this type of particles any of the well known features associated with the UIE bands. This analogue is related with the MAON particles (Kwok and Zhang, 2013), but our calculations do not evince a clear emission behavior.

The SG analogue however does show features typically found in astronomical environments, as will be discussed in the next section. Furthermore different densities lead to slightly modulated spectra. This behavior will allow to change the usual "mixture-of-PAH derivatives" picture to reproduce astronomical spectra to a more flexible "mixture-of-densities of packed analogues", which is the same as to say that the infrared emission spectra can be **effectively modulated by intermolecular interactions**. We are not in a position to discard the influence of free flying PAH, but it is not our purpose either. In fact our SG analogue is not completely able to independently describe the UIE bands, clearly failing at the simulation of the $7.7 \mu\text{m}$ feature, one of the most intense ones. We propose that UIE features could, in fact, arise from several sources and that different positions found in the literature, are not mutually exclusive.

We show in the next figure (Fig 3.18) the infrared spectra of a defective packed PAH structure including an "aromatic" (Micelotta et al., 2012), (heavily photo processed HAC materials) skeleton with several aliphatic inclusions.

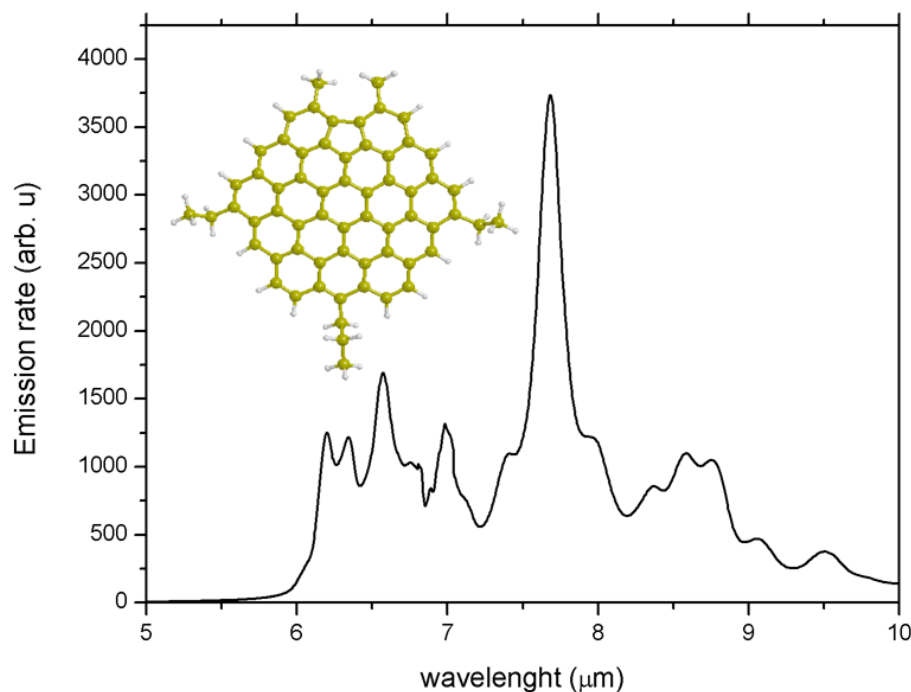


FIGURE 3.18: Emission curve of an aromatic analogue.

This kind of structure show clearly the $7.7 \mu\text{m}$ emission observed toward several sources (Kwok and Zhang, 2011). A problem of our models is that they are homogeneously packed surrounded with identical molecules, not allowing for the required chemical complexity, although they include a big degree of "configurational" (in the sense that molecules can be packed in various ways) complexity. Combining both schemes (PAH fitting and inclusion of embedding) should improve the quality of the fittings, also enhancing the physical and chemical meaning of them. It will allow to explain also observations in harsh environments, with the implicit requirement of energetic processing shielding for the appearance of the UIE bands (Micelotta et al., 2012). As a future goal we intend to calculate the spectra of more realistic particles using quantum mechanics molecular mechanics (QM/MM) embedding schemes of sp^3 matrices (MM), in combination with aromatic islands (QM) (Duley and Williams, 1988).

3.5 Conclusion: Astrophysical implications

Along this chapter we have analyzed different spectroscopic features associated with carbonaceous material. In the ISM this refractory material is thought to be formed by different carbon allotropes with a variable content of hydrogen. The chemical composition affects greatly the spectroscopic behavior and a single carbonaceous analogue is not able to satisfactorily reproduce all the spectroscopic signatures obtained using different

astronomical techniques. In this chapter we have calculated the ultraviolet absorption (UV bump), the infrared absorption spectra between $500\text{-}3500\text{ cm}^{-1}$ and the infrared emission at $5\text{-}10\text{ }\mu\text{m}$, in two different archetypes, evaluating the magnitude of the intermolecular interactions in these features.

The $3.4\text{ }\mu\text{m}$ absorption band is an intense feature easily observable and ubiquitously present towards different lines of sight including the diffuse interstellar medium. The non appearance of such band in dense media will be the subject of the next chapter. However, carbonaceous materials containing this spectroscopic signature present some other lower frequency aliphatic vibrations. The less intense vibration at $\sim 6.9\text{ }\mu\text{m}$, $7.40\text{ }\mu\text{m}$ and the complex landscape between $5.5\text{-}6.6\text{ }\mu\text{m}$ have been observed toward several sources, albeit scarcely (Dartois et al., 2007; Chiar et al., 2013). This lack of information makes difficult to effectively estimate the aliphatic to aromatic ratio of the carbonaceous materials. As has been discussed, these ratios are a key quantity for exploring the aging processes of carbonaceous dust in different astronomical regions (Pendleton and Allamandola, 2002; Dartois et al., 2004; Jones, 2012) (Galactic Center IRS6E, Cyg OB2 No. 12 and IRS7 lines of sight). As an example, we present in Fig 3.19 the mid IR spectrum of the IRAS 08572+3915 galaxy spectrum (Dartois et al., 2007), that shows absorptions not only at $3.4\text{ }\mu\text{m}$, but also in the $5.5\text{-}8.33\text{ }\mu\text{m}$ range. This source is compared with our calculated IR spectra for the RC and SG analogues.

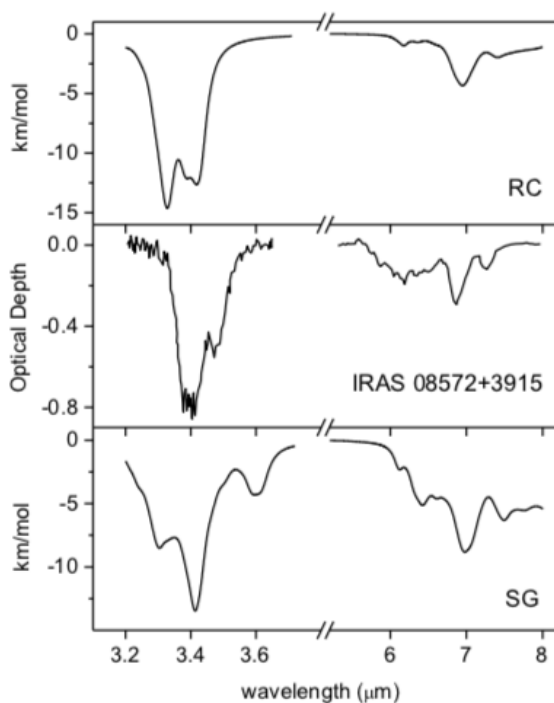


FIGURE 3.19: Infrared absorption comparison of our analogues with information from IRAS 08572+3915

Data on IRAS 08572+3915 extracted from (Dartois et al., 2007)

With figure 3.19 we provide a simple comparison based on theoretically calculated vibrations, but the methodology to obtain information from these spectra is to decompose the bands, which are only partially solved, using the gaussian decomposition fit presented above in the chapter. Chiar et al., 2013 fitted the IRAS 08572+3915 spectrum, concluding that the vibration carriers should be highly aromatic. However, as has been pointed out in the appropriate section, the determination of the aromatic to aliphatic content is generally biased to aromatic structures as a result of the general overestimation of the 1625 cm^{-1} feature. On the basis of this conclusion, and comparing the performance of our models to reproduce our selected astronomical feature, we suggest that aromatic structures such as the SG archetype might not be the adequate to describe this particular astrophysical material. To fit the same astronomical spectrum, Dartois et al., 2007 used spectra of laboratory generated HAC materials combined with astronomically biased neural network generated spectra. In that work, the gaussian fitting procedure was not used, but a combination of potential low aromatic HAC material candidates spectra was summed in order to reproduce the astronomical spectrum. These materials, of the exact same nature as our RC analogue, were completely able to reproduce the source spectrum. Furthermore, the first principles RC spectrum calculated in our group has also been able to match, with a reasonable degree of accordance, the features (see Fig 3.19). RC model shows a good agreement in the whole spectra ($3100\text{-}1200\text{ cm}^{-1}$), with a good degree of matching for the $3100\text{-}2800\text{ cm}^{-1}$ and the $1500\text{-}1300\text{ cm}^{-1}$ absorptions. It is important to note that our model underestimates the olefinic and aromatic $1680\text{-}1550\text{ cm}^{-1}$ absorptions, making us to consider a slightly higher amount of aromatic sub units might be necessary to properly reproduce this particular source.

Our main conclusion here is that a gaussian decomposition is not able to satisfactorily give an insight of the molecular composition of an interstellar dust grain. The internal structure of a dust grain showing those absorption features is highly likely to lie in between our two extremal aliphatic and aromatic archetypes. However, on the basis of the above arguments, such structure is possibly closer to the RC analogue.

The PAH hypothesis has been a workhorse for the explanation of astronomical observations for 30 years now. The achievements of this hypothesis are among the greatest in the field of molecular astrophysics and its scope goes far beyond the general description of only their spectroscopic properties, with implications in astrobiology thanks to heteroatom bearing PAHs (Hudgins, Bauschlicher, Jr., and Allamandola, 2005; Ehrenfreund et al., 2006). However several items regarding the applicability of a classical free-flying PAH hypothesis have appeared during the lifetime of this theory (Duley, 1988; Duley and Williams, 1988; Kwok and Zhang, 2011; Kwok and Zhang, 2013). Among the several drawbacks of a free-flying regime we find three major points to be addressed. Recalling them here: 1. single photon transient heating mechanisms require the absorption of such photon. Free flying PAH show a strong absorption with different absorption position for each PAH, in clear contrast with the shape of extinction curves which show a remarkably constant feature, the UV Bump. (Mennella et al., 1998; Kwok and Zhang, 2013) 2. not a single, individual PAH molecule, even including PAH with strong dipole moments, has been positively identified in the ISM (Lovas et al., 2005; Mattiotta et al., 2009; Schnitzler, Zenchyzen, and Jäger, 2015) 3. PAH signatures have been found in regions in which the harsh environment conditions should induce dissociation (Micelotta, Jones, and Tielens, 2009a; Micelotta, Jones, and Tielens, 2009b)

Following the literature we have tested our previously studied-in-absorption analogues to try to answer the items above. In the first place we have determined that packed aromatic analogues are able to absorb a UV photon at a constant position, which is in agreement with the astronomical models and observations in different sources (Orion (Beitia-Antero and Castro, 2017) or Taurus (Whittet et al., 2004) among others). Secondly, our analogues do show resistance against radiation, as has been shown in works by our group (Maté et al., 2014; Maté et al., 2016) or other several groups (see next chapter) (Dartois et al., 2005; Godard et al., 2011; Mennella et al., 2003). In fact, the processing of aliphatic domains in photodissociation regions, hot gas regions or diffuse interstellar medium leads to aromatisation and subsequently to a potential increase of the UV absorption (Mennella et al., 1996; Gadallah, Mutschke, and Jäger, 2011). In a second step, we have calculated the IR emission spectra of our analogues assuming a transient heating mechanism to have happened. We must remark that in order to provide a coherent fit with astronomical observations, we need to take into account structures with enough chemical complexity for reproducing the 7.6-7.9 μm emission feature, one of the most important toward several sources (NGC 7027, IRAS 22272+5435, Orion bar (Kwok and Zhang, 2011)). Packed defective PAH structures do allow to account for this band, so simulations with enough chemical and "configurational" flexibility will ultimately lead to better fittings and are in accordance with experimental evidence of PAH like graphitic islands in HAC (Scott and Duley, 1996).

It is worth noting that our proposal is not incompatible with free flying PAH and is coherent with sputtering processes of aromatic and arophatic (Dominik, Jones, and Tielens, 1995; Micelotta et al., 2012) material to the ISM (Jones et al., 1994). In this way this proposal could be incorporated to the cycling of carbonaceous interstellar dust (Jones et al., 2013). Furthermore emission of the particles is hindered in big size dust grains (Duley, 1988), which leads us to conclude that in order to account for the emission features, an equilibrium between free flying PAH, emission of aromatic islands in small size grains or even adsorbed PAHs in grains (Wang, Chen, and Chen, 2014) should be considered.

On the basis of this discussion, we can hypothesize if aliphatic to aromatic materials transformation eventually lead to a drastic change in the spectroscopic absorption to emission behavior, reinforcing the vision of the carriers of the different spectroscopic features as the signature of different evolutionary stages of the same material (Scott and Duley, 1996; Jones et al., 2013; Jones et al., 2014), providing an elegant, yet coherent explanation of the evolution of carbonaceous matter in the ISM.

References

- Akkermans, Reinier L.C., Neil A. Spenley, and Struan H. Robertson (2013). "Montecarlo methods in materials studio". In: *Molecular Simulation* 39.14-15, pp. 1153–1164.
- Alata, I., G. A. Cruz-Diaz, G. M. Muñoz Caro, and E. Dartois (2014). "Vacuum ultraviolet photolysis of hydrogenated amorphous carbons". In: *Astronomy & Astrophysics* 569, A119.

- Allamandola, L. J., A. G. G. M. Tielens, and J. R. Barker (Mar. 1985). "Polycyclic aromatic hydrocarbons and the unidentified infrared emission bands - Auto exhaust along the Milky Way". In: *The Astrophysical Journal Letters* 290, pp. L25–L28.
- Allamandola, L. J., S. A. Sandford, A. G. G. M. Tielens, and T. M. Herbst (1992). "Infrared spectroscopy of dense clouds in the C-H stretch region - Methanol and 'diamonds'". In: *The Astrophysical Journal* 399, p. 134.
- Álvaro Galué, Héctor and Grisell Díaz Leines (2017). "Origin of Spectral Band Patterns in the Cosmic Unidentified Infrared Emission". In: *Physical Review Letters* 119.17, p. 171102.
- Bartlett, S. and W. W. Duley (June 1996). "Grain Temperature and Infrared Emission from Carbon Dust of Mixed Composition". In: *The Astrophysical Journal* 464, p. 805.
- Beitia-Antero, Leire and Ana I. Gómez de Castro (2017). "Interstellar extinction in Orion: Variation of the strength of the ultraviolet bump across the complex". In: *Monthly Notices of the Royal Astronomical Society* 469.3, pp. 2531–2538. arXiv: 1704.06059.
- Berné, O., C. Joblin, M. Rapacioli, J. Thomas, J.-C. Cuillandre, and Y. Deville (2008). "Extended Red Emission and the evolution of carbonaceous nanograins in NGC 7023". In: *Astronomy and Astrophysics* 479.3, pp. L41–L44. arXiv: 0801.3400.
- Calzetti, D. (Mar. 2011). "Polycyclic Aromatic Hydrocarbons as Star Formation Rate Indicators". In: *EAS Publications Series*. Ed. by C. Joblin and A. G. G. M. Tielens. Vol. 46. EAS Publications Series, pp. 133–141. arXiv: 1010.4996.
- Campbell, E. K., M. Holz, D. Gerlich, and J. P. Maier (2015). "Laboratory confirmation of C60+ as the carrier of two diffuse interstellar bands". In: *Nature* 523.7560, pp. 322–323.
- Chiar, J. E., A. G. G. M. Tielens, A. J. Adamson, and A. Ricca (2013). "The structure, origin, and evolution of interstellar hydrocarbon grains". In: *Astrophysical Journal* 770.1, p. 78.
- Clark, S. J., M. D. Segall, C. J. Pickard, P. J. Hasnip, M. I. J. Probert, K. Refson, and M. C. Payne (2005). "First principles methods using CASTEP". In: *Z. Kristallogr.* 220, pp. 567–570.
- Cook, D. J. and R. J. Saykally (1998). "Simulated Infrared Emission Spectra of Highly Excited Polyatomic Molecules: A Detailed Model of the PAH-UIR Hypothesis". In: *The Astrophysical Journal* 493.2, pp. 793–802.
- Dartois, E., G. M. Muñoz Caro, D. Deboffle, and L. D'Hendecourt (2004). "Diffuse interstellar medium organic polymers". In: *Astronomy and Astrophysics* 423.3, pp. L33–L36.
- Dartois, E., G. M. Muñoz Caro, D. Deboffle, G. Montagnac, and L. D'Hendecourt (2005). "Ultraviolet photoproduction of ISM dust". In: *Astronomy and Astrophysics* 432, pp. 895–908.
- Dartois, E., T. R. Geballe, T. Pino, A.-T. Cao, A. Jones, D. Deboffle, V. Guerrini, Ph. Bréchnac, and L. D'Hendecourt (2007). "IRAS 08572+3915: constraining the aromatic versus aliphatic content of interstellar HACs". In: *Astronomy and Astrophysics* 463.2, pp. 635–640.
- Dominik, C., A. P. Jones, and A. G. G. M. Tielens (1995). "Disintegration of dust aggregates in interstellar shocks and the lifetime of dust grains in the ISM". In: *Astrophysics and Space Science* 233.1-2, pp. 155–159.
- Duley, W. W. (1988). "Amorphous carbon and interstellar emission excesses". In: *Monthly Notices of the Royal Astronomical Society* 234.1, 61P–65P.
- Duley, W. W. and Anming Hu (2012). "The 217.5 nm band, infrared absorption, and infrared emission features in hydrogenated amorphous carbon nanoparticles". In: *The Astrophysical Journal* 761.2, p. 115.

- Duley, W. W. and S. S. Seahra (1999). "2175 Å and 3.4 Micron Absorption Bands and Carbon Depletion in the Diffuse Interstellar Medium". In: *The Astrophysical Journal* 522.2, pp. L129–L132.
- Duley, W. W. and D. A. Williams (2011). "Excitation of the Aromatic Infrared Emission Bands: Chemical Energy in Hydrogenated Amorphous Carbon Particles?" In: *The Astrophysical Journal* 737.2, p. L44.
- Duley, W.W., S. Seahra, and D.A. Williams (1997). "Luminescence from Hydrogenated Amorphous Carbon and Extended Red Emission from Nebulae". In: *The Astrophysical Journal* 482.2, p. 866.
- Duley, W.W. W. and D. A. Williams (1988). "Excess infrared emission from large interstellar carbon grains". In: *Monthly Notices of the Royal Astronomical Society* 231.4, pp. 969–975.
- Ehrenfreund, Pascale, Steen Rasmussen, James Cleaves, and Liaohai Chen (2006). "Experimentally Tracing the Key Steps in the Origin of Life: The Aromatic World". In: *Astrobiology* 6.3, pp. 490–520.
- Ferrari, A. C. and J. Robertson (2000). "Interpretation of Raman spectra of disordered and amorphous carbon". In: *Phys. Rev. B* 61 (20), pp. 14095–14107.
- Gadallah, K. A. K., H. Mutschke, and C. Jäger (2011). "UV irradiated hydrogenated amorphous carbon (HAC) materials as a carrier candidate of the interstellar UV bump at 217.5 nm". In: *Astronomy & Astrophysics* 528, A56.
- (2013). "Analog of solid nanoparticles as precursors of aromatic hydrocarbons". In: *Astronomy & Astrophysics* 554, A12.
- Gavilan, L, K C Le, T Pino, I Alata, A Giuliani, and E Dartois (2017). "Polyaromatic amorphous carbons as carriers of the UV bump : FUV to mid-infrared spectroscopy of laboratory analogs". In: *Astronomy & Astrophysics* Submitted. arXiv: [1711.06175](https://arxiv.org/abs/1711.06175).
- Geballe, T. R. (July 2016). "The diffuse interstellar bands - a brief review". In: *Journal of Physics Conference Series*. Vol. 728. Journal of Physics Conference Series, p. 062005.
- Godard, M. and E. Dartois (2010). "Photoluminescence of hydrogenated amorphous carbons". In: *Astronomy and Astrophysics* 519, A39.
- Godard, Marie, G. Féraud, Marin Chabot, Yvain Carpentier, Thomas Pino, Rosario Brunetto, Jean Duprat, C. Engrand, P. Bréchnignac, L. D'Hendecourt, and Emmanuel Dartois (2011). "Ion irradiation of carbonaceous interstellar analogues - Effects of cosmic rays on the 3.4 micron interstellar absorption band". In: *Astronomy & Astrophysics* 529.16228, A146.
- Godby, R. W. (1992). "Exchange and correlation in solids". In: *Unoccupied Electronic States: Fundamentals for XANES, EELS, IPS and BIS*. Ed. by John C. Fuggle and John E. Inglesfield. Springer Berlin Heidelberg, pp. 51–88.
- Golubok, A. O., O. M. Gorbenko, T. K. Zvonareva, S. A. Masalov, and V. V. Rozanov (2000). "Scanning Tunneling Microscopy of Films of Amorphous Carbon Doped with Copper". In: *Semiconductors* 34.2, pp. 223–226.
- Gordon, Karl D., Adolf N. Witt, and Brian C. Friedmann (1998). "Detection of Extended Red Emission in the Diffuse Interstellar Medium". In: *The Astrophysical Journal* 498.2, pp. 522–540.
- Grimme, S (2006). "Semiempirical GGA-type density functional constructed with a long-range dispersion correction". In: *J. Comput. Chem.* 27, p. 1787.

- Hammonds, M., T. Mori, F. Usui, and T. Onaka (2015). "Variations in the 3.3 μ m feature and carbonaceous dust in AKARI data". In: *Planetary and Space Science* 116. Cosmic Dust VII, pp. 73–83.
- Heger, M. L. (1922). "Further study of the sodium lines in class B stars". In: *Lick Observatory Bulletin* 10, pp. 141–145.
- Hudgins, Douglas M., Charles W. Bauschlicher, Jr., and L. J. Allamandola (2005). "Variations in the Peak Position of the 6.2 μ m Interstellar Emission Feature: A Tracer of N in the Interstellar Polycyclic Aromatic Hydrocarbon Population". In: *The Astrophysical Journal* 632.1, pp. 316–332.
- Iarlori, Simonetta, Giulia Galli, and Orlandina Martini (1994). "Microscopic structure of hydrogenated amorphous carbon". In: *Physical Review B* 49.10, pp. 7060–7063.
- Iwaki, Masaya (2002). "Estimation of the atomic density of amorphous carbon using ion implantation, SIMS and RBS". In: *Surface and Coatings Technology* 158-159, pp. 377–381.
- Jacob, W., W. Möller, W. Jacob, W. Müller, Max-planck-Institut Plasmaphysik, Eura T O M Association, Boltzmann Str, and D Garching (1993). "On the structure of thin hydrocarbon films On the structure of thin hydrocarbon films". In: *Applied Physics Letters* 63.13, pp. 1771–1773.
- Jäger, C., H. Mutschke, and T. Henning (Apr. 1998). "Optical properties of carbonaceous dust analogues". In: *Astronomy and Astrophysics* 332, pp. 291–299.
- Jones, A. P. (2012). "Variations on a theme - the evolution of hydrocarbon solids I. Compositional and spectral modelling – the eRCN and DG models". In: *Astronomy and Astrophysics* 540, A1. arXiv: [1511.01673](https://arxiv.org/abs/1511.01673).
- Jones, A. P., L. Fanciullo, M. Köhler, L. Verstraete, V. Guillet, M. Bocchio, and N. Ysard (2013). "The evolution of amorphous hydrocarbons in the ISM: dust modelling from a new vantage point". In: *Astronomy & Astrophysics* 558, A62. arXiv: [1411.6293](https://arxiv.org/abs/1411.6293).
- Jones, Anthony, A. G. G. M. Tielens, D. J. Hollenbach, and Christopher McKee (Nov. 1994). "Grain destruction in shocks in the interstellar medium". In: *The Astrophysical Journal* 433, pp. 797–810.
- Jones, Anthony P., Nathalie Ysard, Melanie Köhler, Lapo Fanciullo, Marco Bocchio, Elisabetta Micelotta, Laurent Verstraete, and Vincent Guillet (2014). "The cycling of carbon into and out of dust". In: *Faraday Discussions* 168.0, pp. 313–326. arXiv: [1411.5877](https://arxiv.org/abs/1411.5877).
- Jones, Brant M., Fangtong Zhang, Ralf I. Kaiser, Adeel Jamal, Alexander M. Mebel, Martin A. Cordiner, and Steven B. Charnley (2011). "Formation of benzene in the interstellar medium". In: *Proceedings of the National Academy of Sciences* 108.2, pp. 452–457.
- Kislov, V. V., A. I. Sadovnikov, and A. M. Mebel (2013). "Formation Mechanism of Polycyclic Aromatic Hydrocarbons beyond the Second Aromatic Ring". In: *The Journal of Physical Chemistry A* 117.23, pp. 4794–4816.
- Kovačević, E., I. Stefanović, J. Berndt, Y. J. Pendleton, and J. Winter (2005). "A Candidate Analog for Carbonaceous Interstellar Dust: Formation by Reactive Plasma Polymerization". In: *The Astrophysical Journal* 623.1, pp. 242–251.
- Krasnokutski, Serge, Friedrich Huisken, C. Jäger, and Thomas Henning (Feb. 2017). "Growth and Destruction of PAH Molecules in Reactions with Carbon Atoms". In: *The Astrophysical Journal* 836, p. 32.
- Krełowski, J. (2002). "Organic molecules and the diffuse interstellar bands". In: *Advances in Space Research* 30.6, pp. 1395–1407.
- Kroto, H. W. and M. Jura (Sept. 1992). "Circumstellar and interstellar fullerenes and their analogues". In: *Astronomy and Astrophysics* 263, pp. 275–280.

- Kwok, Sun (2016). "Complex organics in space from Solar System to distant galaxies". In: *Astronomy and Astrophysics Review* 24.1, pp. 1–27.
- Kwok, Sun, Kevin Volk, and Peter Bernath (2001). "On the Origin of Infrared Plateau Features in Proto-Planetary Nebulae". In: *The Astrophysical Journal* 554.1, pp. L87–L90.
- Kwok, Sun and Yong Zhang (2011). "Mixed aromatic-aliphatic organic nanoparticles as carriers of unidentified infrared emission features". In: *Nature* 479.7371, pp. 80–83.
- (2013). "Unidentified infrared emission bands: Paha or maons?" In: *The Astrophysical Journal* 771.1, pp. 5–9. arXiv: [1304.7629](https://arxiv.org/abs/1304.7629).
- Lai, Thomas S.-Y., Adolf N. Witt, and Ken Crawford (2017). "Extended red emission in IC59 and IC63". In: *Monthly Notices of the Royal Astronomical Society* 469.4, pp. 4933–4948.
- Leger, A. and J. L. Puget (Aug. 1984). "Identification of the 'unidentified' IR emission features of interstellar dust?" In: *Astronomy and Astrophysics* 137, pp. L5–L8.
- Léger, A, L Verstraete, L D'Hendecourt, D Défourneau, O Dutuit, W Schmidt, and J Lauer (1989). "The PAH Hypothesis and the Extinction Curve". In: *Interstellar Dust* 135, p. 173.
- Li, A. (May 2007). *Modeling the Infrared Emission Spectra of Specific PAH Molecules in Interstellar Space*. Spitzer Proposal.
- Lin, S. H. (1976). "Theory of vibrational relaxation and infrared absorption in condensed media". In: *The Journal of Chemical Physics* 65.3, pp. 1053–1062.
- Lovas, F J, Robert J. McMahon, Jens Uwe Grabow, Melanie Schnell, James Mack, Lawrence T Scott, and Robert L Kuczkowski (2005). "Interstellar chemistry: A strategy for detecting polycyclic aromatic hydrocarbons in space". In: *Journal of the American Chemical Society* 127.12, pp. 4345–4349.
- Marciniak, A, V Despré, T Barillot, A Rouzée, M C E Galbraith, J Klei, C. H. Yang, C T L Smeenk, V Loriot, S Nagaprasad Reddy, A G G M Tielens, S Mahapatra, A I Kuleff, M J J Vrakking, and F Lépine (2015). "XUV excitation followed by ultrafast non-adiabatic relaxation in PAH molecules as a femto-astrochemistry experiment". In: *Nature Communications* 6.
- Maté, Belén, Isabel Tanarro, Miguel A. Moreno, Miguel Jiménez-Redondo, Rafael Escribano, and Víctor J. Herrero (2014). "Stability of carbonaceous dust analogues and glycine under UV irradiation and electron bombardment". In: *Faraday Discuss.* 168.0, pp. 267–285.
- Maté, Belén, Germán Molpeceres, Miguel Jiménez-Redondo, Isabel Tanarro, and Víctor J. Herrero (2016). "High-Energy Electron Irradiation of Interstellar Carbonaceous Dust Analogs: Cosmic-Ray Effects on the 3.4 μ m absorption band". In: *The Astrophysical Journal* 831.1, p. 51.
- Mattioda, A. L., A. Ricca, J. Tucker, C. W. Bauschlicher Jr., and L. J. Allamandola (Apr. 2009). "Far-Infrared Spectroscopy of Neutral Coronene, Ovalene, and Dicononylene". In: *The Astrophysical Journal* 137, 4054–4060, pp. 4054–4060.
- McCall, Benjamin J. and R. Elizabeth Griffin (2013). "On the discovery of the diffuse interstellar bands". In: *Proceedings of the Royal Society A: Mathematical, Physical and Engineering Sciences* 469.2151, pp. 20120604–20120604.
- Mennella, V., L. Colangeli, P. Palumbo, A. Rotundi, W. Schutte, and E. Bussoletti (1996). "Activation of an ultraviolet resonance in hydrogenated amorphous carbon grains by

- exposure to ultraviolet radiation". In: *The Astrophysical Journal* 464.2 PART II, pp. L191–L194.
- Mennella, V., L. Colangeli, E. Bussoletti, P. Palumbo, and A. Rotundi (1998). "A new approach to the puzzle of the ultraviolet interstellar extinction bump". In: *Astrophysical Journal* 507.2 PART II, pp. L177–L180.
- Mennella, V, G A Baratta, A Esposito, G Ferini, and Y J Pendleton (2003). "The Effects of Ion Irradiation on the Evolution of the Carrier of the 3.4 Micron Interstellar Absorption Band". In: *The Astrophysical Journal* 587.2, p. 727.
- Micelotta, E. R., A. P. Jones, and A. G. G. M. Tielens (2009a). "Polycyclic aromatic hydrocarbon processing in a hot gas". In: *Astronomy and Astrophysics* 510, A37. arXiv: [0912.1595](#).
- (2009b). "Polycyclic aromatic hydrocarbon processing in a hot gas". In: *Astronomy and Astrophysics* 510, A37. arXiv: [0912.1595](#).
- Micelotta, Elisabetta R., Anthony P. Jones, Jan Cami, Els Peeters, Jeronimo Bernard-Salas, and Giovanni Fanchini (2012). "The Formation of Cosmic Fullerenes from Aromatic Clusters". In: *The Astrophysical Journal* 761.1, p. 35.
- Molpeceres, Germán, Vicente Timón, Miguel Jiménez-Redondo, Rafael Escribano, Belén Maté, Isabel Tanarro, and Víctor J Herrero (2017). "Structure and infrared spectra of hydrocarbon interstellar dust analogs". In: *Physical Chemistry Chemical Physics* 19.2, pp. 1352–1360.
- Morris, Andrew J., Rebecca J. Nicholls, Chris J. Pickard, and Jonathan R. Yates (2014). "OptaDOS: A tool for obtaining density of states, core-level and optical spectra from electronic structure codes". In: *Computer Physics Communications* 185.5, pp. 1477–1485.
- NIST (1980). *The Coblenz Society desk book of infrared spectra*.
- Palik, E.D. (1998). *Handbook of Optical Constants of Solids*. Academic Press handbook series. Elsevier Science. ISBN: 9780080533780.
- Pech, C., C. Joblin, and P. Boissel (2002a). "The profiles of the aromatic infrared bands explained with molecular carriers". In: *Astronomy and Astrophysics* 388.2, pp. 639–651. arXiv: [arXiv:0901.0974v2](#).
- (2002b). "The profiles of the aromatic infrared bands explained with molecular carriers". In: *Astronomy & Astrophysics* 388.2, pp. 639–651. arXiv: [arXiv:0901.0974v2](#).
- Peeters, Els (2011). "The PAH hypothesis after 25 years". In: *Proceedings of the International Astronomical Union*. Vol. 7. S280. Cambridge University Press, pp. 149–161. ISBN: 9781107019805. arXiv: [1111.3680](#).
- Peláez, R J, B Maté, I Tanarro, G Molpeceres, M Jiménez-Redondo, V Timón, R Escribano, and V J Herrero (2018). "Plasma generation and processing of interstellar carbonaceous dust analogs". In: *Plasma Sources Science and Technology* 27.3, p. 035007.
- Pendleton, Y. J. and L. J. Allamandola (2002). "The Organic Refractory Material in the Diffuse Interstellar Medium: Mid-Infrared Spectroscopic Constraints". In: *The Astrophysical Journal Supplement Series* 138.1, pp. 75–98.
- Perdew, John P., Kieron Burke, Matthias Ernzerhof, Department of Physics, and New Orleans Louisiana 70118 John Quantum Theory Group Tulane University (1996). "Generalized Gradient Approximation Made Simple". In: *Physical Review Letters* 77.18, pp. 3865–3868.
- Pino, Thomas, Emmanuel Dartois, A.-T Cao, Yvain Carpentier, Thierry Chamaillé, R Vasquez, Anthony Jones, Louis Dhendecourt, and Philippe Brechignac (Nov. 2008). "The 6.2 m band position in laboratory and astrophysical spectra: A tracer of the

- aliphatic to aromatic evolution of interstellar carbonaceous dust". In: *Astronomy and Astrophysics* 490, pp. 665–672.
- Popovic, Zoran D. (1982). "Electric field induced fluorescence quenching and photo-carrier generation in x-metal-free phthalocyanine". In: *The Journal of Chemical Physics* 76.5, pp. 2714–2719. arXiv: [arXiv:1011.1669v3](https://arxiv.org/abs/1011.1669v3).
- Puget, J. L. and A. Leger (1989). "A new component of the interstellar matter - Small grains and large aromatic molecules". In: *Annual Review of Astronomy and Astrophysics* 27, pp. 161–198.
- Purcell, E. M. (June 1976). "Temperature fluctuations in very small interstellar grains". In: *The Astrophysical Journal* 206, pp. 685–690.
- Rappé, A. K., C. J. Casewit, K. S. Colwell, W. A. Goddard, and W. M. Skiff (1992). "UFF, a Full Periodic Table Force Field for Molecular Mechanics and Molecular Dynamics Simulations". In: *Journal of the American Chemical Society* 114.25, pp. 10024–10035. arXiv: [1305.7119](https://arxiv.org/abs/1305.7119).
- Robertson, J. (2002). "Diamond-like amorphous carbon". In: *Materials Science and Engineering: R: Reports* 37.4, pp. 129–281.
- Robertson, J. and E. P. O'Reilly (1987). "Electronic and atomic structure of amorphous carbon". In: *Phys. Rev. B* 35 (6), pp. 2946–2957.
- Salama, F and L J Allamandola (1995). "Polycyclic aromatic hydrocarbon ions and the diffuse interstellar bands". In: *Adv. Space Res.* 15.3, pp. 413–422.
- Sandford, Scott A., Max P. Bernstein, and Christopher K. Materese (2013). "The infrared spectra of polycyclic aromatic hydrocarbons with excess peripheral H atoms (Hn-PAHs) and their relation to the 3.4 and 6.9 μm pah emission features". In: *Astrophysical Journal, Supplement Series* 205.1, p. 8.
- Schmidt, G. D., M. Cohen, and B. Margon (Aug. 1980). "Discovery of optical molecular emission from the bipolar nebula surrounding HD 44179". In: *The Astrophysical Journal Letters* 239, pp. L133–L138.
- Schnitzler, Elijah G., Brandi L.M. Zenchyzen, and Wolfgang Jäger (2015). "HIGH-resolution fourier-transform microwave spectroscopy of methyl- and dimethylnaphthalenes". In: *The Astrophysical Journal* 805.2, p. 141.
- Scott, A. and W. W. Duley (1996). "The Decomposition of Hydrogenated Amorphous Carbon: A Connection with Polycyclic Aromatic Hydrocarbon Molecules". In: *The Astrophysical Journal* 472.2, pp. L123–L125.
- Scott, A. D., W. W. Duley, and H. R. Jahani (1997). "Infrared Emission Spectra from Hydrogenated Amorphous Carbon". In: *The Astrophysical Journal* 490.2, pp. L175–L177.
- Sellgren, K. (Feb. 1984). "The near-infrared continuum emission of visual reflection nebulae". In: *The Astrophysical Journal* 277, pp. 623–633.
- Sellgren, K. (2001). "Aromatic hydrocarbons, diamonds, and fullerenes in interstellar space: puzzles to be solved by laboratory and theoretical astrochemistry". In: *Spectrochimica Acta Part A: Molecular and Biomolecular Spectroscopy* 57.4, pp. 627–642.
- Seok, Ji Yeon, Hiroyuki Hirashita, and Ryosuke S Asano (2014). "Formation history of polycyclic aromatic hydrocarbons in galaxies". In: *Monthly Notices of the Royal Astronomical Society* 439.2, pp. 2186–2196.
- Shan, Jun, Masako Suto, and L.C. Lee (1992). "IR emissions from UV excitation of benzene and methyl derivatives". In: *Journal of Photochemistry and Photobiology A: Chemistry* 63.2, pp. 139–147.

- Shannon, Matthew J., Els Peeters, Jan Cami, and Joris A. D. L. Blommaert (2018). "Polycyclic aromatic hydrocarbon emission toward the Galactic bulge". In: *The Astrophysical Journal* 855.1, p. 32. arXiv: 1802.04282.
- Snow, T. P. (1997). "The Diffuse Interstellar Bands and Large Interstellar Molecules". In: *From Stardust to Planetesimals*. Ed. by Y. J. Pendleton. Vol. 122. Astronomical Society of the Pacific Conference Series, p. 147.
- Stecher, T. P. and B. Donn (Nov. 1965). "On Graphite and Interstellar Extinction". In: *The Astrophysical Journal* 142, p. 1681.
- Steglich, M, C Jäger, F Huisken, M Friedrich, W Plass, H.-J. Räder, K Müllen, and Th. Henning (2013). "the Abundances of Hydrocarbon Functional Groups in the Interstellar Medium Inferred From Laboratory Spectra of Hydrogenated and Methylated Polycyclic Aromatic Hydrocarbons". In: *The Astrophysical Journal Supplement Series* 208.2, p. 26. arXiv: 1308.4080.
- Tappe, A, J Rho, and William Reach (Sept. 2006). "Shock Processing of Interstellar Dust and Polycyclic Aromatic Hydrocarbons in the Supernova Remnant N132D". In: *The Astrophysical Journal* 653.
- Thaddeus, P (2006). "The prebiotic molecules observed in the interstellar gas". In: *Philosophical Transactions of the Royal Society B: Biological Sciences* 361.1474, pp. 1681–1687.
- Tielens, A. G. G. M. and L. J. Allamandola (1987). "Composition, structure, and chemistry of interstellar dust". In: *Interstellar Processes*. Vol. 134. Springer, Dordrecht, pp. 397–469.
- Tielens, A.G.G.M. (2008). "Interstellar Polycyclic Aromatic Hydrocarbon Molecules". In: *Annual Review of Astronomy and Astrophysics* 46.1, pp. 289–337.
- Tran, Fabien, Bassam Alameddine, Titus Jenny, and Tomasz Wesolowski (Oct. 2004). "-Stacking Behavior of Selected Nitrogen-Containing PAHs". In: *Journal of Physical Chemistry A* 108, pp. 9155–9160.
- Van Meer, R., O. V. Gritsenko, and E. J. Baerends (2014). "Physical meaning of virtual kohn-sham orbitals and orbital energies: An ideal basis for the description of molecular excitations". In: *Journal of Chemical Theory and Computation* 10.10, pp. 4432–4441.
- Vega, O, A Bressan, P Panuzzo, R Rampazzo, M Clemens, G L Granato, L Buson, L Silva, and W W Zeilinger (2010). "Unusual PAH Emission in Nearby Early-Type Galaxies: A Signature of an Intermediate-AGE Stellar Population?" In: *The Astrophysical Journal* 721, pp. 1090–1104.
- Wang, Jun, Zaiming Chen, and Baoliang Chen (2014). "Adsorption of polycyclic aromatic hydrocarbons by graphene and graphene oxide nanosheets". In: *Environmental Science and Technology* 48.9, pp. 4817–4825.
- Whittet, D.C.B., S.S. Shenoy, G.C. Clayton, and K.D. Gordon (2004). "The Ultraviolet Extinction Curve of Intraclump Dust in Taurus (TMC-1): Constraints on the 2175 {Å} Bump Absorber". In: *The Astrophysical Journal* 602.Crutcher 1985, pp. 291–297.
- Witt, Adolf N. and Uma P. Vijh (2003). "Extended Red Emission: Photoluminescence by Interstellar Nanoparticles". In: *arXiv* 1, pp. 1–25. arXiv: 0309674 [astro-ph].
- Zhang, Yong and Sun Kwok (2015). "On the viability of the PAH model as an explanation of the unidentified infrared emission features". In: *The Astrophysical Journal* 798.1, p. 37.

Chapter 4

Survivability of Carbonaceous Dust Chemical Analogues

Previous chapter has established the fundamental basis for the study of the microscopic structure of carbonaceous dust chemical analogues and the calculation of the relevant spectroscopical features associated with such structures.

The models proposed in the previous section show several limitations from an astrophysical point of view. The utilization of mean structures, archetypes and guessed densities, allow to sample different functional groups and delimit extremal structures suitable for the rationalization of astrophysical observations. However, the time evolution of this analogues in astrophysical environments is hard to simulate from first principles.

We present there the experimental results concerning the interaction of high energy electrons with laboratory generated HACs. We expect that this study will give insight in the understanding of the aliphatic and aromatic content in carbonaceous dust chemical analogues under harsh ISM conditions. Some of the results of this chapter can be found in the paper: "High energy electron irradiation of interstellar carbonaceous dust analogs: Cosmic ray effects on the carriers of the 3.4 μm absorption band" (Maté et al., 2016).

4.1 Introduction

It has been stated that interstellar dust do not present a homogeneous composition through the different observed astronomical regions. In fact, in Chapter 3, we have shown how analogues with the same chemical groups but different structural arrangements lead to amorphous packings that present very different spectral properties (Jones et al., 2013). From the IR absorption features considered in the last chapter, the strongest and more easily traceable one during irradiation experiments is the characteristic C-H stretching band at 3.4 μm . This feature has been thoughtfully inspected during the last chapter.

In this chapter we will show the problem arising from the nature of the observations of this stretching band in different regions. First, we will present the mechanisms of creation and destruction of these functional groups. After that, a brief review of the literature concerning the energetic processing of HAC by cosmic rays will be held.

4.1.1 Dense vs Diffuse Molecular Clouds: The case of the $3.4 \mu\text{m}$ band

C-H stretching bands span in a wide range of frequencies from ~ 2800 to $\sim 3050 \text{ cm}^{-1}$. In the astrophysical literature, this broad range is referred as the $3.4 \mu\text{m}$ band, usually observed in absorption, but also in emission (Joblin et al., 1995). The presence of this band is evinced in the interstellar medium and in extragalactic sources (Duley and Williams, 1983; Sandford et al., 1991; Pendleton et al., 1994; Whittet et al., 2001; Chiar et al., 2002; Kondo et al., 2012). Fig 4.1 show a typical profile for the $3.4 \mu\text{m}$ absorption band in several Diffuse Interstellar Medium environments.

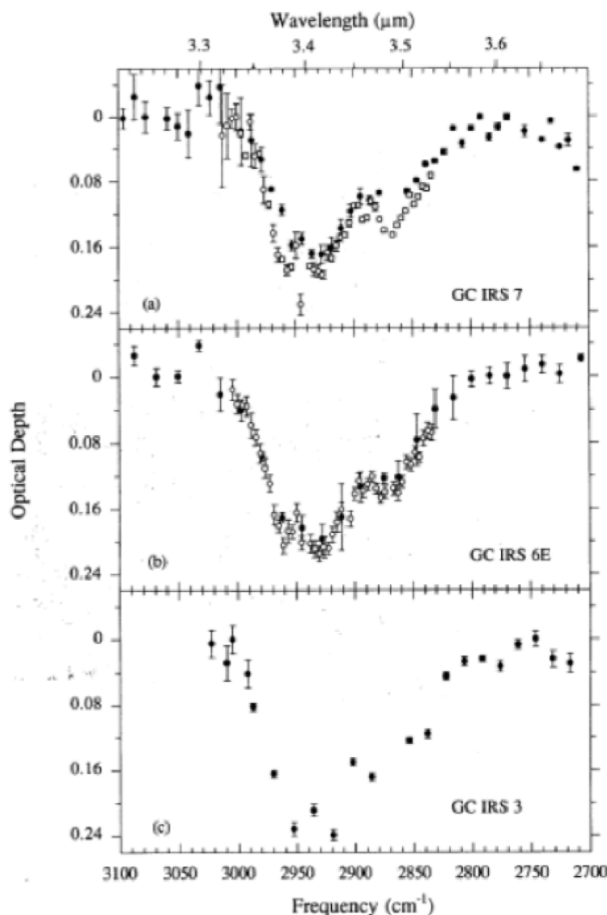


FIGURE 4.1: $3.4 \mu\text{m}$ absorption band towards diffuse clouds
Extracted from (Pendleton et al., 1994)

As has been mentioned before, this band is assigned to C-H vibrations, combining both aliphatic CH_2 and CH_3 vibrations, both symmetric and anti symmetric. Depending on the amount of aromatic material, the band can show a shoulder at $\sim 3.3 \mu\text{m}$, responsible for the C-H aromatic stretchings. This characteristic profile is observed in diffuse molecular clouds but disappears in dense ones.

As has been explained before, molecular clouds are regions of the interstellar medium with conditions that allow the formation of molecules. Within molecular clouds, there exist at least two extreme cases, dense and diffuse, each one defining two well separated

astronomical objects. Between these two, the main differentiating factor is the strength of the UV radiation field, magnitude that also permeates other indirect magnitudes such as f^n , that refers to the fraction of a molecular or ionic species with respect to their immediate atomic component or A_v , as the extinction coefficient. Table 4.1 summarizes the main features of different molecular clouds, being n_H the number density of atomic hydrogen in the cloud, and T the mean temperature of the cloud.

TABLE 4.1: Different Molecular Clouds and classification attending to their physical parameters

	Diffuse Atomic	Diffuse Molecular	Traslucent	Dense Molecular
Defining Characteristic	$f_{H_2}^n < 0.1$	$f_{H_2}^n > 0.1$ $f_{C_+}^n > 0.5$	$f_{C_+}^n < 0.5$ $f_{CO}^n < 0.9$	$f_{CO}^n > 0.9$
A_v (min)	0	~ 0.2	$\sim 1 - 2$	$\sim 5 - 10$
Mean n_H (cm^{-3})	10-100	100-500	500-5000	$>10^4$
Mean T	30-100	30-100	15-50	10-50

Extracted from Snow and McCall, 2006

The magnitude of the UV field deeply affects the chemistry and the physical state of the chemical species present in the region. As a consequence of the UV radiation filtering mainly by dust micrometer sized particles, in dense molecular clouds the temperature drops below 50 K, down to 10 K. This low temperature leads to the formation of layers of ice of different compositions on top of the dust grain substrate (Cuppen and Herbst, 2007; Jones et al., 2013). These two factors, the magnitude of the UV radiation field and the temperature drop, influence a lot the chemical processes and structure of the grain.

The Carbon-Hydrogen nature of the 3.4 μm band has been clearly validated during this thesis, but little to no comments have been done on the origin of that band. For origin here, we refer to the chemical synthesis of the functional groups responsible for such vibrations.

The chemical evolution of a dust grain, is a complicated and debated topic (Henning and Salama, 1998; Fonfria et al., 2008; Mauney and Lazzati, 2016; Fonfría et al., 2017). It is always dependent on where we are considering the formation to take place or the conditions of the region, the type of star, etc. We are not interested in discussing the primary process leading to a partially hydrogenated structure, but in the chemical processes than contribute to maintain this structure in diffuse clouds across many lines of sight (Wickramasinghe and Allen, 1980; Duley and Williams, 1981; Pendleton et al., 1994; Whittet et al., 1997; Chiar et al., 2006). This maintenance process is mainly due to the competence of two crucial factors:

1. C-H bond formation via hydrogenation of hydrogen poor materials, amorphous carbon as an example. (Sugai, Yoshida, and Toyoda, 1989; Mennella et al., 1999; Mennella et al., 2002; Mennella, 2006; Mennella et al., 2008; Jones et al., 2011; Potapov et al., 2017). This effect leads to an increase of the C-H absorption.
2. C-H bond breaking is mainly carried out by UV photons. A high flux of them, known as the primary UV field, is present in diffuse clouds and is the responsible of the high fraction of atomic versus molecular hydrogen observed in these regions. (See 4.1). (Mennella et al., 2001; Dartois et al., 2005; Jones et al., 2011; Alata et al., 2014; Maté et al., 2014; Dartois et al., 2017)

In diffuse clouds, both above mentioned mechanisms are in equilibrium (Mennella et al., 2001; Mennella et al., 2002), ensuring the appearance of the 3.4 μm . However, in dense molecular clouds, the shielding of the UV field leads to the following consequences regarding the 3.4 μm absorption band:

- Molecular hydrogen is the most abundant species due to the filtering of the radiation leading to its dissociation. Hydrogenation of amorphous carbon structures via H_2 is no longer a barrierless process and thus, the total formation rate should decrease.
- Low temperatures arising from the reduction of the UV field induce the growth of layers of ice on top of the grains. This blocks the processing with low penetration particles or the hydrogenation, which is mostly superficial.
- On the opposite, the lower UV field in these regions leads to a decrease of the rate of C-H groups.

All the above mentioned factors should point out to a *status quo* between formation and destruction of the C-H bonds, but in reality what is observed in dense clouds is the disappearance of the 3.4 μm band. Understanding the disappearance of the 3.4 μm feature in dense environments is an open topic in the astrochemical community. There seems to be consensus in the factors that lead to the inhibition of the C-H formation but there is not a clear explanation for the destruction. Cosmic Rays (CR), charged particles with sufficient energy to traverse dense clouds because of their high energy (several orders of magnitude higher than a typical chemical bond) are thought to process carbonaceous matter effectively. In diffuse clouds the magnitude of the processing by CR is neglected in comparison with the strong UV field, with characteristic times of destruction that vary by a factor of 10^{3-4} years (Mennella et al., 2001; Mennella et al., 2003). In dense media however, the effect of cosmic rays become much more relevant.

4.1.2 Cosmic Rays Interaction with Carbonaceous Grains: Previous Works

Cosmic Rays are charged particles, generally ions with very high energy. Their discovery is attributed to Victor Hess and it was awarded with the Nobel Prize in Physics in 1936 due to it. The history of such discovery is quite interesting but will not be held here. What we will gather though, is the chemical distribution of the ions as a function of the energy, extracted from two different work groups (CREAM and PAMELA) in air showers (Gaisser, Stanev, and Tilav, 2013). Air showers are the collection of particles and radiation produced by the interaction of a cosmic ray with the molecules in our atmosphere. Detection of the primary cosmic rays is thus an indirect process. Fig 4.2 shows the fit (solid lines) for the total energy deposited by cosmic rays and a decomposition of the fit into their individual nuclei contributions gathered by the above mentioned groups.

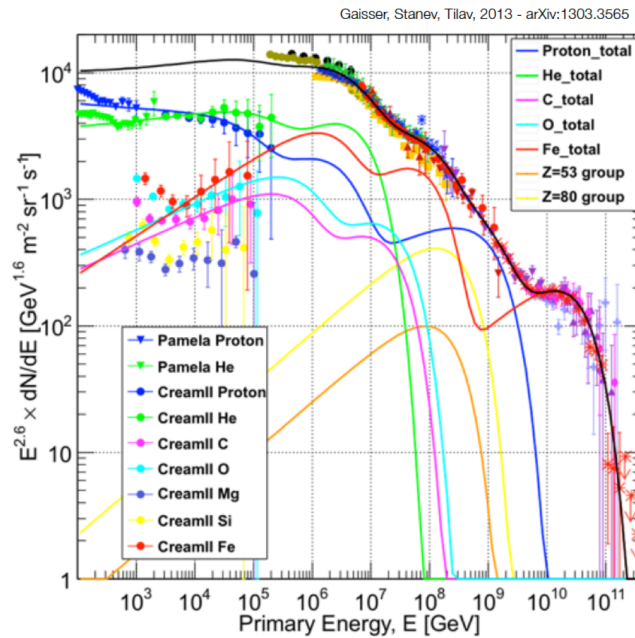


FIGURE 4.2: Cosmic Ray Energy Distribution from Atmospheric Air Showers
 Extracted from (Gaisser, Stanev, and Tilav, 2013)

The interaction of cosmic rays analogues with carbonaceous matter of some sort is a topic that has been studied by several authors before (Mennella et al., 2003; Godard et al., 2011; Godard et al., 2013; Maté et al., 2014; Maté et al., 2016; Dartois et al., 2017). This chapter is dedicated to develop a framework and present the results of Maté et al., 2016 concerning the destruction of C-H bonds by CR analogues. We will present our experimental setup and models employed for calculating the destruction cross sections in the first sections. Our experimental results will be presented afterwards in comparison with the works by Mennella et al., 2003 and Godard et al., 2011.

In the work by the group of Mennella (Mennella et al., 2003) they have employed 30 keV He^+ ions to simulate the cosmic rays interaction with HAC materials grown from pyrolyzed and laser ablated carbon in a hydrogen atmosphere. In that work, under their considered assumptions, the main conclusion was that their cosmic ray analogues are able to account for the destruction of the C-H stretching bands in dense clouds. Godard's group (Godard et al., 2011), on the other hand, employed a variety of high-energy ions up to Ni^{9+} and fitted the decay of the CH bond band intensity to a hydrogen recombination model. We will describe this model in the methods section. The results of the two groups not only differ by more than one order of magnitude, but they also lead to opposed astrophysical implications. The values of Godard do not account for the full destruction of the band, being necessary to include side mechanisms to provide meaningful arguments for the destruction of the C-H band within the time frame of existence of a dense cloud.

For mimicking the results of the interaction of cosmic rays with carbonaceous samples we have used 5keV electrons. The possibility of employing electrons as analogues of

cosmic rays has been debated over the last years in the literature (Kaiser et al., 2013; Mason et al., 2014). The reason behind this hypothesis is the fact that chemical effects in carbonaceous materials and ices by cosmic rays are not directly related with the nature of cosmic rays itself (that are several orders of magnitude more energetic than the range of energies of a typical chemical bond), but from the cascade of secondary particles (bremsstrahlung photons, electrons and protons) that arise from their interaction with the material. This is equivalent to say that, in first approximation, the processing of a material do not depend on the nature of the processing agent but on the deposited energy in the sample. This is, of course, an approximation and the destruction efficiency do vary within a range depending in each particular ion as shown in (Godard et al., 2011). In particular, electrons behave in a similar way that high energetic particles, as has been corroborated in the previous mentioned works (Gerakines et al., 2012; Kaiser et al., 2013; Mason et al., 2014; Maté et al., 2014).

The present study is devoted to the calculation of quantitative destruction rates of C-H bonds in HAC materials, grown in our group using 5 keV electrons to simulate CR. The design of our experiments is done accordingly to Montecarlo simulations of electron trajectories in solids, determining the exact penetration depths of the e^- and thus the thickness needed (within a range) to obtain full processed samples and meaningful destruction cross sections. To the best of our knowledge, these are the first quantitative results of electron-matter interaction in these kind of materials. The sample is processed with electrons and the change in the $3.4 \mu\text{m}$ band is monitored by in situ IR spectroscopy.

The results of this chapter complement the results of chapter 3, showing the evolution of our chemical analogues under harsh astrophysical conditions. Our results are always guided by the parent works of Mennella et al., 2003 and Godard et al., 2011, being complementary and helpful for the clarification of the discordant results of both groups.

4.2 Experiment and Model

The current section is divided as follows:

1. Description of the experimental conditions for the growth of the different carbonaceous materials studied in this section
2. Calibration of the electron gun.
3. Description of the main points of the hydrogen recombination model employed in the analysis of our experimental results.

4.2.1 Experimental setup

Deposits of HAC have been generated on top of IR transparent Si substrates. For doing so, CH_4 :He gas mixtures have been used as hydrocarbon precursor. Flows of 5 sccm and 10 sccm of CH_4 and He, respectively, were introduced in the plasma reactor with a total in-flow pressure of 0.32 mbar before ignition. The deposits were grown using the Plasma Enhanced Chemical Vapour Deposition Technique (PECVD, see Methodology

section for further details) using a 40 W discharge, and a deposition time of 15 min. The intensity and shape of the IR features of the HAC deposits obtained under these conditions were measured readily after formation, with an excellent degree of reproducibility between them. Sample thickness is monitored from the IR interference fringes when the thickness of the sample is near the micron regime (≥ 800 nm). For thinner samples, an extrapolation with respect to the deposition time is considered. All samples employed for the processing lie in the range between 460 ± 50 nm. The estimated thickness for each sample is provided at each individual experiment. Fig 4.3 show the typical look of a HAC samples grown in our group.

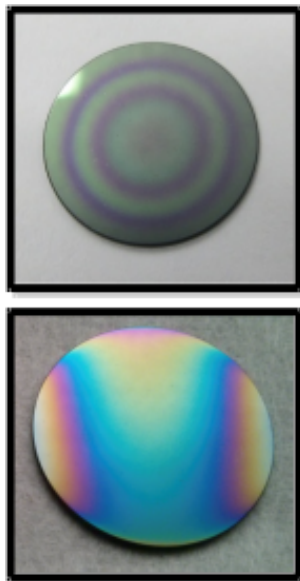


FIGURE 4.3: HAC samples grown in our laboratory

Once the samples are grown, they are transferred to our high vacuum chamber for IR spectroscopy and electron processing. The HAC covered silicon substrates were placed in an appropriate Cu holder mounted at the bottom of our liquid Nitrogen cryostat. In order to avoid contamination of the samples, we have processed them soon after its generation. The sample is alternatively faced against the IR beam of the FTIR spectrometer and the electron beam from the electron gun. An homogeneous electron flux of $7.9 \times 10^{12} \text{ e}^- \text{ cm}^{-2} \text{ s}^{-1}$ of 5 keV electrons has been selected. Experiments have been carried out at two different temperatures, 85 and 300 K. Irradiation times of 6 hours have been used for all the samples.

Penetration depth and linear energy transfer of the electrons when interacting with our carbonaceous material have been calculated using electronic classical trajectories via the CASINO code (Drouin et al., 2007; Demers et al., 2011).

From the IR spectra taken during the processing of the sample, decays of the $3.4 \mu\text{m}$ band in the HAC materials are obtained. These decays are then fitted to a hydrogen recombination kinetic model to obtain C-H destruction cross sections.

4.2.2 Calibration of the Electron Gun

The electron current emitted by the filament (I_{em} in the μA range) of the electron gun is three orders of magnitude lower than the final electric current that reach the sample (I_{blank} in the nA range). Such emission current is also three orders of magnitude lower than the current circulating through the filament. A precise stabilizing source is needed in order to obtain reproducible target currents between different experiments. For doing so, an special **Emission** Stabilized Source (JR212) has been constructed in our group. Results have been deeply validated for a various range of materials (Maté et al., 2014; Maté et al., 2015; Maté et al., 2016). A scheme of our electron gun is shown in Fig 4.4.

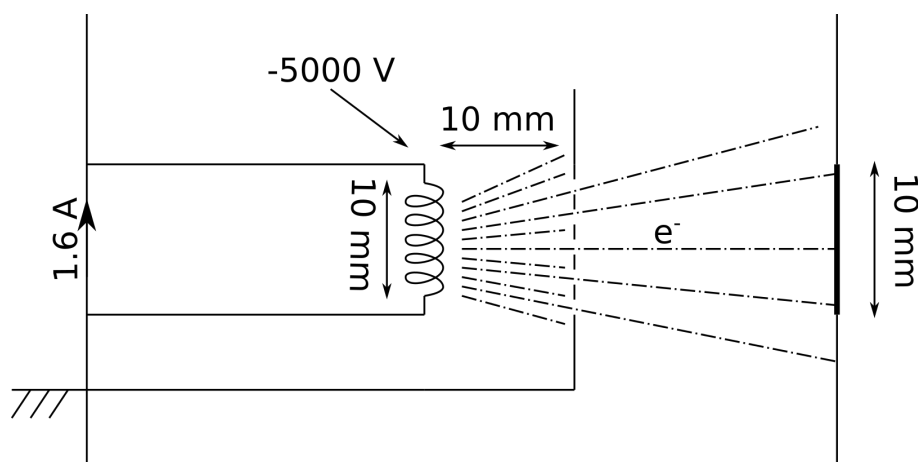


FIGURE 4.4: Scheme of the electron gun used in our experiments

A calibration of the electron flux that reaches the sample as a function of the emission current in the filament is required. The emission stabilized source displays the emitted current for a given electron energy and filament current. In order to measure the real flux of electrons that reaches the sample, an aluminum plate of the dimensions of the sample holder window (10 mm diameter) is placed in the substrate position, electrically isolated from its copper walls, and connected to a high precision nanoammeter. Then, a particular current is stabilized in emission in the power source, and the current that reaches the aluminum plate (I_{blank}) is measured. For 5 keV emission currents between 50 - 500 μA , the filament amperage varied between 1.3-1.6 A. Fig 4.5 show the results of the calibration of the stabilized emission current vs the final current in the blank. The distance between the accelerating mesh and the sample is 30 mm for all of our experiments.

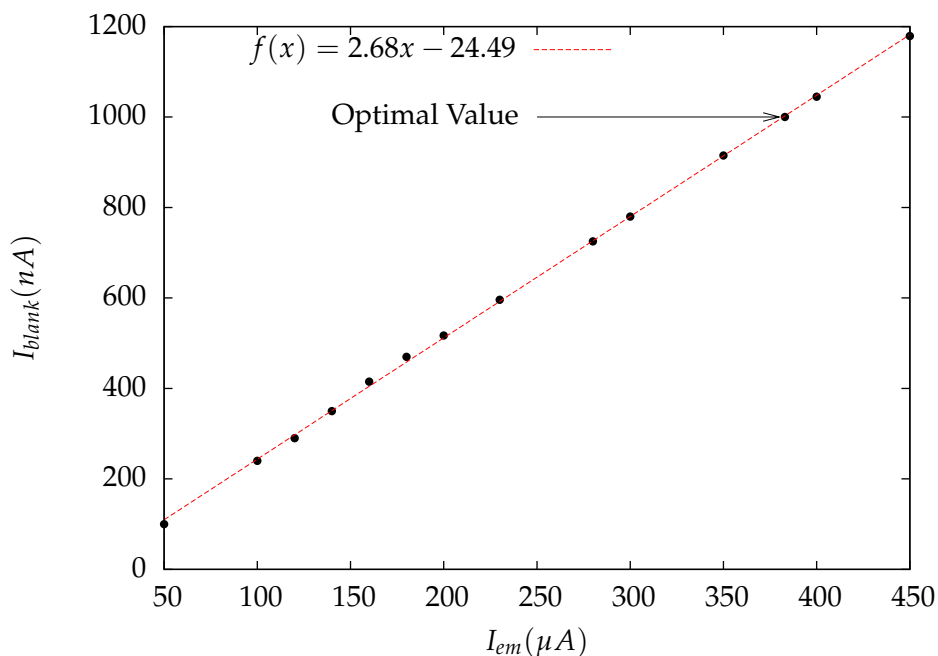


FIGURE 4.5: Calibration of the Electron Gun.

From this graph we can infer a linear dependence between both currents, which in many ways is optimal to tune the desired flux that will reach the sample. In our applications, a current in the sample of $1000 \text{ nA} = 1 \text{ }\mu\text{A}$ has been used as a compromise value between a reasonable processing time, without overheating the sample. This current in the exposed sample (of 10 mm of diameter) correspond to the flux of $7.9 \times 10^{12} \text{ e}^- \text{ cm}^{-2} \text{ s}^{-1}$. Looking at Fig 4.5, it can be seen that the magnitude of the emitted electrons chosen corresponds to $383 \text{ }\mu\text{A}$. The ratio between both quantities (emitted vs blank) gives us a rough idea of the fraction of electrons lost in the travelling. From this simple calculation we obtain a ratio of impinging electrons of 0.26% indicating the that most of the electrons are either neutralized in the fine mesh, fine mesh holder, sample holder or chamber walls.

4.2.3 Kinetic Model

We have fitted the experimental CH-band-intensity decays obtained during the electron processing to two different kinetic models to obtain CH destruction cross sections, σ_d . The first model, phenomenological, consists in a simple exponential fitting of the decay plus an added term accounting for the asymptotic behavior at the end of the processing (Mennella et al., 2003; Godard et al., 2011):

$$\frac{I(F)}{I_0} = ae^{\sigma_d^e F} + \frac{I_f}{I_0}, \quad (4.1)$$

where $I(F)/I_0$ is the ratio of the CH band integrated absorbance at fluence F (flux x time) with respect the initial one, a is pre-exponential fittable parameter and I_f is the C-H integrated absorbance of the last spectrum, at the end of the processing. At the early stages of the processing, when no asymptotic regime have been reached, the decay can be directly fitted with an exponential expression:

$$\frac{I(F)}{I_0} = ae^{\sigma_a^c F} \quad (4.2)$$

A more sophisticated model is proposed in Adel et al., 1989. This bulk-molecular recombination model propose that the hydrogen atoms that are liberated from the energetic processing, disregarding the nature of the incoming particles, diffuse until recombining with another hydrogen atom, with exothermic formation of H_2 molecules. For this mechanism to be efficient enough, a constant flux with an homogeneous deposited energy (enough for the breaking of all C-H bonds in the structure) should be present in the sample. From this condition two clauses subsequently appear:

- The C-H bond breaking is a fast process in which a certain particle interacts immediately with the target.
- Once a H_2 molecule is formed, it diffuses from the bulk to the environment, without further interactions with the valence uncompensated C atoms.

These two conditions are fulfilled both from the homogeneous nature of the beam and its high energy, and from the kinetic barrier appearing in the $R - C * + H_2$ reaction (especially at low temperatures).

For the description of the model, let us consider a recombination volume V in which we place two hydrogen, to be recombined, atoms. At the end of the processing a condition imposed to this volume is that the volume density of hydrogen atoms equals the recombination volume $V = \rho_{f,H}^{-1}$.

In hydrogen molecule formation regime, the probability of creating a single molecule, P , is given by the probability of breaking a C-H bond squared times the probability of recombination. The number of hydrogen molecules formed per ion is the probability of creating a pair times the number of possible pairs $\rho V(\rho V - 1)/2$:

$$N = P\rho V(\rho V - 1)/2. \quad (4.3)$$

Adel et al., 1989 defined the rate of hydrogen atoms per ion implanted as $d\rho/dt = -2N/V$, and considered the volume of recombination cylindrical, with cross section K . Then, $dt = KdF$ with F being the fluence of electrons. Combining all the terms we arrive to the following differential equation:.

$$\frac{d\rho}{dF} = -PK\rho(\rho V - 1). \quad (4.4)$$

Equation 4.4 admits a solution of the type:

$$\rho(F) = \left[\frac{1}{\rho_f} + \left(\frac{1}{\rho_0} - \frac{1}{\rho_f} \right) e^{(-\sigma_d^r F)} \right]^{-1}, \quad (4.5)$$

with $\sigma_d^r = PK$ as the fittable parameter that has a direct comparison with the σ_d^e cross section of the exponential fitting. In this way a chemical meaningful expression is derived to explain the mechanism of hydrogen abstraction using high energetic particles. Equation 4.5 provide an exceptional fitting of bibliographic results using both high energy ions and electrons (Godard et al., 2011; Maté et al., 2016), and the consequences of this will be further discussed later. It is also worth noticing that considering H_2 to be the only recombinable species introduces an error since more complex hydrocarbons can be formed from the breaking of more complex functional groups (Alata et al., 2014; Alata et al., 2015; Martín-Doménech, Dartois, and Muñoz Caro, 2016).

With the corresponding cross sections (σ_d will be used indistinctly of the model), assuming zero order kinetics for the process, the destruction rate, R_d (in s^{-1}) of our material is:

$$R_d = \sigma_d(5keV)f_e(5keV), \quad (4.6)$$

with f_e (in cm^2s^{-1}) being an effective flux of electrons in dense molecular clouds. The energetic processing we are trying to simulate is caused via bremsstrahlung electrons from the quick interaction of MeV cosmic rays (CR) with our material. It is advisable therefore to reformulate eq 4.6 into its CR counterpart $R_d = \sigma_d(1MeV)f_{CR}(1MeV)$. f_{CR} fluxes are known from the bibliography and $\sigma_d(1MeV)$ from CR can be directly inferred from our cross sections, considering a direct proportionality relationship (Mennella et al., 2003) as:

$$\sigma_d(1MeV) = \frac{S(1MeV)}{S(5keV)}\sigma_d(5keV), \quad (4.7)$$

with $S(1MeV)$ being the 1 MeV stopping power taken from the literature, calculated using specific Ion/Matter codes (SRIM) (Ziegler, Ziegler, and Biersack, 2010). The 5 keV stopping power $S(5keV)$ is defined as $S(5keV) = LET/\rho_{HAC}$ where LET is the **linear energy transfer** of the electrons and ρ_{HAC} is the density of the HAC material. Linear Energy Transfer (LET) is defined as the energy that is deposited by the electrons per unit of thickness, and is obtained from our Montecarlo simulations using the CASINO code.

With R_d calculated, it is possible to obtain a characteristic time of destruction τ_d , indicating the amount of time that is needed to account for the full destruction of the C-H band, as:

$$\tau_d = R_d^{-1}. \quad (4.8)$$

4.3 Results

The results section in this chapter is divided as follows. Firstly, Montecarlo simulations of the electron trajectories are briefly described. Calculated LETs and deposited energies per sample mass are provided at different ρ_{HAC} and C/H ratios. In the next two sections, we will present the results of the processing experiments of HAC analogues, and their astrophysical implications.

4.3.1 Montecarlo Simulations

As has been explained above, we need electron-sample energetic parameters as input for the kinetic model. Furthermore, we need *a priori* information on the adequate HAC thickness to guarantee electron irradiation of the whole sample in our experiments. In order to do so, Montecarlo simulations of electronic trajectories have been carried out with the CASINO code (Drouin et al., 2007; Demers et al., 2011). The main capabilities of the code are presented in the cited references, and more importantly in the references therein, since CASINO gathers several of the main algorithms for the calculation of stochastic classical electron trajectories. For our applications a general overview of the algorithms will be given before the presentation of the results. In this section we will deal with the penetration power and linear energy transfer of a homogeneous beam of electrons passing through different layers of HAC materials, focusing mainly in two differentiated factors, the **H/C ratio** and the **density**.

The scattering cross sections (of the electrons by the material) in our calculations are obtained using the default parameters of the Monsel (Montecarlo Simulation of SEM Signals for Linewidth Metrology, Lowney, 1994) package following the fittings to empirical Mott tabulated cross sections (Mott and Massey, 1949; Czyżewski et al., 1990), adequate for medium incident energies. Scattering events are randomized and weighted as a function of the density and the H/C ratio. The elastic cross section of an electron with an atom, required for determining the trajectories of the electrons is determined as (in cm^{-2}):

$$\sigma_e = \frac{3.0 \cdot 10^{-18} Z^{1.7}}{(E + 0.005 Z^{1.7} \sqrt{E} + 0.0007 Z^2 / \sqrt{E})}, \quad (4.9)$$

with E being the incident energy of the particles and Z the atomic number of the atoms. The differential cross section has a complex expression, with contributions coming both from a screened Rutherford cross section and a cross section being an isotropic distribution. The scattering angle (θ) is determined as:

$$\cos(\theta) = 1 - \frac{2\alpha RND}{1 + \alpha - RND}, \quad (4.10)$$

where RND is a random number between 0 and 1 and $\alpha = 7 \times 10^{-3} / E$. With the scattering angle, a new propagation direction for the electrons can be defined until the next scattering event takes place. The mean free path between events is given by:

$$\lambda_e = \frac{W}{N_A \rho \sigma_e}, \quad (4.11)$$

where W is the atomic weight, N_A the Avogadro number, and ρ is the input density. In between two events, the energy loss of an electron is given by the following expression by Joy and Luo, 1989:

$$\frac{dE}{dS} = \frac{-7.85 \times 10^{-3} \rho}{E} \sum_{j=1}^n \frac{C_j Z_j}{W_j} \ln \left(1.116 \left(\frac{E_i}{J_j} + k_j \right) \right), \quad (4.12)$$

C_j being the weight fraction of the atom in consideration, J_j the mean ionization potential of such atom and k_j a statistical parameter depending on Z_j (Gauvin and L'Espérance, 1992). Each trajectory is sampled iteratively until the energy of an electron by successive scattering events is lower than 50 eV.

From the trajectories of each electron we can infer the linear energy transfer, LET, as the energy that the electrons loss in (or transfer to) the material over a certain thickness. In an incomplete processing, in which all the electrons remain in the bulk without sampling the full thickness, the LET will be defined as E/l , being l an estimation of the penetration depth obtained by inspection of the calculated electron trajectories. When the electrons either cross through or are scattered backwards and escape the material, the LET is defined as $\frac{\sum_i \alpha_i (E_0 - E_i)}{d}$. In this expression, α_i is the fraction of electrons at a certain energy that escape the material with an energy E_i , E_0 the initial energy (5 keV) and d the thickness of the sample. Usually we are involved with intermediate situations, with combination of deposited, transmitted and backscattered electrons, with the LET expressed as:

$$LET = \frac{\alpha_0 E_0 + \sum_i \alpha_i (E_0 - E_i)}{d} \quad (4.13)$$

being α_0 the fraction of electrons whose trajectory do not escape the material. As an example, Fig 4.6 show typical profiles for a simulation of an incident electron beam of 5 keV hitting a 530 nm layer with a C/H ratio of 1 and with densities of 1 gcm^{-3} and 2 gcm^{-3} , left and right, respectively. For visualization purposes only 200 trajectories are presented. In this figure, color of the segments reproduce the energy loss of each trajectory. The left hand side figure represents the situation that we have considered full processing regime, where the whole sample is processed with the electrons. The right hand side show and incomplete processing, situation that is not desirable to obtain reliable C-H destruction cross sections.

In particular, to simulate our experimental HAC, we have chosen densities of 1.0 and 1.2 gcm^{-3} , values that were taken from the literature (Godard and Dartois, 2010; Godard et al., 2011; Molpeceres et al., 2017). A C/H ratio of one was always considered although some authors also present lower bounds for this magnitude (Schwarz-Selinger, Keudell, and Jacob, 1999). We have also used the experimental determined density for our samples (Peláez et al., 2018), that is $1.1 \pm 0.1 \text{ gcm}^{-3}$ and lie within the range obtained in the previous chapter. Using Eq 4.13, we have calculated the LET at several densities along

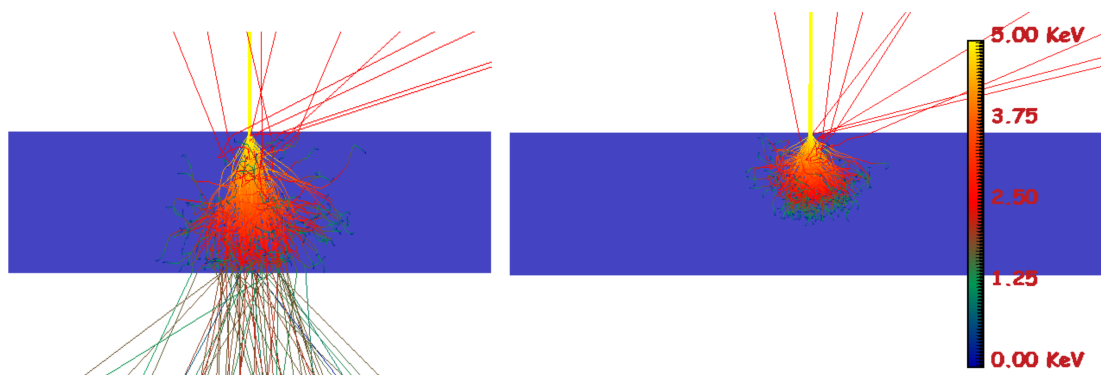


FIGURE 4.6: Classical Electron Trajectories in Different HAC Materials

with the number of electrons per escape event (transmission or backscattering). They are gathered in Table 4.2.

TABLE 4.2: LETs of the HAC materials (530 nm, C/H=1) as a function of the density using 10000 trajectories

$\rho(gcm^{-3})$	$n_{backscattered}$	$n_{transmitted}$	LET (eV/nm)
1.0	529	2231	8.55
1.1	575	875	8.95
1.2	541	66	9.11

It can be seen that the LET does not markedly depend on the density in this particular range, and that the values differ for less than a 10%. We are in all cases in full processing regime. The LET increase with density is also seen as a decrease in the number of transmitted electrons, that is related with an increase in the deposited energy. When all the energy of the 5 keV electrons is deposited in a full processed sample of 530 nm, the LET is thus $5000/530 = 9.4$ eV/nm.

One important assumption of this method to obtain the LET is that the material composition remains constant during the processing. This is a big assumption to take, since as we have mentioned in previous chapters, structures with less content of hydrogen are more likely to have higher densities. The likely density increase during the irradiation, would contribute to a higher LET, following the trend of Table 4.2, reaching the value of 9.4 eV/nm. At the light of the simulations, and with the above mentioned arguments **we have assumed this value for the LET** in our experiments.

4.3.2 HAC analogues processing

We have irradiated the 10 mm diameter exposed sample with a constant flux of 7.9×10^{12} electron. $cm^{-2}.s^{-1}$. In these experiments two different temperatures have been considered, 298 and 85 K. Fig 4.7 represents the typical spectra of our analogues after subtraction of an appropriate baseline. These kind of materials are closer to what in the last chapter we defined as "Rings and Chains" archetype, or the E1 experimental sample.

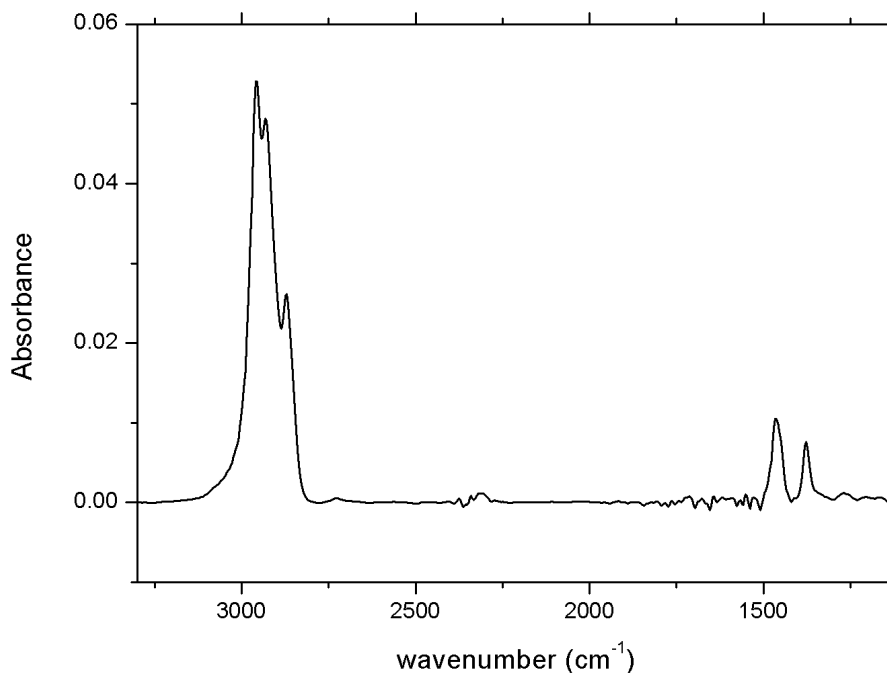


FIGURE 4.7: Infrared Spectra of our deposited HAC analogues between $3300\text{-}1100\text{ cm}^{-1}$. Sample thickness of 500 nm.

For electron processing experiments we have grown four identical samples, 460 ± 50 nm thick. This thickness was chosen to ensure that we are under the full processing regime, as exposed in the previous section. We have labeled them as S1, S2, S3 and S4. Electron processing have been done at room temperature for S2 and S4 samples and at 85 K for S1 and S3. Fig 4.8 shows the initial profile of the $3.4\text{ }\mu\text{m}$ band (top panels) along with its gaussian decomposition, that was described in the last chapter. The bottom panels of the figure show the decay of the band after six hours of electronic processing at the two different temperatures. In the bottom panels of Fig 4.8 we observe both a significant decrease in the overall band intensity and a marked change of shape, indicating a change in the dominant carriers of these vibrations, namely asymmetric stretchings.

We have performed a gaussian decomposition of all the individual vibrations blended in the C-H stretching band at certain irradiation times. As it was mentioned in chapter three, the employment of a gaussian decomposition scheme has an associated error arising from the amorphous nature of the material, not allowing us for a clear identification of the chemical composition of it. However, and assuming a constant error in the decomposition of the bands obtained during the electronic processing, we can use the gaussian fitting to extract evolution trends. We have considered the band strengths displayed in Table 3.3. The total band is decomposed as the sum of five gaussians (Chiar et al., 2013), as opposed to the six used to some authors debating about a Fermi resonance at 2928 cm^{-1} of bending modes (Dartois et al., 2007) or tertiary carbons (Allamandola et

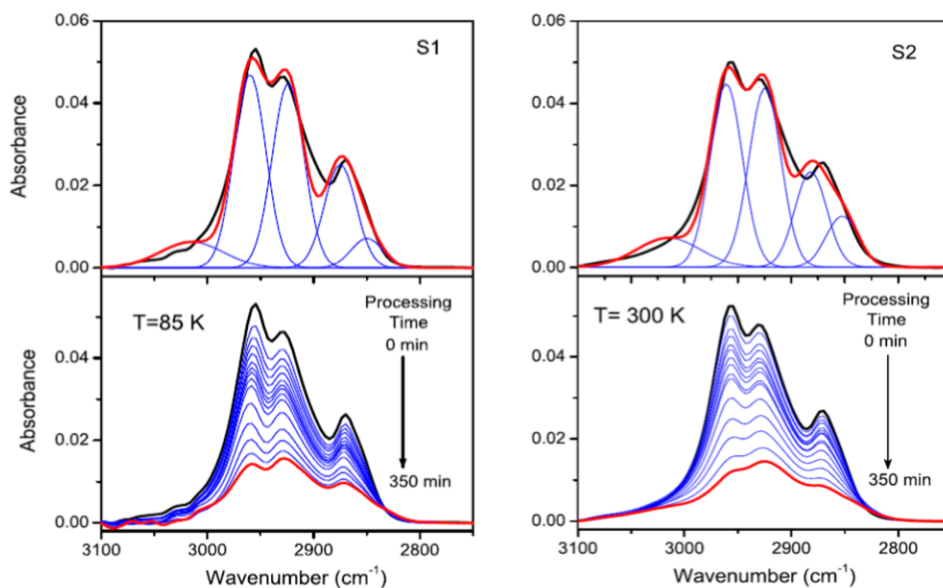


FIGURE 4.8: 3.4 μm band decrease upon processing and Gaussian deconvolution analysis such band

al., 1992). Table 4.3 show the band positions (P), widths (W) and integrated absorbance areas (I) of the decomposition analysis of the band for the four samples under investigation. The data correspond to the unprocessed samples at the temperature of the experiments.

TABLE 4.3: Band decomposition of unprocessed HAC Deposits (all in cm^{-1})

Stretch Mode	S1 (85K)			S2 (300K)			S3 (85K)			S4 (300K)		
	P	W	I	P	W	I	P	W	I	P	W	I
CH arom	3010	60	0.51	3008	60	0.55	3010	60	0.60	3010	60	0.5
CH ₃ asym	2959	30	1.83	2959	30	1.81	2960	30	1.85	2959	30	1.75
CH ₂ asym	2921	30	1.63	2922	30	1.70	2922	30	1.57	2922	30	1.57
CH ₃ sym	2876	30	0.86	2876	30	0.94	2875	30	0.75	2877	30	0.83
CH ₂ sym	2851	30	0.35	2851	30	0.33	2845	30	0.45	2853	30	0.34

P, W and I indicate gaussian position, width and area, respectively

At the light of the results shown at the bottom panel of Fig 4.8 some comments regarding selectivity of the destroyed chemical groups can be done. Peaks corresponding to CH₃ stretchings decrease faster than the ones describing primarily CH₂ vibrations. This result has a lot of sense from the statistical point of view since the dehydrogenation of a CH₃ group should be faster than the CH₂ employing simple statistical arguments of three hydrogens per group vs two hydrogens per group. Moreover, the destruction of a CH₃ group **leads to the formation of a CH₂ one** increasing that signal. Furthermore, the volume of a methyl group is higher than a methylene one, affecting to its particular destruction. This trend can be visualized in Fig 4.9 but should be taken with care due

to the mode mixing. CH_3 symmetric stretches are blended with the more intense asymmetric CH_2 feature, and thus its quantification has a very big associated error. For that reason we assume that asymmetric stretches are more reliable and less blended. Taking into account these errors only qualitative results and not real quantitative values such as particular cross sections should be extracted from here.

We have not been able to distinguish any remarkable increase of the aromatic C-H stretching band. As mentioned in the past chapter, this band has a much lower intrinsic band strength and therefore its not easy to quantify, even in the full processed sample.

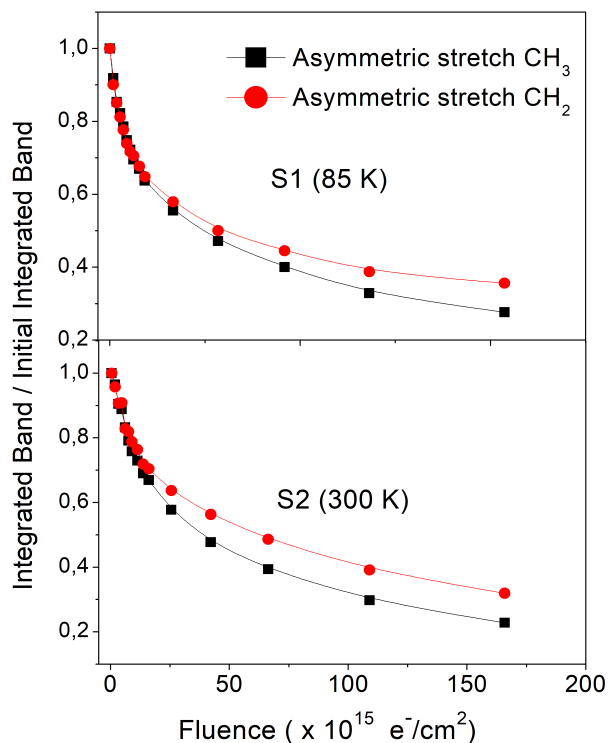


FIGURE 4.9: Asymmetric stretches $3.4 \mu\text{m}$ band decay of the HAC materials

One conclusion that remains from the results shown in Fig 4.8 is a seemingly independence of the decay with temperature. This is the same as to say that recombination of H_2 takes place very quickly.

4.3.3 Kinetic Study

We have assumed a proportionality between the hydrogen density and the integrated intensity of the C-H stretching band, making possible to rewrite eq 4.5 as follows (Gordard et al., 2011):

$$\frac{I(F)}{I_0} = \left[\frac{I_0}{I_f} + \left(1 - \frac{I_0}{I_f} \right) e^{(-\sigma_d^r F)} \right]^{-1} \quad (4.14)$$

Fig 4.10 represents the normalized decay of the total band area as a function of the fluence of electrons. Filled symbols represent experiments performed at 85 K whereas open ones represent experiments at room temperature. Solid curves show the fit using the H₂ recombination model, eq 4.5, and dashed lines the asymptotically corrected exponential fit, eq 4.1. In Fig 4.10 there are two different trends depending on the irradiation time we observe. The decay is faster at the beginning than after some irradiation time, when it enters in an asymptotic regime. From an atomistic point of view the behavior could be understood as if in the early stages of the processing the recombination of released hydrogen atoms was easier due to the lower mean distance between them. Unfortunately, we are not able to prove this affirmation experimentally, since our experimental set up configuration do not allow to detect the signal of the released H₂ molecules in the mass spectrometer. Nonetheless experimental results by other groups confirm this description (Alata et al., 2014; Martín-Doménech, Dartois, and Muñoz Caro, 2016)

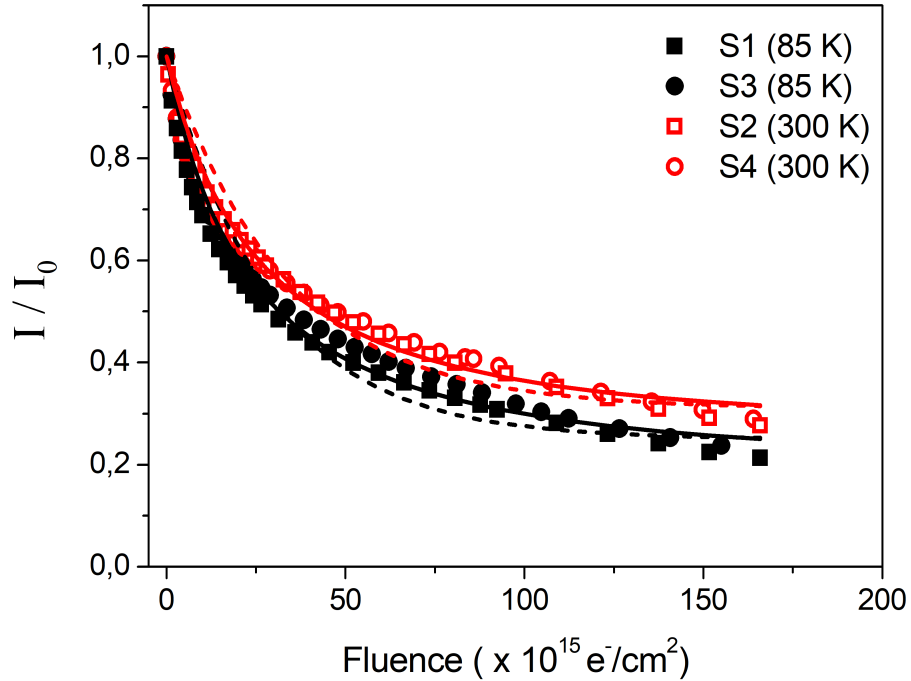


FIGURE 4.10: Total decay of the 3.4 μm band of the HAC materials

We gather in Table 4.4 our obtained values for the main parameters of each model. As advanced before, we do not find a clear dependence of our values with the temperature, and the values for the corresponding destruction cross sections vary within the experimental error. If any, the slightly higher σ_d at room temperature in the recombination model would imply a more favorable formation of H₂, intuitively due to the higher thermal budget for diffusion within the recombination volume. Again, the differences are low to confirm our suspicions.

With respect to the recombination volume, it is defined as the inverse of the density of hydrogen at the last stages of the processing $V = 1/\rho_{f,H}$. We do not have an exact value for ρ_H but we can make assumptions based on the considered density of the material (1.2 g cm^{-3}) and a hydrogen to carbon ratio of 1. Under this assumption we find $\rho_{0,H} = 5.6 \times 10^{22} \text{ cm}^{-3}$ ($V_0 = 18 \text{ \AA}$), and from the fitted curve we can obtain I_f/I_0 and thus

TABLE 4.4: Parameters for the different kinetic models employed in the fit of the e^- processing of HAC

Temperature (K)	σ_d ($\times 10^{17}$) cm^2	I_f/I_0	V \AA^3
Recombination Model			
85	1.0 ± 0.2	0.21 ± 0.02	85
298	1.2 ± 0.2	0.28 ± 0.02	64
Exponential fit			
85	3.4 ± 0.2	0.25 ± 0.02	71
298	3.0 ± 0.2	0.31 ± 0.02	57

$\rho_{f,H}$. Recombination volumes at the last stages of the processing (the ones presented in the table) are in the order of tens of angstroms, near to 10 nm^3 . This value is lower at different stages of the processing, but much more difficult to calculate, without a clear estimation of the hydrogen density. Nevertheless, these values give an insight of the mean distances for the hydrogen atoms to diffuse in Adel's (Adel et al., 1989) mechanism.

With regards to the exponential fitting, it is important to remark that it has been found to provide a fairly weak fitting with the experimental results (Godard et al., 2011) for a wide range of ions, and in our case for electrons. It provides systematically higher values than the recombination model for the destruction cross section, both in our case and in the literature. If we only fit the initial stages of the processing, before reaching $1 \times 10^{17} e^- / cm^2$ fluences, we obtain, employing eq 4.2, values on the order of $\sigma_d = 3.6 \pm 0.1 \times 10^{17} \text{ cm}^{-2}$, higher than the ones considering the asymptotic I_f/I_0 term of eq 4.2. The inclusion of the asymptotic term is needed then for obtaining meaningful results.

We have compared our results with other literature experiments (Godard et al., 2011), to inspect the validity of employing high energy electrons as cosmic rays analogues, as suggested in the bibliography (Kaiser et al., 2013; Mason et al., 2014). For doing so, we have determined the energy deposited by the electrons per unit mass of sample using the following relationship:

$$\Delta E(F) = \frac{LET * F}{\rho_{HAC}}, \quad (4.15)$$

where we have taken a LET value of 9.4 eV/nm and a ρ_{HAC} of 1.2 gcm^{-3} . The results of our comparative study are presented in Fig 4.11.

The comparison between our data and those of Godard shows similar decays for C^{5+} ions at the early stages of the processing. This allows us to confirm the viability of using e^- as processing agents mimicking CR-HAC interaction. Our data deviates from theirs for lighter and heavier ions, such as H^+ and Si^{7+} respectively. A good advantage of our measurements is that we are able to irradiate for longer times (or equivalently to deposit more energy) due to electron irradiation being an easier and cheaper technique. Longer irradiation times allow us to obtain a better fit due to a better determination of the asymptotic limit.

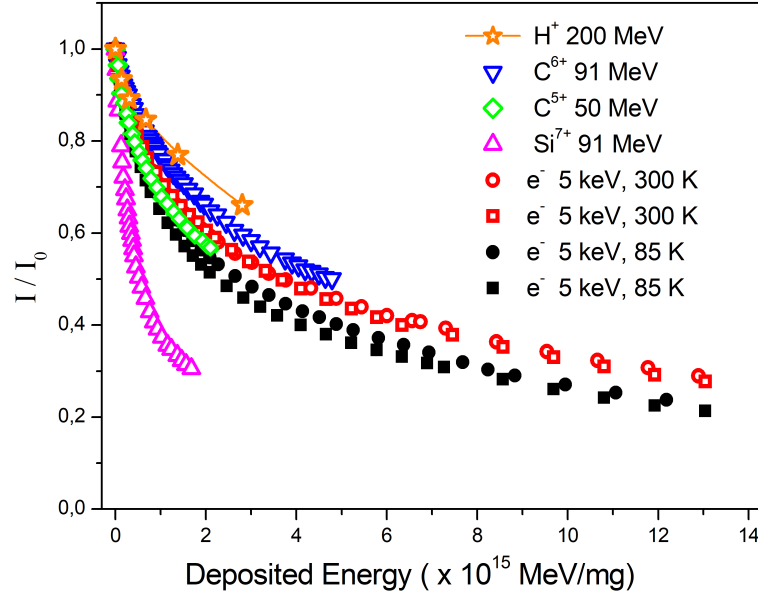


FIGURE 4.11: Normalized decay curves for the destruction of the total $3.4 \mu\text{m}$ band with high energy ions (Godard et al, 2011) and electrons (our results)

The different nature of the samples processed by Godard is also worth to be evaluated. In its paper, Godard studied three kinds of samples: a-C:H1 grown using PECVD with methane as precursor gas (similar to us), a-C:H2, grown with the same technique using butadiene as precursor and soot (1.8 g cm^{-3}), the combustion product of propylene in an O_2 atmosphere. The obtained cross sections differ within the experimental error for all the samples, showing a negligible contribution as evinced with values ranging from $\sigma_d = 3.2 \text{ (a-C:H1)} \times 10^{-16} \text{ cm}^2$ to $\sigma_d = 8.8 \text{ (a-C:H2)} \times 10^{-16} \text{ cm}^2$ for C^{6+} , for a-C:H1 and a-C:H2, respectively, with the soot in between. The dependence of the destruction cross sections with the nature of the material is lower than the one found with the type of incoming ion.

We are now in position to obtain destruction rates based in the equations presented in section 1.2.3. In all our estimations we are working in a monoenergetic proton approximation (Strazzulla and Johnson, 1991; Moore, Hudson, and Gerakines, 2001; Mennella et al., 2003). Briefly, as the name suggests, this approximation considers the effects of cosmic rays as if it were caused by an effective flux of 1 MeV protons that lead to the same ionisation rates as a discrete distribution of CR with different individual energies. We have employed the values of Mennella (Mennella et al., 2003) for the effective fluxes in dense ($f_{\text{CR}} = 1 \text{ cm}^{-2} \text{ s}^{-1}$) and diffuse ($1.8 \text{ cm}^{-2} \text{ s}^{-1}$) molecular clouds that are based on ionization rates by Spitzer (Spitzer and Tomasko, 1968). With this set of data, we employ eq 4.7, that considers a direct relationship between the stopping power and the destruction cross section. Stopping powers for cosmic rates are extracted from the literature $S_p(1\text{MeV}) = 0.262 \text{ MeV mg}^{-1} \text{ cm}^2$ (Godard et al., 2011) for materials with similar composition to ours (C/H ratio of 1), using the SRIM code (Ziegler, Ziegler, and Biersack, 2010). Our stopping power is calculated as $S_e(5\text{keV}) = \text{LET}/\rho_{\text{HAC}} = 7.9 \times 10^{-2} \text{ MeV mg}^{-1} \text{ cm}^2$. Substituting all of our values in eq 4.7 we obtain our results for diffuse

molecular clouds (Table 4.5).

TABLE 4.5: Extrapolated e^- - Cosmic rays destruction rates in diffuse clouds under the monoenergetic proton approximation for our HAC samples

Sample T K	R_d Recombination s^{-1}	R_d Exponential s^{-1}
85	7.0×10^{-17}	2.0×10^{-16}
300	5.9×10^{-17}	1.8×10^{-16}

The conclusions with respect to the destruction rates are equivalent to the ones for the cross sections. The exponential model always provide higher values than the recombination one, with or without the asymptotic limit. Again, a comparison with the two archetypical literature values (Mennella et al., 2003; Godard et al., 2011) is held in Table 4.6.

TABLE 4.6: Literature Comparison of Cosmic Rays C-H destruction Rates

Source	$R_d s^{-1}$
85 K This work	7.0×10^{-17} (Recomb), 2.0×10^{-16} (Exp)
300 K This work	5.9×10^{-17} (Recomb), 1.8×10^{-16} (Exp)
Mennella et al (2003)	1.7×10^{-15}
Godard et al (2011)	3.0×10^{-17} - 3.3×10^{-16}

The values of Godard consider an explicit dependence on the type of ion used as a CR analogue, modifying accordingly the cross sections using the expression $\sigma_d = KS^\alpha$ with K and α being two constants. In any case, from our results (hereafter we assume a temperature independence for the discussion) we have a good degree of agreement between our results and the ones of Godard. Our results lie, with independence of the fitting model within his proposed destruction rates. This again, arises the conclusion of the validity of employing high energy electrons as CR analogues. Of course, we are not in a position to distinguish the subtleties that arise from the processing of a discrete distribution of ions, with each one of them depositing a different amount of energy and yielding different destruction rates. In the bright part, experiments with electrons allow for higher irradiation times, allowing for a better fit of the experimental data with a better description of the asymptotic regime.

However, our values are in disagreement with the ones of Mennella (Mennella et al., 2003) by a factor of one order of magnitude more or less. The origin of this disagreement is not clear. Mennella employs He^+ ions as processing ions along with condensation of vaporized graphite rods in a hydrogen atmosphere and hydrogenation of laser ablated carbon electrodes for the preparation of the samples. These two factors, could yield different values even though we have already mentioned that the nature of the sample should not yield enough variability. Perhaps the combination of the two factors can lead to more accused variations, as presented in the general review of (Compagnini and Calcagno, 1994). In any case, we are not in a position to pinpoint a precise reason for such discrepancy.

4.4 Astrophysical Implications

From an astrophysical point of view destruction rates are less visual than C-H characteristic times of destruction, representing the time needed for the total destruction of a material. These characteristic times are calculated as the inverse of the destruction rates (eq 4.8).

The main purpose of the study presented in this chapter is the disappearance of the 3.4 μm band in dense molecular clouds. The factors behind such disappearance have been enumerated in the introduction section. As mentioned there, the mechanism of destruction is not well understood given the shielding of the galactic UV photons field in dense molecular clouds. It is true that the penetration of these photons is not entirely known and clearly depends on the dust properties (Howe et al., 1991; Goicoechea and Le Bourlot, 2007). Nonetheless, the so called secondary UV field (Prasad and Tarafdar, 1983; Cecchi-Pestellini and Aiello, 1992) generated due to cosmic ray excitation of different molecular and atomic systems is present, and acts in addition to the direct processing by cosmic rays. However, this secondary field is up to three orders of magnitude lower ($10^4 \text{ cm}^{-2}\text{s}^{-1}$) (Prasad and Tarafdar, 1983; Dopita and Sutherland, 2003) than the primary field ($8 \times 10^7 \text{ cm}^{-2}\text{s}^{-1}$) (Mathis, Mezger, and Panagia, 1983) in diffuse clouds. In addition, in dense molecular clouds, the appearance of layers of ice on top of the grains (Cuppen and Herbst, 2007) also takes part of the energy of the UV photons, with small penetration depths. **This leaves CR processing as the hypothetical main mechanism to account for the destruction of C-H bonds in core grains of carbonaceous material.**

Cosmic Rays (and UV photons by Mennella et al., 2001) characteristic times for the destruction of carbonaceous materials in diffuse and dense clouds are presented in Table 4.7:

TABLE 4.7: Characteristic times for C-H bond destruction by cosmic rays and UV photons in dense and diffuse clouds

Work	Characteristic Time (yr)	
	Diffuse Media A_v (mag) $< 10^{-4}$	Dense Media A_v (mag) > 3
	CH Destruction by Cosmic Rays	
Our Values	$2\text{-}5 \times 10^8$	$3\text{-}9 \times 10^8$
Mennella et al (2003)	2×10^7	3×10^7
Godard et al (2011)	$10^9 - 10^9$	$(3\text{-}9) \times 10^8$
	CH Destruction by UV Photons	
Mennella et al (2001)	4×10^3	$>10^7$

Our results, in accordance with the ones of Godard, lie beyond the expected lifetimes of dense clouds, that has been estimated to be in the order of 4×10^7 years (Jones et al., 1994). Under this assumption, by the time our mechanism is able to destroy all C-H bonds to not be perceptible by IR spectroscopy, there should not be any dense cloud anymore. **The characteristic times of destruction exceed the characteristic times of a dense cloud under this assumptions.** Mennella et al, on the other hand, provides values that are reasonable within the expected lifetimes of the object both with CR and UV

photons. Data on the literature are seemingly contradictory, and although our results are in clear accordance with the Godard's ones, additional laboratory data is required in order to elucidate the real mechanisms operating behind the disappearance of such bands in dense media.

It has been previously mentioned that the $3.4 \mu\text{m}$ band in diffuse clouds is in equilibrium between formation and destruction of CH groups via hydrogenation and dehydrogenation. The characteristic times of formation and destruction are enough to account for such equilibrium in diffuse clouds in 10^4 years (Mennella et al., 2002), within the cloud. In dense clouds however, the formation and destruction mechanism are completely different, being inhibited in the former and severely attenuated in the latter. In this context, CR are of paramount importance, but not enough at the light of our results. In addition to CR and the secondary UV field, a much more difficult to quantify effect is the penetration of the primary galactic UV field, that is usually considered as vanished (Chiar et al., 2013). This, in fact may be concomitant with the more important impact of the cosmic rays. It has been suggested in recent reviews that in the interphase between the diffuse and the dense clouds (translucent clouds), hydrogenation rates could be lowered and CH bond breaking would prevail, leading to a already pre processed material by the time it is incorporated into a dense cloud (Jones et al., 2013; Jones et al., 2014). This attenuation of the hydrogenation rates could appear for extinction values as high as $A_v = 0.01$.

References

- Adel, M. E., O. Amir, R. Kalish, and L. C. Feldman (1989). "Ion-beam-induced hydrogen release from a-C:H: A bulk molecular recombination model". In: *Journal of Applied Physics* 66.7, pp. 3248–3251.
- Alata, I., G. A. Cruz-Diaz, G. M. Muñoz Caro, and E. Dartois (2014). "Vacuum ultraviolet photolysis of hydrogenated amorphous carbons". In: *Astronomy & Astrophysics* 569, A119.
- Alata, I., A. Jallat, L. Gavilan, M. Chabot, G. A. Cruz-Diaz, G. M. Muñoz Caro, K. Béroff, and E. Dartois (2015). "Vacuum ultraviolet of hydrogenated amorphous carbons". In: *Astronomy & Astrophysics* 584, A123.
- Allamandola, L. J., S. A. Sandford, A. G. G. M. Tielens, and T. M. Herbst (1992). "Infrared spectroscopy of dense clouds in the C-H stretch region - Methanol and 'diamonds'". In: *The Astrophysical Journal* 399, p. 134.
- Cecchi-Pestellini, C. and S. Aiello (Sept. 1992). "Cosmic ray induced photons in dense interstellar clouds". In: *Monthly Notice of the Royal Astronomical Society* 258, pp. 125–133.
- Chiar, J. E., A. J. Adamson, Y. J. Pendleton, D. C. B. Whittet, D. A. Caldwell, and E. L. Gibb (2002). "Hydrocarbons, Ices, and "XCN" in the Line of Sight toward the Galactic Center". In: *The Astrophysical Journal* 570.1, pp. 198–209.
- Chiar, J. E., A. J. Adamson, D. C. B. Whittet, A. Chrysostomou, J. H. Hough, T. H. Kerr, R. E. Mason, P. F. Poche, and G. Wright (2006). "Spectropolarimetry of the 3.4 micron Feature in the Diffuse ISM toward the Galactic Center Quintuplet Cluster". In: *The Astrophysical Journal* 651.1, pp. 268–271. arXiv: 0607245 [astro-ph].

- Chiar, J. E., A. G.G.M. Tielens, A. J. Adamson, and A. Ricca (2013). "The structure, origin, and evolution of interstellar hydrocarbon grains". In: *Astrophysical Journal* 770.1, p. 78.
- Compagnini, Giuseppe and Lucia Calcagno (1994). *Structural disorder in ion irradiated carbon materials*.
- Cuppen, H. M. and Eric Herbst (2007). "Simulation of the Formation and Morphology of Ice Mantles on Interstellar Grains". In: *The Astrophysical Journal* 668.1, pp. 294–309. arXiv: 0707.2744.
- Czyżewski, Zbigniew, Danny O'Neill MacCallum, Alton Romig, and David C. Joy (1990). "Calculations of Mott scattering cross section". In: *Journal of Applied Physics* 68.7, pp. 3066–3072.
- Dartois, E., G. M. Muñoz Caro, D. Deboffle, G. Montagnac, and L. D'Hendecourt (2005). "Ultraviolet photoproduction of ISM dust". In: *Astronomy and Astrophysics* 432, pp. 895–908.
- Dartois, E., T. R. Geballe, T. Pino, A.-T. Cao, A. Jones, D. Deboffle, V. Guerrini, Ph. Bréchignac, and L. D'Hendecourt (2007). "IRAS 08572+3915: constraining the aromatic versus aliphatic content of interstellar HACs". In: *Astronomy and Astrophysics* 463.2, pp. 635–640.
- Dartois, E, M Chabot, T Pino, K Béro, M Godard, D Severin, M Bender, and C Trautmann (2017). "Astrophysics Swift heavy ion irradiation of interstellar dust analogues Small carbonaceous species released by cosmic rays". In: *Astronomy & Astrophysics* 599, A130.
- Demers, Hendrix, Nicolas Poirier-Demers, Alexandre Réal Couture, Dany Joly, Marc Guilmain, Niels De Jonge, and Dominique Drouin (2011). "Three-dimensional electron microscopy simulation with the CASINO Monte Carlo software". In: *Scanning* 33.3, pp. 135–146.
- Dopita, M. A. and R. S. Sutherland (2003). *Astrophysics of the diffuse universe*.
- Drouin, Dominique, Alexandre Réal Couture, Dany Joly, Xavier Tastet, Vincent Aimez, and Raynald Gauvin (2007). "CASINO V2.42 - A fast and easy-to-use modeling tool for scanning electron microscopy and microanalysis users". In: *Scanning* 29.3, pp. 92–101.
- Duley, W. W. and D. A. Williams (July 1981). "The infrared spectrum of interstellar dust - Surface functional groups on carbon". In: 196, pp. 269–274.
- Duley, W. W. and D. A. Williams (1983). "A 3.4 micron absorption band in amorphous carbon Implications for interstellar dust". In: *MNRAS* 205.1, 67P–70P.
- Fonfria, J. P., J. Cernicharo, M. J. Richter, and J. H. Lacy (2008). "A Detailed Analysis of the Dust Formation Zone of IRC +10216 Derived from Mid-Infrared Bands of C 2 H 2 and HCN". In: *The Astrophysical Journal* 673.1, pp. 445–469. arXiv: 0709.4390.
- Fonfría, J. P., M. Agúndez, J. Cernicharo, M. J. Richter, and J. H. Lacy (2017). "Carbon chemistry in IRC+10216: Infrared detection of diacetylene". In: *The Astrophysical Journal* 852.2, p. 80. arXiv: 1711.10926.
- Gaisser, T. K., T. Stanev, and S. Tilav (2013). "Cosmic ray energy spectrum from measurements of air showers". In: *Frontiers of Physics* 8.6, pp. 748–758.
- Gauvin, Raynald and Gilles L'Espérance (1992). "A Monte Carlo code to simulate the effect of fast secondary electrons on κ AB factors and spatial resolution in the TEM". In: *Journal of Microscopy* 168.2, pp. 153–167.

- Gerakines, Perry A., Reggie L. Hudson, Marla H. Moore, and Jan-Luca Bell (2012). "In situ measurements of the radiation stability of amino acids at 15–140K". In: *Icarus* 220.2, pp. 647–659.
- Godard, M. and E. Dartois (2010). "Photoluminescence of hydrogenated amorphous carbons". In: *Astronomy and Astrophysics* 519, A39.
- Godard, M., G. Féraud, M. Chabot, Y. Carpentier, T. Pino, R. Brunetto, J. Duprat, C. Engrand, P. Bréchnignac, L. D'Hendecourt, and E. Dartois (2013). "Effects of cosmic rays on hydrocarbon interstellar dust". In: *EAS Publications Series* 58.2012, pp. 395–398.
- Godard, Marie, G. Féraud, Marin Chabot, Yvain Carpentier, Thomas Pino, Rosario Brunetto, Jean Duprat, C. Engrand, P. Bréchnignac, L. D'Hendecourt, and Emmanuel Dartois (2011). "Ion irradiation of carbonaceous interstellar analogues - Effects of cosmic rays on the 3.4 micron interstellar absorption band". In: *Astronomy & Astrophysics* 529.16228, A146.
- Goicoechea, J. R. and J. Le Bourlot (2007). "The penetration of Far-UV radiation into molecular clouds". In: *Astronomy & Astrophysics* 467.1, pp. 1–14. arXiv: [0702033 \[astro-ph\]](#).
- Henning, Th and F. Salama (1998). *Carbon in the universe*.
- Howe, J. E., D. T. Jaffe, R. Genzel, and G. J. Stacey (May 1991). "Parsec-scale penetration of ultraviolet photons into molecular clouds - (C II) 158 micron mapping of W3, NGC 1977, and NGC 2023". In: 373, pp. 158–168.
- Joblin, C., A. G.G.M. Tielens, L. J. Allamandola, A. Léger, L. D'Hendecourt, T. R. Geballe, and P. Boissel (1995). "PAHs as the carriers of the 3.3 and 3.4 μm emission bands". In: *Planetary and Space Science* 43.10-11, pp. 1189–1194.
- Jones, A. P., L. Fanciullo, M. Köhler, L. Verstraete, V. Guillet, M. Bocchio, and N. Ysard (2013). "The evolution of amorphous hydrocarbons in the ISM: dust modelling from a new vantage point". In: *Astronomy & Astrophysics* 558, A62. arXiv: [1411.6293](#).
- Jones, Anthony, A G. G. M. Tielens, D J. Hollenbach, and Christopher Mckee (Nov. 1994). "Grain destruction in shocks in the interstellar medium". In: *The Astrophysical Journal* 433, pp. 797–810.
- Jones, Anthony P., Nathalie Ysard, Melanie Köhler, Lapo Fanciullo, Marco Bocchio, Elisabetta Micelotta, Laurent Verstraete, and Vincent Guillet (2014). "The cycling of carbon into and out of dust". In: *Faraday Discussions* 168.0, pp. 313–326. arXiv: [1411.5877](#).
- Jones, Brant M, Fangtong Zhang, Ralf I Kaiser, Adeel Jamal, Alexander M Mebel, Martin A Cordiner, and Steven B Charnley (2011). "Formation of benzene in the interstellar medium". In: *Proceedings of the National Academy of Sciences* 108.2, pp. 452–457.
- Joy, D. C. and S. Luo (1989). "An empirical stopping power relationship for low-energy electrons". In: *Scanning* 11.4, pp. 176–180.
- Kaiser, R. I., A. M. Stockton, Y. S. Kim, E. C. Jensen, and R. A. Mathies (2013). "On the formation of dipeptides in interstellar model ices". In: *Astrophysical Journal* 765.2, p. 111.
- Kondo, Toru, Hidehiro Kaneda, Shinki Oyabu, Daisuke Ishihara, Tatsuya Mori, Mitsuyoshi Yamagishi, Takashi Onaka, Itsuki Sakon, and Toyoaki Suzuki (2012). "The central region of the barred spiral galaxy NGC1097 probed by AKARI near-infrared spectroscopy". In: *Astrophysical Journal Letters* 751.1, p. L18. arXiv: [1204.5270](#).
- Lowney, Jeremiah. R (1994). *User's Manual for the Program MONSEL-1: Montecarlo Simulation of SEM Signals for Linewidth Metrology*. NIST Publications. ISBN: 3019753058.

- Martín-Doménech, R., E. Dartois, and G. M. Muñoz Caro (2016). "Vacuum ultraviolet photolysis of hydrogenated amorphous carbons". In: *Astronomy & Astrophysics* 591, A107.
- Mason, Nigel J., Binukumar Nair, Sohan Jheeta, and Ewelina Szymańska (2014). "Electron induced chemistry: a new frontier in astrochemistry". In: *Faraday Discuss.* 168 (0), pp. 235–247.
- Maté, B., I. Tanarro, R. Escribano, M. A. Moreno, and V. J. Herrero (2015). "STABILITY OF EXTRATERRESTRIAL GLYCINE UNDER ENERGETIC PARTICLE RADIATION ESTIMATED FROM 2 keV ELECTRON BOMBARDMENT EXPERIMENTS". In: *Astrophysical Journal* 806.2, p. 151.
- Maté, Belén, Isabel Tanarro, Miguel A. Moreno, Miguel Jiménez-Redondo, Rafael Escribano, and Víctor J. Herrero (2014). "Stability of carbonaceous dust analogues and glycine under UV irradiation and electron bombardment". In: *Faraday Discuss.* 168.0, pp. 267–285.
- Maté, Belén, Germán Molpeceres, Miguel Jiménez-Redondo, Isabel Tanarro, and Víctor J. Herrero (2016). "High-Energy Electron Irradiation of Interstellar Carbonaceous Dust Analogs: Cosmic-Ray Effects on the 3.4 μ m absorption band". In: *The Astrophysical Journal* 831.1, p. 51.
- Mathis, J. S., P. G. Mezger, and N. Panagia (Nov. 1983). "Interstellar radiation field and dust temperatures in the diffuse interstellar matter and in giant molecular clouds". In: 128, pp. 212–229.
- Mauney, Christopher M. and Davide Lazzati (2016). "Formation and properties of astrophysical carbonaceous dust". In: *Planetary and Space Science* 133. Cosmic Dust VIII, pp. 31–35.
- Mennella, V. (2006). "Activation energy of CH bond formation in C grains irradiated with hydrogen atoms". In: *The Astrophysical Journal* 647.1, p. L49.
- Mennella, V., J. R. Brucato, L. Colangeli, and P. Palumbo (1999). "Activation of the 3.4 Micron Band in Carbon Grains by Exposure to Atomic Hydrogen". In: *The Astrophysical Journal Letters* 524.1, p. L71.
- Mennella, V., G M Mu, G M M Caro, R. Ruitenkamp, W. A. Schutte, J. M. Greenberg, J. R. Brucato, and L. Colangeli (2001). "UV photodestruction of CH bonds and the evolution of the 3.4 μ m feature carrier II. The case of hydrogenated carbon grains". In: *ASTRONOMY & ASTROPHYSICS* 367.1, pp. 355–361.
- Mennella, V., J. R. Brucato, L. Colangeli, and P. Palumbo (2002). "C–H Bond Formation in Carbon Grains by Exposure to Atomic Hydrogen: The Evolution of the Carrier of the Interstellar 3.4 Micron Band". In: *The Astrophysical Journal* 569.Irs 7, pp. 531–540.
- Mennella, V, G A Baratta, A Esposito, G Ferini, and Y J Pendleton (2003). "The Effects of Ion Irradiation on the Evolution of the Carrier of the 3.4 Micron Interstellar Absorption Band". In: *The Astrophysical Journal* 587.2, p. 727.
- Mennella, V, J Brucato, Luigi Colangeli, and P. Palumbo (Dec. 2008). "C-H Bond Formation in Carbon Grains by Exposure to Atomic Hydrogen: The Evolution of the Carrier of the Interstellar 3.4 Micron Band". In: 569, p. 531.
- Molpeceres, Germán, Vicente Timón, Miguel Jiménez-Redondo, Rafael Escribano, Belén Maté, Isabel Tanarro, and Víctor J Herrero (2017). "Structure and infrared spectra of hydrocarbon interstellar dust analogs". In: *Physical Chemistry Chemical Physics* 19.2, pp. 1352–1360.

- Moore, M. H., R. L. Hudson, and P. A. Gerakines (Mar. 2001). "Mid- and far-infrared spectroscopic studies of the influence of temperature, ultraviolet photolysis and ion irradiation on cosmic-type ices". In: *Spectrochimica Acta Part A: Molecular Spectroscopy* 57, pp. 843–858.
- Mott, N. F. and H. S. W. Massey (1949). *The theory of atomic collisions*.
- Peláez, R J, B Maté, I Tanarro, G Molpeceres, M Jiménez-Redondo, V Timón, R Escribano, and V J Herrero (2018). "Plasma generation and processing of interstellar carbonaceous dust analogs". In: *Plasma Sources Science and Technology* 27.3, p. 035007.
- Pendleton, Yvonne J., S. a. Sandford, L. J. Allamandola, A. G. G. M. Tielens, and K. Sellgren (1994). "Near-infrared absorption spectroscopy of interstellar hydrocarbon grains". In: *The Astrophysical Journal* 437, pp. 683–696.
- Potapov, Alexey, Cornelia Jäger, Thomas Henning, Mindaugas Jonusas, and Lahouari Krim (2017). "The Formation of Formaldehyde on Interstellar Carbonaceous Grain Analogs by O/H Atom Addition". In: *The Astrophysical Journal* 846.2, p. 131.
- Prasad, S. S. and S. P. Tarafdar (Apr. 1983). "UV radiation field inside dense clouds - Its possible existence and chemical implications". In: 267, pp. 603–609.
- Sandford, S. A., L. J. Allamandola, A. G. G. M. Tielens, K. Sellgren, M. Tapia, and Y. Pendleton (Apr. 1991). "The Interstellar C-H Stretching Band near 3.4 Microns: Constraints on the Composition of Organic Material in the Diffuse Interstellar Medium". In: *The Astrophysical Journal* 371, p. 607.
- Schwarz-Selinger, T., A. von Keudell, and W. Jacob (1999). "Plasma chemical vapor deposition of hydrocarbon films: The influence of hydrocarbon source gas on the film properties". In: *Journal of Applied Physics* 86.7, p. 3988.
- Snow, Theodore P. and Benjamin J. McCall (2006). "Diffuse Atomic and Molecular Clouds". In: *Annual Review of Astronomy and Astrophysics* 44.1, pp. 367–414.
- Spitzer Jr., L. and M. G. Tomasko (June 1968). "Heating of H I Regions by Energetic Particles". In: 152, p. 971.
- Strazzulla, G. and R. E. Johnson (1991). "Irradiation effects on comets and cometary debris". In: *IAU Colloq. 116: Comets in the post-Halley era*. Ed. by R. L. Newburn Jr., M. Neugebauer, and J. Rahe. Vol. 167. Astrophysics and Space Science Library, pp. 243–275.
- Sugai, H., S. Yoshida, and H. Toyoda (1989). "Hydrogen retention and release dynamics of amorphous carbon films exposed to a hydrogen plasma". In: *Applied Physics Letters* 54.15, pp. 1412–1414.
- Whittet, D. C. B., A. C. A. Boogert, P. A. Gerakines, W. Schutte, A. G. G. M. Tielens, Th. de Graauw, T. Prusti, E. F. van Dishoeck, P. R. Wesselius, and C. M. Wright (1997). "Infrared Spectroscopy of Dust in the Diffuse Interstellar Medium toward Cygnus OB2 No. 12". In: *The Astrophysical Journal* 490.2, pp. 729–734.
- Whittet, D. C. B., P. A. Gerakines, J. H. Hough, and S. S. Shenoy (2001). "Interstellar Extinction and Polarization in the Taurus Dark Clouds: The Optical Properties of Dust near the Diffuse/Dense Cloud Interface". In: *The Astrophysical Journal* 547.2, pp. 872–884.
- Wickramasinghe, D. T. and D. A. Allen (1980). "The 3.4- μ m interstellar absorption feature". In: *Nature* 287.5782, pp. 518–519.
- Ziegler, James F., M. D. Ziegler, and J. P. Biersack (2010). "SRIM - The stopping and range of ions in matter". In: *Nuclear Instruments and Methods in Physics Research, Section B: Beam Interactions with Materials and Atoms* 268.11-12, pp. 1818–1823.

Chapter 5

Surface Reactions on Dust Grains: Water formation over Forsterite

Until now we have dealt with structural and spectroscopic properties of carbonaceous dust chemical analogues. We have used these properties to study the destruction of HAC by cosmic rays in dense molecular clouds in the past chapter.

The information we have extracted is all made on the basis of statistical properties since hydrogenated amorphous carbon materials show different, but similar responses to the same stimuli. It is because of this that univocal relationships are difficult to establish and clearly depend on the nature of the sample (growth conditions for the plasma polymerization, gaussian decomposition scheme, etc) or of the model (pre screening, guess of density etc).

In this chapter we shift our focus from interstellar amorphous materials to crystalline ones. The use of crystalline materials is an advantage from the methodological point of view, and allows us to extract quantitative results in reactivity without the need of a complex configurational sampling. This chapter will be dedicated to the study of atom addition reactions on top of a validated interstellar crystalline surface. The results of this chapter arise from a stay with Dr. Albert Rimola of the Autonomous University of Barcelona. These results have been gathered and recently published in the MNRAS paper of name "Silicate-mediated interstellar water formation: A theoretical study" (Molpeceres et al., 2019).

Quantum chemistry calculations on dust analogues can help to unravel the various physical and chemical processes occurring in the interstellar medium. We dedicate the last chapter of the thesis to study a process in which interstellar dust is an actor in the complex chemistry play. Until now we have focused in the nature of the chemical analogue of the grain and in its robustness in ISM conditions. Now we are speaking about its role in the interstellar chemistry employing silicates as chemical analogues. It is our firm intention to transfer the acquired knowledge to the study of processes in carbonaceous material in a near future.

5.1 Introduction

Water presence in the Interstellar Medium has been always a matter of intense research for obvious reasons. Water is undoubtedly one of the most important molecules, associated with many biochemical processes and its presence in extraterrestrial conditions is an attractive topic to discuss.

Literature about water in the interstellar medium is abundant, and as old as the field of astrochemistry, with modeling studies dating from nearly 50 years ago (Herbst and Klemperer, 1973). For a recent general purpose review, we encourage the reader to take a look at Van Dishoeck, Herbst, and Neufeld, 2013. Water, along with carbon monoxide, constitutes the main component of interstellar solid bodies in the form of ice (Gillett and Forrest, 1973; Whittet et al., 1988; Dishoeck, 2011; Vidali, Jing, and He, 2013) and it is present in many reaction networks in the gas phase. Water is thought to be the main oxygen bearing species in star forming regions which implies a low atomic oxygen budget for the formation of more complex molecules (Dishoeck, 2011; Van Dishoeck, Herbst, and Neufeld, 2013). Water is also an effective coolant in hot regions, as in star forming regions. This is why water molecule lines are employed as tracers of the chemical evolution and star formation in distant regions (Omont et al., 2011; Liu et al., 2017). The importance of water is even higher when considering its relevance in astrobiology, acting as the first and foremost criterion for the study of habitability of exo-planets (Dishoeck, 2011; Liu et al., 2017).

Chemical mechanisms for the formation of water are a mandatory input parameter across several topics in astrophysics. Traditional low temperature ion-molecule reactions and neutral-neutral reactions happening in hot gas regions (Hollenbach and McKee, 1989; Van Dishoeck, Herbst, and Neufeld, 2013) do not provide a successful explanation when it comes to simulate the abundances observed using radioastronomy. There exists a clear need to expand the chemical scope of those networks to include the study of water formation on top of solid surfaces, not only on bare grains but also ice mantles on top of them. An excellent review concerning water formation processes on top of surfaces can be found in (Hama and Watanabe, 2013) whereas a pictorial description of the main channels of water formation is depicted in Fig 5.1.

The different reaction channels have been studied experimentally. The prevalence of different pathways is not always a direct consequence of the efficiency of that path (evinced by the magnitude of the formation rate constant), but also by the conditions of the astronomical object of interest. In this way, molecular processes on top of ices, are characteristic of cold, radiation shielded regions, such as dense molecular clouds. Archetypal reactions for the formation of water from molecular precursors are the hydrogenation of molecular oxygen (O_2), corresponding to the central path in Fig 5.1 (Oba et al., 2009; Ioppolo et al., 2010; Cuppen et al., 2010; Jing et al., 2013) or the hydrogenation of atomic oxygen (Dulieu et al., 2010; Jing et al., 2011; Jing et al., 2013; Lamberts et al., 2014). The other path is the hydrogenation of ozone (O_3) (Mokrane et al., 2009; He, Jing, and Vidali, 2014), shown in the right hand side of Fig 5.1. In dense molecular clouds, hydrogenation via H_2 : $H_2 + O \rightarrow OH + H$ and $H_2 + O \rightarrow H_2O$ is also a feasible mechanism considering quantum tunneling of the hydrogen molecule (Oba et al., 2012; Taquet et al., 2013), although the $H_2 + O \rightarrow OH + H$ is an endothermic pathway

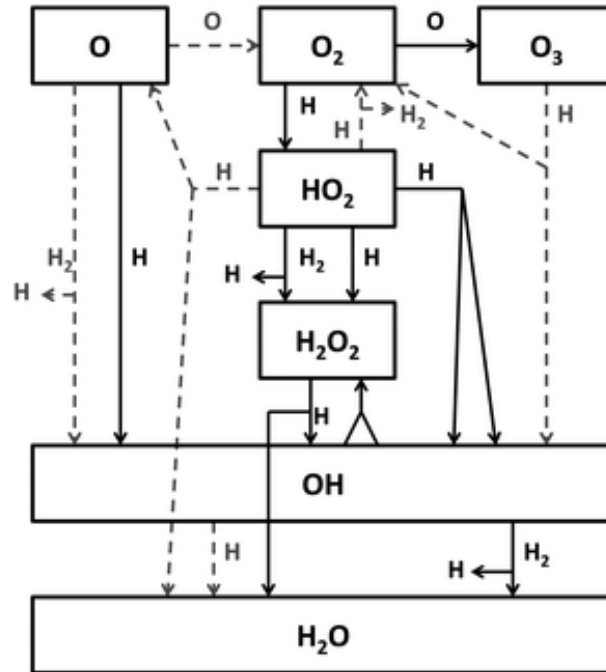


FIGURE 5.1: General scheme for the reaction network leading to the formation of interstellar H_2O .

Extracted from Cuppen et al., 2010

(Oba et al., 2012) and is generally discarded in favor of the second one $\text{H}_2 + \text{O} \rightarrow \text{H}_2\text{O}$ (Lamberts et al., 2014).

In this work we are interested in the hydrogenation of atomic oxygen in a two step mechanism via a two successive incoming hydrogen atoms:



Very recently the subject of theoretical determination of the water formation mechanism in the ISM has been subject of renewed attention (Meisner, Lamberts, and Kästner, 2017; Lamberts and Kästner, 2017), mainly on top of other ice surfaces, instead of bare silicate grains. Several authors have considered and derived the adsorption potentials of H_2O and OH (De Leeuw et al., 2000; King et al., 2010; Prigiobbe, Suarez Negreira, and Wilcox, 2013) on top of silicate surfaces but the calculation of kinetic rate constants is much less common. As a reference paper, we follow the work by Goumans et al., 2009 based on QM/MM calculation in a large forsterite cluster using up to 34 quantum mechanical atoms for the description of the reactivity and the rest treated at the molecular mechanics level. They reported activation energies of 6.2 kcal/mol and 5.2 kcal/mol for reactions 5.1 and 5.2, respectively.

The ultimate goal of our work is to provide thermodynamic and kinetic data to be used in gas-grain chemical network databases, to improve the abundances predicted by astrochemical models and ultimately to help in the rationalization of astronomical derived abundances. In this work we have employed a periodic surface derived from forsterite (Mg_2SiO_4), a positively identified crystalline silicate (Zolensky et al., 2006; Henning, 2010). Amorphous and crystalline silicates IR bands correlate with water infrared absorption bands (Boogert, Gerakines, and Whittet, 2015). See Fig 5.2.

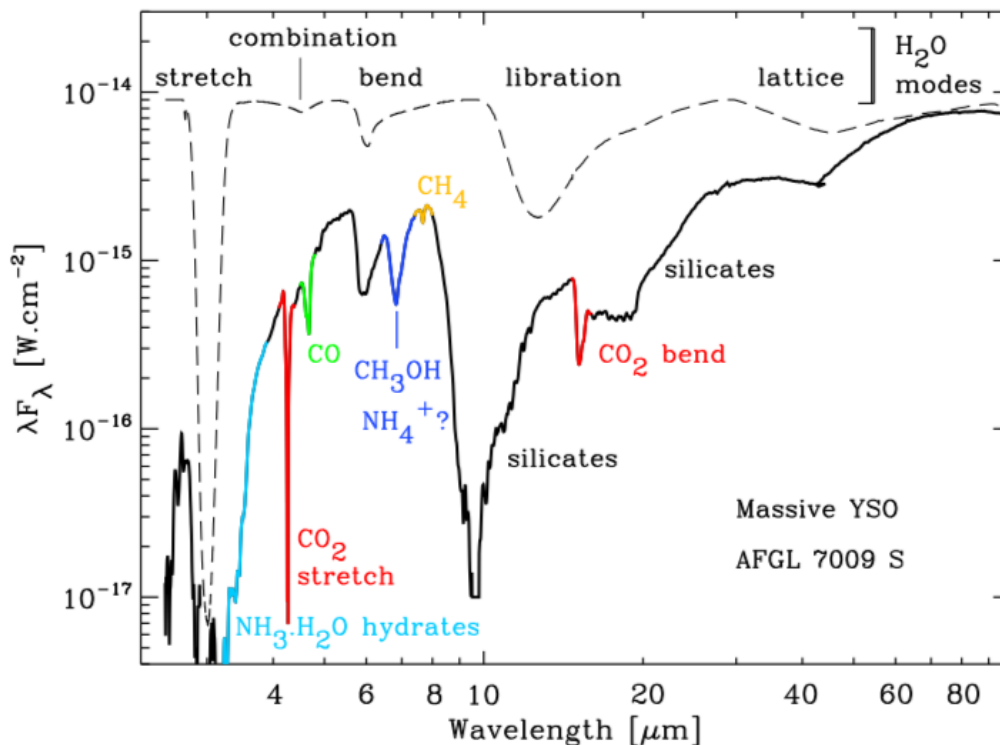


FIGURE 5.2: Dust and Ice IR spectra of MYSO AFGL 7009S
Extracted from Boogert, Gerakines, and Whittet, 2015

All these positive identifications impel us to test the reactions 5.1 and 5.2 on top of the (010) surface of the above mentioned material, a surface extensively validated in previous works by the group of Dr. Rimola (Navarro-Ruiz et al., 2014b; Navarro-Ruiz et al., 2014a; Navarro-Ruiz et al., 2015) and the most stable forsterite surface (Goumans et al., 2009; Navarro-Ruiz et al., 2014a). We expect our results to provide an atomistic scale interpretation of the formation of the initial stages of a water ice mantle (hereafter proto-ice mantle) in cold regions with enough density of energetic particles to maintain oxygen in its atomic form, at the boundary between diffuse and dense molecular clouds, sometimes referred as "translucent clouds" (Snow and McCall, 2006).

5.2 Theoretical Methods

Surface reactions are usually categorized as a function of the general reaction mechanism they belong to. Langmuir-Hinshelwood mechanism (LH) implies the adsorption of both reactants and collision via diffusion on top of the surface (Langmuir, 1922). In the Eley-Rideal one of the reactants interact with an adsorbed species (Eley and Rideal, 1940). Finally, Harris-Kasemo mechanism is an intermediate possibility involving diffusion of an atom with high translational energy or "hot atom" (Harris and Kasemo, 1981). In the astronomical community, the last two mechanisms are mostly discarded in favor of the first one. This is due to the extreme conditions of the ISM in which neither the pressure (discarding Eley-Rideal mechanism) nor the temperature (discarding the Harris-Kasemo mechanism) are large enough to validate them. LH mechanism is assumed as the default mechanism for surface reactions in ISM because it implies the acceptance of the formation of long lasting adsorbates on the surface. A picture of the LH mechanism for the formation of OH is shown in Fig 5.3. Interstellar surfaces, as opposed to their heterogeneous catalysis counterparts, act as an "atom storage room" more than a catalyst. Citing Eric Herbst words (Herbst, 2001) "The surfaces of these dust particles can provide a template (one hesitates to use the word "catalyst") for chemical reactions". We therefore have studied the LH mechanism formation of water employing a periodic approach and sampling up to 8 Å of one dimensional hydrogen diffusion. This is the main difference with the work of Goumans et al., 2009, a full sampling of the different active sites of the forsterite surface.

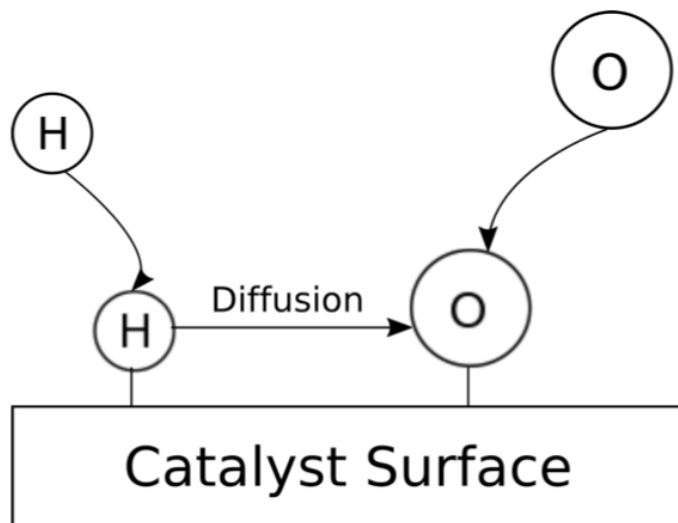


FIGURE 5.3: General Langmuir-Hinshelwood Mechanism Scheme with only H diffusion

5.2.1 Surface Model

We have employed a periodic surface model of the non-polar forsterite Mg_2SiO_4 (010) surface. The procedure of construction of such surface can be found in detail in Navarro-Ruiz et al., 2014a. Briefly, the slab is constructed from the cut of the crystalline unit cell of forsterite perpendicular to the (010) direction. A doubled lattice constant in the c direction in order to sample the diffusion along a big distance has been used. The thickness has been chosen to match the values of the original b lattice constant in the unit cell. The final values of the lattice parameters are $a=4.7892 \text{ \AA}$ and $c=12.0183 \text{ \AA}$ with a thickness of $\sim 12.0183 \text{ \AA}$. Fig 5.4 present the lateral and top view of our model surface.

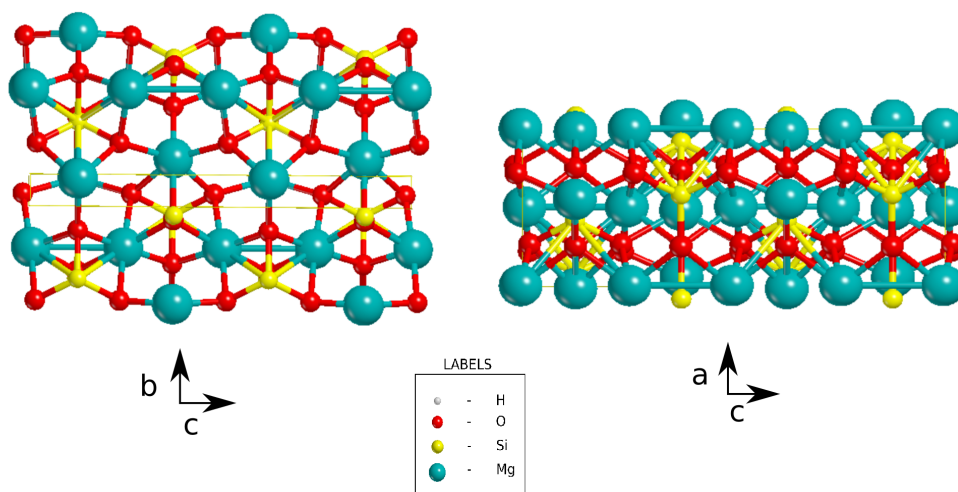


FIGURE 5.4: Lateral and Top view of the model forsterite surface.

From these cuts we can observe that the surface is terminated by uncoordinated Mg^{2+} bonded with only three oxygen atoms instead of the usual four. Ultimately, this leads to charge differences in different regions of the surface showing different chemical behavior, as explained in Navarro-Ruiz et al., 2014a. The nature of the bonding of the adsorbates depends on the nature of the atom it is bonded to. Figure 5.6 show the different possibilities for the coordination of incoming atoms. We will hereafter refer to the positions following the nomenclature presented in this figure:

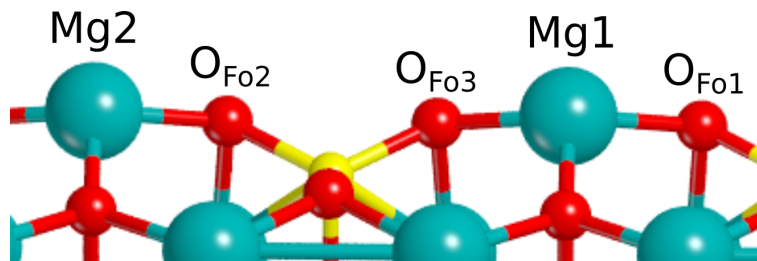


FIGURE 5.5: Zoom of the sites with different adsorption capabilities considered in this job.

5.2.2 Computational Methods

Before starting with the methods employed in our periodic calculations we must determine the adsorption states of the O atom on the surface. DFT notoriously fails when determining the ground state of a system with several choices for the spin multiplicity (Jacob and Reiher, 2012). In order to make meaningful calculations we have performed a calibration study of our exchange and correlation functional. The calibration puts the focus into two main factors. First, to determine the most stable adsorption state between triplet and singlet using the single reference computational gold standard method CCSD(T)/aug-cc-pVTZ, and, second, to determine the best cost/accuracy ratio of different exchange and correlation functionals benchmarking against the CCSD(T) / aug-cc-pVTZ method. The structure for the cluster calculations is presented in Fig 5.6.

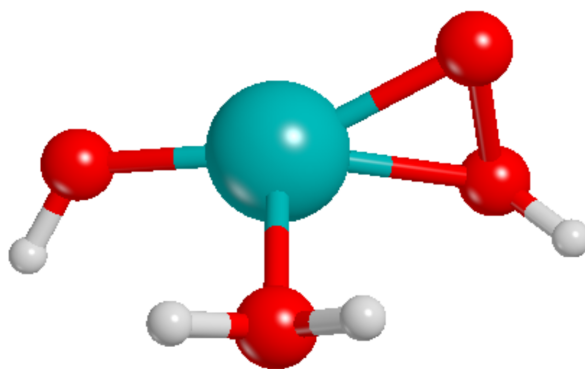


FIGURE 5.6: Cluster employed in the benchmark study (this image correspond to the singlet state)

For the construction of the cluster we have considered the first tetrahedral coordination sphere of a Magnesium atom, passivating with hydrogens all the atoms that would continue forming the surface, and leaving the "adsorbed" atom without passivation. All the cluster calculations have been performed using Gaussian09 (*Gaussian09 Revision E.01*). Two electronic states have been sampled: triplet (in accordance with oxygen 3P ground state) and singlet. Surprisingly, upon adsorption, the forsterite surface induces spin relaxation mechanisms (out of the scope of the present work) favoring the adsorbed single state as the most stable one by 29.7 kcal/mol . This value is high enough to justify the sole study of the singlet adsorption route, as the triplet one is far beyond in energy. Exchange-correlation functional calibration results are presented in Table 5.1, showing the triplet to singlet energy difference ΔE_{T-S} .

We have chosen the B3LYP functional (Becke, 1993) for the periodic calculations. We are aware that it is not the most suitable one but: 1. Not all the tested functionals are implemented in our periodic approach code and are only there for comparison purposes; 2. Not all the supported functionals have meaningful dispersion correction factors. The B3LYP functional has been treated to employ corrections for the dispersion interactions for extended systems (Grimme, 2006; Civalleri et al., 2008) giving rise to the notation B3LYP-D2* notation.

TABLE 5.1: Exchange-correlation functional calibration study on gas phase clusters

Method	ΔE_{T-S}
CCSD(T)	29.7
B97H	22.7
PW91K	22.3
M062X	27.0
BHLYP	17.4
B3PW91	22.6
M06	24.2
B3LYP	21.2
PBE0	22.5
B97	17.9
M06L	17.7
BLYP	19.6
PBE	22.8

After the calibration study we have performed periodic calculations for the rest of the work. We have used the CRYSTAL14 (Dovesi et al., 2014) code for the electronic energy minimization, geometry optimizations and frequency calculations in its unrestricted Kohn-Sham formalism, that is calculating separately the two components of the open-shell system with spin multiplicity > 1 . The employment of CRYSTAL over CASTEP, used in chapter 3, is due to its better description of local effects, more important in the study of reactivity (the drawback of CRYSTAL though is the computational performance, key in the study of demanding tasks such as the calculation of the IR spectra). CRYSTAL code employs Gaussian Type Orbitals as basis functions and therefore two main advantages arise. In the first place, evaluation of the exact exchange term can be done without localization of the basis functions and is affordable for systems of medium size in contrast with plane waves. Secondly, gaussian basis functions are localized in the atomic positions and this gives flexibility to describe interactions between atoms during a chemical reaction in a proper way. No pseudopotentials have been employed in our calculations. The contractions of the gaussian functions (the number of basis functions per shell and angular momentum channel) are: 1. For the geometry optimizations we have employed what we denote B1, a relatively small and cheap basis set with (8s)-(831sp)-(1d) for Si, (6s)-(31sp)-(1d) for O, (6s)-(631sp)-(1d) for the undercoordinated magnesium, (8s)-(511sp)-(1d) for the bulk Mg and (311s)-(1p) for H atoms; 2. Optimized geometries energies have been refined for better numerical accuracy of the results using a basis set denoted B2 (8s)-(831sp)-(1d) for Si; (6s)-(311sp)-(1d) for O; (631111s)-(42111p)-(1d) for the undercoordinated Mg, (8s)-(511sp)-(1d) for the bulk Mg and (311s)-(1p) for H atoms. In the case of this ordered structure, sampling of the special points in the Brillouin zone has been done using an equispaced net as proposed by Monkhorst & Pack (Monkhorst and Pack, 1976). Considering the high lattice constant and that our structure is an insulator, we have applied an integration scheme of the Brillouin Zone of 5 points. Forces in the structure have been calculated analytically and update of the Hessian matrix for the relaxation of such forces has been done employing a variation of the BFGS method that alternates quadratic and linear search (Civalleri

et al., 2001). The convergence criteria for the SCF is 10^{-7} Eh and for the geometry optimization, $\Delta F_{max} = 4 \times 10^{-4}$ Eh/Å and $\Delta R_{max} = 1 \times 10^{-3}$ Å.

With the refined energies in the optimized structures we can define the adsorption energy of the species, oxygen or hydrogen:

$$\Delta E = E(SM//SM) - E(S//S) - E_m(M). \quad (5.3)$$

where $E(SM//SM)$ is the refined energy of the system containing the adsorbed species, $E(S//S)$ the energy of the relaxed bare surface and $E_m(M)$ the energy of the atomic species whose adsorption is under consideration. A well known limitation of gaussian type orbitals is that they introduce a systematic error as a result of the superposition of different fragments because of the finiteness of the employed basis functions. Several algorithms have been proposed in the literature to overcome such error, but in general, the higher the basis set, the lower the basis set superposition error (BSSE). The use of basis sets of the quality of B2 have proven a significant decrease in the magnitude of the BSSE, which is another of the reasons for the choice of B2 (Navarro-Ruiz et al., 2015). For the rest of the work, it is implicit that geometry optimizations have been performed using B1 basis sets for computational saving reasons, and refinements of the energies in order to minimize errors have been done in the relaxed structures using B2. All our results are presented using the B2 values.

Calculation of the rate constant has been made on the basis of Transition State Theory (TST) (section 2.2.4). This theory, widely employed in the physical chemistry literature, establishes that reactions that require an activation energy (E_a) are properly described as the motion of the reactants to the products via a reaction vibrational eigenmode. The structure in which the electronic energy of the system equals E_a , is called transition state or activated complex. The most important characteristic, from a vibrational point of view, is that transition states show an imaginary frequency in their vibrational spectra (not detectable) that corresponds to the reaction eigenmode towards the products. The estimation of the mensurable rate constant is carried out using the Eyring equation, employing not the E_a but its finite temperature magnitude, the free energy ΔG^\ddagger , where \ddagger is standard notation for transition state representation. The Eyring equation then becomes:

$$k^{TST} = \frac{k_b T}{h} e^{-\frac{\Delta G^\ddagger}{RT}}, \quad (5.4)$$

where k^{TST} is the rate constant, k_b is the Boltzmann constant, T the temperature, h the Planck constant and R the ideal gas constant. It is clear then that we need to determine the vibrational frequencies of both reactants and products in order to obtain two things: the magnitude of the entropy required for the estimation of the free energy, and the value of its imaginary frequency. Zero point energy has been added to the energies employed in eq 5.4.

For the calculation of the vibrational frequencies, CRYSTAL employs primitive cell small atomic displacements (0.003 Å in each of the 3N cartesian coordinates), instead of DFPT.

In addition, and due to the enormous computational cost of building the dynamical matrix in a system of this size without pseudopotentials and employing gaussian functions, we have limited the calculation of the frequencies to the first and second layers of atoms in the surface and the reactive species. Vibrational frequencies are calculated at the Γ point $\vec{q} = 0$ in the reciprocal space. Whereas for the calculation of the reactants geometry the algorithms are straightforward to apply, in the case of the determination of the transition state we have employed the Distinguished Reaction Coordinate Technique (Rimola et al., 2010). We have followed the reaction eigenmode (easy in the case of an atomic translation) and computed the approximated barrier. With this, we refine the geometry of the structure at the barrier peak.

In the ISM, thermal effects to the rate constant are negligible and reactions happening with high energetic barriers are not viable unless we consider quantum tunneling to be a factor. Numerous studies have addressed the importance of tunneling in solid state astrophysics (Oba et al., 2015; Hama et al., 2015; Kobayashi et al., 2017). Theoretically tunneling can be calculated in several ways: correcting ad-hoc the rate constant with a multiplicative term depending of the shape on the barrier, or employing path integrals schemes, such as the instanton method to determine the minimum action path below the barrier. The first one will be the one most employed during this chapter, using the Fermann & Auerbach (Fermann and Auerbach, 2000) correction and the Eckart approximation (Eckart, 1930).

Fermann-Auerbach (FA) methodology considers a critical temperature (T_x) below which tunneling dominates the reaction defined as:

$$T_x = \frac{h\nu^\ddagger \Delta E_0^\ddagger / k_b}{2\pi \Delta E_0^\ddagger - h\nu^\ddagger \ln 2} \quad (5.5)$$

with ν^\ddagger and E_0^\ddagger as the absolute value of the imaginary frequency of the transition state and its energy respectively. The semiclassical corrected (SC) reaction rate therefore is:

$$k^{SC-FA}(T) = k^{TST} \Gamma^{FA}(T), \quad (5.6)$$

with $\Gamma^{FA}(T)$:

$$\Gamma^{FA}(T) = \begin{cases} 1 & T > T_x \\ e^{\frac{\Delta E_0^\ddagger}{k_b T}} e^{-\frac{2\pi \Delta E_0^\ddagger}{h\nu^\ddagger}} \left(1 + \frac{2\pi \cdot k_b \cdot T}{h\nu^\ddagger}\right) & T < T_x. \end{cases} \quad (5.7)$$

In the case of the Eckart correction, the expression of the rate is similar:

$$k^{SC-Eckart}(T) = k^{TST} \Gamma^{Eckart}(T), \quad (5.8)$$

with $\Gamma^{Eckart}(T)$ calculated as the fraction of the particle flux (P(E)) towards the one dimensional barrier defined by the quantum chemical calculations:

$$\Gamma^{Eckart}(T) = \int_0^\infty P(E) e^{-\frac{E_0^\ddagger}{RT}} dE. \quad (5.9)$$

The more sophisticated path-integral schemes, materialized in the instanton method (Rommel and Kästner, 2011) have been employed in the study of gas phase interstellar reactions by the group of Prof. Kästner (Lamberts et al., 2014; Meisner, Lamberts, and Kästner, 2017) and recently in condensed phase (Lamberts and Kästner, 2017; Molpeceres et al., 2018) and will be briefly discussed towards the end of the chapter.

We have now described all the theoretical tools that will be employed in the chapter and we are now in a position to start the results discussion.

5.3 Results

The section is organized using a flow scheme that resembles the order in which the processes are likely to happen. In the first place we will study the kind of bonding of the oxygen atom with the surface, pointing to an explanation on why we obtain the singlet state of the surface as the most stable one, in clear contradiction with the oxygen triplet ground state. We will tackle afterwards the description of the movement of the hydrogen atom via superficial diffusion, starting from the farthest possible atom with respect to the adsorbed oxygen (Mg^{2+} in Fig 5.4). We restrict the calculation of diffusion to the hydrogen atom, because of its lower mass. Finally, with all the possible diffusion steps considered, we will move to the calculation of the quantitative rate constants.

5.3.1 Oxygen Adsorption

According to the calibration studies described in the past section the singlet state is, in clusters, the most stable one, with differences of 29.7 kcal/mol at the CCSD(T) level of theory. In any case, we have calculated the electronic energies of the periodic surface, with its associated atom decomposed spin densities and charges in order to analyze the nature of the chemical bond. Before presenting the results it is worth noticing that we have sampled different possible adsorption sites for the incoming oxygen atom, in Mg_1 , O_{F03} or O_{F01} (see Fig 5.6). Such explorations have concluded in the convergence of the optimizations towards the interaction with Mg_1 , so we can discard long lasting adsorbates including pure O-O bonds. The results for our geometry optimizations are therefore:

The adsorption energies for the singlet and triplet employing eq 5.3 (and using zero point energy corrections ΔU) are $\Delta U_{\text{singlet}} = -33.6 \text{ kcal.mol}^{-1}$ and $\Delta U_{\text{triplet}} = -3.2 \text{ kcal.mol}^{-1}$. The difference between triplet and singlet then lies in the same range as the ones obtained in our cluster benchmark. Before starting with the chemical interpretation of such observation, let us present the results of the population analysis (atomic charge (AC) and spin density (SD) of the atoms involved in the interaction) of Mg_1 , O_{Ads} and O_{F01} respectively. These results are gathered in Table 5.2.

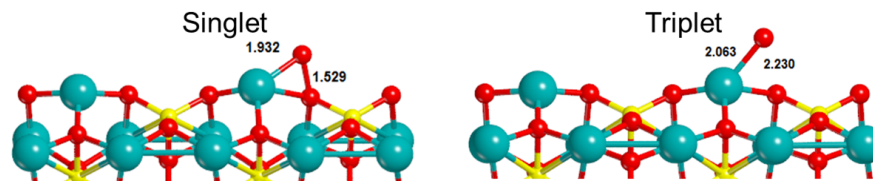


FIGURE 5.7: Triplet and Singlet adsorbed oxygen on the Forsterite surface.

TABLE 5.2: Spin Densities and Atomic Charges of the atoms involved in the Forsterite-Oxygen adsorption in the Singlet and Triplet State (in atomic units)

Atom	SD_s	AC_s	SD_t	AC_t
Mg1	0.00	10.66	0.00	10.43
O_{Ads}	0.00	8.48	1.68	8.24
O_{Fo1}	0.00	8.80	0.32	9.03

In view of the $O_{ads}-O_{Fo1}$ bond distances (1.529 Å in the singlet and 2.230 Å in the triplet) and the inspection of their spin densities and atomic charges we can infer that the main difference between the singlet and triplet adsorption states lies in the interaction of the incoming oxygen atom with the surface oxygen adjacent to the magnesium. This is also evinced by the lower value of the atomic charge of O_{Fo1} in the singlet state, indicating a certain degree of covalency. From a chemical point of view the stabilization that arises from the interaction between the two oxygens can be explained as the formation of a peroxo O_2^{2-} group on the surface forming a triangular shape in coordination with Mg1. The small bond distance in the singlet surface in contrast with the one in the triplet is another proof of such interaction. These kinds of peroxo complexes are well described in the literature, especially in alkaline-earth oxides and α -alumina surfaces. (Kantorovich and Gillan, 1997; Gamallo and Sayós, 2007; Yu et al., 2015; Pašti, Baljžović, and Skorodumova, 2015). A closer inspection at the SD of the triplet surface shows that no pairing is possible between such atoms. A bond length of 2.23 Å (as in the triplet) is too large to consider a bonding interaction. We can conclude that the Forsterite-Singlet Oxygen (hereafter $Fo - O^S$) is **chemisorbed** to the surface with an energy of $\Delta E_{ads} = -33.6 \text{ kcal.mol}^{-1}$. The formation of a chemisorbate has important implications from an astrophysical point of view as it suggests the formation of long lasting adsorbates on the surface, as required during the LH mechanism discussion. However, the interaction energy of our atom with the surface is lower than the adsorption energies reported in the above mentioned works that is in the range of -50 kcal/mol. The formation of the peroxo O_2^{2-} groups is also predicted by our gold standard CCSD(T) calculations yielding a triplet to singlet different of 29.7 kcal/mol. We have been able to reproduce in an excellent way such result, with our values in the periodic structure yielding a triplet-singlet difference of 30.2 kcal/mol.

^3P Oxygen is by far the most abundant form of atomic oxygen in astronomical environments. No mechanism can be viable upon adsorption of a singlet oxygen atom, so in order to continue with the mechanism we should demonstrate that before interacting with the surface, the incoming atom should be in its triplet state and undergoes a spin relaxation transition via an undefined mechanism. We propose lattice phonon relaxation or radiative emission (as in the photoemission domains proposed in chapter 3), but the exact mechanism is out of the scope of this work. In any case we need to prove that such crossing takes place, and in order to do so we have calculated the energy profile obtained when the internal $\text{Mg1-O}_{\text{ads}}$ coordinate is elongated, commonly referred in the literature as a **scan**. The results of such scan are presented in Fig 5.8.

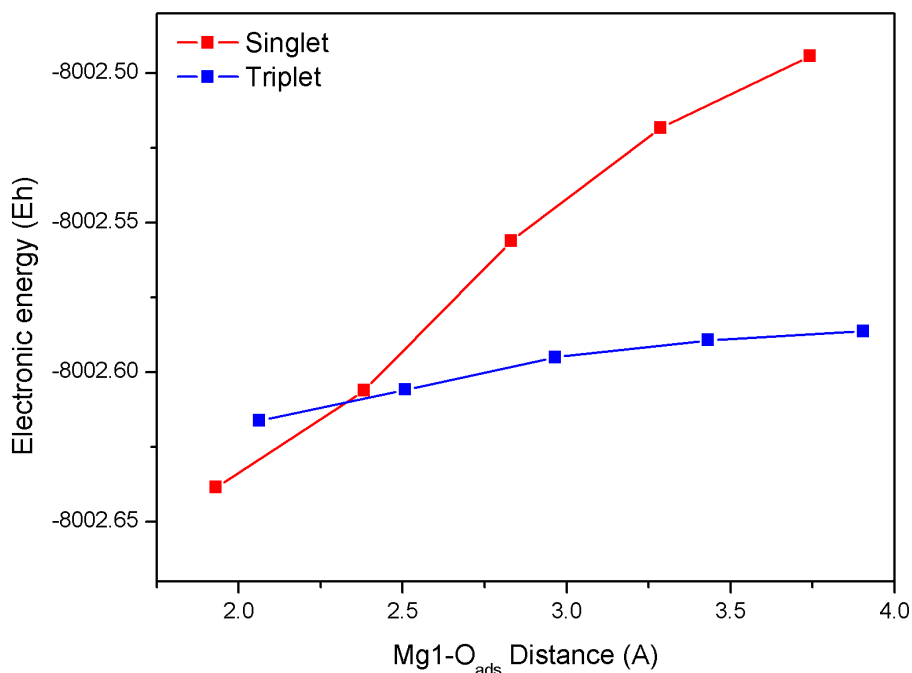


FIGURE 5.8: $\text{Mg1-O}_{\text{ads}}$ coordinate energy scan in the Forsterite-O singlet and triplet adduct.

This figure shows that a system crossing happens at more or less 2.3 \AA , enough distance to consider that our O_{ads} atom is most likely in its triplet state at the moment of the adsorption and rapidly evolves to the singlet one. Taking into account the timescales in which the oxygen atom relaxes and the global timescales of atom-grain collisions, it is a safe bet to calculate the energetic pathway considering only the singlet state.

As a last remark, we should mention that the difference in the adsorption energies with the work of Goumans et al (Goumans et al., 2009) is remarkable, proposing an adsorption value of about $-103 \text{ kcal mol}^{-1}$. This difference is very high to be completely explained in terms of quantitative values of the different computational methods employed. However, both magnitudes are not comparable because in their work the authors study the oxygen adsorption **after** the adsorption of a hydrogen atom. The electronic structure of the surface is not the same in both cases and the spin density of the magnesium atom is different as a result of the unpaired electron of the hydrogen atom.

This leads to a very favorable spin-spin coupling interaction in the surface of Goumans et al., 2009 .

5.3.2 Hydrogen Diffusion: Products Formation

In our workflow we first consider the adsorption of the oxygen atom in order to provide an ordered and pictorial way in that the hydrogen diffuses towards an already adsorbed oxygen. In order to continue with this mechanism the next step is to calculate the diffusion of a single hydrogen to form OH radical as in eq 5.1. Once this radical is formed we repeat the same procedure to form the H₂O molecule.

OH formation

In this first step the spin multiplicity of the total system is considered to be two, as a result of the hydrogen atom unpaired electron. We will name the different minima in the PES energy surface D1 and D2 as a function of the surface atom it is absorbed onto. In order to ease the discussion we present the minimized structures in Fig 5.9.

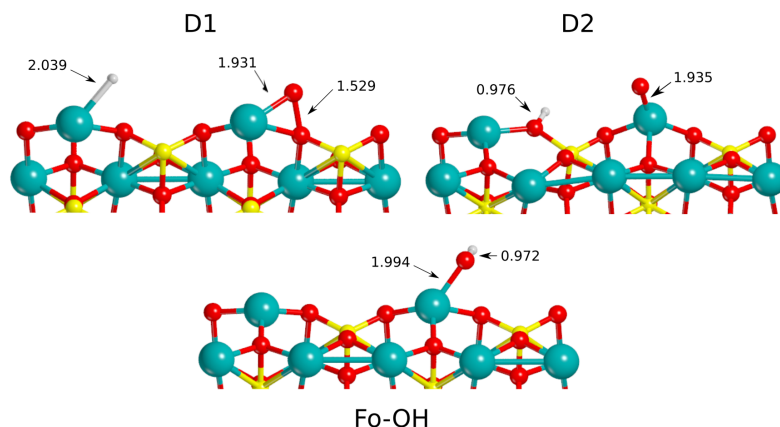


FIGURE 5.9: DFT Optimized Structures Found During H Diffusion Yielding Forsterite-OH

The possibilities for hydrogen adsorption are either Mg2, O_{F02} or O_{F03}. We have successfully obtained structures with guessed geometries in which the H atom is placed on top of Mg2 and O_{F02}. However, we have not been able to isolate a reaction intermediate with the hydrogen placed on top of O_{F03}. All our attempts employing different computational schemes (direct optimization or scan of the reaction coordinate) ultimately yield the formation of the OH radical adsorbed on the surface. This strong interaction can happen at long ranges, and even at approximately 1.80 Å the structure finally collapses to the typical bond distance values of the hydroxyl radical (around 0.97 Å). We

have calculated the adsorption energies (ZPE corrected) for the adsorption of the hydrogen obtaining $\Delta U_{D1} = -4.3 \text{ kcal/mol}$ and $\Delta U_{D2} = -68.2 \text{ kcal/mol}$. Table 5.3 contains the data on atomic charge and spin densities of hydrogen in D1, D2 and Forsterite-OH.

TABLE 5.3: Atomic Charges and Spin Densities of the hydrogen atom for the different adsorbates in the $\text{O}+\text{H} \rightarrow \text{OH}$ reaction (in atomic units)

	AC	SD
D1	1.04	0.75
D2	0.63	0.00
Fo-H	0.70	0.02

The high Mg2-H distance in D1, along with the adsorption energy and the data on its atomic charge and spin density values, point out to a fairly weak interaction of the magnesium with the hydrogen. This allows us to classify such interaction to be of a physisorption nature. Charge on the hydrogen atom remains unaltered and almost all the spin magnetic moment is caused by this atom in the adsorbate. If we take a closer inspection at which atom collects the rest of this magnetic moment (0.25 atomic units) we observe that it is located in the O_{F02} atom. The hydrogen-magnesium bonds is therefore bent and hydrogen is partially bonded to O_{F02} , forming a substructure H-Mg2- O_{F02} leading to, as we will see later, a very low energy barrier for the diffusion towards D2. D2 on the other hand show a completely different chemical behavior, the interaction energy is $\Delta U_{D2} = -68.2 \text{ kcal/mol}$, the O_{F02} -H distance is 0.976 \AA and the atomic charge and density are 0.63 and 0.00 in O_{F02} and H, respectively. These magnitudes clearly indicate the formation of a superficial hydroxyl group via covalent interaction, with bond lengths around the same value than typical covalent O-H bond distances, sharing some of the charge and with a clear chemisorbed behavior. Interestingly enough, we locate the spin density of D2 entirely on the O_{ads} atom. Such accumulation of charge on the O_{ads} produces a repulsive interaction with the electron density of O_{F01} thus breaking the peroxy O_2^- group formed when only atomic oxygen is adsorbed. The formation of a hydroxyl group will have also consequences in the diffusion step, implying tunneling as the effective mechanism for the reaction to take place. Finally it is worth mentioning the O_{ads} - O_{F01} interaction is partially recovered in the Forsterite-OH (Fo-OH) complex, with a bond distance of 2.261 \AA , too big to be considered a bonding interaction, but the hydroxyl group is bent towards O_{F01} nonetheless.

A tempting conclusion would be to disregard the formation of D1 and consider that the only meaningful adsorption state is D2, given the high exothermicity of the adsorption process in D2. However, unlike in D1, formation of the surface hydroxyl radical described in D2 does have a kinetic barrier (Goumans et al., 2009; Navarro-Ruiz et al., 2014b) associated with it, in contrast with the adsorption on top of the magnesium that is barrierless, facilitating the diffusion of the hydrogen towards O_{F02} .

The only thing that remains for the structural study of the stationary points in the potential energy surface is the description of the transition states and their associated energy barriers. The energy profile, ZPE energy corrected, of the total reaction, with the computed structures for the transition states is collected in Fig 5.10.

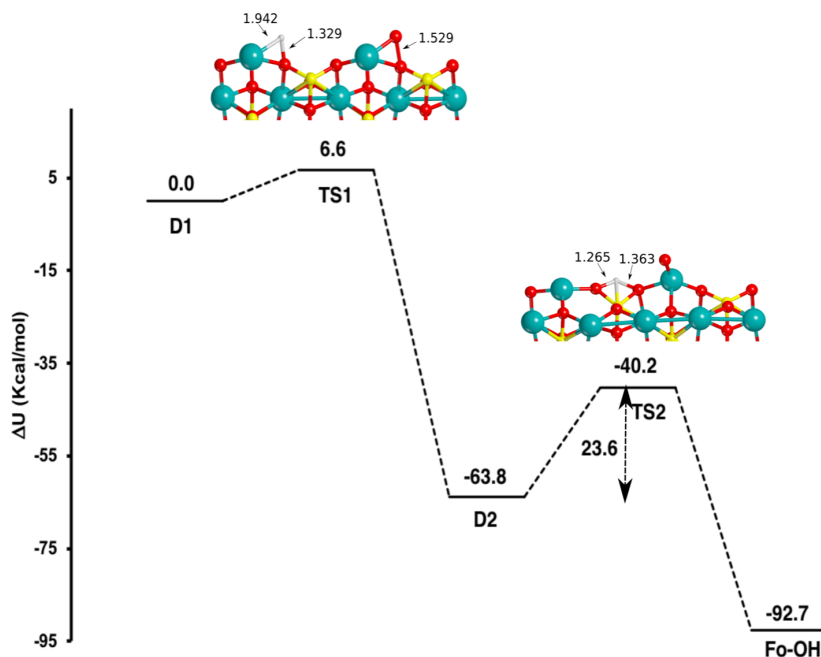


FIGURE 5.10: ZPE corrected reaction path profile for the formation of Forsterite-OH

First, let us talk about the transition state structures. TS1 is an evolution of the H-Mg₂-O complex mentioned in the description of the chemical nature of the D1 analogue but with the O_{F02}-H distance shorter than in D1, 1.329 Å in TS1 vs 2.015 Å in D1. This indicates that the reaction eigenmode is the formation of the OH surface bond in a position orthogonal to the surface and ulterior relaxation onto D2. The energy barrier with ZPE corrections is $\Delta U_{TS1} = 6.6 \text{ kcal/mol}$, a low barrier indicating an easy diffusion even at relatively low temperatures (see rate constant calculation section). TS2 shows some degree of structural complexity since it represents a three center shared hydrogen between O_{F02} y O_{F03} with almost equal bond distances (1.265 vs 1.363 Å) and atomic charges (also almost equal, 9.01 vs 8.99), indicating an equivalent degree of electron sharing and a potential two electron three center bonding (Mayer, 1989). With independence of the nature of the bond, the barrier is high enough (23.6 kcal/mol) for this step to be considered the eq 5.1 reaction kinetic bottleneck. The reaction to form OH is clearly exothermic but the barrier is high due to the need of breaking the previously formed surface hydroxyl group. The requirement of the break of this bond goes in the line of Prof. Herbst comments, cited at the beginning of the chapter. Whereas the radical coupling of O and H is a barrierless reaction, the formation on top of forsterite surface has kinetic barriers. Strictly speaking we can be talking of anticatalytic behavior, but the reality is that given the very low pressures, the formation of long lasting adsorbates make the ISM dust grains to act as **storage rooms for atoms or molecules**. Even if the reaction rate is lower than in the gas phase, the final abundances require of this data because of their role as templates.

H₂O formation

Subsequently to the formation of the hydroxyl radical we have sampled the diffusion of a second hydrogen atom in order to form H₂O, our final product. We have employed the same theoretical method and simulated mechanism. The adsorption of the second hydrogen leads to two possible spin multiplicities in the total system; the first one, triplet, implies parallel spins in the incoming hydrogen and in the Fo-OH surface that locates part of the spin in the oxygen of the adsorbed hydroxyl radical (68%) and the rest of the magnetic moment in O_{Fo1} (32%). This route is discarded due to Pauli exclusion, diffusion over such triplet surface can happen but the reaction should be spin forbidden and therefore no real yield would be expected from this mechanism. The singlet surface, on the other hand, leads to a positive and exothermic interaction when it is near to the hydroxyl radical, as will be shown next.

Again, minima in the PES are illustrated in Fig 5.11. We have named D3 and D4 the adducts in Mg2 and O_{Fo2} respectively. We have not been able to find a reaction intermediate not collapsing into H₂O in O_{Fo3}.

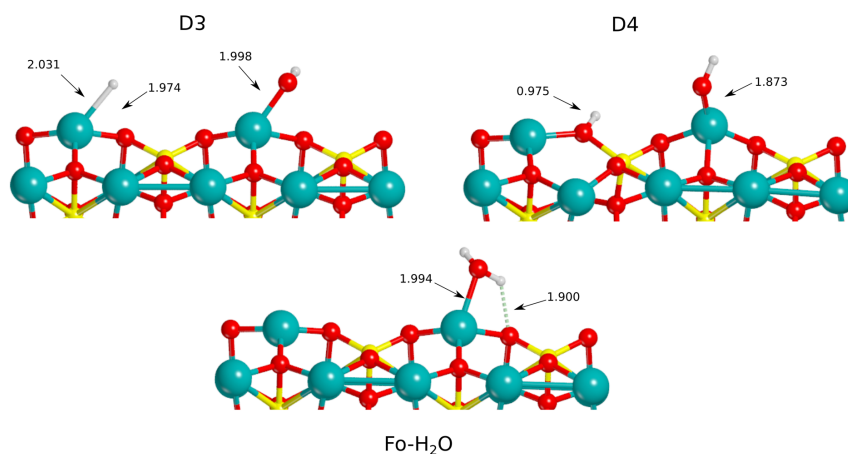


FIGURE 5.11: DFT Optimized Structures Found During H Diffusion Yielding Forsterite-H₂O

The nature of the bonding in the adducts with the second hydrogen adsorbed is in clear analogy with the ones presented in the previous section. The adsorption energies have been found to be $\Delta U_{D3} = -4.6 \text{ kcal/mol}$ and $\Delta U_{D4} = -83.5 \text{ kcal/mol}$ producing a referable energy profile. The same type of interactions have been found in the water formation reaction. Firstly, in D3 (the physisorbed state), we observe that most of the spin density is in the incoming hydrogen atom (0.74), indicating a low degree of interaction, see Table 5.4. However, even at the long distances between H and O_{Fo2}, we can find a partial spin density of 0.19 indicating a low degree of interaction. This is in clear resemblance with the first diffusion process in the formation of OH, pointing to the beginning of a covalent interaction, with the substructure H-Mg₂-O_{Fo2} being formed again. In this adduct we do not find any significant difference in the interactions of

the hydroxyl radical in comparison with the Fo-OH complex, with almost equal spin densities and bond distances.

TABLE 5.4: Atomic Charges and Spin Densities of the diffusing hydrogen atom for the different adsorbates in the OH+H \rightarrow H₂O reaction (in atomic units)

	AC	SD
D3	1.06	0.74
D4	0.63	0.00
Fo-H ₂ O	0.69	0.00

D4 again behaves as expected from the results of the first hydrogen diffusion. The spin populations are practically null in all atoms, as a consequence of the same process found in the first diffusion step, the formation of a surface hydroxyl group. The adsorption energies of the second hydrogen on top of O_{Fo2} is, of the order of -83 kcal/mol. This exothermicity is explained in terms of the formation of a covalent bond between the hydrogen atom and the surface leading to a chemisorbed state. The spin density from the former physisorbed hydrogen migrates towards the O_{ads} atom of the hydroxyl group, effectively forming an O²⁻ anion (and therefore forming an OH⁻ group). This electronic reorganization does not have a severe impact in the nature of the bond between the OH and the Mg²⁺ of the surface with a slight decrease in the bond distance (1.872 Å). However, it has an impact in the side interaction between O_{ads} and the O_{Fo1}, that is broken in this adduct with a bend angle of $\angle (O_{ads} - Mg1 - O_{Fo1})_{D4} = 133.03^\circ$ against $\angle (O_{ads} - Mg1 - O_{Fo1})_{D3} = 69.90^\circ$. This structural reorganization allows us to categorize the Mg1-OH interaction as an adsorption of a hydroxide (OH⁻) with the positive electrostatic part of the surface potential (uncompensated Mg²⁺ cations).

As in the case of the hydroxyl formation we present the PES cut along the reaction coordinate in Fig 5.12.

The trend in the reaction profile is completely referable to the one in the formation of the hydroxyl radical, with very similar bonding properties. It is worth noting the values of the barriers that correspond to $\Delta U_{TS1} = 4.5 \text{ kcal/mol}$ and $\Delta U_{TS1} = 22.3 \text{ kcal/mol}$ very similar to those on the previous section. The reaction bottlenecks of the total reaction are thus the steps involving D2 and D4 as reactants, due to the necessity of breaking chemical bonds, as explained above. The process is extremely exothermic and we have performed preliminary MD simulations in order to determine if that thermal energy is enough to induce the thermal desorption. However, we have not been able to distinguish any spontaneous desorption.

Desorption of the products

A side process that can happen during the reaction, both during the formation of OH or after the formation of H₂O, is the desorption of the products. Desorption can take place through several processes (i.e photodesorption, thermal desorption, etc). All our attempts to release our formed molecule to the gas phase via thermal desorption have been fruitless, because part of the energy is redistributed into the lattice or in small

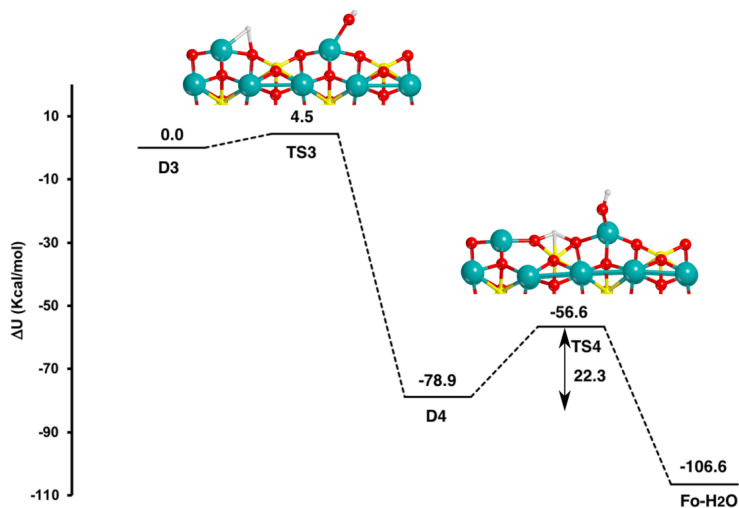


FIGURE 5.12: ZPE corrected reaction path profile for the formation of Forsterite-H₂O

grains via radiative emission. Nevertheless we have calculated the desorption energies of both the hydroxyl radical and the water molecule in order to help models to account for mantle formation with the timescales and photon field densities (or other energetic mechanism) at the interphase between diffuse and dense molecular clouds.

For determining the adsorption energies we have performed a scan sampling the internal O_{ads} -Mg1 coordinate constraining the O-H distances both in the OH and the H₂O species. This is the same as to perform a scan in a fragment of the system, in this case, the molecule. This approximation does not take into account rotational or vibrational degrees of freedom in the total desorption energies, because it fixes all the internal degrees of freedom of the molecule. The results of this scan are presented in Fig 5.13.

Desorption of the molecules is an endothermic step, as expected. However, the scan also shows that there is no energy barrier in the desorption process. Our results indicate that in astronomical cold environments photodesorption could play an important role with an average photon energy on the range of 9.2 eV (Dyson and Williams, 1997). Mechanisms aside, thermal desorption should be viable to liberate our molecules to the ISM, but that clearly depends on the conditions of the astronomical object. It is remarkable the degree of agreement between our desorption values and the ones by Goumans (Goumans et al., 2009) of 22.7 kcal/mol for the water molecule. This indicates that the discrepancies in previous quantities arise from the setup of the model and not from the computational method, provided that we have determined our desorption energies in a similar way as they have.

Table 5.5 reflects the numerical data on adsorptions and desorptions (with and without ZPE) where adsorptions corresponds to negative energies, and desorptions, to positive

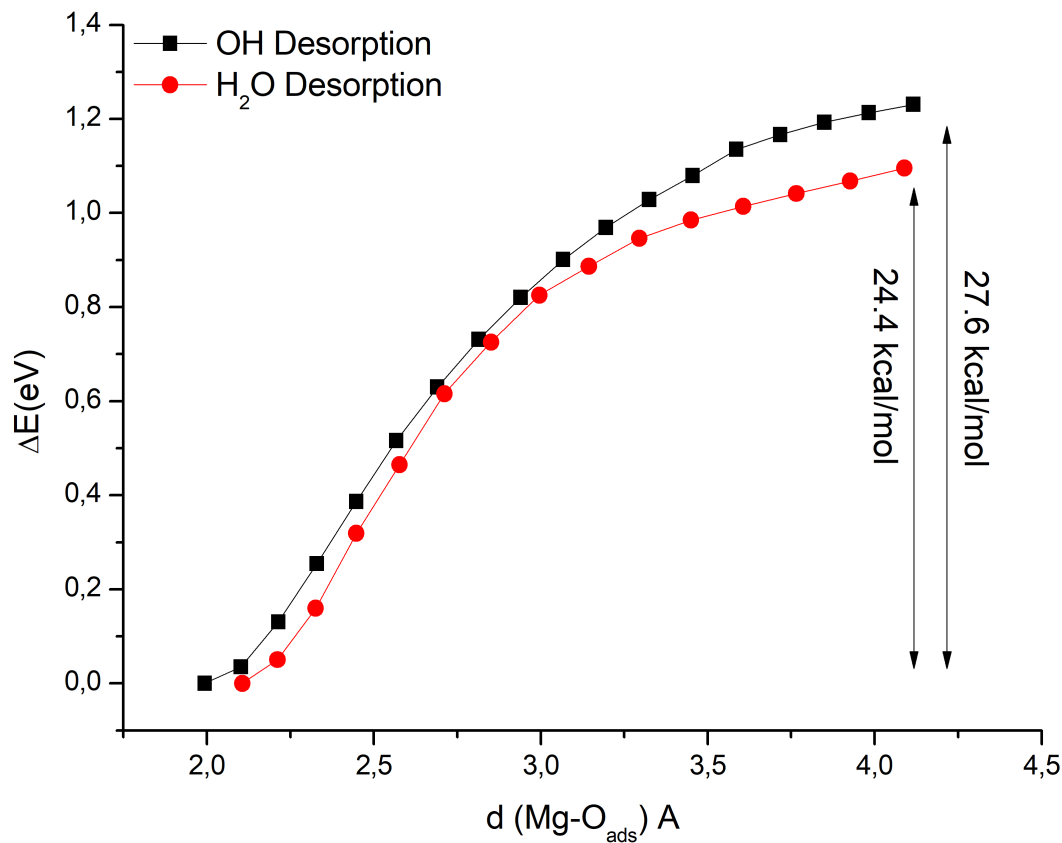


FIGURE 5.13: Calculated desorption curves of the OH and H₂O from the Fo-OH and Fo-H₂O adducts. Desorption energies include ZPE corrections.

ones). Please note that the discrepancies of Table 5.5 and Figs 5.12 and 5.10 come from the different origin of energies; in the case of the images, the first diffusion adduct is always taken as the origin of energies. We hope that the set of data presented in Table 5.5 will be of help to astronomers when modeling gas-grain interactions.

5.3.3 Rate Constant Calculation

After the description of the energetics of the system it is our purpose to evaluate the viability of the whole process on the basis of kinetic arguments as calculated by tunneling corrected transition state theory.

From the kinetic point of view, similarly to the thermodynamics we can distinguish two main processes. First the evolution from a physisorbed state, to a chemisorbed state. This step is relevant as it helps to overcome the initial barrier associated with the direct adsorption, yielding the chemisorbed state. The second one is the conversion of the surface ad-atom complex into our final species. This step involves surpassing a tall barrier of ~ 23 kcal/mol. Such barrier heights are obviously too high to be overcome with the thermal energetic budget of the ISM, usually at temperatures below 50 K. It is an

TABLE 5.5: Energies and ZPE corrected energies for the thermodynamic adsorption and desorptions studied in this work

Process	ΔE		ΔU	
	kcal/mol	eV	kcal/mol	eV
$O(^3P)+Fo \rightarrow Fo^S$	-33.6	-1.45	-31.9	-1.39
$O(^3P)+Fo \rightarrow Fo^T$	-3.2	-0.14	-1.7	-0.08
$Fo^S+H \rightarrow D1$	-6.0	-0.26	-4.3	-0.18
$Fo^S+H \rightarrow D2$	-74.3	-3.22	-68.2	-2.96
$Fo-OH \rightarrow Fo+OH$	+30.0	+1.30	+27.6	+1.19
$Fo-OH+H \rightarrow D3$	-6.4	-0.27	-4.6	-0.20
$Fo-OH+H \rightarrow D4$	-90.2	-3.91	-83.5	-3.62
$Fo-H_2O \rightarrow Fo+H_2O$	+27.1	+1.17	+24.4	+1.05

straightforward conclusion to realize that tunneling plays a crucial role in the determination of astrophysical meaningful rate constants. The calculation of the rate constants has been done in the basis of eq 5.6 and 5.8 using as input the values provided in Table 5.6 for ZPE corrected barrier heights, module of the imaginary frequency and crossover temperatures (for the FA tunneling model).

TABLE 5.6: DFT Calculated ZPE Barrier Heights, Module of the Imaginary Transition Frequencies and Tunneling Crossover Temperatures

Reaction	ΔU^\ddagger	ν^\ddagger	T_x
	kcal.mol ⁻¹	cm ⁻¹	K
D1→D2	6.6	1029	248
D2→Fo-OH	23.6	1605	375
D3→D4	4.5	1485	380
D4→Fo-H ₂ O	22.3	1583	370

Some necessary words regarding the input parameters are related with the difference associated with the magnitude of the imaginary mode, lower in the first physisorbed step and thus leading to a lower crossover temperature. The high values of such temperature clearly evince the importance of tunneling even in the presence of a sufficiently high thermal energy budget. The conversion from D3 to D4 has a reasonably high crossover temperature despite of the low value of its barrier due to the absolute value of its transition frequency. In this case, tunneling and thermal hopping cooperate to obtain very high rate constants. Figure 5.14 presents the Arrhenius plots for the four kinetic processes considered in this work.

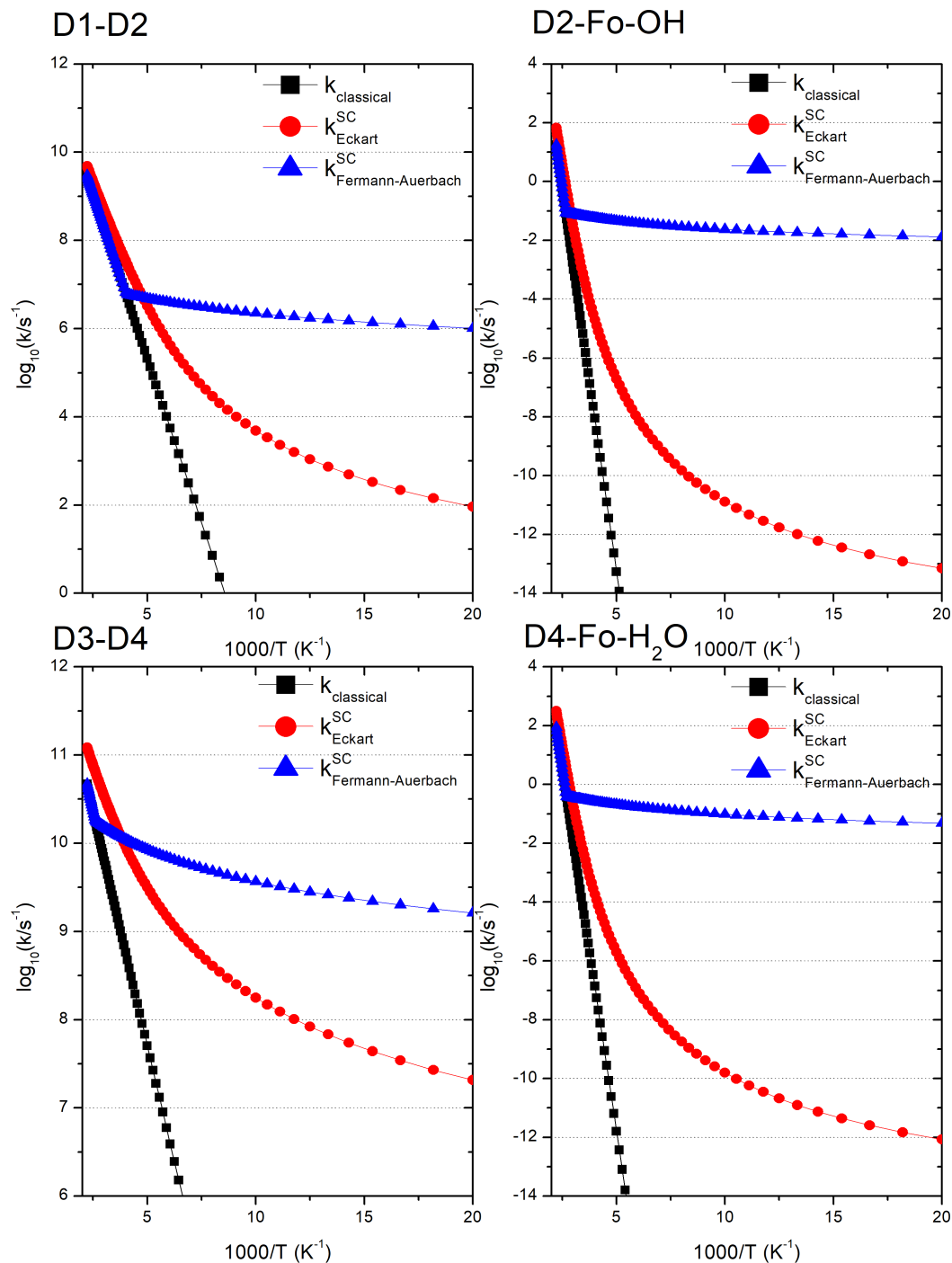


FIGURE 5.14: Arrhenius Plots Between 450 and 50 K Representing Rate Constants with and without Tunneling Corrections (Eckart & Fermann-Auerbach)

We were pretty confident at the light of the energetic barriers that the limiting steps were the product formation ones. This kinetic study clearly supports our assumption, pointing out that tunneling is of great importance for the reaction at low (and not so

low) temperatures. We need to remark two main points with respect to the tunneling corrections.

1. The FA approach has been validated for reactions up to 150 K so the results at lower temperature are not trustworthy enough and the values are probably overestimated.
2. Viability of the Eckart rate constants have been previously validated against more rigorous instanton theory calculations (Lamberts et al., 2016). Eckart based rate constants are determined to be generally underestimated against this more sophisticated approach.

With these two factors into play, we may conclude that the real rate constants should lie in between the values obtained with the two approaches. We are now calculating instanton corrected rate constants in condensed phase, but we need further data to extract conclusions.

In any case, our results show that in astronomical time scales the reaction times are viable, always considering tunneling as driving mechanism in the formation of the species. Employing only classical theories to justify the reaction inevitably lead to very slow reactions (black lines in Fig 5.14).

5.4 Conclusion and Astrophysical Implications

We think that this study provides many meaningful results to the astrochemical community, lacking data in gas-grain databases. The reaction rates provide an atomistic scale picture of the hydrogen diffusion and atom addition reactions on top of interstellar dust grain analogues. The values derived from our kinetic study contain a reasonable degree of assumptions and limitations, namely the crystalline nature of the surface instead of amorphous, the inner limitations of DFT and finite basis sets or the accuracy of the tunneling corrections. Overall, we have been able to identify the main steps of the reaction, including the kinetic bottlenecks and the nature of the chemical adsorbates formed during the reaction. The kinetic values can be systematically improved increasing the range of structures considered, the accuracy of the method, or the tunneling correction calculation framework. However, perfect accuracy in the calculation of the rate constants is currently out of the scope of DFT in periodic systems. What is really useful though are the trends that determine the viability of the reaction in astronomical timescales. From Fig 5.14 we infer that reactions can have rates on the order of several hundreds or thousands of seconds, a relatively low value considering astronomical times. Moreover, we are dealing here with the results of the formation of the first layer of ice material, proto-ice mantles. Reactions on top of this first mantle will have lower reaction barriers due to the lower adsorption energies of atoms on icy surfaces (Lamberts and Kästner, 2017).

Our study also provides relevant data on the energetics of adsorptions and desorptions of the involved species in context with the literature values. In the first place, adsorption energies of OH / H₂O in water ice surfaces and silicate dust grains in the literature are in between or 9 - 9.5 kcal/mol (Minissale et al., 2016). These values are lower than the ones presented by us (24.4 - 27.6 kcal/mol). A likely explanation is that literature

values are probably measured on top of a thin mantle of water ice, given the independence between the desorption energies on bare silicates and on top of ices. Our larger values, associated with the adsorption on top of bare grains indicate much longer interaction times, not accounted for in their model, and point to the formation of a first layer of water tightly bounded to the substrate (proto ice mantle). However, as has been mentioned above, water abundances should be dominated by the reactions on top of the icy surface. It is a safe assumption to consider the formation of this proto ice mantle negligible in the big picture and thus said error is minimized.

Secondly, our values provide a new point of view to the controversy on the desorption energy from computed and experimental values of oxygen atoms in bare silicate surfaces. A first set of values are the ones provided by (Goumans et al., 2009) (around 100 kcal/mol, indicating chemisorption) in contrast with the values of Vidali's group (He, Jing, and Vidali, 2014; He et al., 2015) (of around 3.7 kcal/mol, indicating physisorption). The reason of this discrepancy is fundamentally the nature of the experimental technique employed for the creation of the covered oxygen silicate surface. An atomic beam of oxygen atoms impinging on top of a bare surface should very easily saturate the surface (given Goumans' values) and a subsequent TPD desorption experiment at low temperatures would yield atoms that are in interaction with the saturated surface, physisorbed in nature, with weak (in comparison) $O_{atom}-O_{ads}$ interactions. The strong $O_{ads}-Fo$ interaction implies that the TPD should be carried out up to very high temperatures in order to desorb this first layer, hindering an easy experimental detection of our very high adsorption (and thus desorption) energies. The reason behind the high interaction energy is found in the formation of the peroxy group on top of the surface, between the adsorbed oxygen and other oxygen in the surface. This also leads to an electronic reorganization in the system, in which an inter system crossing (triplet→singlet) has been detected to take place at about 2.3 Å. The difference between our results and the ones of Goumans et al., 2009 are a consequence of the different electronic structure of the surfaces but the picture of the chemisorbed nature of the first layer remains the same.

This obtained set of data may be of use in gas-grain codes with the purpose of completing the dynamical picture of the formation of grain-ice interphases and beyond (ice-ice interphases).

References

- Becke, Axel D (1993). "Density-functional thermochemistry. III. The role of exact exchange". In: *The Journal of Chemical Physics* 98.7.
- Boogert, Adwin, Perry Gerakines, and Douglas Whittet (2015). "Observations of the Icy Universe". In: arXiv: 1501.05317.
- Civalleri, B., Ph. D'Arco, R. Orlando, V. R. Saunders, and R. Dovesi (2001). "Hartree-Fock geometry optimisation of periodic systems with the CRYSTAL code". In: *Chemical Physics Letters* 348.1-2, pp. 131–138.
- Civalleri, B., C. M. Zicovich-Wilson, Loredana V., and P. Ugliengo (2008). "B3LYP augmented with an empirical dispersion term (B3LYP-D*) as applied to molecular crystals". In: *Cryst Eng Comm* 10.4, pp. 405–410.

- Cuppen, H. M., S. Ioppolo, C. Romanzin, and H. Linnartz (2010). "Water formation at low temperatures by surface O₂ hydrogenation II: The reaction network." In: *Physical Chemistry Chemical Physics* 12.38, pp. 12077–12088. arXiv: 1009.5272.
- De Leeuw, N. H., S. C. Parker, C. R. A. Catlow, and G. D. Price (2000). "Modelling the effect of water on the surface structure and stability of forsterite". In: *Physics and Chemistry of Minerals* 27.5, pp. 332–341.
- Dishoeck, Ewine F. van (2011). "Water in space". In: *Europhysics News* 42.1, pp. 26–31.
- Dovesi, Roberto, Roberto Orlando, Alessandro Erba, Claudio M. Zicovich-Wilson, Bartolomeo Civalleri, Silvia Casassa, Lorenzo Maschio, Matteo Ferrabone, Marco De La Pierre, Philippe D'Arco, Yves Noël, Mauro Causà, Michel Rérat, and Bernard Kirtman (2014). "CRYSTAL14: A program for the ab initio investigation of crystalline solids". In: *International Journal of Quantum Chemistry* 114.19, pp. 1287–1317.
- Dulieu, F., L. Amiaud, E. Congiu, J.-H. Fillion, E. Matar, A. Momeni, V. Pirronello, and J. L. Lemaire (2010). "Experimental evidence for water formation on interstellar dust grains by hydrogen and oxygen atoms". In: *Astronomy and Astrophysics* 512, A30. arXiv: 0903.3120.
- Dyson, J.E. and D.A. Williams (1997). *The Physics of the Interstellar Medium, Second Edition*. Series in Astronomy and Astrophysics. CRC Press. ISBN: 9780585368115.
- Eckart, Carl (1930). "The penetration of a potential barrier by electrons". In: *Physical Review* 35.11, pp. 1303–1309.
- Eley, D. D. and E. K. Rideal (1940). *Parahydrogen conversion on tungsten* [5].
- Fermann, Justin T. and Scott M. Auerbach (2000). "Modeling proton mobility in acidic zeolite clusters. II. Room temperature tunneling effects from semiclassical rate theory". In: *Journal of Chemical Physics* 112.15, pp. 6787–6794.
- Frisch, M. J. et al. *Gaussian09 Revision E.01*. Gaussian Inc. Wallingford CT 2009.
- Gamallo, P. and R. Sayós (2007). "A density functional theory study of atomic oxygen and nitrogen adsorption over α -alumina (0001)". In: *Physical Chemistry Chemical Physics* 9.37, pp. 5112–5120.
- Gillett, F. C. and W. J. Forrest (Jan. 1973). "Spectra of the Becklin-Neugebauer point source and the Kleinmann-Low nebula from 2.8 to 13.5 microns." In: *The Astrophysical Journal* 179, pp. 483–491.
- Goumans, T. P. M., C. Richard A. Catlow, Wendy A. Brown, Johannes Kästner, and Paul Sherwood (2009). "An embedded cluster study of the formation of water on interstellar dust grains." In: *Physical chemistry chemical physics* 11.26, pp. 5431–6.
- Grimme, S (2006). "Semiempirical GGA-type density functional constructed with a long-range dispersion correction". In: *J. Comput. Chem.* 27, p. 1787.
- Hama, Tetsuya and Naoki Watanabe (2013). *Surface processes on interstellar amorphous solid water: Adsorption, diffusion, tunneling reactions, and nuclear-spin conversion*.
- Hama, Tetsuya, Hirokazu Ueta, Akira Kouchi, and Naoki Watanabe (2015). "Quantum tunneling observed without its characteristic large kinetic isotope effects". In: *Proceedings of the National Academy of Sciences* 112.24, pp. 7438–7443.
- Harris, J. and B. Kasemo (1981). "On precursor mechanisms for surface reactions". In: *Surf. Sci.* 105.2-3, p. L281.
- He, Jiao, Dapeng Jing, and Gianfranco Vidali (2014). "Atomic oxygen diffusion on and desorption from amorphous silicate surfaces". In: *Physical Chemistry Chemical Physics* 16.8, pp. 3493–3500.

- He, Jiao, Jianming Shi, Tyler Hopkins, Gianfranco Vidali, and Michael J. Kaufman (2015). "A new determination of the binding energy of atomic oxygen on dust grain surfaces: Experimental results and simulations". In: *The Astrophysical Journal* 801.2, p. 120. arXiv: [1501.03836](#).
- Henning, Thomas (2010). "Cosmic Silicates". In: *Annual Review of Astronomy and Astrophysics* 48.1, pp. 21–46.
- Herbst, E. and W. Klemperer (Oct. 1973). "The Formation and Depletion of Molecules in Dense Interstellar Clouds". In: *The Astrophysical Journal* 185, pp. 505–534.
- Herbst, Eric (2001). "The chemistry of interstellar space". In: *Chemical Society Reviews* 30.3, pp. 168–176.
- Hollenbach, D. and C. F. McKee (July 1989). "Molecule formation and infrared emission in fast interstellar shocks. III - Results for J shocks in molecular clouds". In: *The Astrophysical Journal* 342, pp. 306–336.
- Ioppolo, Sergio, Herma M. Cuppen, Claire Romanzin, Ewine F. van Dishoeck, and Harold Linnartz (2010). "Water formation at low temperatures by surface O₂ hydrogenation I: Characterization of ice penetration." In: *Physical chemistry chemical physics* 12.38, pp. 12065–12076. arXiv: [1009.5272](#).
- Jacob, Christoph R. and Markus Reiher (2012). "Spin in density-functional theory". In: *International Journal of Quantum Chemistry* 112.23, pp. 3661–3684. arXiv: [1206.2234](#).
- Jing, Dapeng, Jiao He, John Brucato, Antonio De Sio, Lorenzo Tozzetti, and Gianfranco Vidali (2011). "On water formation in the interstellar medium: Laboratory study of the O+D reaction on surfaces". In: *Astrophysical Journal Letters* 741.1, p. L9.
- Jing, Dapeng, Jiao He, Massimo Bonini, John R. Brucato, and Gianfranco Vidali (2013). "Sputtering effects and water formation on an amorphous silicate surface". In: *Journal of Physical Chemistry A* 117.14, pp. 3009–3016.
- Kantorovich, L. N. and M. J. Gillan (1997). "The energetics of N₂O dissociation on CaO(001)". In: *Surface Science* 376.1-3, pp. 169–176.
- King, H. E., M. Stimpfl, P. Deymier, M. J. Drake, C. R.A. Catlow, A. Putnis, and N. H. de Leeuw (2010). "Computer simulations of water interactions with low-coordinated forsterite surface sites: Implications for the origin of water in the inner solar system". In: *Earth and Planetary Science Letters* 300.1-2, pp. 11–18.
- Kobayashi, Hitomi, Hiroshi Hidaka, Thanja Lamberts, Tetsuya Hama, Hideyo Kawakita, Johannes Kästner, and Naoki Watanabe (2017). "Hydrogenation and Deuteration of C₂H₂ and C₂H₄ on Cold Grains: A Clue to the Formation Mechanism of C₂H₆ with Astronomical Interest". In: *The Astrophysical Journal* 837.2, p. 155.
- Lamberts, T., H. M. Cuppen, G. Fedoseev, S. Ioppolo, K.-J. Chuang, and H. Linnartz (2014). "Relevance of the H₂ + O reaction pathway for the surface formation of interstellar water". In: *Astronomy & Astrophysics* 570, A57. arXiv: [1409.3055](#).
- Lamberts, Thanja and Johannes Kästner (2017). "Influence of surface and bulk water ice on the reactivity of a water-forming reaction". In: *The Astrophysical Journal* 846, p. 43. arXiv: [1708.05555](#).
- Lamberts, Thanja, Pradipta Kumar Samanta, Andreas Köhn, and Johannes Kästner (2016). "Quantum tunneling during interstellar surface-catalyzed formation of water: The reaction H + H₂O₂ → H₂O + OH". In: *Physical Chemistry Chemical Physics* 18.48, pp. 33021–33030.

- Langmuir, Irving (1922). "The mechanism of the catalytic action of platinum in the reactions $2\text{Co} + \text{O}_2 = 2\text{Co}_2$ and $2\text{H}_2 + \text{O}_2 = 2\text{H}_2\text{O}$ ". In: *Transactions of the Faraday Society* 17.0, p. 621.
- Liu, L., A. Weiss, J. P. Perez-Beaupuits, R. Güsten, D. Liu, Y. Gao, K. M. Menten, P. van der Werf, F. P. Israel, A. Harris, J. Martin-Pintado, M. A. Requena-Torres, and J. Stutzki (2017). "HIFI Spectroscopy of H_2O submm Lines in Nuclei of Actively Star Forming Galaxies". In: *The Astrophysical Journal* 846.1, p. 5. arXiv: 1707.04914.
- Mayer, I. (1989). "Bond orders in three-centre bonds: an analytical investigation into the electronic structure of diborane and the three-centre four-electron bonds of hypervalent sulphur". In: *Journal of Molecular Structure: THEOCHEM* 186, pp. 43–52.
- Meisner, Jan, Thanja Lamberts, and Johannes Kästner (2017). "Atom Tunneling in the Water Formation Reaction $\text{H}_2 + \text{OH} \rightarrow \text{H}_2\text{O} + \text{H}$ on an Ice Surface". In: *ACS Earth and Space Chemistry* 1.7, pp. 399–410. arXiv: 1708.05559.
- Minissale, M., F. Dulieu, S. Cazaux, and S. Hocuk (2016). "Astrophysics Dust as interstellar catalyst I. Quantifying the chemical desorption process". In: *Astronomy and Astrophysics* 585, A24.
- Mokrane, H., H. Chaabouni, M. Accolla, E. Congiu, F. Dulieu, M. Chehrouri, and J. L. Lemaire (2009). "Experimental evidence for water formation via ozone hydrogenation on dust grains at 10 K". In: *The Astrophysical Journal* 705, pp. L195–L198. arXiv: 0907.5173.
- Molpeceres, Germán., Albert Rimola, Belén Maté, and Johannes Kästner (2018). "The role of tunneling in gas-grain reactions in diffuse molecular clouds." In: Poster presented at the Electronic Structure Principles and Applications (ESPA) conference.
- Molpeceres, Germán, Albert Rimola, Cecilia Ceccarelli, Johannes Kästner, Piero Ugliengo, and Belén Maté (2019). "Silicate-mediated interstellar water formation: a theoretical study". In: *Monthly Notices of the Royal Astronomical Society* 482.4, pp. 5389–5400.
- Monkhorst, H and J Pack (1976). "Special points for Brillouin zone integrations". In: *Physical Review B* 13.12, pp. 5188–5192. arXiv: arXiv:1011.1669v3.
- Navarro-Ruiz, Javier, Piero Ugliengo, Albert Rimola, and Mariona Sodupe (2014a). "B3LYP periodic study of the physicochemical properties of the nonpolar (010) Mg-pure and Fe-containing olivine surfaces". In: *Journal of Physical Chemistry A* 118.31, pp. 5866–5875.
- Navarro-Ruiz, Javier, Mariona Sodupe, Piero Ugliengo, and Albert Rimola (2014b). "Interstellar H adsorption and H_2 formation on the crystalline (010) forsterite surface: a B3LYP-D2* periodic study". In: *Phys. Chem. Chem. Phys.* 16.33, pp. 17447–17457.
- Navarro-Ruiz, Javier, José Ángel Martínez-González, Mariona Sodupe, Piero Ugliengo, and Albert Rimola (2015). "Relevance of silicate surface morphology in interstellar H_2 formation. Insights from quantum chemical calculations". In: *Monthly Notices of the Royal Astronomical Society* 453.1, pp. 914–924.
- Oba, Y., N. Miyauchi, H. Hidaka, T. Chigai, N. Watanabe, and A. Kouchi (2009). "Formation of compact amorphous H_2O ice by codeposition of hydrogen atoms with oxygen molecules on grain surfaces". In: *Astrophysical Journal* 701.1, pp. 464–470.
- Oba, Y., N. Watanabe, T. Hama, K. Kuwahata, H. Hidaka, and A. Kouchi (2012). "Water Formation Through a Quantum Tunneling Surface Reaction, $\text{OH} + \text{H}_2$, at 10K". In: *The Astrophysical Journal* 749.1, p. 67.

- Oba, Yasuhiro, Naoki Watanabe, Yoshihiro Osamura, and Akira Kouchi (2015). "Chiral glycine formation on cold interstellar grains by quantum tunneling hydrogen deuterium substitution reactions". In: *Chemical Physics Letters* 634, pp. 53–59.
- Omont, A. et al. (2011). "Observation of H₂O in a strongly lensed Herschel -ATLAS source at $z = 2.3$ ". In: *Astronomy & Astrophysics* 530, p. L3. arXiv: [arXiv:1107.4979v1](https://arxiv.org/abs/1107.4979v1).
- Pašti, Igor A., Miloš Baljžović, and Natalia V. Skorodumova (2015). "Adsorption of nonmetallic elements on defect-free MgO(001) surface - DFT study". In: *Surface Science* 632, pp. 39–49.
- Prigiobbe, Valentina, Ana Suarez Negreira, and Jennifer Wilcox (2013). "Interaction between olivine and water based on density functional theory calculations". In: *Journal of Physical Chemistry C* 117.41, pp. 21203–21216.
- Rimola, Albert, Claudio Marcelo Zicovich-Wilson, Roberto Dovesi, and Piero Ugliengo (2010). "Search and characterization of transition state structures in crystalline systems using valence coordinates". In: *Journal of Chemical Theory and Computation* 6.4, pp. 1341–1350.
- Rommel, Judith B. and Johannes Kästner (2011). "Adaptive integration grids in instanton theory improve the numerical accuracy at low temperature". In: *Journal of Chemical Physics* 134.18, p. 184107.
- Snow, Theodore P. and Benjamin J. McCall (2006). "Diffuse Atomic and Molecular Clouds". In: *Annual Review of Astronomy and Astrophysics* 44.1, pp. 367–414.
- Taquet, V., P. S. Peters, C. Kahane, C. Ceccarelli, A. López-Sepulcre, C. Toubin, D. Duflot, and L. Wiesenfeld (2013). "Water ice deuteration: a tracer of the chemical history of protostars". In: *Astronomy & Astrophysics* 550, A127. arXiv: [1211.0514](https://arxiv.org/abs/1211.0514).
- Van Dishoeck, Ewine F., Eric Herbst, and David A. Neufeld (2013). *Interstellar water chemistry: From laboratory to observations*. arXiv: [1312.4684](https://arxiv.org/abs/1312.4684).
- Vidali, G., D. Jing, and J. He (2013). "Hydrogen and water in the interstellar medium". In: *AIP Conference Proceedings*. Vol. 1543. 1. American Institute of Physics, pp. 31–47. ISBN: 9780735411678.
- Whittet, Douglas C.B., M. F. Bode, A. J. Longmore, A. J. Adamson, A. D. McFadzean, D. K. Aitken, and P. F. Roche (1988). "Infrared spectroscopy of dust in the Taurus dark clouds - Ice and silicates". In: *Monthly Notices of the Royal Astronomical Society* 233.2, pp. 321–336.
- Yu, Xiaohu, Xuemei Zhang, Xinxin Tian, Shengguang Wang, and Gang Feng (2015). "Density functional theory calculations on oxygen adsorption on the Cu₂O surfaces". In: *Applied Surface Science* 324, pp. 53–60.
- Zolensky, Michael E. et al. (2006). "Mineralogy and petrology of comet 81P/wild 2 nucleus samples". In: *Science* 314.5806, pp. 1735–1739.

Chapter 6

Conclusions

In this last chapter we would like to summarize the main points and achievements of this thesis in the form of propositions.

Structure and Spectral Features of Hydrogenated Amorphous Carbon

- We have created a work flow for the simulation of interstellar HAC dust grains. These models are generated by packing molecular analogues with different C/H ratio and number of aromatic rings using a Montecarlo routine into cubic cells matching a certain density. These analogues are relaxed using Density Functional Theory calculations. We have been able to simulate the main components of the IR spectra of these materials and compare them with spectra of HAC analogues grown in our laboratory.
- Low densities are favored in our calculations due to steric interactions. Structures with more hydrogen content have lower densities than structures with higher C/H ratio.
- Approximating an exact density from first principles in amorphous materials is risky, and only qualitative arguments can be extracted. It is worth noticing though that densities higher than 1.5 gcm^3 are not likely to be found in HAC materials.
- We have generated two kind of HAC materials in a plasma reactor corresponding with two sets of experimental conditions. The spectra of H_2 -plasma-processed HAC match the theoretical spectrum of aromatic rich analogues. On the other hand, the spectra of non-processed HAC are in accordance with aliphatic analogues.
- We propose that the gaussian decomposition of a complex IR absorption band of HAC has associated an error arising from the mixing of normal modes due to the amorphous nature of the material.
- Comparing experimental and theoretical analogues, a similar position in the ternary diagram is found for the aliphatic materials but in aromatic ones this does not hold anymore. We suggest that to rely on the 1625 cm^{-1} absorption band to obtain the C (sp^2) proportion is misleading, and thus, aromatic rich interstellar material abundances may be overestimated.

- We have calculated the relative magnitude of UV absorption of our analogues using DFT methods. Aromatic rich materials show absorption in the UV at similar frequencies than the prominent bump of the interstellar extinction curve. Aliphatic materials absorption is dependent on the density and lower than in aromatic rich ones.
- Absorption in the UV increases with the density in aromatic materials but an erratic dependence is obtained in the case of the aliphatic ones.
- We have calculated the IR emission curves of our analogues to simulate the general appearance of Unidentified Infrared Emission Bands. Aromatic models show a rich spectra in that region whereas aliphatic ones do not show any particular interstellar recognizable profile.
- Density induces changes in the emission spectra, modulating the appearance of the different bands. This is an alternative vision to the traditional mixture of gas phase PAHs to explain the appearance of interstellar emission bands. Nonetheless, under this approach, PAHs like analogues will still be needed to account for certain components like the $7.7 \mu m$ band.
- We do not discard the presence of free flying PAH molecules as bearers of the unidentified emission bands, but we suggest that several possibilities could be considered in order to reduce the chemical complexity of the PAH hypothesis.

Survivability of Carbonaceous Dust Chemical Analogues

- The linear energy transfer of 5 keV electrons on HAC materials with C/H ratio of 1 and densities between $1 - 1.2 \text{ gcm}^{-3}$ has been calculated to vary between 8.5 and 9.4 eV/nm. These values allow to consider samples of $\sim 500 \text{ nm}$ thick to be homogeneously processed in its whole.
- We have irradiated our HAC samples during six hours under the above mentioned conditions, and the intensity of the $3.4 \mu m$ band has dropped a $\sim 75 \%$ its initial value.
- Irradiation with electrons allow us to deposit higher energy doses on the samples than when using cosmic ray analogues.
- A decomposition of the $3.4 \mu m$ band has been carried out for the asymmetric stretches, the features that contains less error. Destruction of CH_3 groups is more favored than CH_2 . This variation can be explained on the basis of statistical arguments.
- Band decays (and derived magnitudes) are seemingly independent of the temperature.
- We have fitted our decays to two different models, exponential and recombination. The results in the exponential one yield systematically higher values for the fitted cross sections.
- Focusing on the deposited energy per unit mass, the effect of electrons on the dehydrogenation of HAC analogues is similar to the effect of high energetic ions. Our results in particular simulate the irradiation with medium size ions (C^{5+}).

- Considering the cosmic ray flux in dense clouds, the estimated characteristic times of dehydrogenation of our HAC materials are on the order of 10^8 years.
- Our characteristic times for dehydrogenation are higher than the expected lifetimes of a dense cloud. Additional mechanisms of destruction must be considered in order to account for the full destruction of the $3.4 \mu\text{m}$ IR band.

Surface Reactions on Dust Grains: Water Formation over Forsterite

- Two different structural models have been tested to determine the spin multiplicity of the Forsterite Oxygen system, one in gas phase and another in condensed phase. Both of them point to the singlet adsorbate to be the most stable one, with only 3.3 kcal/mol of difference between models. The energy difference between the two states, singlet and triplet, is on the order of 30 kcal/mol.
- The most likely explanation for such behavior is the formation of a peroxy complex between the incoming atom and a Mg-O bond of the forsterite surface.
- The formation of the peroxy complex is relevant at distances below 2.3 \AA . At this distance, the inter system crossing takes place, between the triplet (most stable at larger distances) and the singlet.
- Oxygen can only be adsorbed on top of a magnesium atom. We have not been able to isolate pure adsorbates with direct oxygen-oxygen interactions.
- Hydrogen diffusion takes place upon adsorption of a hydrogen atom on top of a magnesium of the surface, leading to a physisorbed state. Direct adsorption on top of an oxygen atom presents a kinetic barrier that is severely lowered when diffusion takes place from the initial physisorbed state.
- The interaction of the diffusive hydrogen atom with an oxygen of the surface leads to a huge stabilization of the system via formation of a superficial hydroxyl group.
- The formation of this covalent bond makes the next diffusion step (to form the OH radical) to be the slowest step of the reaction ($H + O \rightarrow OH$). The energetic barrier is about 22 kcal/mol.
- The second reaction ($H + OH \rightarrow H_2O$) shares the same general trends that the first one, with slightly different thermodynamic and kinetic parameters.
- We have calculated the rate constants for the four diffusion steps considered in this work, both classical and tunneling corrected, using two different semi-classical corrections. The values at low temperature lie probably in between the two sets of corrected rate constants.
- According to our values the reaction should be relevant considering astronomical timescales.
- Both OH and H_2O desorption upon formation is not likely to happen, according to our calculated desorption values (27.6 and 24.4 kcal/mol, respectively).

- We propose that disagreement with the oxygen desorption values found in the literature could arise from the saturation of adsorption sites under experimental conditions, unlike the single adsorption of an atom in the bare surface.

Appendix A

Producción Científica

A continuación se enumeran y describen brevemente las distintas publicaciones que se han derivado de la investigación realizada en el Instituto de Estructura de la Materia. Un inventario actualizado de mi lista de publicaciones puede ser encontrada en https://www.researchgate.net/profile/German_Molpeceres_De_Diego

Optical Constants and Band Strengths of CH₄:C₂H₆ Ices in the Near- and Mid- Infrared

Germán Molpeceres, Miguel Angel Satorre, Juan Ortigoso, Carlos Millán, Rafael Escribano, y Belén Maté. *The Astrophysical Journal*, 825(2), 1569.

En este trabajo, el primero de una serie dedicado al cálculo de índices ópticos de hielos de interés astrofísico estudiamos mezclas de hielos de metano y etano en diferentes proporciones moleculares. Dichas proporciones son 3:1, 1:1 y 1:3, así como las especies puras. El laboratorio de caracterización de hielos astrofísicos de la UPV en Alcoy, ha medido para dichas mezclas las densidades exactas y los índices de refracción en el visible para los mismos materiales en las mismas condiciones experimentales. En nuestro laboratorio hemos caracterizado el espectro de las mezclas en el infrarrojo cercano y medio, determinando el cambio en el espectro debido a las interacciones entre las moléculas. Asimismo, el espectro teórico en el infrarrojo medio ha sido determinado para tratar de justificar los cambios espectrales desde una perspectiva atomística. Usando los espectros experimentales, hemos ajustado las constantes ópticas de todos los materiales en el rango espectral considerado con la esperanza de que nuestros datos sean de utilidad para la comunidad modeladora en astrofísica.

High energy electron irradiation of interstellar carbonaceous dust analogs: Cosmic ray effects on the carriers of the 3.4 μm absorption band

Belén Maté, Germán Molpeceres, Miguel Jiménez-Redondo, Isabel Tanarro y Víctor J. Herrero. *The Astrophysical Journal*, 831(1), 51.

Hemos abordado el estudio de los efectos de los rayos cósmicos sobre los portadores de las vibraciones C-H a 3.4 μm . Las vibraciones en dicha banda corresponden a tensiones simétricas y antisimétricas CH₃ y CH₂ de polvo cósmico. Para llevar a cabo el

estudio hemos usado electrones de alta energía (5 keV) para procesar muestras de carbono amorfo hidrogenado (HAC o a:C-H) crecidas en nuestro laboratorio Este estudio es relevante a la hora de esclarecer el debate en torno a la aparente desaparición de estas vibraciones en nubes moleculares densas. El decaimiento encontrado en nuestros experimentos no es lo suficientemente grande como para dar cuenta de la destrucción total de la banda en dichos objetos astronómicos, en claro acuerdo con parte de la bibliografía. Estos resultados sugieren ahondar mas en el problema y en las causas detrás de la desaparición de dicha banda.

Structure and infrared spectra of hydrocarbon interstellar dust analogs

Germán Molpeceres, Vicente Timón, Miguel Jiménez-Redondo, Rafael Escribano, Belén Maté, Isabel Tanarro y Víctor J. Herrero. *Physical Chemistry Chemical Physics*, 19, 1352,1360.

Usando métodos teóricos de teoría del funcional de la densidad hemos determinado la estructura y el espectro infrarrojo de análogos de polvo cósmico basados en modelos moleculares empaquetados, imitando estructuras amorfas. Dos arquetipos moleculares han sido utilizados, representando dos valores extremos propuestos en la literatura. El primero de ellos, esencialmente alifático, con pequeñas subunidades aromáticas. El segundo, asume un núcleo poliaromático con cadenas alifáticas en los bordes de las estructuras. Hemos estudiado el efecto de la densidad de empaquetamiento en el espectro. Nuestros resultados teóricos han sido testeados frente a análogos de polvo crecidos en nuestro laboratorio, así como con espectros de fuentes astronómicas. Se ha determinado que los esquemas presentes en la literatura para determinar la composición del polvo carbonáceo adolecen de ciertas limitaciones debido a la mezcla en sus modos de vibración. A la luz de nuestros resultados concluimos que las observaciones astronómicas deben corresponder a una estructura intermedia entre los dos arquetipos considerados, con un cierto sesgo a favor de las estructuras alifáticas.

Physical and spectroscopic properties of pure C₂H₄ and CH₄:C₂H₄ ices

Germán Molpeceres, Miguel Ángel Satorre, Juan Ortigoso, Alexandre Zanchet, Ramón Luna Molina, Carlos Millán Verdú, Rafael Escribano, Isabel Tanarro, Víctor J. Herrero y Belén Maté. *Monthly Notices of the Royal Astronomical Society*, 466(2), 1894,1902.

Se ha llevado a cabo el estudio de las propiedades espectroscópicas, de densidades e índices de refracción en el visible para mezclas de etileno metano en proporciones 3:1, 1:1 y 1:3, así como de las especies puras, siguiendo el trabajo anterior usando mezclas con etano. Como en dicho trabajo, hemos ajustado un set de constantes ópticas en todo el rango infrarrojo, con utilidad en el modelado de granos. Nuestros estudios han arrojado luz con respecto a las fases cristalinas de las especies puras.

Densities and refractive indices of ethane and ethylene at astrophysically relevant temperatures

Miguel Ángel Satorre, Carlos Millán Verdú, Germán Molpeceres, Ramón Luna Molina, Belén Maté, Manuel Domingo, Rafael Escribano y Carmina Santonja. *Icarus*, 296, 179,182.

Un estudio riguroso de la influencia de la temperatura en hielos de etano y etileno, complementando los estudios en las mezclas, ha sido realizado midiendo los índices ópticos y las densidades del material en el intervalo de temperatura entre 13 y 65 K. Las medidas se han realizado usando interferometría laser (con dos láseres) para el índice de refracción y con una microbalanza de cuarzo para la estimación de las densidades. El etano muestra comportamiento amorfo en sus fase sólida para temperaturas de depósito por debajo de 40 K. En el caso del etileno, esta tendencia se ve por debajo de 20 K. A temperaturas superiores hemos encontrado variabilidad en las fases en ambas moléculas. Estos cambios se evidencian a raíz de cambios bruscos en la densidad y en el índice de refracción con la temperatura. Los resultados son relevantes para conocer el estado físico de estos materiales en objetos transneptunianos de nuestro propio sistema solar.

Laboratory study of methyl isocyanate ices under astrophysical conditions

Belén Maté, Germán Molpeceres, Vicente Timón, Isabel Tanarro, Rafael Escribano, Jean-Claude Guillemin, José Cernicharo y Víctor J. Herrero. *Monthly Notices of the Royal Astronomical Society*, 4, 4222,4230.

La molécula de isocianato de metilo ha sido encontrada recientemente por la misión Rosetta en el cometa 67P/Churyumov-Gerasimenko (67P/CG) así como en el medio interestelar (en fase gas). En este trabajo abordamos la espectroscopía de dicha molécula a temperaturas relevantes para el medio interestelar. El espectro del hielo puro de isocianato de metilo contiene mucha información estructural en el multiplete entre 2350-2250 cm^{-1} . Esta componente puede ser interpretada en términos de tensiones NCO. De nuestras investigaciones, hemos extraído que existe una transición de fase amorfo-cristalina a 90 K. Hemos propuesto una posible estructura cristalina, puesto que no existen difractogramas de rayos X en base a teoría del funcional de la densidad. Finalmente, hemos estudiado el comportamiento espectroscópico y químico de la molécula diluida en hielo de agua, no encontrando un cambio apreciable en el espectro y concluyendo que se forma una mezcla estable a 20 K. Hemos tratado de simular las condiciones de dilución encontradas en diferentes objetos astronómicos con objeto de facilitar las posibles campañas de búsqueda de esta molécula.

Spectroscopy of Interstellar Carbonaceous Dust

Víctor J. Herrero, Belén Maté, Germán Molpeceres, Miguel Jiménez-Redondo, Isabel Tanarro. *Laboratory Astrophysics*

En el capítulo de este libro (Laboratory Astrophysics) se hace una breve introducción a las características espectroscópicas atribuibles a material carbonáceo en el medio interestelar, así como a la relación estructura / propiedades que podemos inferir de dicha espectroscopía. El capítulo también incluye información acerca de la evolución estructural

del material carbonáceo en diferentes partes del medio interestelar, haciendo hincapié en la aparente destrucción y mecanismos para la misma de la banda a $3.4 \mu\text{m}$.

Plasma generation and processing of interstellar carbonaceous dust analogs

Ramón Peláez, Belén Maté, Isabel Tanarro, Germán Molpeceres, Miguel Jiménez-Redondo, Vicente Timón, Rafael Escribano y Víctor J. Herrero. *Plasma Sources and Technology*, 27, 3.

En este artículo hemos agrupado todo el conocimiento adquirido en los últimos años concerniente a la estructura y la espectroscopía de polvo carbonáceo incluyendo nuevas medidas de reflectancia ultravioleta visible y microscopía de electrones secundarios. Junto con las nuevas medidas, las simulaciones computacionales anteriormente presentadas y la irradiación con electrones de alta energía son nuevamente revisadas. Las conclusiones son referibles a las de los anteriores artículos, pero agrupando resultados que ayuden a clarificar nuestras hipótesis.

Stability of CH_3NCO in Astronomical Ices under Energetic Processing: A Laboratory Study

Belén Matén, Germán Molpeceres, Isabel Tanarro, Ramón Peláez, Jean Claude Guillemin, José Cernicharo y Víctor J. Herrero. *Astrophysical Journal* 861(1), 61.

Siguiendo nuestro anterior trabajo con isocianato de metilo, hemos estudiado los efectos de la irradiación con electrones de alta energía y fotones ultravioleta en su química tanto en su forma pura como diluida en hielo de agua, así como sus secciones eficaces de destrucción. Para hacerlo hemos elegido su banda mas intensa, caracterizada en el anterior trabajo. Tras el procesado, las bandas IR pertenecientes a CO , CO_2 , OCN^- , y HCN/CN^- han sido encontradas. No hemos encontrado diferencias apreciables en la química inducida por fotones y por electrones. El agua es un escudo efectivo de radiación cuando usamos protones, pero no previene de la destrucción del isocianato usando electrones de alta energía. Además, la mezcla isocianato / agua es estable en todo el rango de temperaturas considerado en el experimento (20 - 200 K). Con las secciones eficaces de destrucción hemos concluido que la molécula debe de ser suficientemente resistente como para permanecer en fase sólida hasta su evaporación en *hot cores*. En cometas, la molécula debe también resistir en la fase condensada.

Densities, infrared band strengths, and optical constants of solid methanol

Ramón Luna, Germán Molpeceres, Juan Ortigoso, Miguel Ángel, Manuel Domingo Beltrán y Belén Maté. *Astronomy and Astrophysics*, 617, A116.

El último trabajo dedicado a la medida de índices ópticos y densidades de moléculas en fase sólida corresponde a la revisión de las medidas de una de las moléculas mas importantes en hielos interestelares, como es el hielo de metanol. Los datos de la bibliografía son erráticos. Hemos usado el mismo procedimiento explicado en las publicaciones anteriores para determinar las magnitudes de interés, prestando especial atención a las transiciones de fase del metanol sólido, ocurriendo en nuestro montaje experimental a ~

105 K. Hemos recalculado las constantes ópticas en el infrarrojo en todo el rango espectral entre 15.4 - 2 μm . Nuestros resultados difieren de los de otros grupos y por primera vez proporcionamos una razón coherente para los dispares valores encontrados en la literatura, debiéndose a un cambio en la morfología del hielo como consecuencia de los diferentes métodos y montajes experimentales.

Silicate-mediated interstellar water formation: A theoretical study

Germán Molpeceres, Albert Rimola, Cecilia Ceccarelli, Johannes Kästner, Piero Ugliengo y Belén Maté. *Monthly Notices of the Royal Astronomical Society*, 482, 4, 5389-5400.

Se han calculado teóricamente las constantes de velocidad para las reacciones $\text{H}+\text{O} \rightarrow \text{OH}$ y $\text{H}+\text{OH} \rightarrow \text{H}_2\text{O}$ sobre una superficie de forsterita, concretamente la superficie apolar (010), la mas estable termodinámicamente. El procedimiento supone un proceso escalonado involucrando en primer lugar la quimisorción de un átomo de oxígeno, con procesos de relajación de espín involucrados. Posteriormente la adición de un hidrógeno a la superficie se hace por un proceso de fisorción sin barrera y subsecuente difusión lateral hasta que se produce el evento de combinación entre ambos adsorbatos, siguiendo un esquema Langmuir-Hinshelwood de reacción en superficie. Este proceso ha sido simulado para obtener datos termodinámicos y cinéticos, incluyendo correcciones de efecto túnel. Estos datos han sido utilizados en un estudio cinético posterior, que ha concluido que la reacción simulada debe ser lo suficientemente rápida en entornos astrofísicos como para ser relevante en la formación de protomantos de hielo en regiones frías.

Appendix B

Curriculum Vitae

Molpeceres de Diego, German

C. Serrano 123, 28006, Madrid, Spain
+34 605 98 88 14
german.molpeceres@csic.es

Education

2008-2013 - Licenciatura (BSc+MSc) in **Chemistry**, Universidad de Valladolid, Spain.

2013-2015 - Master degree in **Theoretical Chemistry and Computational Modeling**, Universidad de Valladolid/Universidad Autónoma de Madrid. **Master dissertation: Theoretical Study of the Molecular Structure of Plutonium Tricarbide.**

2015-Present - Phd in **Chemistry**. Supervisor: Dr. Belén Maté Naya. Department of Molecular Physics IEM-CSIC, Title: Structure, survivability and physical processes in interstellar dust grain chemical analogues.

Research Topics

Computational studies of actinide carbides. (2012 - 2015) **Keywords:** *Nuclear fuel, Cluster chemistry, Quantum chemistry, Electron correlation, AIM analysis.*

Computational study of gas phase halogen abstraction reactions. (2012 - 2015) **Keywords:** *Reaction kinetics, Reaction mechanisms, Transition state theory, Density Functional Theory.*

Physical and optical properties of molecular solids of astrophysical relevance (2015 - 2018) **Keywords:** *Astrochemistry, Infrared spectroscopy, Molecular solids, Optical constants*

Structure, spectra and survivability of carbonaceous interstellar dust. (2015 - 2019) **Keywords:** *Astrochemistry, Infrared spectroscopy, Hydrogenated amorphous carbon, Electron bombardment, Density Functional Theory*

Quantum chemical study of the formation of interstellar water over dust grain surfaces (In collaboration with Autonomous University of Barcelona) (2017) **Keywords:** *Astrochemistry, Quantum Chemistry, Reaction Mechanisms, Catalysis.*

Survivability of hydrogen bearing molecules under the monolayer regime: Water proto-ice mantles over amorphous carbon (In collaboration with Univ. Hokkaido) (2017) **Keywords:** *Astrochemistry, Infrared Spectroscopy, Water photodissociation, Cosmic Dust.*

The role of tunneling in gas-grain reactions in diffuse molecular clouds: Hydrogen diffusion using instanton theory. (In collaboration with Univ. Stuttgart) (2018) **Keywords:** *Astrochemistry, Quantum Tunneling, Reaction Mechanism, Density Functional Theory.*

Scientific Stays

2017 - Three months stay in the department of chemistry of the Autonomous University of Barcelona under the supervision of Dr. Albert Rimola.

2017 - Two months stay in the Institute for Low Temperature Science of the University of Hokkaido, Japan under the supervision of Prof. Naoki Watanabe.

2018 - Three months stay in the Institute for Theoretical Chemistry of the University of Stuttgart, Germany, under the supervision of Prof. Johannes Kästner

Publications

1. Halogen-abstraction reactions from chloromethane and bromomethane molecules by alkaline-earth monocations. Redondo. P., Largo. A., Rayón. V.M., Molpeceres. G. et al. (2014). *PCCP*, 16(30), 16121-36.
2. Molecular Structure and Bonding in Plutonium Carbides: A Theoretical Study of PuC₃. Molpeceres, G., Rayón, V. M., Barrientos, C., & Largo, A. (2016). *J. Phys. Chem. A*, 120(14), 2232-2239.
3. Optical Constants and Band Strengths of CH₄:C₂H₆ Ices in the Near- and Mid-Infrared. Molpeceres, G., Satorre, M. A., Ortigoso, J., Millán, C. et al. (2016). *ApJ*, 825(2), 1569.
4. High-Energy Electron Irradiation of Interstellar Carbonaceous Dust Analogs: Cosmic-Ray Effects on the Carriers of the 3.4 Absorption Band. Maté, B., Molpeceres, G., Jiménez-Redondo, M., Tanarro, I., & Herrero, V. J. (2016). *ApJ*, 831(1), 51.

5. Structure and infrared spectra of hydrocarbon interstellar dust analogs. Molpeceres, G., Timón, V., Jiménez-Redondo, M., Escribano, R. et al. (2016). *PCCP*, 19, 1352,1360.
6. Physical and spectroscopic properties of pure C₂H₄ and CH₄:C₂H₄ ices. Molpeceres, G., Satorre, M. A., Ortigoso, J., Zanchet, A. et al. (2017). *MNRAS*, 466(2), 1894,1902.
7. Densities and refractive indices of ethane and ethylene at astrophysically relevant temperatures. Satorre, M. A., Millán, C., Molpeceres, G., Luna, R., A. et al. (2017). *Icarus*, 296, 179,182.
8. Laboratory study of methyl isocyanate ices under astrophysical conditions. Maté, B., Molpeceres, G., Timón, V., Tanarro, I., et al. (2017). *MNRAS*, 4, 4222,4230.
9. Plasma generation and processing of interstellar carbonaceous dust analogs. Peláez, R., Maté, B., Tanarro, I., Molpeceres, G., Jiménez-Redondo, M., et al. (2018). *Plasma Sources Sci. Technol*, 27 3.
10. Stability of CH₃NCO in Astronomical Ices under Energetic Processing: A Laboratory Study. Maté, B., Molpeceres, G., Tanarro, I., Peláez, R., et al. (2018). *ApJ*, 861(1), 61
11. Densities, infrared band strengths, and optical constants of solid methanol. Luna, R., A., Molpeceres, G., Ortigoso, J., Satorre, M. A., et al. (2018). *Astron & Astrophys*, 617, A116
12. Silicate-mediated interstellar water formation: A theoretical study. Molpeceres, G., Rimola, A., Ceccarelli, C., Kästner, J., et al. (2018). *MNRAS*, Accepted

Other Contributions

1. Reactivity of Alkaline-Earth Monocations with Halomethane Molecules. A computational Kinetic Study. Poster WATOC, Santiago de Chile (5-10 October 2014). Redondo, P., Largo, A., Rayón, V. M., Molpeceres, G., Sordo, J. A., & Barrientos, C.
2. Molecular structure of Plutonium Tricarbide. Poster ESPA 2014. Badajoz (2-4 July 2014) Molpeceres, G., Rayón, V. M., Barrientos, C., & Largo, A.
3. Molecular Astrophysics: Ices. Oral communication. Fourth Workshop in Theoretical Chemistry and Computational Modelling. Universidad Autónoma de Madrid (5-6 October 2015)
4. Spectroscopy of CH₄:C₂H₆ ices. Oral communication. Ailab Workshop. CSIC (7-8 March 2016)
5. Modeling of plasma deposited analogues of interstellar carbonaceous dust. Poster. 23rd Europhysics Conference on atomic and molecular physics of ionized gases (12-16 July 2016). Molpeceres, G., Jiménez-Redondo, M., Timón, V., Moreno, M.A., Herrero, V.J, Escribano, R. Maté, Tanarro, I.
6. Modeling and irradiation experiments of cosmic dust analogs. Oral communication XXV Reunión Nacional de Espectroscopía. Alicante (20-22 July 2016)

7. Theoretical models for the spectroscopy of methane/ethane ice mixtures. Poster. XXV Reunión Nacional de Espectroscopía. Alicante (20-22 July 2016) Escribano. R, Molpeceres. G, Satorre. M.A, Millán. C, Ortigoso. J, Maté. B.
8. Plasma generated analogs of interstellar carbonaceous dust: Theoretical modeling and electron bombardment. Poster. Gordon research conference: Plasmas with complex interactions: Exploiting the Non-Equilibrium.(24-29 July 2016) Herrero. V.J, Tanarro. I, Molpeceres. G, Timón. V, Maté. B, Jiménez-Redondo. M, Escribano.R
9. Infrared spectra of ices mixtures: Methane/Ethylene. Poster ISM 2016. Sapporo (17-19 October 2016) Molpeceres. G, Satorre M.A, Ortigoso. J, Millán. C, Escribano.R, Herrero. V, Tanarro. I, Luna. R, Maté. B.
10. Diffusion of methane on amorphous solid water. Poster ECLA 2016. Madrid (21-25 November 2016) Maté. B, Molpeceres. G, Ortigoso. J, Tanarro.I, Herrero. V.J.
11. Spectroscopy of Methane/Ethylene mixtures. Poster ECLA 2016. Madrid 21-25 (November 2016) Maté. B, Molpeceres. G, Satorre M.A, Ortigoso. J, Millán. C, Escribano. R.
12. Structure and spectra of models of HAC particles. Poster ECLA 2016. Madrid 21-25 (November 2016) Molpeceres. G, Timón, V, Jiménez-Redondo. M, Moreno. M.A, Herrero. V.J, Escribano. R, Maté. B, Tanarro.I.
13. Quantum chemical study of the formation of interstellar water over dust grain surfaces. Flash Communication 2017 Biannual Reunion of the Spanish Royal Society of Chemistry . Sitges (June 2017). Molpeceres. G, Rimola. A.
14. Silicate mediated interstellar water formation: A theoretical study. Poster IBER 2017. Barcelona (September 2017). Molpeceres. G, Enrique-Romero. J, Maté. B, Rimola. A.
15. Spectroscopy of Interstellar Carbonaceous Dust. Herrero, V.J, Maté, B. Molpeceres, G et al. Laboratory Astrophysics. ISBN: 978-3-319-90019-3 (Jan 2018)
16. Structure, survivability and physical processes in interstellar dust grain chemical analogues. Theoretical Chemistry Institute Seminars. Stuttgart (May 2018)
17. Gas grain Mobility in Molecular Clouds: The Role of Tunneling. Poster ESPA 2018. Molpeceres.G, Rimola.A, Maté. B, Kästner. J. Toledo (Jul 2018)

Appendix C

Resumen de la Tesis

En este apéndice se recoge el resumen en español requerido para la presentación de la tesis doctoral, de acuerdo con el punto a) del artículo 8 de la normativa para la presentación y defensa de la tesis doctoral en la Universidad de Valladolid.

Objetivos

En la presente memoria se recogen los resultados obtenidos en el estudio de la estructura de análogos de polvo cósmico, de su supervivencia en entornos astrofísicos, y sobre los procesos que pueden tener lugar en su superficie. Dicho trabajo se ha llevado a cabo en el Instituto de Estructura de la Materia, del Consejo Superior de Investigaciones Científicas, en Madrid. Asimismo, se incluyen las colaboraciones llevadas a cabo en sendas estancias de investigación en la Universidad Autónoma de Barcelona y la Universidad de Stuttgart, en Alemania.

El principal objetivo de la tesis es establecer relaciones entre la estructura microscópica o atomística de análogos de polvo cósmico con una serie de propiedades químico-físicas de interés astrofísico. En primer lugar, se ha estudiado la relación entre la estructura de diferentes arquetipos de carbono amorfo hidrogenado (HAC) y sus propiedades espectroscópicas en el infrarojo, por métodos teóricos y experimentales. En segundo lugar, se han determinado experimentalmente los tiempos de vida de los enlaces carbono-hidrógeno de los mencionados análogos en entornos astrofísicos como las nubes moleculares densas, mediante el procesado con electrones de muestras de HAC. Finalmente, y usando silicatos como análogos de polvo cósmico, se han estudiado rutas de síntesis de agua en entornos astrofísicos.

Metodología

Para la consecución de los objetivos presentados en la pasada sección se ha utilizado una combinación de simulaciones experimentales (empleando un reactor de plasma para la generación de los análogos y una cámara criogénica de alto vacío para su estudio espectroscópico) y computacionales (empleando diversos códigos comerciales para el estudio de sistemas en fase sólida, así como códigos propios).

Resultados y Conclusiones

Hemos obtenido experimentalmente los espectros infrarrojos de absorción de dos análogos de polvo cósmico, usando dos condiciones diferentes de depósito en el reactor de

plasma, una más energética y otra más suave. Además, se ha determinado computacionalmente el espectro de absorción y emisión infrarroja de arquetipos aromáticos y alifáticos de HAC, tratando de reproducir los espectros experimentales obtenidos inicialmente. Combinando estos esfuerzos hemos acotado los valores extremos de densidad en estos análogos. Usando las densidades más estables se han comparado resultados teóricos y experimentales, lo que ha permitido concluir que es muy difícil estimar el contenido gráfico de un material carbonáceo mediante espectroscopía infrarroja. Con relación a las curvas de emisión, se ha determinado que la densidad modula la presencia de diferentes bandas en el espectro, dando una explicación coherente a la riqueza espectral en el rango entre 20 y 10 μm , región en la que se encuentran las llamadas "bandas de emisión no identificadas" (UIE o UIB por sus siglas en inglés).

Del procesado electrónico de estos análogos se han extraído curvas de decaimiento de la banda de tensión CH a dos temperaturas, evidenciando la independencia de este factor en la destrucción de los enlaces carbono e hidrógeno. Mediante un modelo cinético y usando parámetros obtenidos de simulaciones de trayectorias de electrones en sólidos, se han determinado los tiempos de vida y las velocidades de destrucción de estos análogos en el medio interestelar denso y difuso. El uso de los datos experimentales en estos modelos tiende un puente entre los resultados de laboratorio y las observaciones astrofísicas. Simulando el efecto de los rayos cósmicos mediante electrones se ha podido concluir que estos no son suficientes para explicar la completa destrucción de la banda de tensión C-H, en acuerdo con otros resultados de la bibliografía. Se requieren más datos para determinar mecanismos paralelos, dado que la banda desaparece completamente en el medio interestelar denso.

Finalmente, con relación a la química en superficie en análogos de polvo, se han determinado las constantes de velocidad para la formación de agua sobre forsterita, un silicato con presencia en el medio interestelar. El mecanismo simulado es la adición de hidrógeno a un oxígeno adsorbido a dicha superficie, simulando un mecanismo Langmuir-Hinshelwood con la sucesiva adición de un primer átomo de hidrógeno para formar el radical hidroxilo y la posterior adición de un segundo hidrógeno, concluyendo la molécula de agua. Del estudio cinético derivado de estas simulaciones se concluye que la reacción no puede explicarse únicamente en términos clásicos, pues se requiere de correcciones de efecto túnel cuántico como condición necesaria para obtener constantes de velocidad que transcurran en lapsos de tiempo razonables desde el punto de vista astronómico. Una vez incluidas estas correcciones, se concluye que las reacciones son viables y contribuyen de forma relevante a la formación de agua tanto en fase sólida como gas en entornos astrofísicos.